University of Padova

Department of Astronomy

The Star Formation History of the Magellanic Clouds from HST and VISTA data

Author:
Stefano Rubele

Supervisor:
Dr. Leo Girardi
and
Dr. Paola Marigo

January 26, 2011

Summary

This thesis presents a study of the Star Formation History on the Magellanic Clouds using HST and VISTA data.

Chapter 2 introduces the VMC survey and then describes the observing strategy and first observations, the data reduction steps for producing images and catalogs for individual observations. Than present a description of the subsequent stages of reduction for deep and linked observations and presents the archival procedures.

In chapter 3 as part of the preparation for the VMC survey, we aim to access the accuracy in the Star Formation History (SFH) that can be expected from VMC data, in particular for the Large Magellanic Cloud (LMC). We first simulate VMC images containing LMC stellar populations and the foreground Milky Way (MW) stars and background galaxies. We then evaluate the expected errors in the recovered star formation rate as a function of stellar age, SFR(t), starting from models with a known Age–Metallicity Relation (AMR).

In chapter 4 we applied to the NGC 419 SMC star cluster data the classical method of star formation history (SFH) recovery via CMD reconstruction, deriving for the first time this function for a star cluster with multiple turn-offs. The values for the cluster metallicity, reddening, distance and binary fraction, were varied within the limits allowed by present observations. Star formation is found to last for at least 700 Myr, and to have a marked peak at the middle of this interval, for an age of 1.5 Gyr. Our findings argue in favour of multiple star formation episodes (or continued star formation) being at the origin of the multiple main sequence turn-offs in Magellanic Cloud clusters with ages around 1 Gyr.

In chapter 5 we studied the HST/ACS colour–magnitude diagrams (CMD) of the populous LMC star cluster NGC 1751 that present both a broad main sequence turn-off and a dual clump of red giants. We show that the latter feature is real and corresponds to the first appearance of electron-degeneracy in the H-exhausted cores of the cluster stars. We then apply to the NGC 1751 data the classical

method of star formation history (SFH) recovery via CMD reconstruction. After considering the random and systematic errors in the analysis, star formation in the cluster centre is found to last for a time span of 460 Myr.

In chapter 6 we present the preliminary results on the recovery of the SFH with VISTA data of 3 LMC VMC (Cioni et al. 2010) fields located around the LMC main body. Following the method described in Kerber et al. (2009a), Harris & Zaritsky (2004), Gallart et al. (1999) we evaluated the SFH deriving at the same time the Age Metallicity Relation AMR, the distance modulus $(m-M)_0$ and the extinction A_V . The comparison of ours results on the A_V and $(m-M)_0$ with Zaritsky et al. (2004) (for the A_V), Nikolaev et al. (2004), van der Marel & Cioni (2001b) and van der Marel et al. (2002) (for the $(m-M)_0$) to the VMC field 8_3 show an agreement with this authors in all subregions analyzed.

Chapter 7 summarizes and comments the results obtained in this work.

Riassunto

Questa tesi presenta uno studio sulla storia della formazione stellare delle nubi di Magellano usando dati osservati con i telescopi HST e VISTA.

Il capitolo 2 introduce il programma osservativo VMC e ne descrive la strategia osservativa e i primi risultati, la riduzione dati e i passi fatti per produrre le immagini scientifiche finali e i relativi cataloghi.

Il capitolo 3 presenta il lavoro di preparazine al programma VMC al fine di valutare l'accuratezza sulla ricostruzione della storia della formazione stellare (SFH) che ci si aspetta dai dati ottenuti con il telescopio VISTA nel caso della grande nube di Magellano (LMC). In questa parte della tesi sono state simulate le immagini del programma VMC nel caso della LMC contenenti tipiche popolazioni stellari osservate nella LMC, stelle appartenenti alla Via Lattea (MW) piu le galassie. In seguito sono stati analizzati gli errori dovuti al recupero della SFH in funzione dell' et*à*, partendo da modelli con conosciuta relazione et*à*–metallicita (AMR)

Nel capitolo 4 *è* stato applicato il metodo per il recupero della SFH attraverso il diagramma colore magnitudine all'ammasso NGC 419 nella SMC. E stato possibile derivare per la prima volta la SFH per un ammasso che presenta un turn-offs multiplo. Si sono potuti derivare inoltre la metallicit*à*, l'estinzione, il modulo di distanza e la frazione di binarie nei limiti degli errori stocastici e sistematici. Abbiamo valutato per questo ammasso un periodo prolungato di formazione stellare con ampiezza pari a 700 Myr, e con un picco di et*à* a 1.5 Gyr. I nostri risultati favoriscono l'idea che all'origine del turn-offs multiplo di sequenza principale in ammassi delle nubi di Magellano con et*à* vicine a 1 Gyr ci siano episodi di formazione stellari multipli.

Nel capitolo 5 abbiamo studiato il diagramma colore–magnitudine (CMD) ottenuto utilizzando i dati HST/ACS dell'ammasso stellare NGC 1751 nella LMC, il quale presenta un turn-off di sequenza principale allargato ed un doppio clump per le giganti rosse. Abbiamo dimostrato che queste caratteristiche nel CMD si

spiegano allo stesso modo di quanto fatto per l'ammasso NGC419 nel capitolo precedente. Applicando anche a questo ammasso il metodo per la ricostruzione della SFH via CMD abbimo valutato il tasso di formazione stellare in funzione del tempo trovando un'ampiezza pari a 460 Myr.

Il capitolo 6 presnta i primi risultati sul recupero della SFH con dati VMC (Cioni et al. 2010) per 3 campi della LMC localizzati attorno alla parte centrale della galassia. Seguendo il metodo descritto nel capitolo 3, Harris & Zaritsky (2004), Gallart et al. (1999) abbiamo misurato la SFH e derivato contemporaneamente la relazione et*à* metallicit*à* AMR, il modulo di distanza $(m-M)_0$ e l'estinzione A_V . In fine abbiamo confrontato i nostri risultati per A_V e $(m-M)_0$ con quelli ottenuti in Zaritsky et al. (2004) (per A_V), Nikolaev et al. (2004), van der Marel & Cioni (2001b) e van der Marel et al. (2002) (per $(m-M)_0$). Per il campo 8_3 il confronto mostra un buon accordo nella gran parte delle aree considerate.

In fine il capitolo 7 riassume e commenta tutte le parti affrontate in questo lavoro.

Contents

List of Figures

List of Tables

Chapter 1

Introduction

Determining the star formation histories (SFH) of the Magellanic Clouds (MC) is one of the most obvious goals in the study of nearby galaxies, for a series of reasons. First, this SFH does likely keep record of the past interactions between both Clouds and the Milky Way (Olsen 1999; Holtzman et al. 1999; Smecker-Hane et al. 2002; Harris & Zaritsky 2004), which are still to be properly unveiled (Kallivayalil et al. 2006b,a; Besla et al. 2007; Piatek et al. 2008). Detailed SFH studies may also provide unvaluable hints on how star formation is triggered and proceeds in time, from the smallest to galactic-size scales, and how these processes depend on dynamical effects (e.g. Harris & Zaritsky 2007; Harris 2007a).

The Magellanic Clouds are also a rich laboratory for studies of star formation and evolution, and the calibration of primary standard candles, thanks to the simultaneous presence of a wide variety of interesting objects such as red clump giants, Cepheids, RR Lyrae, long period variables, carbon stars, planetary nebulae, the tip of the red giant branch (RGB), dust-enshrouded giants, pre-main sequence stars, etc. Although the system contains several hundreds of star clusters for which age and metallicity can be measured, the bulk of the interesting stellar objects are actually in the field and irremediably mixed by the complex SFH, and also partially hidden by the presence of variable and patchy extinction across the MCs. Unveiling this complex SFH may help in calibrating stellar properties – like luminosities, lifetimes, periods, chemical types, etc. – as a function of age and metallicity.

In the last two decades, many authors demonstrated that recovering the SFH of the MC from optical photometry is indeed feasible and well worth of the effort. Such works are, usually, based either on deep Hubble Space Telescope (HST) photometry reaching the oldest main sequence turn-off for small MC areas (e.g. Gal-

lagher et al. 1996; Holtzman et al. 1999; Olsen 1999; Elson et al. 1997; Smecker-Hane et al. 2002; Ardeberg et al. 1997; Dolphin et al. 2001; Javiel et al. 2005), or on relatively shallow ground-based photometry covering larger areas over the MCs (Stappers et al. 1997; Gardiner & Hatzidimitriou 1992; Harris & Zaritsky 2001, 2004). Only in very few cases (e.g. Gallart et al. 2004; Noël et al. 2007) have the ground-based optical photometry been deep enough to reach the oldest main sequence turn-offs. The near infrared VMC survey (Cioni et al. 2010) will permit to derive with high accuracy not only on the SFR(t) but also the 3D Magellanic clouds structure and its extinction map. All these information will help astronomers to understand the origin and evolution of the interactive system LMC + SMC + MW typical on a ΛCDM cosmological view.

Also using ACS HST data archive help us to study the substructure as star cluster and small field portion of MC system, improving results on the determination of $(m-M)_0$, A_V, stellar evolution, and compare the results with those obtained with VMC data.

This thesis is organized as follows:

- Chapter 2 introduces the VMC survey and then describes the observing strategy and first observations, the data reduction steps for producing images and catalogs for individual observations. Than present a description of the subsequent stages of reduction for deep and linked observations and presents the archival procedures.

- In chapter 3 as part of the preparation for the VMC survey, we aim to access the accuracy in the Star Formation History (SFH) that can be expected from VMC data, in particular for the Large Magellanic Cloud (LMC). To this aim, we first simulate VMC images containing not only the LMC stellar populations but also the foreground Milky Way (MW) stars and background galaxies. The simulations cover the whole range of density of LMC field stars. We then perform aperture photometry over these simulated images, access the expected levels of photometric errors and incompleteness, and apply the classical technique of SFH-recovery based on the reconstruction of colour-magnitude diagrams (CMD) via the minimization of a chi-squared-like statistics. We verify that the foreground MW stars are accurately recovered by the minimization algorithms, whereas the background galaxies can be largely eliminated from the CMD analysis due to their particular colors and morphologies. We then evaluate the expected errors in the recovered star formation rate as a function of stellar age, SFR(t), start-

ing from models with a known Age–Metallicity Relation (AMR). It turns out that, for a given sky area, the random errors for ages older than $\sim$ 0.4 Gyr seem to be independent of the crowding; this can be explained by a counterbalancing effect between the loss of stars due to a decrease in the completeness, and the gain of stars due to an increase in the stellar density. For a spatial resolution of $\sim 0.1\,\mathrm{deg}^2$, the random errors in SFR(t) will be below 20% for this wide range of ages. On the other hand, due to the smaller stellar statistics for stars younger than $\sim$ 0.4 Gyr, the outer LMC regions will require larger areas to achieve the same level of accuracy in the SFR(t). If we consider the AMR as unknown, the SFH-recovery algorithm is able to accurately recover the input AMR, at the price of an increase of random errors in the SFR(t) by a factor of about 2.5. Experiments of SFH-recovery performed for varying distance modulus and reddening indicate that these parameters can be determined with (relative) accuracies of $\Delta(m-M)_0 \sim 0.02$ mag and $\Delta E_{B\text{-}V} \sim 0.01$ mag, for each individual field over the LMC. The propagation of these latter errors in the SFR(t) implies systematic errors below 30%.

- In chapter 4 we applied to the NGC 419 SMC star cluster data the classical method of star formation history (SFH) recovery via CMD reconstruction, deriving for the first time this function for a star cluster with multiple turn-offs. The values for the cluster metallicity, reddening, distance and binary fraction, were varied within the limits allowed by present observations. The global best-fitting solution is an excellent fit to the data, reproducing all the CMD features with striking accuracy. The corresponding star formation rate is provided together with estimates of its random and systematic errors. Star formation is found to last for at least 700 Myr, and to have a marked peak at the middle of this interval, for an age of 1.5 Gyr. Our findings argue in favour of multiple star formation episodes (or continued star formation) being at the origin of the multiple main sequence turn-offs in Magellanic Cloud clusters with ages around 1 Gyr. It remains to be tested whether alternative hypotheses, such as a main sequence spread caused by rotation, could produce similarly good fits to the data.

- In chapter 5 we studied the HST/ACS colour–magnitude diagrams (CMD) of the populous LMC star cluster NGC 1751 that present both a broad main sequence turn-off and a dual clump of red giants. We show that the latter feature is real and corresponds to the first appearance of electron-

degeneracy in the H-exhausted cores of the cluster stars. We then apply to the NGC 1751 data the classical method of star formation history (SFH) recovery via CMD reconstruction, for different radii corresponding to the cluster centre, the cluster outskirts, and the underlying LMC field. The mean SFH derived from the LMC field is taken into account during the stage of SFH-recovery in the cluster fields, in a novel approach which is shown to significantly improve the quality of the SFH results. In the case of the cluster centre, the global best-fitting solution provides an excellent fit to the data – with χ^2 and residuals close to the theoretical minimum – reproducing all the CMD features with striking accuracy. After considering the random and systematic errors in the analysis, star formation in the cluster centre is found to last for a time span of 460 Myr. The results for a larger ring region around the centre indicates even longer star formation, but in this case the results are of lower quality and less reliable, probably because of the presence of differential extinction in the area. Together with our previous findings for the SMC cluster NGC 419, the present results argue in favour of multiple star formation episodes (or continued star formation) being at the origin of the multiple main sequence turn-offs in Magellanic Cloud clusters with ages around 1.5 Gyr.

- In chapter 6 we present the preliminary results on the recovery of the SFH with VISTA data of 3 LMC VMC (Cioni et al. 2010) fields located around the LMC main body. Following the method described in Kerber et al. (2009a), Harris & Zaritsky (2004), Gallart et al. (1999) we evaluated the SFH deriving at the same time the Age Metallicity Relation AMR, the distance modulus $(m-M)_0$ and the extinction A_V . We have Combined Paw-Print (Irwin 2010) pre-reduced images obtaining deep tiles on witch we made Point Spread Function PSF photometry and Artificial Star Tests AST to derive errors and completeness of the data. Finally we have run our pipeline to recover the SFH as described in Kerber et al. (2009a) and Rubele et al. 2011 . The comparison of ours results on the A_V and $(m-M)_0$ with Zaritsky et al. (2004) (for the A_V), Nikolaev et al. (2004), van der Marel & Cioni (2001b) and van der Marel et al. (2002) (for the $(m-M)_0$) to the VMC field 8_3 show an agreement with this authors in all subregions analyzed.

- Chapter 7 summarizes and comments the results obtained in this work.

Chapter 2

The VMC survey

2.1 Introduction

The new VISual and Infrared Telescope for Astronomy (VISTA) has started operations. Over its first five years it will be collecting data for six Public Surveys, one of which is the near-infrared YJK_s VISTA survey of the Magellanic Clouds system (VMC). This survey comprises the Large Magellanic Cloud (LMC), the Small Magellanic Cloud, the Magellanic Bridge connecting the two galaxies and two fields in the Magellanic Stream.This work provides an overview of the VMC survey strategy and presents first science results. The main goals of the VMC survey are the determination of the spatially-resolved star-formation history and the three-dimensional structure of the Magellanic system. The VMC survey is therefore designed to reach stars as faint as the oldest main sequence turn-off point and to constrain the mean magnitude of pulsating variables such as RR Lyrae stars and Cepheids. This work focuses on observations of VMC fields in the LMC obtained between November 2009 and March 2010. These observations correspond to a completeness of 7% of the planned LMC fields.The VMC data are comprised of multi-epoch observations which are executed following specific time constraints. The data were reduced using the VISTA Data Flow System pipeline with source catalogues, including astrometric and photometric corrections, produced and made available via the VISTA Science Archive. The VMC data will be released to the astronomical community following the European Southern Observatory's Public Survey policy. The analysis of the data shows that the sensitivity in each wave band agrees with expectations. Uncertainties and completeness of the data are also derived.The first science results, aimed at assessing the scien-

tific quality of the VMC data, include an overview of the distribution of stars in colour-magnitude and colour-colour diagrams, the detection of planetary nebulae and stellar clusters, and the K_s band light-curves of variable stars.The VMC survey represents a tremendous improvement, in spatial resolution and sensitivity, on previous panoramic observations of the Magellanic system in the near-infrared, providing a powerful complement to deep observations at other wavelengths.

2.2 The survey

The VMC[1] is a uniform and homogeneous survey of the Magellanic system in the near-IR with VISTA. The main parameters of the survey are summarised in Tab. 2.1. It is the result of a letter of intent submitted in 2006 and a science and management plan approved early in 2008. The main science goals of the survey are the determination of the spatially-resolved star-formation history (SFH) and the three-dimensional (3D) structure of the Magellanic system. VMC observations will detect stars encompassing most phases of evolution: main-sequence stars, subgiants, upper and lower red giant branch (RGB) stars, red clump stars, RR Lyrae and Cepheid variables, asymptotic giant branch (AGB) stars, post-AGB stars, planetary nebulae (PNe), supernova remnants (SNRs), etc. These different populations will help assess the evolution of age and metallicity within the system.

The SFH will be recovered from the analysis of colour-magnitude diagrams (CMDs) and simulations of the observed stellar populations, accounting for foreground stars and extinction. Kerber et al. (2009b) show a preliminary assessment of the SFH accuracy that can be expected from VMC data. Modelling near-IR colours bears no greater uncertainty than optical colours and the near-IR is particularly sensitive to the colour of the oldest turn-off stars. The 3D geometry will be derived using different density and distance indicators like the luminosity of red clump stars and the Cepheid and RR Lyrae period-luminosity relation, and period-luminosity-colour and Wesenheit relations. These results will complement those based on 2MASS data for the AGB and upper RGB populations of the LMC van der Marel & Cioni (2001a) and those from optical data of the central regions of the galaxies that are affected by a higher reddening e.g. Subramanian & Subramaniam (2010a) and crowding. We will constrain the epoch of formation of each galactic component by mapping the extent of different kinds of stars and deriving, using up-to-date stellar evolutionary models, ages and metallicities. The VMC

[1] http://star.herts.ac.uk/~mcioni/vmc

survey science addresses many other issues in the field of star and galaxy formation and evolution, such as: stellar clusters and streams; extended sources; proper motions; star formation; distance scale; models of Magellanic system evolution; extinction mapping.

2.2.1 The VISTA telescope and camera

VISTA is a new 4m class telescope developed in the United Kingdom (UK). It formed part of the in-kind contribution of the UK to joining the European Southern Observatory (ESO). The telescope has an alt-azimuth mounting and is located just 1.5 km from the Very Large Telescope (VLT) site. The VISTA infrared camera (VIRCAM) (see picture 2.1) is equipped with an array of 16 Raytheon detectors (see picture 2.2) with a mean pixel size of 0.339″ and a field of view of 1.65 deg^2. The VIRCAM has a set of broad-band filters: Z, Y, J, H and K_s and a narrow-band filter at 1.18 μm. The point spread function of the system is specified to have 50% of the light from a point source contained within a circle of diameter 0.51″. The telescope and its camera are described by Eme Emerson et al. (2006) and Dalton et al. (2006), while the performance during commissioning is presented by Emerson & Sutherland (2010). The science verification programmes are summarised by Arnaboldi et al. (2010).

VISTA is the largest wide-field near-IR imaging telescope in the world and it is designed to perform survey observations; at present there are six Public Surveys underway[2]. VISTA observes a continuous area of sky by filling in the gaps between the detectors using a sequence of six offsets, each by a significant fraction of a detector. The combined image corresponds to a VISTA *tile* that covers ~ 1.5 deg^2, while individual offset positions are named *paw-prints* and cover an area of 0.59 deg^2. The resulting VISTA tile observes each part of sky within it at least twice, except for two edge strips in the extreme 'Y' directions of the array. The tiling process for the VMC survey ensures that adjacent tiles overlap sufficiently to provide two observations of these areas as well. The combination of offsets generates small overlapping areas with exposures as large as six times a single paw-print. These steps are described in the VISTA user manual[3].

The VMC survey is a near-IR YJK_s survey of the Magellanic system. Compared to previous surveys using the 2MASS and DENIS telescopes, the choice of VISTA filters for the VMC survey was driven by the following considerations.

[2]http://www.eso.org/sci/observing/policies/PublicSurveys/sciencePublicSurveys.html
[3]http://www.eso.org/sci/facilities/paranal/instruments/vista/doc/

Table 2.1: VMC survey parameters.

Filter	Y	J	K_s
Wavelength (μm)	1.02	1.25	2.15
Bandwidth (μm)	0.10	0.18	0.30
DIT (sec)	20	10	5
DITs	4	8	15
Exposures	1	1	1
Micro-stepping	1	1	1
Jitters	5	5	5
Paw-prints in tile	6	6	6
Pixel size (arcsec)	0.339	0.339	0.339
System FWHM	0.51	0.51	0.51
Exposure(t) (sec)	800	800	750
Number of epochs	3	3	12
Total exposure(t) (sec)	2400	2400	9000
Predicted sensitivity (Vega mag)	21.3	20.8	18.9
Signal-to-noise required	5.7	5.9	2.9
Total predicted sensitivity (Vega mag)	21.9	21.4	20.3
Total S/N at depth required	10	10	10
Saturation limit (Vega mag)	12.9	12.7	11.4
Area (deg^2)	184	184	184
Number of tiles	110	110	110

Jitter pattern = $Jitter5n$. Tile pattern = $Tile6zz$.

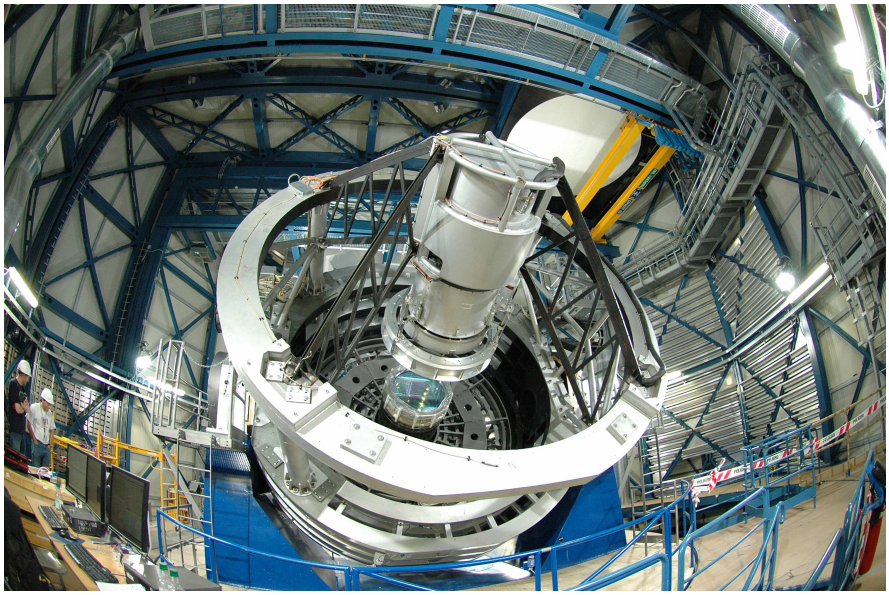

Figure 2.1: View of the VISTA infrared camera (VIRCAM) mounted on the telescope

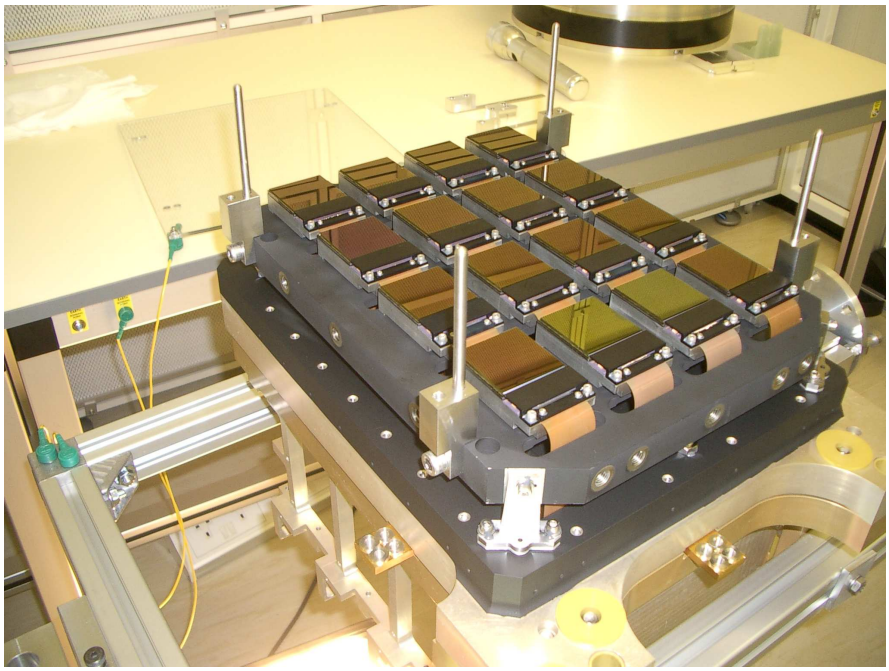

Figure 2.2: View of the 16 detectors array

A total of three filters were chosen to be able to analyse colour-colour diagrams. The availability of a large colour spacing to allow for a good characterisation of the subgiant branch population to derive the SFH. The relation between $J-H$ and $J-K_s$ is quite linear for MC giants, so observations in the H band would have provided very little information and priority was given to a bluer filter. The J band was preferred over H as it also suffers less from atmospheric effects, and provides comparative observations with respect to previous surveys. The choice of Y over Z was motivated by a reduced confusion limit. The K_s filter was required to determine the average magnitude of variable stars that, at this wavelength, obey a clear period-magnitude relation that is unaffected by other stellar parameters that degrade the relation at bluer wavelengths. A comparison among the filter transmission curves for the VMC, 2MASS and DENIS observations is shown in Fig. 2.3. The exposure time for the VMC survey (Tab. 2.1) is designed to meet the two key scientific objectives: the SFH and the 3D geometry. An accurate determination of the SFH requires CMDs reaching the oldest main sequence turn-off, to allow for sampling of different stellar populations. The investigation of RR Lyrae stars and Cepheids requires monitoring observations across specific time intervals. The stacking of the observations that are needed for deriving the mean magnitude of variable stars in the K_s band meets also the depth requirement for the SFH. The split of epochs in the Y and J filters is instead purely driven by scheduling requirements.

2.2.2 VMC area coverage

Observing the entire Magellanic system extending over hundreds of kpc (the Stream covers half the sky) is a daunting task. The VMC survey concentrates, therefore, on a moderately extended area (~180 deg^2) that includes the classical diameter limit at $B \approx 25$ mag arcsec^{-2} for both galaxies Bothun & Thompson (1988) as well as major features traced by the distribution of stars (e.g. Irwin (1991), Bica et al. (2008)) and H I gas (e.g. Staveley-Smith et al. (2003), Hatzidimitriou et al. (2005), Muller et al. (2003)), the Bridge and two fields at specific locations in the Stream.

The LMC area (116 deg^2) is covered by 68 tiles, while 27 tiles cover the SMC (45 deg^2) and 13 cover the Bridge (20 deg^2), see Fig. 2.4. Additionally, 2 tiles (3 deg^2) are positioned in the Stream, one approximately to the North of the centre of the Bridge (corresponding to a dense area of gas) and the other, at similar right ascension, to the North of the SMC, corresponding to a dense area of stars following the simulations by Mastropietro (2009). VMC tile centre coordinates

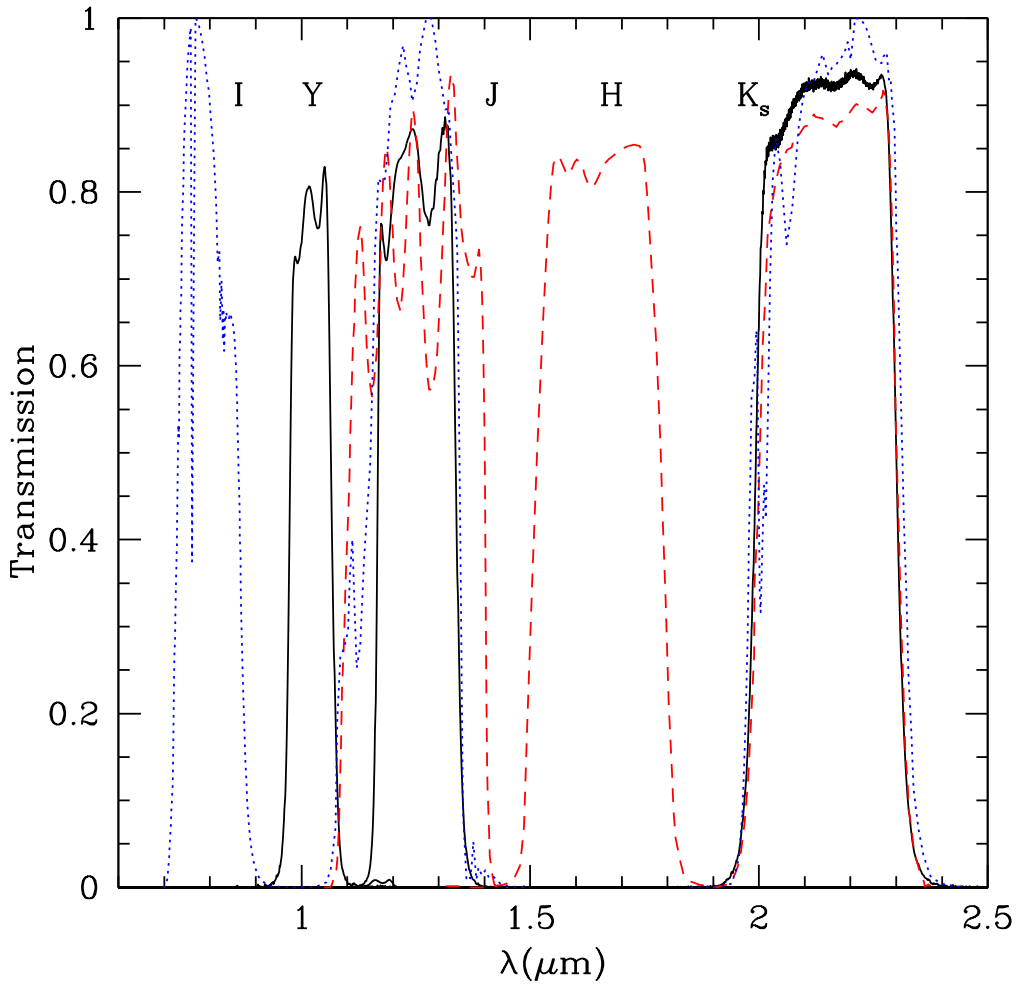

Figure 2.3: Filter transmission curves for the VMC survey (YJK_s – black continuous lines) compared with the transmission of the 2MASS (JHK_s – red dashed lines) and DENIS (IJK_s – blue dotted lines) surveys.

are given in the Appendix. Each tile is identified by two numbers: the first number indicates the row and the second the column of the position of the tile in the mosaic that covers the system. Note that a separate tiling pattern has been defined for each region (Figs. A.1, A.2, A.3). Row numbers increase from South to North and column numbers increase from West to East.

Tiles covering the LMC were oriented at a position angle of +90 deg. The default orientation (position angle = 0 deg) points the 'Y' axis to the North and the 'X' axis to the West. The position angle is defined to increase from North to East. This represents the best compromise between minimum number of tiles and maximum area, increasing the efficiency of the survey. The overlap between the doubly-covered sky areas in adjacent tiles corresponds to 60″ in both 'X' and 'Y' directions. The LMC mosaic was created using the Survey Area Definition Tool (SADT – Arnaboldi et al. (2008)). A geodesic rectangle centred at α = 05:35:50, $\delta = -69$:27:12 (J2000), with width = 11.8 deg and height = 15.9 deg, was created as the basis of the tiling process. Outer tiles were removed leading to the pattern shown in Fig. 2.4 (see also Fig. A.1). The area covered by the tiles was checked against the distribution of stellar associations, carbon stars and other stellar objects using Aladin (Bonnarel et al. 2000). The centre of the rectangle was adjusted to include the 30 Doradus nebulosity within a single tile and, similarly, the field that the future space mission Gaia[4] will repeatedly observe for calibration.

In the process of creating the mosaic, SADT requires as input the observing parameters that are associated to small (i.e. jittering) and large (i.e. mosaicking) displacements in the tile position. For the VMC survey the maximum jitter was set to 15″, the *backtrackStep* to 100 and the tiling algorithm to $Tile6zz$ (these parameters are described in the SADT user manual). Guide stars were assigned automatically to each tile using the GSC-2 reference catalogue (Lasker et al. (2008)). This process may result in shifting the tile centre in case an insufficient number of reference stars is available, but this was not the case for LMC tiles.

Tiles covering the SMC region were placed at a position angle of 0 deg. Keeping the wide tile-edge approximately along the right ascension direction produces maximum coverage for a minimum number of tiles. This also implies centring the geodesic rectangle at α = 00:50:00, $\delta = -73$:00:00 (J2000), with width = 8.0 deg and height = 8.0 deg. This rectangle represents the basis of the tiling process and outer tiles were subsequently removed leading to the pattern shown in Fig. 2.4 (see also Fig. A.2). As before, the area covered by tiles was checked against the distribution of different stellar objects. The position of the centre of the rectangle

[4]http://sci.esa.int/science-e/www/area/index.cfm?fareaid=26

was tuned to match the area that will be observed in the optical domain by the VST[5] (VLT Survey Telescope) as part of the STEP survey (P.I. Ripepi; Capaccioli et al. (2005)) and to provide sufficient overlap for a consistent calibration with the Bridge area.

Previous observations of the Magellanic Bridge by Battinelli & Demers (1992) and Harris (2007b) covered fields departing from the LMC and tracing arcs at different declinations with only a few fields between the two. In order to maximise the total population of stars that the VMC survey will detect the 2MASS, DENIS and SuperCOSMOS[6] databases were explored for stellar densities and compared with the previous observations. VMC tiles were then positioned to overlap with the area that provides a good sampling of the stellar population while also following a continuous pattern. Following a similar procedure for the LMC and SMC areas, a geodesic rectangle was drawn with centre at α = 03:00:00, $\delta = -74$:30:00 (J2000), with width 13.5 deg and height 3 deg. Outer tiles were subsequently removed leading to the pattern shown in Fig. 2.4 (see also Fig. A.3).

The two tiles positioned in the Stream region were prepared using the same parameters as for LMC tiles, except for the position angle set to 0 deg. Two geodesic rectangles centred on the two fields were defined, each with a default size equal to a single tile.

2.2.3 VMC observations

The VMC data described here were mostly obtained during Science Verification observations (15−31 October 2009) and the so-called dry-run period (1 November 2009 – 31 March 2010) when VISTA was tested and survey operations were still being defined. A small amount of data was also taken during ESO Period 85 (1 April 2010 – 30 September 2010). The bulk of the VMC observations will be carried out during the odd–numbered ESO periods starting in October every year and ending in March the following year because of the seasonal observability of the Magellanic system.

Observations of the VISTA Public Survey are obtained in service mode by ESO staff. This guarantees efficiency of operations and a high level of data homogeneity. The requested observing conditions for the VMC survey are summarised in Table 2.2. A dozen tiles, centred on the most crowded regions i.e. 30 Dor and the central regions of both LMC and SMC, have more stringent seeing conditions.

[5] http://vstportal.oacn.inaf.it/

[6] http://surveys.roe.ac.uk/ssa/index.html

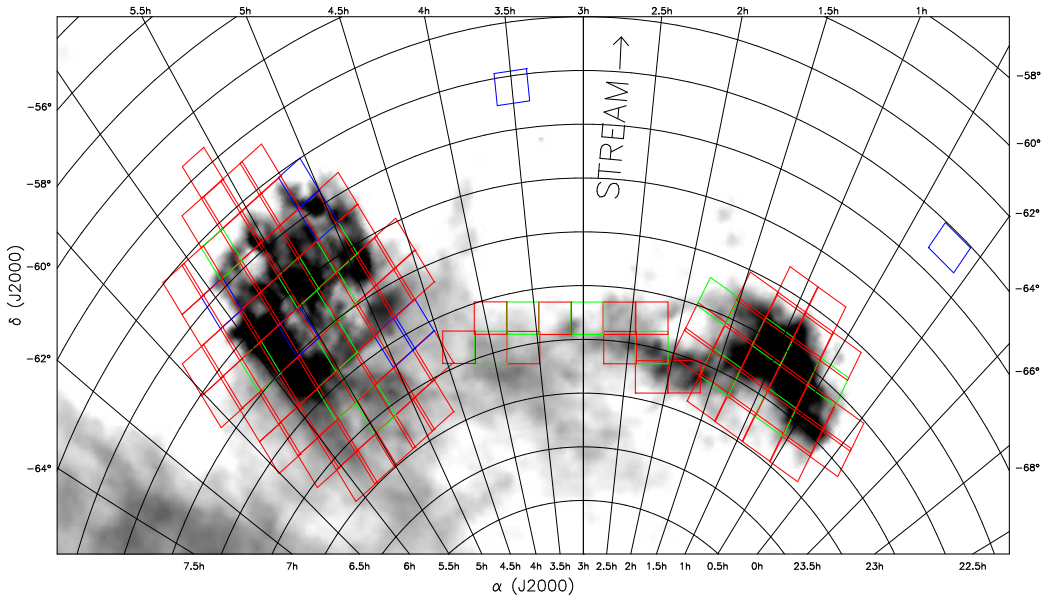

Figure 2.4: Magellanic system area tiled for VMC observations. The underlying image shows the HI distribution (McClure-Griffiths et al. McClure-Griffiths et al. (2009)). VISTA tiles are colour coded as follows. Blue rectangles represent tiles for which observations have started during the dry-runs and P85, green rectangles are for tiles with observations in P86, and red tiles are observations that will not being before P87.

Table 2.2: VMC required weather conditions.

Band	Seeing (arcsec) uncrowded	Seeing (arcsec) crowded
Y	1.2	1.0
J	1.1	0.9
K_s	1.0	0.8
Field	**Tile row**	**Airmass**
LMC	2, 3, 4	1.7
LMC	5, 6, 7	1.6
LMC	8, 9, 10, 11	1.5
Stream	1, 2	1.5
SMC	2, 3, 4, 5	1.7
SMC	6, 7	1.6
Bridge	1, 2, 3	1.7

Moon distance > 80 deg. Sky transparency = variable, thin cirrus.

This is necessary to prevent confusion in the bluest bands, while K_s band observations will not be limited by confusion for a seeing $\leq 0.9''$. The best FWHMs in the VISTA images are $0.6 - 0.7''$ and undersampling, with respect to a pixel size of $0.334''$, is not a cause of concern in the data treatment.

The Magellanic system never rises above 50° from the horizon. Therefore, a compromise had to be made between observing at reasonable airmass and achieving continuous observability over about five months for the monitoring process. The maximum airmass constraints were optimised as a function of the tile declination, as shown in Tab. 2.2. A violation of any observing constraint by 10% is still considered as if observations were obtained within specifications. It is also assumed that the airmass constraint may be violated by more than 10% provided the seeing constraint is not.

Table 2.1 describes the main parameters of the VMC observations. The total exposure time is calculated as follows: (number of epochs) $\times 2 \times$ (number of jitters) $\times$ (number of DITs) $\times$ DIT. The factor of two comes from the tiling pattern, during which most points of the sky are observed twice (on average). The exceptions are the tile edges, observed once, and some areas of extra overlap among the detectors that are observed four or six times. For example, for the K_s band the total exposure time is: $12 \times 2 \times 5 \times 15 \times 5 = 9000$ sec.

The observations follow the nesting sequence FPJME (see VISTA User Manual[7]). This sequence first sets a filter, then obtains images at all jittered positions of the first paw-print, before moving to the next paw-print and taking all the jittered images at that position, and so on, until all six paw-prints that form the tile are completed. The jittern pattern was *jitter5n* and the tile pattern was *Tile6zz*.

The progress of the VMC survey is shown in Fig. 2.4 and detailed in Tab. 2.3. The reader is referred to the VMC[1] public web page for following up the survey progress beyond that described in this work.

Science Verification

The observation of a single paw-print in the YJK_s filters was requested during the instrument Science Verification (SV) time. The main goal was to verify the observing strategy and to test the saturation limits for the adopted DITs of 6, 10 and 20 sec in the K_s, J and Y bands, respectively. The observations were carried out on the night of 17 October 2009, but the data were only available after the dry-runs had started.

[7] http://www.eso.org/sci/facilities/paranal/instruments/vista/doc/

Table 2.3: VMC survey progress.

Description	VMC all	LMC all	LMC season I
Total number of tiles	110	68	6
Total number of epochs	1980	1224	108
Total number of Y-band epochs	330	204	18
Total number of J-band epochs	330	204	18
Total number of K_s-band epochs	1320	816	72
Observed number of Y-band epochs	18	18	18
Observed number of J-band epochs	18	18	18
Observed number of K_s-band epochs	51	51	51
Total number of observed epochs	87	87	87
Completion in the Y-band	5.4%	8.8%	100%
Completion in the J-band	5.4%	8.8%	100%
Completion in the K_s-band	3.9%	6.2%	71%
Total completion	4.4%	7.1%	80%

The SV data indicate that the saturation limit varies from one detector to another. On average, it is 11.6 mag for the 6 sec K_s band exposure, with seeing of 0.94″. The linearity is mild at 11.6 mag, but becomes severe for point sources brighter than 10.7 mag. These limiting magnitudes are somewhat fainter than predicted. Prior to the beginning of the dry-runs it was decided to reduce the K_s band DIT down to 5 sec, which improves the photometry of the bright stars and maximises the range of overlapping magnitudes with 2MASS. The observing strategy was then established and no modification was needed for the observations that had already started.

Other SV observations were obtained on 28 Nov 2009 in the SMC. These are K_s band observations of one tile, with a six paw-print mosaic and DIT= 10 sec, with the purpose of checking the sky-subtraction procedures. Images were obtained to test an off-sky algorithm which is not applicable to VMC data. In addition, some 2MASS touchstone fields that are observed for photometric checks are located in the VMC survey area, providing extra, albeit shallow (DIT= 5 sec), multi-epoch data in all VIRCAM filters.

2.3 Data Reduction

The raw VISTA images acquired for the VMC survey were reduced by the VISTA Data Flow System (VDFS) pipeline at the Cambridge Astronomical Survey Unit (CASU[8]). The VDFS pipeline is specifically designed for reducing VISTA data (Irwin et al. (2004)) and is used to process up to 250 GB/night of data. The pipeline is a modular design allowing straightforward addition or removal of processing stages. The VMC data are reduced together with other VISTA data on a weekly basis. Prior to this science reduction the data are checked at the observatory site (ESO Chile) using a simplified version of the VDFS pipeline and library calibrations. The data are subsequently checked at ESO in Garching for monitoring the instrument performance and to feed updated information back to the observatory.

The most relevant VDFS steps for the reduction of VMC survey data are as follows:

- reset, dark, linearity, flat and de-striping (removing horizontal stripes in the background) correction;
- sky background correction (tracking and homogenisation during image stacking and mosaicking);
- jittered and paw-print stacking;
- point source extraction;
- astrometric and photometric calibration (the latter put in an internally uniform system);
- bad pixel handling, propagation of uncertainties and effective exposure times by use of confidence maps;
- nightly extinction measurements.

The different observational uncertainties are propagated during the data processing, to give the users a clear picture of the final data quality. Various quality control parameters are calculated during the data reduction to monitor the data, and to evaluate both the observing conditions (in retrospect) during the observation, and the individual data reduction steps. Among them are: the zero-point to

[8]http://casu.ast.cam.ac.uk/surveys-projects/vista

measure the atmospheric extinction, the FWHM to measure the seeing, the ellipticity to evaluate the quality of the guiding and active optics correction, the sky level to estimate the background level and its variations, etc.. The processing history is recorded directly in FITS headers.

A tile image is produced by combining 96 different images (16 detector images per each of 6 paw-prints). Their sky level and individual paw-print astrometric and photometric distortion are adjusted in the drizzling (combination) process. Tile catalogues are produced following the application of a nebulosity filter to the paw-prints in order to remove diffuse varying background on scales of 30″ or larger (Irwin (2010)). This method has shown that the detection of objects and their characterisation (astrometry, photometry and morphological classification) are considerably improved.

The first VMC reduced images and catalogues, corresponding to observations obtained during November 2009, were received in January 2010. These data were reduced with version 0.6 (v0.6) of the VDFS pipeline and refer to individual paw-prints, not yet combined into tiles. This means that in practise, for example, the observation of a Y-band OB of a given field has 6 associated images, 6 catalogues and 6 confidence maps. Each image and catalogue are delivered in Rice compressed format and are multi-extension FITS files containing each the information for all of the 16 detectors covering the VIRCAM field-of-view. In March 2010 we received more data processed with an upgraded version of the pipeline (v0.8). These data include all observations obtained until the end of January 2010. The processed observations obtained after this date and until the end of the Magellanic season (March 2010) were received in April 2010. Following quality inspection a few images were re-reduced (v0.9) to fix some specific problems with a small subset of the data. The v0.8 data were ingested into the VISTA Science Archive (VSA) by June 2010 (Sect. 2.4). They include astrometry and photometry in single-band, band-merged and epoch-merged tables as well as deep stacks. In October 2010 v1.0 data have become available and the main difference from previous releases is that they include tile images and catalogues.

Figure 2.5 shows most of a tile of the 6_6 LMC field including the star forming region 30 Dor. This image was produced for an ESO press release[9] where other zoomed-in images are also available. The exposure time in the three wave bands was 2400 sec in Y, 2800 sec in J and 4850 sec in K_s.

[9]http://www.eso.org/public/news/eso1033/

Figure 2.5: Most of VMC tile of LMC field 6_6. This is a colour composite image where Y is shown in blue, J in green and K_s in red. East is to the left and North at the top. The 30 Doradus star forming region is visible together with other smaller regions towards the South as well as stellar clusters and the field population. For more details and a high resolution image refer to http://www.eso.org/public/news/eso1033/.

2.3.1 Linearity and background

The individual VISTA detectors have different non-linearity and saturation properties and these properties may also vary across a given detector. The detector system is non-linear and linearity corrections are applied at the pixel level during the initial image processing stages. The saturation levels are stored in the image header keywords and, together with the peak flux derived from the photometry of the observed sources, it is possible to establish a correction that enables recovery of stars up to a few magnitudes brighter than the saturation limit (Irwin (2009)). This correction is not implemented by VDFS prior to the production of VMC catalogues but it is applied at a further stage of the data processing (Sect. 2.4). The expected saturation values listed in Tab. 2.1 are sensitive to seeing variations. In fact, the 30 Dor region was observed under very good conditions, and saturation appears at fainter magnitudes.

The application of a nebulosity filter to the paw-print images prior to the construction of a tile image (Irwin (2010)), may influence the recovery of the magnitude of stars close to the saturation limit. This would, however, only affect heavily saturated stars, i.e. those where a significant halo with a diameter comparable to that of the filter size ($\sim 30''$) is visible.

The sky background for VMC observations is estimated, for each paw-print, from all paw-prints observed for one tile in a given band and at a given time. This method, referred to as 'tilesky', has shown very good results even for the 30 Dor tile where there is a substantial emission from the nebula.

Persistence effects due to bright stars are usually automatically removed by the VDFS pipeline when the observations, like for VMC, follow the FPJME sequence (see VISTA User Manual[6]). Adding up all VMC images for a given field and filter does not produce any noticeable effect due to persistence.

The moon has a negligible effect on the VMC background because it is always >80 deg away from any of the fields. This results in low contamination, even in the *Y* band which is most susceptible to the lunar contamination. The major absorption is caused by water vapour and carbon dioxide in the atmosphere. At the VMC filters the background will also be dominated by non-thermal aurora emission, OH and O_2 lines especially in observations obtained 1.5 – 2 hours after twilight.

2.3.2 Astrometry

Astrometry is based on positions of the many 2MASS sources within each detector. The astrometric calibration of a paw-print is encoded in the FITS image headers using the Zenithal Polynomial projection (ZPN) while a tile refers to a single tangent plane World Coordinate System (WCS) image (Calabretta & Greisen (2002)). The median astrometric root-mean-square is 80 mas and is dominated by 2MASS uncertainties. Residual systematic distortions across the VISTA field-of-view are at the ∼25 mas level and can be further improved, if required, by directly characterising the distortion pattern. In a dithered sequence the detectors are rotated slightly to maintain the position angle on the sky; a comparison between identical VISTA observations shows a residual rotation of ∼0.5 pix.

Figure 2.6 shows a comparison between the right ascension (α) and declination (δ) coordinates of stars that are in common between VISTA and 2MASS in the VMC field 8_8. The excellent match shows the quality of the astrometry. A systematic shift is perhaps present at the level of $\sim$ 0.01″ in both axes. This accuracy is perfectly adequate for cross-correlation studies between external catalogues and VMC. The relative accuracy within VMC data is higher and a more detailed investigation of the suitability of VMC data for studies of, for example, proper motions will be addressed elsewhere.

2.3.3 Photometry

The photometric calibration relies on the observation of stars from the 2MASS catalogue with magnitudes in the range 12 – 14 mag in all bands. The procedure is similar to that adopted to calibrate data from the Wide-Field Camera (WFCAM) mounted at the United Kingdom Infrared Telescope (UKIRT). For the WFCAM filters, which are very similar to VISTA's (except that WFCAM has K and VISTA has K_s), Hodgkin et al. (2009) have shown that the calibration of the Y band, not included in 2MASS, is possible where the extinction is not too high, i.e. $E(B-V) < 1.5$. This is well within the average extinction values towards the Magellanic system (Westerlund (1997)). However, in star-forming regions the extinction can reach larger values and the calibration may not be reliable. To remedy this situation a calibration based on the observations of standard stars will be produced together with a thorough investigation of star-forming regions from previous data.

A high quality global photometric calibration of the VMC survey will be supported by the homogeneity and accuracy of the 2MASS catalogue. The best ab-

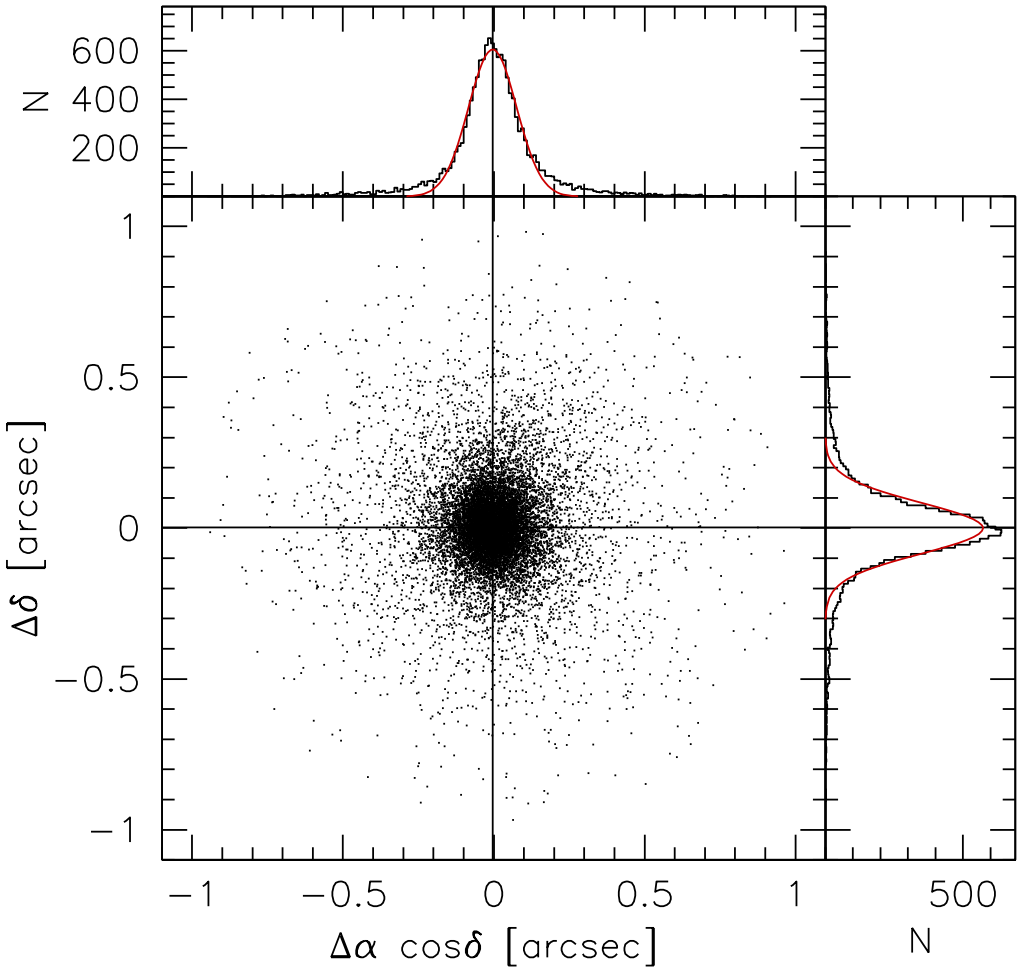

Figure 2.6: Comparison between VISTA and 2MASS astrometry in the 8_8 field. Histograms have bins of 0.01″ in size. The best fitting gaussians are indicated and correspond to σ of 0.080″ and 0.085″ for $\Delta\alpha$ and $\Delta\delta$, respectively.

Table 2.4: VMC-2MASS* comparison.

Band	Range (mag)	Mean (mag)	Median (mag)	Sigma (mag)
Y	10.5 – 15.0	+0.018	+0.012	0.110
J	10.5 – 14.5	−0.005	−0.003	0.092
K_s	10.0 – 14.0	−0.003	−0.003	0.069

solute photometry is expected to be accurate to about 1% and, on average, 2%, but relative photometry will reach a much greater accuracy (~milli-magnitudes for brighter sources). At periodic intervals and at the end of the survey the global photometric calibration will be assessed.

Figure 2.7 shows the behaviour of VISTA photometric uncertainties in the VMC 8_8 field where data represent stacked paw-prints and tiles. Note that the uncertainties reduce by about $\sim 50\%$ compared to the individual tiles, and will reduce further for deep tiles. In the VMC catalogues several aperture flux magnitudes are given that sample the curve of growth of all images. The recommended aperture 'aper3', used in this work, corresponds to a core radius of 1″ (3 pixels) that contains 75% of the total stellar flux in a 0.8″ seeing observation.

Figure 2.8 shows a comparison between VMC and 2MASS* magnitudes. By selecting a suitable range of magnitudes the parameters of the comparison (mean, median and sigma) are indicated in Tab. 2.4. Note that by 2MASS* we do not refer to 2MASS magnitudes, but to the magnitudes obtained using the following colour equations:

$$Y_{\rm 2MASS^*} = J_{\rm 2m} + 0.550 \times (J_{\rm 2m} - H_{\rm 2m}) \tag{2.1}$$

$$J_{\rm 2MASS^*} = J_{\rm 2m} - 0.070 \times (J_{\rm 2m} - H_{\rm 2m}) \tag{2.2}$$

$$K_{\rm 2MASS^*} = K_{\rm 2m} + 0.020 \times (J_{\rm 2m} - K_{\rm 2m}) \tag{2.3}$$

where $J_{\rm 2m}$, $H_{\rm 2m}$ $K_{\rm 2m}$ are 2MASS magnitudes. These are the formulas used to calibrate the VISTA photometry[10]. They include the correct colour term but do not include the small zero-point shifts (see chapter 6) that are necessary to bring the observations into a Vega magnitude system.

[10] http://casu.ast.cam.ac.uk/surveys-projects/vista/technical/vista-sensitivity

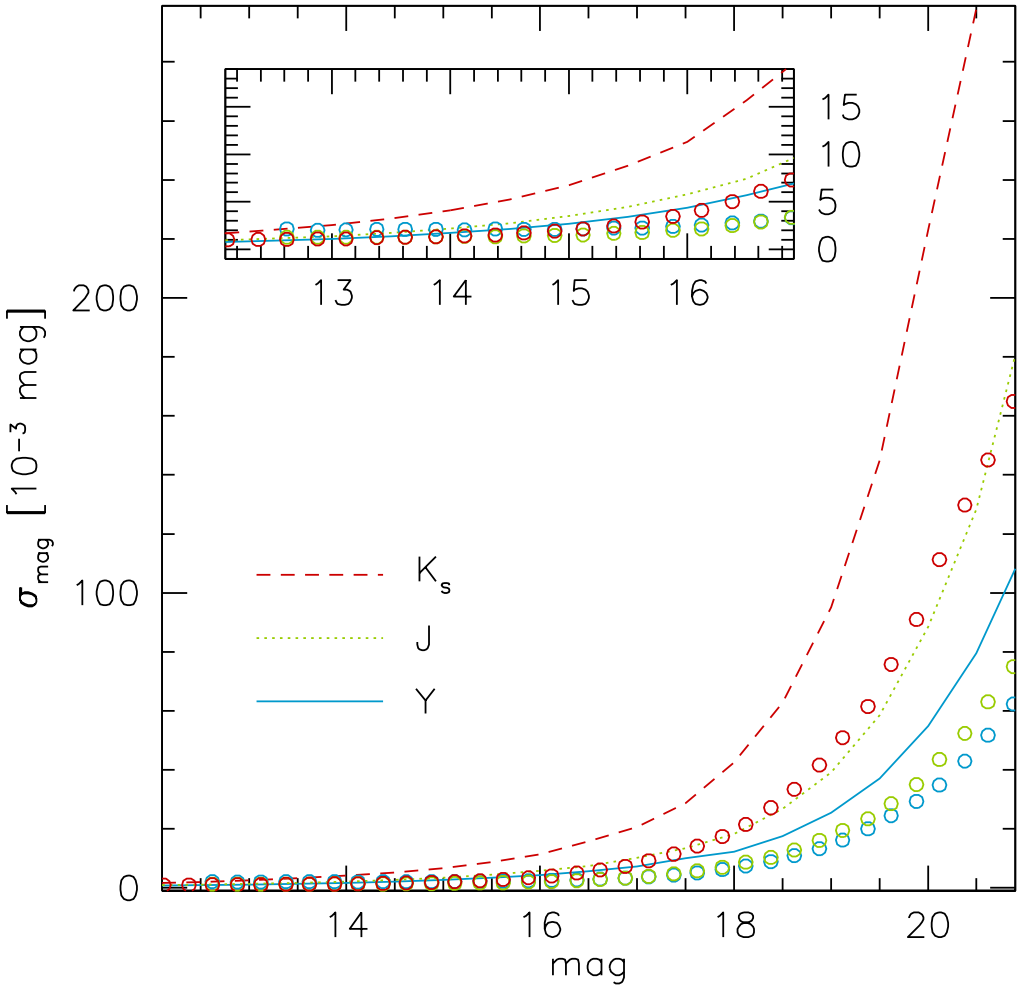

Figure 2.7: Photometric uncertainties in the VMC data for stacked paw-prints (dashed, dotted and continuous lines in the K_s, J and Y bands respectively) and tiles (red, green and blue circles in the K_s, J and Y bands respectively) in the 8_8 field. Uncertainties are progressively smaller from K_s to Y and are systematically smaller in tiles than in stacked paw-prints.

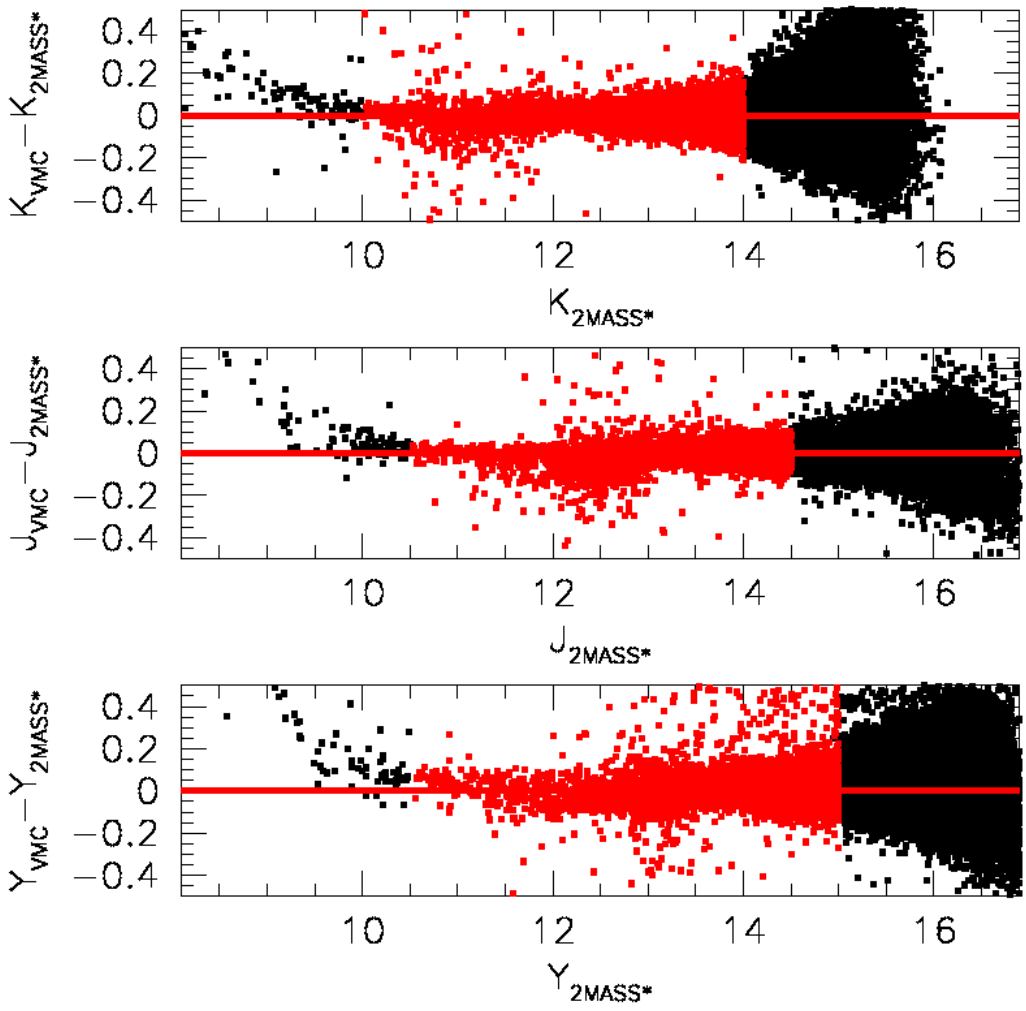

Figure 2.8: Magnitude difference between VMC and 2MASS* sources for stars in the 8_8 field. Horizontal lines were defined within a specific range of magnitudes that is given in the text and is indicated in red in the colour version of the figure.

The morphological classification is encoded in a flag with values: -1 for stellar, $+1$ for non-stellar, 0 for noise and -2 for borderline stellar sources. This classification indicates the most probable source morphology and is affected by crowding and sensitivity. For details about the photometric apertures, the source classification and other catalogue parameters the reader is referred to the CASU web pages.

2.3.4 Image quality

The quality of the VMC images is evaluated at three different steps – during the observations, the data reduction, and the archiving process. The VMC team performs additional quality control checks that interleave with each of these three steps. The first identifies obvious causes for re-observation, such as observations that exceeded the required constraints or that failed to be completed because of technical reasons. These observations are usually repeated almost immediately. All images are processed by CASU and archived at the VSA, regardless of whether their observing constraints are met.

All CASU-reduced VMC survey images for individual detectors have been inspected visually for quality control. The purpose of this inspection is to recognise artefacts and residuals from the reduction process but also to identify features that are intrinsic to the observations. The results of the quality inspection are as follows:

- The upper $1/3$ of detector #16 is effectively noisy in the bluer bands, this also causes a calibration problem for that region: so the VMC Y band observations suffer more than the J and K_s ones. This problem causes an increasing background level and influences the detection capabilities.

- The observations obtained before 20 November 2009 suffer from intermittent problems in detector #6 channel #14 (each detector has 16 channels, processed by different analog-to-digital convertors) that required replacement of a video board in the controller. These stripes cover an area comparable to that of a bright foreground star.

- A special sky frame needs to be used for reducing images obtained during the night of 19 November 2009, due to investigations on the component responsible for the previous problem. This step is implemented in the pipeline reduction from version 0.9 onwards.

Table 2.5: Average VMC parameters from all single tile images.

Band	FWHM (arcsec)	Ellipticity	Zero – point (mag)	5σ Mag. Limit (mag)
Y	1.03 ± 0.13	0.065 ± 0.011	23.520 ± 0.070	21.111 ± 0.395
J	1.00 ± 0.10	0.064 ± 0.011	23.702 ± 0.206	20.527 ± 0.382
K_s	0.93 ± 0.08	0.051 ± 0.009	22.978 ± 0.245	19.220 ± 0.340

- A low quality region at the bottom ('−Y') of detector #4 creates a horizontal pattern that does not cancel out with stacking images obtained from the exposure and jittering sequence. This problem will likely not affect subsequent reductions of the data.

- Overall the reduced images show a smooth gradient most noticeable in the K_s band (possibly caused by the baffling system of VIRCAM as a result of thermal radiation), but does not present a problem for the source extraction.

None of these problems require re-observation of the tiles that have been obtained for the VMC survey.

The quality of the images was further inspected by comparing the FWHM of the extracted sources with the expected seeing requirements. As expected the FWHM varies among the VIRCAM detectors. For example, the average FWHM in the corners of detector #1 is larger than in other detectors. This implies that some detectors will have a FWHM that exceeds the seeing requirement by more than 10%. The average seeing among the detectors and the average seeing among the six paw-prints of a tile is, however, always within the required limit, except in a few cases.

Table 2.5 shows the average seeing, ellipticity, zero-point and limiting magnitude from all VMC images. These parameters have been calculated excluding problematic observations and represent average values regardless of their execution as part of a concatenation, group or monitoring sequence, as well as from the specific requirements of the different VMC fields with respect to crowding.

2.4 Data archive

The data reduced by the VDFS pipeline at CASU are ingested into the VSA[11] at the Wide Field Astronomy Unit (WFAU) in Edinburgh which is similar to the WFCAM Science Archive (Hambly et al. (2008)). At present, these are data reduced with v1.0 of the CASU pipeline and include all VMC data observed until end of May 2010 . At VSA the data are curated to produce standardised data products. The software that runs at WFAU and populates the VSA is the same that runs at CASU and this guarantees that the data are processed homogeneously throughout the entire processing chain.

The most important processes, available at present, for the VMC survey are: individual passband frame association and source association to provide multi-colour, multi-epoch source lists; cross-association with external catalogues (list-driven matched photometry); deeper stacking in specified fields; quality control procedures.

There are three main types of VSA tables that are important for the VMC survey. These are the *vmcDetection* table, the *vmcSource* table and the *vmcSynoptic* table(s). The vmcDetection table contains the catalogues corresponding to individual observations. At the moment there is one catalogue per paw-print, regardless of band and tile of origin. The vmcSource table contains the list of sources obtained from deep stack images and each source is matched in the three VMC bands. In practise, each row of the vmcSource table will contain Y, J and K_s magnitudes for a source. At present, because VSA is organised by paw-prints, the same source may appear two or more times in the vmcSource table depending on its location with respect to the overlap among the six paw-prints forming a tile. The synoptic tables contain the colour information and the multi-epoch information for individual observations (a single OB). More details about the synoptic tables are given by Cross et al. (2009). The position and magnitude for each source in any given table refers to the astrometrically and photometrically calibrated measurements using the parameters specified in the image headers. These parameters are discussed in Sect. 5.2. In addition, there are several quality flags that are specifically introduced at the VSA level. These flags identify problems occurring during the ingestion of the data into the archive, incompleteness in the set of data (for example missing exposures in a paw-print sequence), problems related to the pairing of data, etc.

The magnitudes of the brightest stars are corrected for saturation effects (Sect.

[11] http://horus.roe.ac.uk/vsa/login.html

2.3.1). Figure 2.9 shows the K_s magnitude difference for stars in the 8_8 field compared to 2MASS before and after saturation correction. Saturation effects are present for $K_s < 12$ mag, with the magnitudes of brighter stars recovered to at least $K_s = 10$ mag after correction.

The VSA is queried using Structured Query Language (SQL) and a point-and-click web form for browsing. This is a dual (sophisticated and simple) end-user interface for the data. A key feature to note is the design with multi-waveband catalogue data that allows the user to track back to the individual source images and merged-source tables, and present the user with a generally applicable, science-ready dataset. The VSA has a high-speed query interface, links to analysis tools such as TopCat, and advanced new VO services such as MySpace. The VSA supports a different range of queries and the most common for the VMC survey are: (i) querying the archive to check which data have been ingested, (ii) querying the vmcSource table to extract magnitudes from the deep stacks, (iii) querying the synoptic tables to extract light-curves and statistics on the levels of variability and (iv) querying the VSA using an input list of sources and searching for their VMC counterpart. For each source in (i) it is possible to inspect postage stamp images in each wave band.

Before creating the deep stack images, the quality control results discussed in Sect. 2.3.4 need to be taken into account. In particular, all images except those with a large seeing and/or ellipticity are included in the deep stacks. This means that tile images with a reduced number of jitters or paw-prints are included into the deep stacks if their observing conditions are met. The latter will still be available as individual epochs, and will be linked to the other observations in the synoptic tables, because they may contain useful information for variable stars or for source confirmation.

In the future it may be possible to automatically join the under-exposed areas at the two ends of each tile with those of the adjacent tiles prior to source extraction. The VSA also contains external catalogues, like 2MASS, that can be linked with the VMC data via an SQL query. Catalogues that are specifically important for the Magellanic system, e.g. the MCPS and the SAGE catalogues are also being ingested into the VSA. VMC is intrinsically a multi-wavelength project and a large fraction of its science will come from the linking of VISTA data with those from other surveys; the VSA is designed to enable such links.

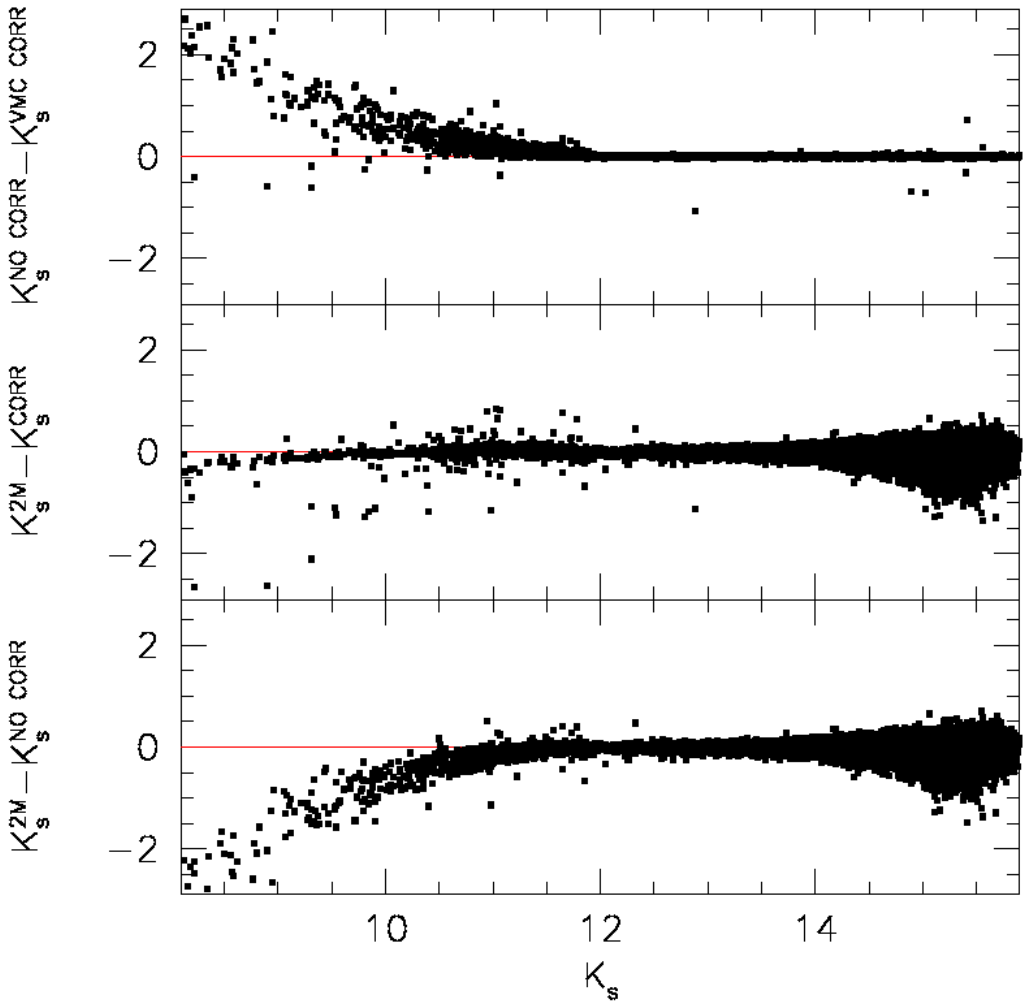

Figure 2.9: Magnitude difference for stars in the 8_8 field in common between VMC and 2MASS before (bottom) and after (middle) correcting the magnitude of VMC stars approaching the saturation limit, and (top) the correction itself developed by (Irwin (2009)).

2.5 Analysis and Results

Figure 2.10 shows the CMDs of the VMC data in the 6_6 (30 Dor) and 8_8 (Gaia) LMC fields. These data were extracted from the VSA. The magnitudes and colours of each source correspond to a single detector, i.e. if the same source was detected in another detector it is not included in the CMDs. This is because at this stage the archiving process is organised by paw-prints. When tiles, resulting from the combination of six paw-prints, become available at VSA then the exposure time per source will be at least doubled. At present the exposure times per band for the sources shown in the CMDs correspond to 1200 sec in Y, 1400 sec in J and to $\sim$ 4000 sec in K_s.

The distribution of stars in the CMDs shows clearly the different stellar populations characterising these LMC fields. The blue-most conic structure bending to red colours at bright magnitudes is formed by main-sequence (MS) stars of increasing mass with increasing brightness. The MS joins, via the sub-giant branch, the RGB beginning at $\sim$2 mag below the red clump, the approximately circular region described by the highest concentration of stars. The structure of the red clump depends on stellar parameters (age and metallicity) but also on interstellar extinction. Extinction causes the clump to elongate to red colours, as seen in the CMDs for the 30 Dor field where extinction is higher than in the Gaia field. The RGB continues beyond the red clump at brighter magnitudes describing a narrow structure bending to red colours. The abrupt change in source density at the tip of the RGB marks the transition to brighter AGB stars. The broad vertical distribution of stars below the RGB is populated by MW stars. In the CMDs of the Gaia field these are easily distinguished from LMC stars. Cepheid and supergiant stars occupy the region of the diagram to the bright and blue side of the RGB while RR Lyrae stars are somewhat fainter than the red clump and lie more or less parallel to the sub-giant branch.

Figure 2.11 shows the colour-colour diagram of the VMC data in the 8_8 field. The data shown here are the same as in the CMDs (Fig. 2.10) described above. The distribution of sources in the colour-colour diagram resembles the body of an ant. Following this analogy:

- The lower part of the ant body (*gaster*) at $-0.1 < (Y - J) < 0.2$, $-0.3 < (J - K_s) < 0.2$, corresponds to the location of MS stars in the LMC, with the youngest stars being at the bluest extremity. The width of this feature is mainly caused by photometric uncertainties. Its extension to the red is also set by the limited depth of the VMC data, since the faint MS should continue to even redder colours.

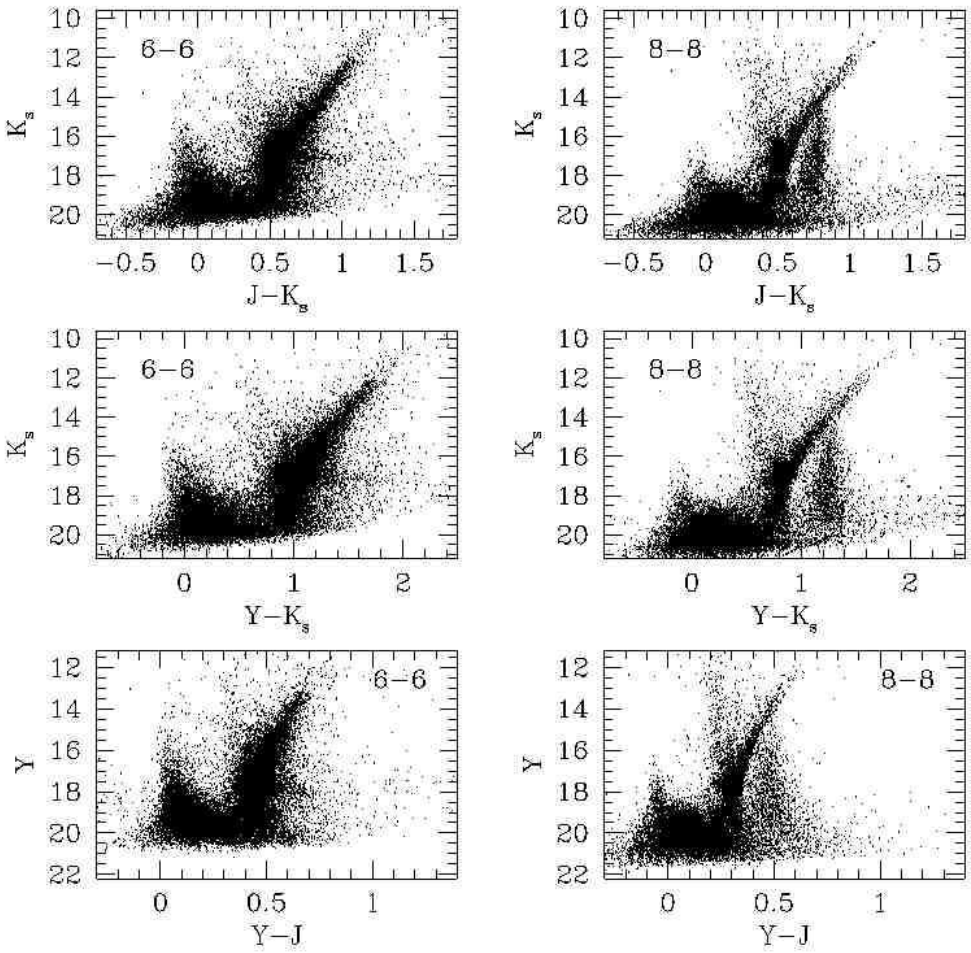

Figure 2.10: Colour-magnitude diagrams of VMC sources in part of the 6_6 (30 Dor) and 8_8 (Gaia SEP) LMC fields.

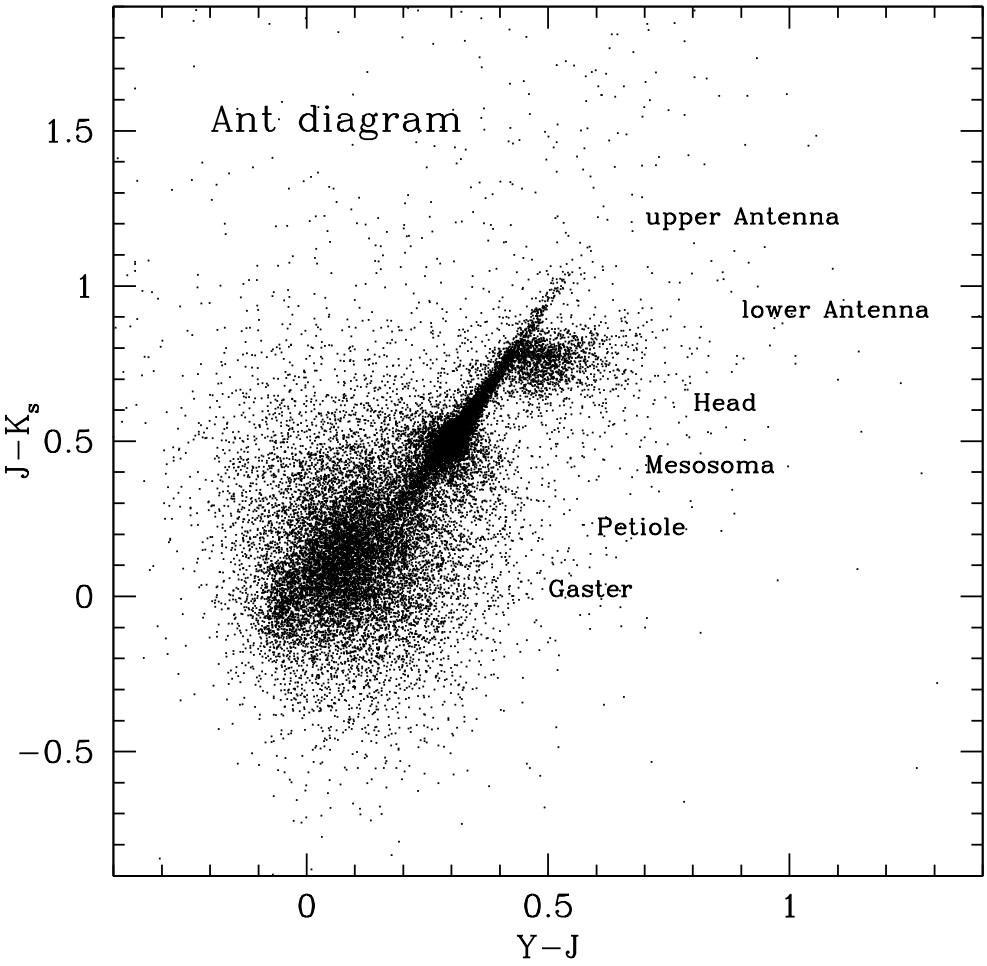

Figure 2.11: Ant diagram: the colour-colour diagram of VMC sources in part of the 8_8 LMC field.

- The middle part of the ant body (*mesosoma*) at $0.2 < (Y - J) < 0.4$, $0.3 < (J - K_s) < 0.65$, corresponds to the main locus of helium-burning giants in the LMC. The bulk of them are in the red clump (see Fig. 2.10), but also brighter helium burning giants, and stars in the faint extension of the red clump, fall in this same blob.

- The *petiole* is a small thin extension of the mesosoma at its red side, at $0.2 < (Y - J) < 0.3$, $0.2 < (J - K_s) < 0.3$, and is mainly caused by bright stars in the MW foreground – more specifically by the intermediate-age and old turn-offs of MW disk populations (at $K_s < 15$).

In addition to this well-defined petiole, gaster and mesosoma are also connected by the relatively less populated LMC sub-giants, lowest-luminosity RGB stars, and horizontal branch stars in the LMC.

- The upper part of the ant body (*head*) is a more complex feature. Its main blob at $0.4 < (Y - J) < 0.6$, $0.6 < (J - K_s) < 0.8$ is defined by low-mass stars in the MW foreground, especially those with masses < 0.5 $M_\odot$ which clump at the same near-IR colours ($J - K_s \sim 0.7$; see Nikolaev & Weinberg (2000a), Marigo et al. (2003a)). The same structure forms a marked vertical feature in the CMDs.

- Two *antennae* depart from this head, the upper one at $0.5 < (Y - J) < 0.6$, $0.8 < (J - K_s) < 1$ being formed by the more luminous RGB stars in the LMC, close to their tip of the RGB, extending up to $(J - K_s) = 1$ mag. This upper antenna finishes abruptly because the tip has been reached. The lower antenna at $(J - K_s) \sim 0.8$, $(Y - J) > 0.6$, is more fuzzy, and corresponds to the $Y - J$ red-ward extension of low-mass stars in the MW foreground. This red ward extension is partially caused by photometric uncertainties and by the particular colour-colour relation followed by the coolest M dwarfs.

2.5.1 Completeness

Some key science goals of the VMC survey require accurate estimates of the completeness of the stellar photometry as a function of location across the Magellanic system, and position in the CMDs. This is estimated via the usual procedure of adding artificial stars of known magnitudes and positions to the images, then looking for them in the derived photometric catalogues.

For this work, the paw-print images, available for the 8_8 LMC field, were combined to produce a tile image using the SWARP tool (Bertin et al. 2002a). A

region of the tile image with a size of 4000×4000 pixels was selected. Then, PSF photometry using the DAOPHOT and ADDSTARS packages in IRAF was performed. Figure 2.12 shows an example of the photometry on the (preliminary) stacked image.

The artificial stars are positioned at the same random position on the YJK_s images. Their mutual distances are never smaller than 30 pixels, so that the process of adding stars does not increase the typical crowding of the image. Later on, artificial stars spanning small bins of colour and magnitude are grouped together to provide estimates of number ratio between added and recovered stars – i.e. the completeness – as a function of position in the CMDs.

Typical results of this process are illustrated in the Fig. 2.13, which shows the completeness as a function of magnitude, for both cases of single epoch and deep stacked images. For this relatively low density tile, the figure shows that the ~50% completeness limit goes as deep as 22.20, 21.90, and 21.40 mag in the Y, J and K_s bands, respectively. These results are in good agreement with the expectations derived from simulated VMC images (Kerber et al. 2009b).

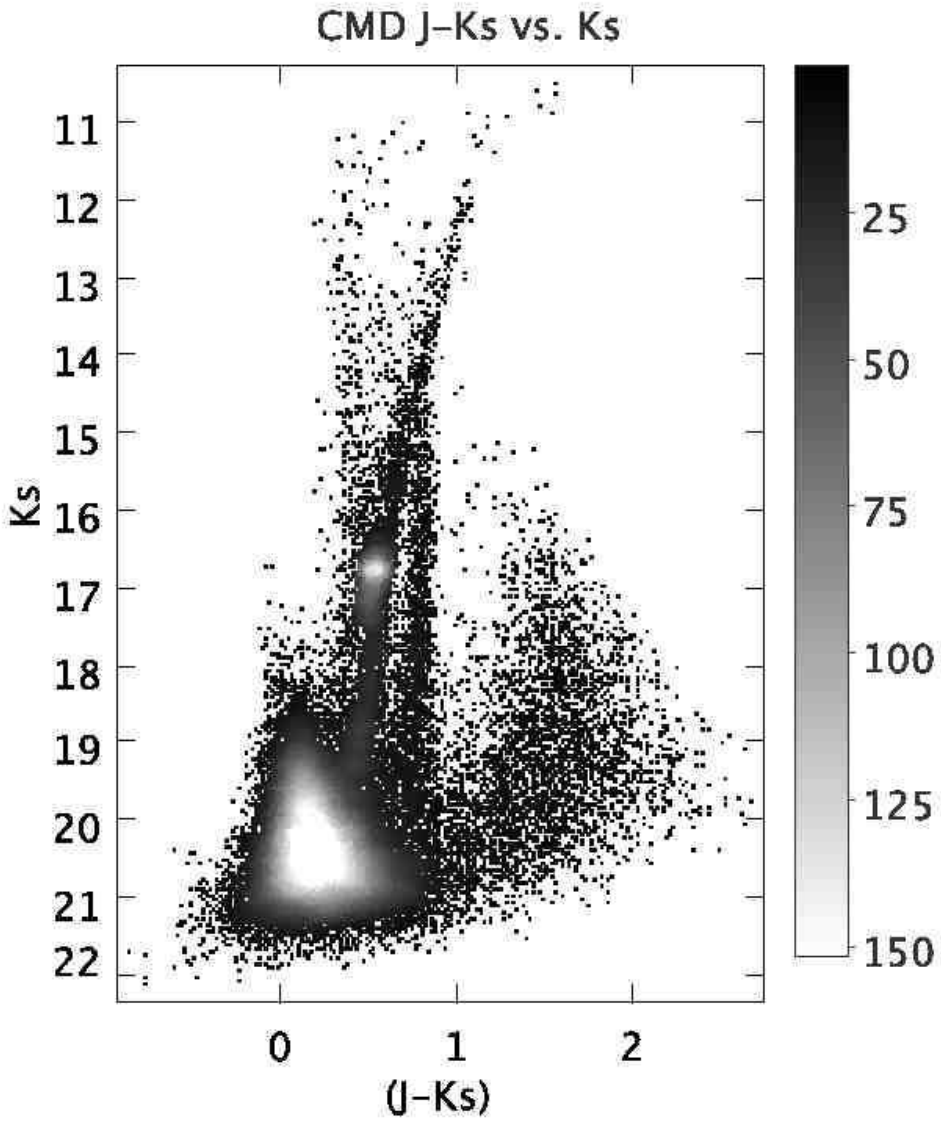

Figure 2.12: CMD for a region of 4000×4000 pixels extracted from the 8_8 LMC deep tile. Objects with $J - K_s > 1$ and fainter than $K_s = 16$ mag are background galaxies.

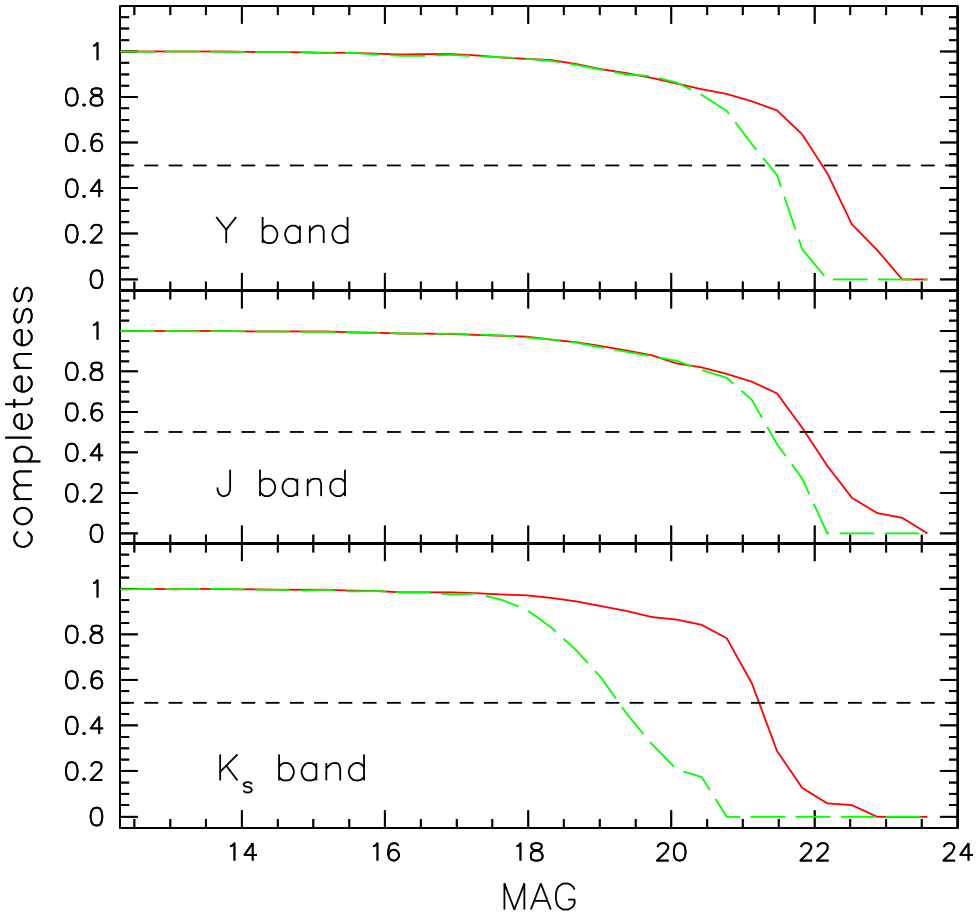

Figure 2.13: Completeness results for the 8_8 LMC tile with a single epoch (dashed line) and with deep stacked images (continuous line).

Chapter 3

Simulating the VMC data and the recovery of Star Formation History

3.1 Introduction

The VISTA Survey of the Magellanic System[1] (Cioni et al. 2010, VMC, see) is an ESO public survey project which will provide, in the next 5 years, critical near-infrared data aimed – among other goals – to improve upon present-day SFH determinations. This will hopefully open the way to a more complete understanding of how star formation relates to the dynamical processes under way in the system, and to a more accurate calibration of stellar models and primary standard candles. Regarding the SFH, the key contributions of the VMC survey will be: (1) It will provide photometry reaching as deep as the oldest main sequence turn-off *over the bulk of* the MC system, as opposed to the tiny regions sampled by HST, and the limited area covered by most of the dedicated ground-based observations. (2) VMC will use the near-infrared YJK_s passbands, hopefully reducing the errors in the SFH-recovery due to variable extinction across the MCs.

On the other hand, the use of near-infrared instead of optical filters will bring along some complicating factors, like an higher degree of contamination of the MC photometry by foreground stars and background galaxies, and the extremely high noise contributed by the sky, especially in the K_s band.

Indeed, VMC will be the first near-infrared wide-area survey to provide data

[1] See http://www.vista.ac.uk and http://www.star.herts.ac.uk/~mcioni/vmc/ for further information.

suitable for the classical methods of SFH-recovery[2]. With the new space-based near-infrared cameras (the HST/WFC3 IR channel, and JWST) and ground-based adaptive optics facilities, observations similar to VMC ones will likely be available for many nearby galaxies. VMC may become the precursor of detailed SFH-recovery in the opening window of near-infrared wavelengths. Demonstrating the feasibility of VMC goals, therefore, is of more general interest.

Another particularity of the VMC survey is that, once started, its data flow will be so huge that algorithms of analysis have better to be prepared in advance, in the form of semi-automated pipelines. Similar approaches have been/are being followed by some ambitious nearly-all-sky (SDSS, 2MASS), micro-lensing (MACHO, OGLE, EROS), and space astrometry (e.g. Hipparcos, GAIA) surveys.

In this work, we describe part of the preparatory work for the derivation of the SFH from VMC data, which can be summarised in the following way: First we simulate the VMC images for the LMC (Sect. 3.2), where we later perform the photometry and artificial stars tests (Sect. 3.3) that allow us to access the expected levels of photometric errors, completeness, and crowding, and the contamination by foreground stars and background galaxies. We then proceed with many experiments of SFH-recovery (Sect. 6.3), evaluating the uncertainties in the derivation of the SFH as a function of basic quantities such as the stellar density over the LMC, the area included in the analysis, and the adopted values for the distance and reddening. Doing this, we are able to present the expected random and systematic errors in the space-resolved SFH. Such information may be useful to plan complementary observations and surveys of the LMC in the next few years. as well as better explore the effect in the recovered SFH due to the uncertainties associated with the MC geometry, differential reddening, initial mass function, fraction of binaries, etc.

3.2 Simulating VMC data

Our initial goal is to obtain realistic simulations of VMC images, containing all of the objects that are known to be present towards the MCs and likely to be detectable within the survey depth limits. These objects are essentially stars belonging to the MW and the MCs, and background galaxies. Moreover, an essential

[2]The previous attempts of Cioni et al. (2006a,b) based on IJK_s data, were based on the shallow observations from DENIS and 2MASS, which are limited to the upper RGB and above. Consequently, they could access the general trends in the mean age and metallicity across the MCs, but not the detailed age-resolved SFH.

component of the images is the high signal from the infrared sky. Each one of these components will be detailed below. Diffuse objects such as emission nebulae and star clusters will, for the moment, be ignored.

3.2.1 VISTA and VMC specifications

VMC will be performed with the VIRCAM camera mounted at the 4m VISTA telescope at ESO's Paranal Observatory in Chile. VIRCAM has 16 2048×2048 detectors which, with the image scale of 0.339 *arcsec* per pixel on average, cover a sky area of 0.037 deg^2 each. The basic mode of the observations will be to perform 6 exposures (paw-prints) with the subsequent construction of 1.0×1.5 deg^2 tiles. In the following, we will adopt the area of each detector (i.e. 0.037 deg^2) as the basic unit of our simulations.

The specifications of the VMC survey will be detailed in another work (Cioni et al., in preparation). For our aims, suffice it to mention the following: Despite for the crowded fields, it is expected that the observations will be sky-noise dominated. The mean sky brightness at Cerro Paranal is of 17.2, 16.0, 13.0 mag arcsec^{-2} in YJK_s, respectively. The required seeing is of 1.0 *arcsec* (FWHM) in the Y band, being the most crowded regions observed in nights with seeing better than 0.8 *arcsec*. The targetted signal-to-noise ratio (SNR) is equal to 10 at magnitudes of 21.9, 21.4, 20.3 mag respectively. The photometric zero-points in our simulations were fixed via the VISTA exposure time calculator, so as to be consistent with these values. Considering these survey limits, in our simulations we include all objects brighter than $K_s = 22.5$, which at the LMC distance correspond to a stellar mass of $\sim 0.8\ M_\odot$ in the main sequence turn-off.

VMC tiles will cover most of the Magellanic System, summing to a total area of 184 deg^2 (see Cioni et al. 2007, Cioni et al., in preparation, for details). Fig. 3.1 shows a histogram of the total area to be observed as a function of the density of upper RGB stars, $N_{\rm RGB}$, which is defined as the number of 2MASS stars inside a box in the K_s vs. $J-K_s$ CMD ($0.60 \leq J-K_s \leq 1.20$ and $12.00 \leq K_s \leq 14.00$ for the LMC and $12.30 \leq K_s \leq 14.30$ for the SMC), for each unit area of 0.05 deg^2. Notice the higher mean and maximum stellar densities of the LMC, as compared to the SMC. The stellar densities vary over an interval of about 2.5 dex.

3.2.2 Stars in the UKIDSS photometric system

Since VISTA is still being commissioned at the time of this writing, the throughputs of VISTA filters, camera, and telescope are still not available. It is however

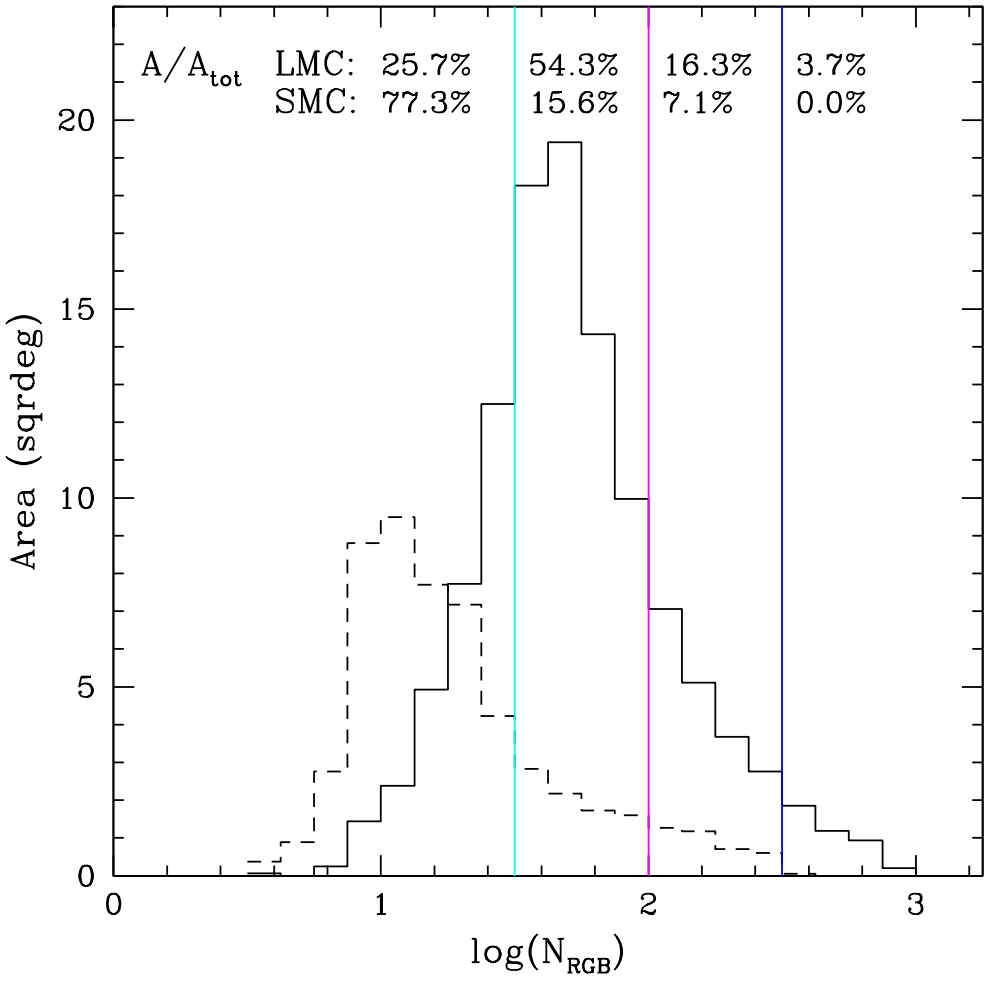

Figure 3.1: The area VMC will likely cover in the LMC (solid line) and SMC (dashed line) as a function of the surface density of RGB stars, $N_{\rm RGB}$. The fraction of the covered area in each MC, for four ranges of density, is also shown in the top of the figure.

clear that the VISTA photometric system will be very similar to the UKIDSS one, with the differences being mainly in the higher performance of VISTA, and in the fact that VISTA will use a K-short filter (K_s) similar to the 2MASS one.

Given the present situation, we have so far used the UKIDSS system as a surrogate of the future VISTA one. Tests using the preliminary VISTA filter curves (Jim Emerson, private communication) indicate very small differences in the synthetic photometry, typically smaller than 0.02 mag, between VISTA and UKIDSS. [3]

Stellar isochrones in the UKIDSS system have been recently provided by Marigo et al. (2008)[4]. The conversion to the UKIDSS system takes into account not only the photospheric emission from stars, but also the reprocessing of their radiation by dusty shells in mass-losing stars, as described in Marigo et al. (2008). The filter transmission curves and zero-point definitions come from Hewett et al. (2006). The stellar models in use are composed of Girardi et al. (2000a) tracks for low- and intermediate-mass stars, replacing the thermally pulsing asymptotic giant branch (AGB) evolution with the Marigo & Girardi (2007) ones. In this work, these models are further complemented with white and brown dwarfs as described in Girardi et al. (2005, also Zabot et al., in preparation), and with the Bertelli et al. (1994) isochrones for masses higher than 7 $M_\odot$. Fig. 3.2 presents some of the Marigo et al. (2008) isochrones in the M_K vs. $Y-K$ diagram, for a wide range in age and metallicity. As can be readily noticed, the isochrones contain the vast majority of the single objects that can be prominent in the near-infrared observations of the LMC, going from the lower Main-Sequence (MS) stars, up to the brightest AGB stars and red supergiants. The stellar masses in the MS and the apparent magnitude for a typical LMC distance, $(m-M)_0 = 18.50$ (Clementini et al. 2003; Alves 2004; Schaefer 2008) are also indicated in this figure. We recall that our models contain, in addition, the very-low mass stars, brown dwarfs and white dwarfs, which are important in the description of the foreground MW population (Marigo et al. 2003b).

The interstellar extinction coefficients adopted in this work do also follow from Marigo et al. (2008): $A_Y = 0.385\,A_V$, $A_J = 0.283\,A_V$, and $A_K = 0.114\,A_V$, which imply $E_{Y\text{–}J} = 0.351\,E_{B\text{–}V}$ and $E_{Y\text{–}K} = 0.931\,E_{B\text{–}V}$. They have been derived from synthetic photometry applied to a G2V star extincted with Cardelli et al. (1989) extinction curve. Although the approach is not the most accurate one (see Girardi et al. 2008), it is appropriate to the conditions of moderate reddening ($E_{B\text{–}V} \lesssim$

[3] Throughout this work, we will name the 2.2 μm filter as K_s when referring to VISTA, 2MASS and DENIS, and as K when referring to our simulations and to UKIDSS data. Notice however that, for all practical purposes, the actual difference between these filters is not a matter of concern.

[4] http://stev.oapd.inaf.it/dustyAGB07

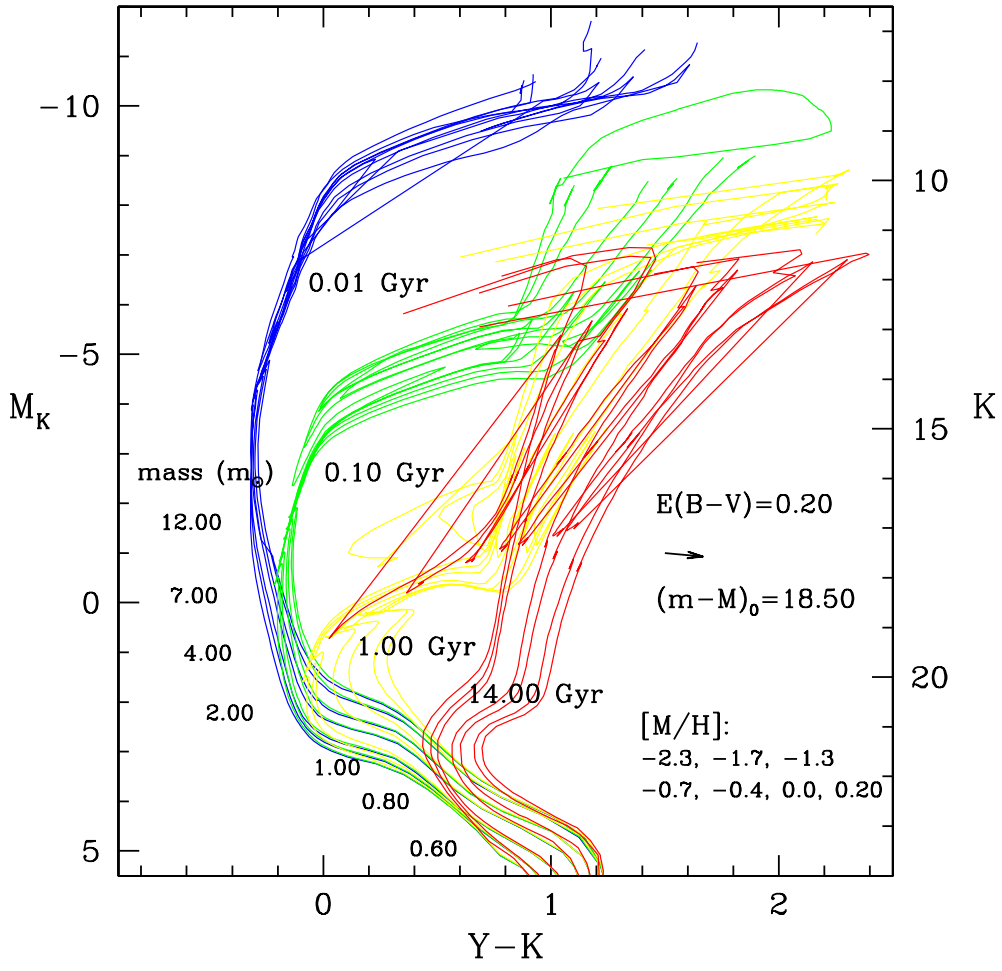

Figure 3.2: A series of Marigo et al. (2008) isochrones in the UKIDSS photometric system. The figure shows the absolute (M_K, $Y-K$) CMD as well as the apparent (K, $Y-K$) one for a typical distance to the LMC. Stellar masses and isochrone ages and metallicities are also indicated in the figure.

0.2 mag) typical of the Magellanic Clouds.

The simulation of the input photometric catalogues and the generation of artificial images are described in the next subsections. In brief, the input catalogues for the LMC (Sect. 3.2.3) and the foreground MW stars (Sect. 3.2.4) come from the predictions made with the TRILEGAL code (Girardi et al. 2005), that simulates the photometry of resolved stellar populations following a given distribution of initial masses, ages, metallicities, reddenings and distances. The catalogues of background galaxies (Sect. 3.2.5) are randomly drawn from UKIDSS (Lawrence et al. 2007). The simulation of images is performed with the DAOPHOT and ARTDATA packages in IRAF[5] (Sect. 3.2.6), always respecting the photometric calibration and expected image quality required by the VMC survey.

3.2.3 The LMC stars

The stellar populations for the LMC are simulated as an "additional object" inside the TRILEGAL code (Girardi et al. 2005), where the input parameters for a field are:

- the star formation rate as a function of stellar age, SFR(t);
- the stellar AMR, $Z(t)$ or [M/H](t);
- the total stellar mass, $M_{\rm tot,LMC}$;
- the distance modulus, $(m-M)_0$;
- the reddening, $E_{B\text{-}V} = 3.1\,A_V$;
- the Initial Mass Function (IMF), $\psi(M_{\rm i})$;
- the fraction of detached unresolved binaries, $f_{\rm bin}$.

As commented before, for convenience we are simulating an area of 0.037 deg^2, equivalent to a 2048×2048 VIRCAM detector. The value of $M_{\rm tot,LMC}$ is suitably chosen such as to generate the total number of RGB stars observed by 2MASS, $N_{\rm RGB}$, inside this same area.

[5]IRAF is distributed by the National Optical Astronomy Observatory, which is operated by the Association of Universities for Research in Astronomy (AURA) under cooperative agreement with the National Science Foundation.

In the LMC simulations presented in this work, we adopt an input AMR consistent with the one given by stellar clusters (Olszewski et al. 1991; Mackey & Gilmore 2003; Grocholski et al. 2006; Kerber et al. 2007) and field stars (Cole et al. 2005; Carrera et al. 2008), together with a constant SFR(t). Since the SFR(t) in the LMC is clearly spatial dependent (Holtzman et al. 1999; Smecker-Hane et al. 2002; Javiel et al. 2005), the assumption of a constant SFR(t) shall be considered as just a way to ensure a uniform treatment for all stellar populations over the LMC.

In terms of distance we are initially using the canonical value of $(m-M)_0 = 18.50$ (Clementini et al. 2003; Alves 2004; Schaefer 2008) also adopted by the HST Key Project to measure the Hubble constant (Freedman et al. 2001), whereas for the reddening we are assuming a value of $E_{B\text{-}V} = 0.07$, typical for the extinction maps from Schlegel et al. (1998a). For real VMC images, these two parameters are expected to be free parameters, since the LMC presents disk-like geometries with a significant inclination ($\sim$ 30–40 deg) (van der Marel & Cioni 2001b; van der Marel et al. 2002; Nikolaev et al. 2004) and non-uniform extinction (Zaritsky et al. 2004; Subramaniam 2005; Imara & Blitz 2007).

Finally the assumed values for the remaining inputs are: the Chabrier (2001) lognormal IMF [6] , and $f_{\rm bin} = 30\,\%$ with a constant mass ratio distribution for $m_2/m_1 > 0.7$ [7]. There are no strong reasons to expect significant deviations for these choices, especially for the IMF since we are dealing with stars with masses approximately between 0.8 and 12.0 $M_\odot$ where the IMF slope seems to be universal and similar to the Salpeter one (Kroupa 2001, 2002). Concerning the fraction of binaries, our choice is consistent with the values found for the stellar clusters in the LMC (Elson et al. 1998a; Hu et al. 2008). For the moment, these will be considered as fixed inputs. Further works will use simulations in order to quantify the systematic errors in the recovered SFH introduced by the uncertainties related to these choices.

3.2.4 The Milky Way foreground

The MW foreground stars are simulated using the TRILEGAL code as described in Girardi et al. (2005). Towards the MCs, the simulated stars are located both in a

[6] With a slope $\alpha \sim -2.3$ for $0.8 < m/M_\odot < 5.0$ and $\alpha \sim -3.0$ for $m > 5.0 M_\odot$, where the Salpeter slope is $\alpha = -2.35$.

[7] This is the mass ratio interval in which the secondary significantly affects the photometry of the system.

disk which scale-height increasing with age, and in a oblate halo component. Diffuse interstellar reddening within 100 pc of the Galactic Plane is also considered, although it affects little the near-infrared photometry.

In Girardi et al. (2005), it has been shown that for off-plane line-of-sights, TRILEGAL predicts star counts accurate to within about 15% over a wide range of magnitudes and down to $J \simeq 20.5$ and $K \simeq 18.5$. This accuracy is confirmed by the $K \lesssim 20.5$ observations of Gullieuszik et al. (2008) for a field next to the Leo II dwarf spheroidal galaxy. Moreover, Marigo et al. (2003b) shows that TRILEGAL describes very well the position of the three "vertical fingers" observed in 2MASS K vs. $J - K_s$ diagrams. Similarly-comforting comparisons with UKIDSS data (including the Y band) are presented in Sect. 3.3.2 below.

Although predicting star counts with an accuracy of about 15% may be good enough for our initial purposes, we are working to further improve this accuracy: In short, we are applying the minimisation algorithm described in Vanhollebeke et al. (2008) – which was successfully applied to the derivation of Bulge parameters using data for inner MW regions – to recalibrate the TRILEGAL disk and halo models. It is likely that before VMC starts, foreground star counts will be predicted with accuracies of the order of 5%.

3.2.5 The background galaxies

In order to simulate the population of galaxies background to the MCs, we make use of the large catalogues of real galaxies obtained by the UKIDSS Ultra-Deep (UDS; Foucaud et al. 2007) and Large Area Surveys (LAS; Warren et al. 2007), from their Data Release 3 (December 2007). The LAS includes data for an area of 4000 deg^2 down to $K = 18.4$, for YJK filters, whereas the UDS includes an area of 0.77 deg^2 observed down to $K \sim 23$, but only for JHK passbands.

In our input catalogue for each simulation, we include the number of UKIDSS galaxies expected for our total simulated area. More precisely, we randomly pick up from the UDS catalogue, a fraction of galaxies given by the ratio between the areas covered by UDS and by our image simulation. From the catalogue, we extract their J and K magnitudes, and morphological parameters (position angle, size, and axial ratio). In this way, our simulations respect the observed K-band luminosity function of galaxies, and their $J - K$ colour distribution, down to faint magnitudes. The Y-band magnitudes, instead, have been assigned in the following way: we take the $J-K$ colour of each galaxy in the UDS, and then randomly select a galaxy from the LAS which has the most similar $J - K$ (within 0.2 mag), and take its $Y - J$. This means that the $Y - J$ vs. $J - K$ relation from LAS is being

extrapolated down to deeper magnitudes[8].

3.2.6 Simulating images

Once defined the input catalogues for stars and galaxies we simulated the images inside IRAF, in accordance with the VISTA and VMC specifications (see Sect.3.2.1). The basic sequence of steps (and the IRAF *task*) performed for a given filter is the following:

1. Definition of the image size (*rtextimage*) and introduction of the sky brightness and noise (*mknoise*);

2. simulation of a Gaussian stellar profile (*gauss*) respecting the expected seeing for an image of a photometric calibrated (using the VISTA ETC v1.3) delta function with a known number of electrons;

3. addition of the LMC and MW stars in the sky images (*addstars*) following the previous calibrated Gaussian stellar profile with random poissonian errors in the number of electrons;

4. addition of galaxies (*mkobject*) in the previous image respecting all information concerning the morphological type, position angle, size and axial ratio.

To assure a uniform distribution of the objects in the image, stars and galaxies are always added at random positions. Fig. 3.3 shows an example of image simulation for a typical field in the LMC disk. The false-colour plot evidences the colour and morphologic differences between stars and background galaxies – with the latter being significantly redder than the former. In the same image, we have inserted two populous stellar clusters typical for the LMC with different ages, masses and concentration of stars (following a King's profile), just to illustrate our capacity to simulate also this kind of stellar object.

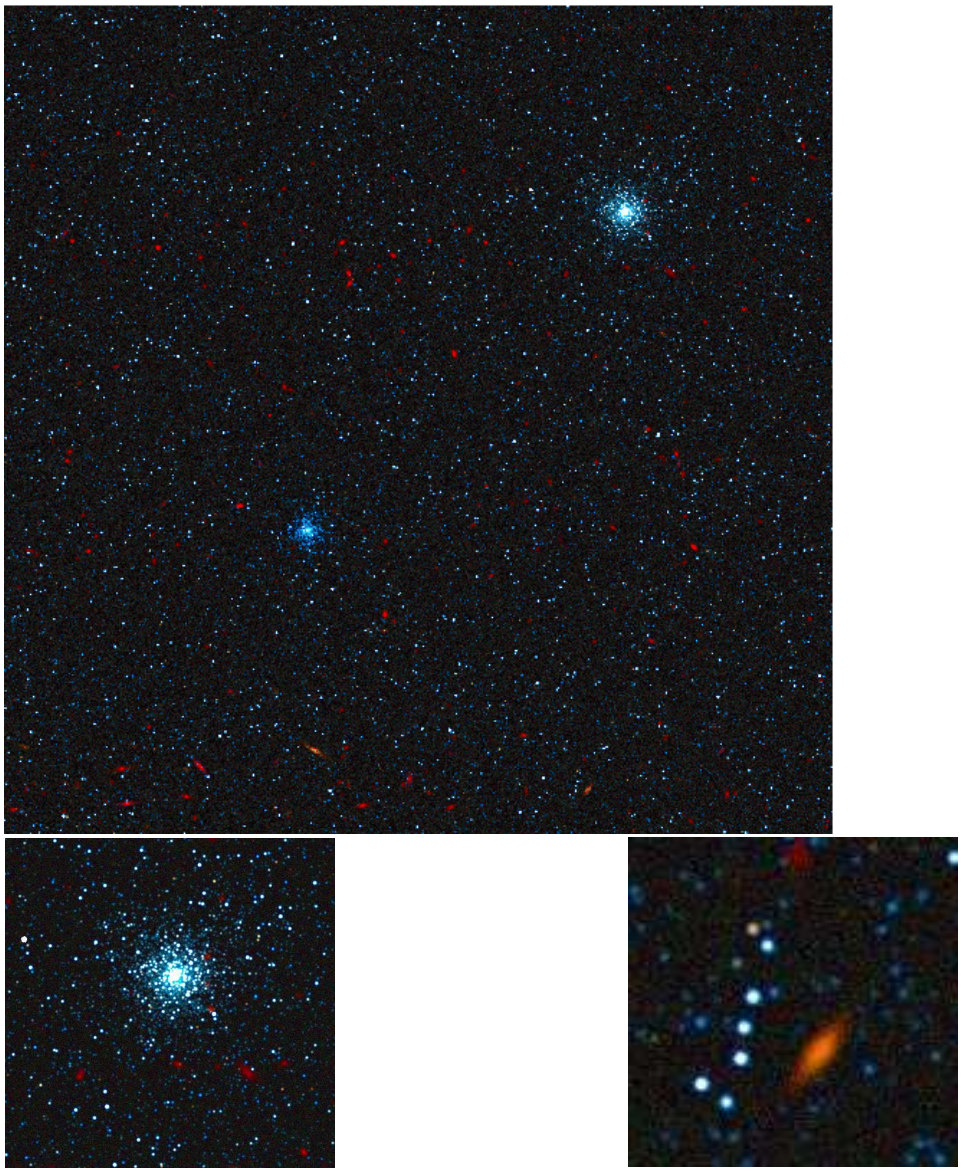

Figure 3.3: An image simulation for the area next to the star cluster NGC1805 (α = 5.03 h, $\delta = -66.07°$), for a single 2048 × 2048 array detector of VIRCAM. This is a false-color image where blue-green-red colours were associated to the *YJK* filters, respectively. The location corresponds to a $\log N_{\rm RGB} \sim 2.00$ in Fig. 3.1. The detector area corresponds to 0.0372 deg^2 (11.6×11.6 arcmin) in the sky, which is about 1/40 of a single VIRCAM tile, and 1/5000 of the total VMC survey area. The two small panels at the bottom present details of the simulated stars, stellar clusters and galaxies for 2.9×2.9 arcmin and 0.7×0.7 arcmin areas. At the LMC distance the top panel corresponds approximately to a box of 175×175 pc, whereas the bottom panels correspond to 44×44 pc and 11×11 pc, respectively (1 *arcsec* $\sim$ 0.25 pc).

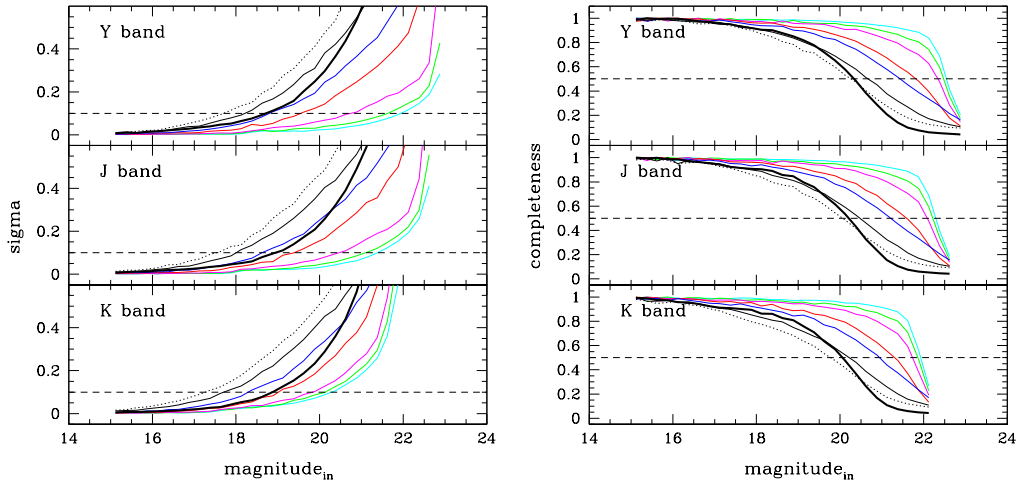

Figure 3.4: Photometric errors (left panels) and completeness curves (right panels) in the artificial YJK images for the LMC for different levels of crowding. The thin curves present the results for the aperture photometry covering the entire expected range of density of field stars ($\log N_{\rm RGB}$ = 1.50, 1.75, 2.00, 2.25, 2.50, 2.75, 2.90, see also Fig. 3.1). The three highest density levels were simulated with the smallest values for seeing required for the LMC centre. The thick black line illustrates the results of performing PSF photometry for the highest density level ($\log N_{\rm RGB}$ = 2.90). The expected error in magnitude for a SNR=10 is shown by the dashed line.

3.3 Performing photometry on simulated data

3.3.1 Aperture and PSF photometry

The IRAF DAOPHOT package was used to detect and to perform aperture photometry in our simulated images. Candidate stars were detected using *daofind*, with a peak intensity threshold for detection set to $4\,\sigma_{\rm sky}$, where $\sigma_{\rm sky}$ corresponds to the rms fluctuation in the sky counts. The aperture photometry was carried out running the task *phot* for an aperture radius of 3 pix ($\sim 1.0 arcsec$).

The photometric errors and completeness curves that come from this aperture photometry in our simulated LMC images can be seen in Fig. 6.5. The photometric errors in this case are estimated using the differences between the input and output magnitudes; more specifically, for each small magnitude bin we compute the half-width of the error distribution, with respect to the median, that comprises 70% of the recovered stars. The completeness instead is simply defined as the ratio between total number of input stars, and those recovered by the photometry package. Fig. 6.5 presents the results for different simulations covering a wide range of density of field stars in the LMC, from the outer disk regions to the centre regions in the bar (see Fig.3.1). Notice that in these simulations we are following the requirement that the most central and crowded regions ($\log N_{\rm RGB} \geq 2.50$) will be observed under excellent seeing conditions only.

It can be noticed that the VMC expected magnitudes at SNR=10 for isolated stars ($Y = 21.9$, $J = 21.4$, $K = 20.3$) is well recovered in the simulations for the lowest density regions, attesting the correct photometric calibration of our simulated images. For these regions the 50% completeness level is reached at $Y \sim 22.5$, $J \sim 22.2$ and $K \sim 21.8$.

Crowding significantly affects in the quality of the aperture photometry, making the stars measured in central LMC regions to appear significantly brighter, and with larger photometric errors, than in the outermost LMC regions. As shown in Fig. 6.5, crowding clearly starts to dominate the noise for fields with $\log N_{\rm RGB} \gtrsim 2.00$ that correspond to about 20% (7%) of the total area covered in the LMC (SMC) (see Fig. 3.1). Therefore, PSF photometry is expected to be performed whenever crowding will prevent a good aperture photometry over VMC images. The significant improvements that can be reach by a PSF photometry are also illustrated by the thick black lines in Fig. 6.5. These results correspond to a PSF

[8]This is of course a crude approximation since deeper surveys sample larger galaxy redshifts. However, it is justified by the lack of deep-enough *Y* data, and by the little impact that such faint galaxies have in our stellar photometry (see Sect. 3.3.2).

photometry applied to the LMC centre ($\log N_{\rm RGB} = 2.90$), where the PSF fitting and the photometry were done using the IRAF tasks *psf* and *allstar*.

Figure 3.5 shows an example of CMD obtained from the aperture photometry in a simulated field with an intermediate level of density in the LMC. This figure reveals the expected CMD features – and the wealth of information – that will become available thanks to the VMC survey: well evident are the AGB, red supergiants, RGB, red clump (RC), Sub-Giant Branch (SGB) as well as the MS, from the brightest and youngest stars down to the oldest turn-off point. In comparison, the present-day near-infrared surveys of the MCs are complete only for the most evolved stars – excluding those in the most crowded regions, and those highly extincted by circumstellar dust. DENIS and 2MASS, for instance, are limited to $K_{\rm s} \lesssim 14$, revealing the red supergiants, AGB and upper RGB, and including just a tiny fraction of the upper MS (Nikolaev & Weinberg 2000b; Cioni et al. 2007). IRSF (Kato et al. 2007) extends this range down to $K_{\rm s} \lesssim 16.6$, which is deep enough to sample the RC and RGB bump, but not the SGB and the low-mass MS.

3.3.2 Comparison with UKIDSS data

Since the present work depends on simulations, it is important to check if they reproduce the basic characteristics of real data already obtained under similar conditions. UKIDSS represents the most similar data to VMC to be available for the moment. Therefore, in the following we will compare a simulated UKIDSS field with the real one.

For this exercise, we take the 0.21 deg^2 field towards Galactic coordinates $\ell = -220$ *degree*, $b = 40$ *degree*, which due to its similar distance from the Galactic Plane as the MCs, offers a good opportunity to test the expected levels of Milky Way foreground, and the galaxy background.

We have taken the original image from the UKIDSS archive, and performed aperture photometry with both DAOPHOT (Stetson 1987) ad SExtractor (Bertin & Arnouts 1996). A image for the same area has been simulated using UKIDSS specifications (pixel scale, SNR, etc.) and submitted to the same kind of catalogue extraction. Fig. 3.6 shows the results, comparing the K vs. $Y-K$ diagrams for the UKIDSS observed (left panel) and simulated (right panel) fields, for both stars (blue points) and galaxies (red points). Stars and galaxies were separated using the SExtractor Stellarity parameter *st*. We adopted $st > 0.85$ for stars, and $st \leq 0.85$ for galaxies.

Both DAOPHOT ad SExtractor aperture photometries turned out to be remarkably consistent with the ones provided by the Cambridge Astronomical Survey

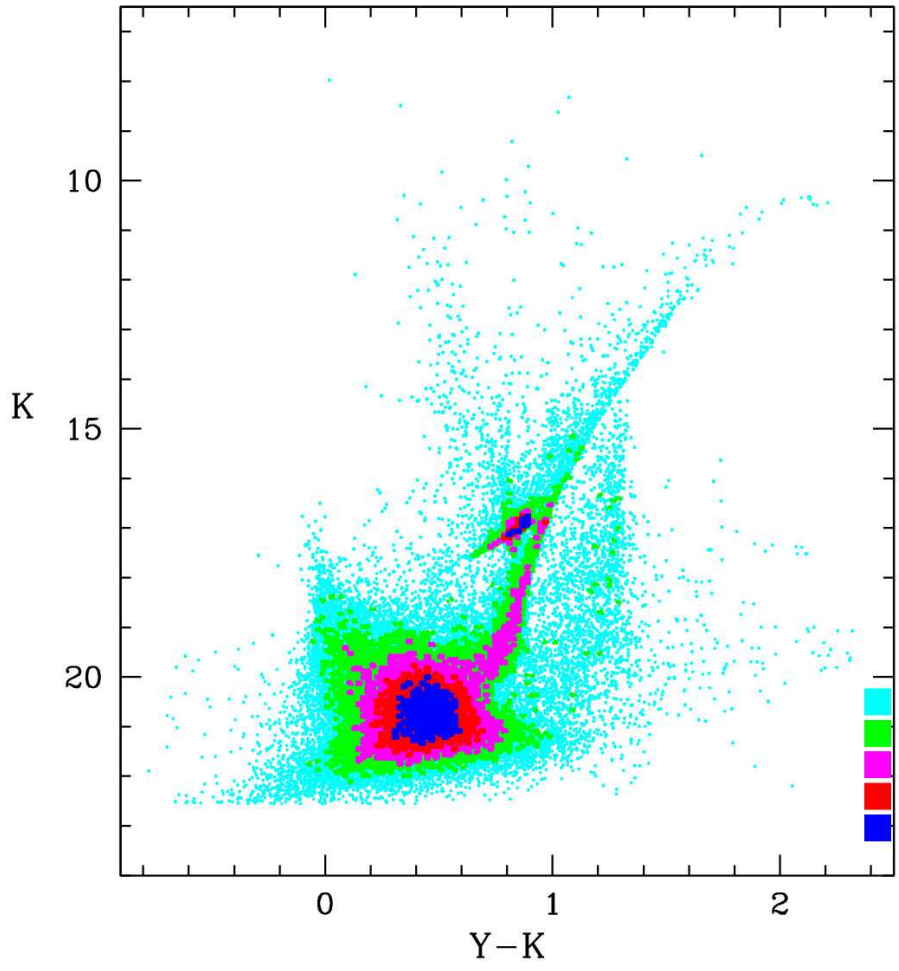

Figure 3.5: Example of (K, $Y-K$) CMD from aperture photometry in a simulated image for the VMC survey. The choices in the parameters represent a field of ~ 0.1 deg^2 with $\sim 10^5$ stars ($\log(N_{\rm RGB}) = 2.00$) following a constant SFR(t) and a AMR typical for the LMC clusters (see details in the text). The colours represent the density of points in a logarithmic scale. The information about approximated stellar masses, ages and metallicities can be obtained from Fig. 3.2.

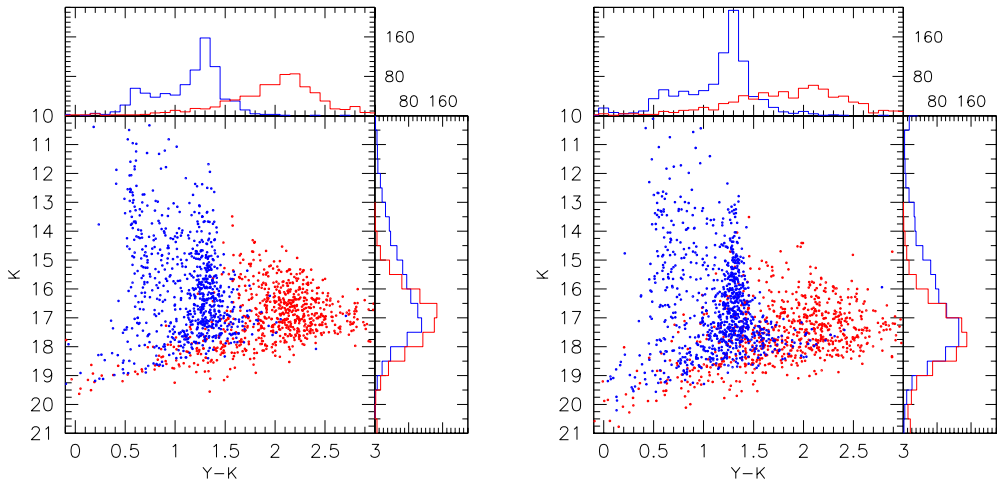

Figure 3.6: A comparison between the aperture photometry from UKIDSS image data (left) and the corresponding simulation (right), for a 0.21 deg^2 area towards $\ell = -220 degree, b = 40 degree$. The photometry was performed using both DAOPHOT and SExtractor. The main panels show the CMD obtained combining DAOPHOT photometry with SExtractor star/galaxy classification (blue/red dots, respectively). The histograms show the total colour and magnitude distributions of stars and galaxies (blue and red lines, respectively).

Unit (CASU) data reduction pipeline. This is very comforting since the CASU will adopt the same data reduction pipeline to the future VISTA data. The histograms at the right and top of the CMD panels show the object number count distribution in both colour and magnitude. As can be appreciated, our simulated objects distribute very similarly in colour and magnitude as the observed ones. The discrepancies are limited to a few aspects of the simulations, for instance the peak in the colour distribution at $Y-K \sim 1.3$ is clearly narrower in the models than in the simulations. This peak is caused by thin disk dwarfs less massive than 0.4 $M_{\odot}$ (Marigo et al. 2003b), and its narrowness in the models could be indicating that TRILEGAL underestimates the colour spread of these very-low mass stars.

The most important point of the model–data comparison of Fig. 3.6, however, is that the simulations reasonably reproduce the numbers (with errors limited to $\sim$ 20%), magnitudes and colours of the observed objects. This gives us confidence that our MC simulations contain the correct contribution from foreground Milky Way stars and background galaxies.

3.4 Recovering the SFH

3.4.1 Basics

The basic assumption behind any method to recover the SFH from a composite stellar population (CSP) is that it can be considered as a simply sum of its constituent parts, which are ultimately simple stellar populations (SSPs) or combinations of them. Therefore determining the SFH of any CSP – like the field stars in a galaxy – means to recover the relative weight of each SSP. The modern stellar population analysis in the late 80's (Tosi et al. 1989; Ferraro et al. 1989) and in the early 90's (Tosi et al. 1991; Bertelli et al. 1992) – marked by the advent of the first CCD detectors – was done assuming parameterized SFH, which revealed the main trends in the SFH but was still limited by a small number of possible solutions. The techniques to recover the SFH from a resolved stellar population started to become more sophisticated with the works of Gallart et al. (1996b,a), but they were significantly improved by Aparicio et al. (1997) and Dolphin (1997), who developed for the first time statistical methods to recover non-parameterized SFH from the CMD of a CSP. In practice these two works were the first to deal with a finite number of free independent components, obtained by adding the properties of SSPs inside small, but finite, age and metallicity bins. These "partial models" (Aparicio et al. 1997) are so computed for age and metallicity bins that should be

small enough so that the SSP properties change just little inside them, and large enough so that the limited number of bins ensures reasonable CPU times for the SFH-recovery. Furthermore, being the partial models computed for the same and constant star formation rate inside each age bin, implied that they needed to be generated only once, saving a large amount of computational resources (Dolphin 2002).

Considering that a CMD is a distribution of points in a plane divided into $N_{\rm box}$ boxes, these ideas can be expressed (Dolphin 2002) by

$$m_i = \sum_j r_j c_{i,j} \tag{3.1}$$

where m_i is the number of stars in the full model CMD for an CSP in the $i^{\rm th}$ box, r_j is the SFR for the $j^{\rm th}$ partial model, and $c_{i,j}$ is the number of stars in the CMD for the $j^{\rm th}$ partial model in the $i^{\rm th}$ CMD box.

Notice that the above equation is in fact written in terms of Hess diagrams since we are dealing with the number of stars in CMDs. So it means that the "observed" Hess diagram for a CSP can be described as a sum of independent synthetic Hess diagrams of partial models, being the coefficients $r_{\rm j}$ the SFRs to be determined. Fig. 3.7, to be commented later, illustrate the generation of such synthetic Hess diagrams for the partial models of the LMC.

The classical approach to determine the set of $r_{\rm j}$s is to compute the differences in the number of stars in each CMD box between data and model, searching for a *minimisation of a chi-squared-like statistics*. This kind of approach was applied for the first time to recover the SFH of a real galaxy by Aparicio et al. (1997), and has been successfully used in the analysis of the field stars in the dwarf galaxies in the Local Group (Gallart et al. 1999; Dolphin 2002; Dolphin et al. 2003; Skillman et al. 2003; Cole et al. 2007; Yuk & Lee 2007), including the MCs (Olsen 1999; Holtzman et al. 1999; Harris & Zaritsky 2001; Smecker-Hane et al. 2002; Harris & Zaritsky 2004; Javiel et al. 2005; Chiosi & Vallenari 2007; Noël et al. 2007). Although these works have in common the same basic idea of how to recover the SFH, there are clear variations in terms of the adopted statistics and strategy to divide the CMD in boxes (Gallart et al. 2005).

An interesting alternative to recover the SFH from the analysis of CMDs is offered by the *maximum likelihood* technique using a Bayesian approach (Tolstoy & Saha 1996; Hernandez et al. 1999, 2000; Vergely et al. 2002). In this approach the basic idea is to establish for each observed star a probability to belong to a SSP (based on the expected number of stars from this SSP in the position of the

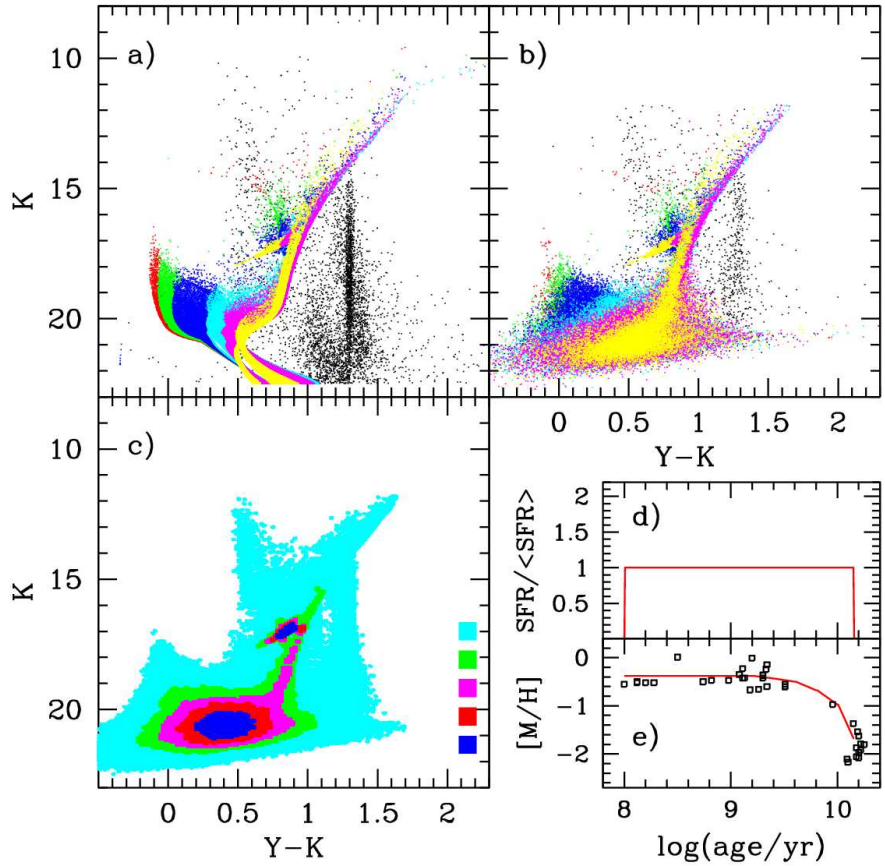

Figure 3.7: Simulated $(K, Y-K)$ CMD illustrating the building of partial models for the analysis of LMC stellar populations and its foreground MW stars. Panel (a) shows the theoretical stars generated from TRILEGAL, corresponds to the following ranges in $\log(t/\mathrm{yr})$: 8.00–8.40 (red), 8.40–8.80 (green), 8.80–9.20 (blue), 9.20–9.60 (cyan), 9.60–10.00 (magenta), 10.00–10.15 (yellow), plus the foreground MW (black). Panel (b) shows the same after considering the effects of photometric errors and completeness. Panel (c) is the Hess diagram for the sum of all partial models. Panels (d) and (e) show the input SFR(t) and AMR, respectively, the latter in comparison with LMC clusters (squares – data from Mackey & Gilmore 2003; Kerber et al. 2007; Grocholski et al. 2006, 2007). To avoid an extremely large size for this figure only 5% of all stars typically used ($\sim 10^7$) to build the partial models are shown in the top panels.

observed star in the CMD). Doing it for all observed stars, one can recover the SFRs that maximises the likelihood between data and model. It is interesting to note that in the recent years there is an increasing number of works applying this kind of technique for a wide range of problems, which include the determination of physical parameters of stellar clusters (Jørgensen & Lindegren 2005; Naylor & Jeffries 2006; Hernandez & Valls-Gabaud 2008) as well as of individual stars (Nordström et al. 2004; da Silva et al. 2006).

It is beyond the scope of the present work to discuss in depth the particularity of each aforementioned approach, but there are no strong reasons to believe that one can intrinsically recover a more reliable SFH than the other (Dolphin 2002; Gallart et al. 2005). So for a question of simplicity and coherence with the majority of the works devoted to the MCs, we adopted the classical *minimisation of a chi-squared-like statistics* technique to determine the expected errors in the SFH for the VMC data, using the framework of the StarFISH code (Harris & Zaritsky 2001, 2004), the χ^2-like statistics defined by Dolphin (2002) assuming that stars into CMD boxes follow a Poisson-distributed data, and a uniform grid of boxes in the CMD.

3.4.2 StarFISH and TRILEGAL working together

The StarFISH code[9] has been developed by Harris & Zaritsky (2001) and successfully applied by Harris & Zaritsky (2004) and Harris (2007c) to recover SFHs for the MCs inside the context of the Magellanic Clouds Photometric Survey (Zaritsky et al. 1997, MCPS)[10]. This code, originally designed to analyse CMDs built with *UBVI* data from the MCPS, and using Padova isochrones (Girardi et al. 2000a, 2002), offers the possibility of different choices for generating synthetic Hess diagrams (set of partial models, CMD binning and masks, combination of more than one CMD, etc.) and χ^2-like statistics, being also sufficiently generic to be implemented for new stellar evolutionary models, photometric systems, etc.

As illustrated in Fig. 3.7, the TRILEGAL code can also simulate the synthetic Hess diagram for a set of partial models, with the advantage of easily generating them in the UKIDSS photometric system, allowing also a greater control of all input parameters involved (see Sect. 3.2.3). Therefore we decide to directly provide these Hess diagrams to StarFISH, using it as a platform to determine the SFRs for our VMC simulated data by means of a χ^2-like statistics minimisation. The search

[9] Available at http://www.noao.edu/staff/jharris/SFH/
[10] http://ngala.as.arizona.edu/dennis/mcsurvey.html

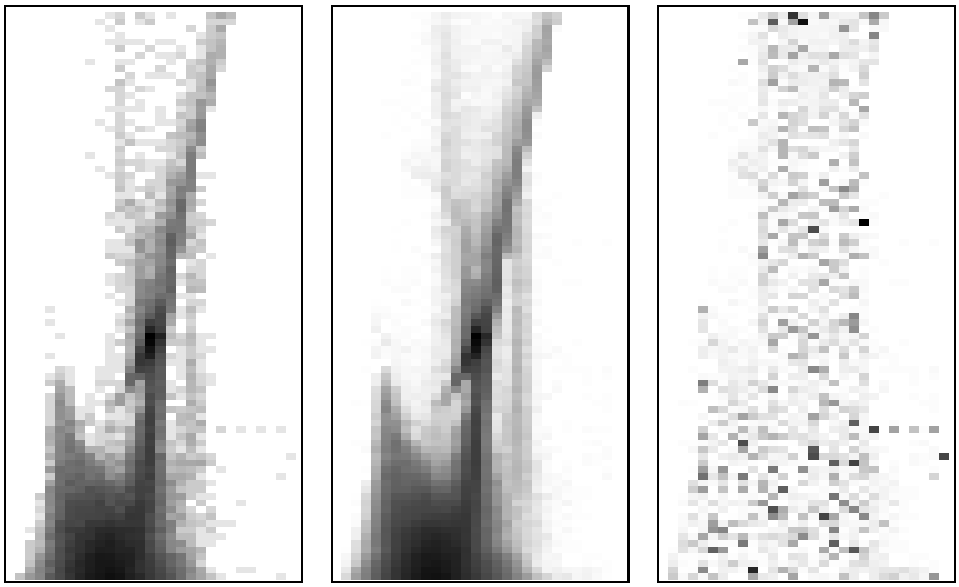

Figure 3.8: Example of simulated $(K, Y-K)$ Hess diagrams for the VMC (left panel) and for the best solution found by StarFISH (middle panel). The χ^2-like statistics map is also shown in the right panel. These Hess diagrams are limited to $12.00 < K < 20.50$ and $-0.50 < Y-K < 2.20$ and were built with bin sizes of 0.10 mag both in colour and in magnitude.

of the best solution is done internally in StarFISH by the *amoeba* algorithm that uses a downhill strategy to find the minimum χ^2-like statistics value.

An extra possibility offered by TRILEGAL is the construction of an additional partial model for the MW foreground [11]. Indeed, this is done by simulating the MW population towards the galactic coordinates under examination, for the same total observed area but averaging over many simulations so as to reduce the Poisson noise. This partial model is provided to StarFISH and used in the χ^2-like statistics minimization together with those used to describe the MC population. With this procedure, the presence of the MW foreground is taken into account in the SFH determination, without appealing to the (often risky) procedures of *statistical decontamination* based on the observation of external control fields. To our knowledgement, this is the first time that such a procedure is adopted in SFH-recovery work. Notice that, once the MW foreground model is well calibrated, its corresponding r_j could be set to a fixed value, instead of being included into the χ^2-like statistics minimization.

Figure 3.7 illustrates the generation of a complete set of partial models, covering ages from $\log(t/\mathrm{yr}) = 8.00$ to 10.15 (t from 0.10 to 14.13 Gyr) divided into 11 elements with a width of $\Delta \log t = 0.20$ each, and following an AMR consistent with the LMC clusters (see the panel d, and Sect. 3.2.3). In this figure we have grouped the partial models in just 6 age ranges (plus the MW foreground one) just for a question of clarity. What is remarkable in the figure is the high degree of superposition of the different partial models over the RGB region of the CMD – except of course for the partial model corresponding to the MW foreground. The MS region of the CMD, instead, allows a good visual separation of the different populations over the entire age range, even after considering the effects of photometric errors and incompleteness.

3.4.3 Results: Input vs. output SFR(t)

An example of SFH-recovery is presented in the Hess diagrams of Fig. 3.8. The input simulation (left panel) was generated for a constant SFR(t), for an area equivalent to 1 VIRCAM detector (0.037 deg^2) inside a region with a stellar density typical for the LMC disk ($\log N_{\mathrm{RGB}} = 2.00$, that produces a total number of stars of $N_{\mathrm{stars}} \sim 5{\times}10^4$). For this simulation, StarFISH fits the solution represented in the middle panel. Not surprisingly, the data–model χ^2-like statistics residuals (right panel) are remarkably evenly distributed across the Hess diagram.

[11] See http://stev.oapd.inaf.it/trilegal

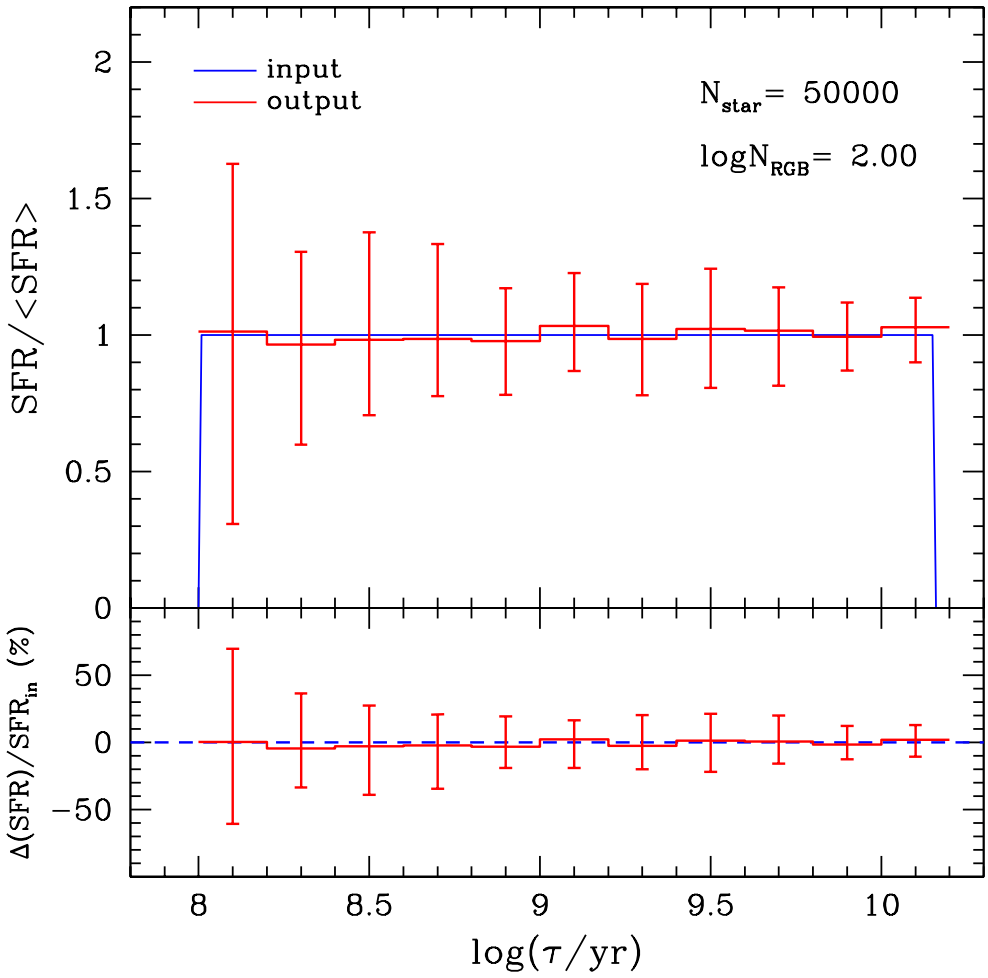

Figure 3.9: Errors in the recovered SFR(t) in terms of the mean SFR(t) (top panel) and input SFR(t) (bottom panel). The input simulations correspond to a typical LMC disk region ($\log N_{\rm RGB} = 2.00$) inside a single VIRCAM detector (~ 0.037 deg^2). The central solid line corresponds to the median solution found over 100 realizations of the same simulation, whereas the error bars correspond to a confidence level of 70%.

Figure 3.9 presents the median of recovered SFR(t), and its error, obtained after performing 100 realizations of the same simulation. As expected, the median SFR(t) over this 100 realizations reproduces remarkably well the input one, with no indication of systematic errors in the process of SFH-recovery[12] . The error bars correspond to a confidence level of 70%, which means that 70% of all individual realizations are confined within these error bars. Error bars are almost symmetrical with respect to the expected SFR(t). Furthermore, errors are typically below 0.4 in units of mean SFR(t) (top panel), which means uncertainties below 40% (bottom panel) for almost all ages. The only exception is the youngest age bin which presents errors in the SFR that are about two times larger than those for the intermediate-age stellar populations.

There are a many factors that can affect the accuracy of a recovered SFR(t). Among them, the most important are:

1. the quality of the data in terms of stellar statistics and photometry, that depends in principle (for the same photometric conditions of seeing, exposure times, calibration, etc.) on the density of the field and its covered area in the sky;

2. the uncertainties in the models themselves, that come from the possible errors in the adopted input parameters (distance, reddening, IMF, $f_{\rm bin}$, AMR, etc.), in the stellar evolutionary models, and in the imperfect reproduction of photometric errors and completeness;

3. the incorrect representation of the contamination from other sources, like foreground MW stars, stars from LMC star clusters, and background galaxies;

4. the non-uniform properties of the analysed field, like differential reddening or depth in distance.

Notice that the first factor affects the generation of observed Hess diagrams, while the synthetic Hess diagrams may become unrealistic due to the other factors. Furthermore, they produce different types of errors: whereas the first preferentially rules the *random* errors, the second is the main source of the *systematic* errors. A discussion on errors is addressed below.

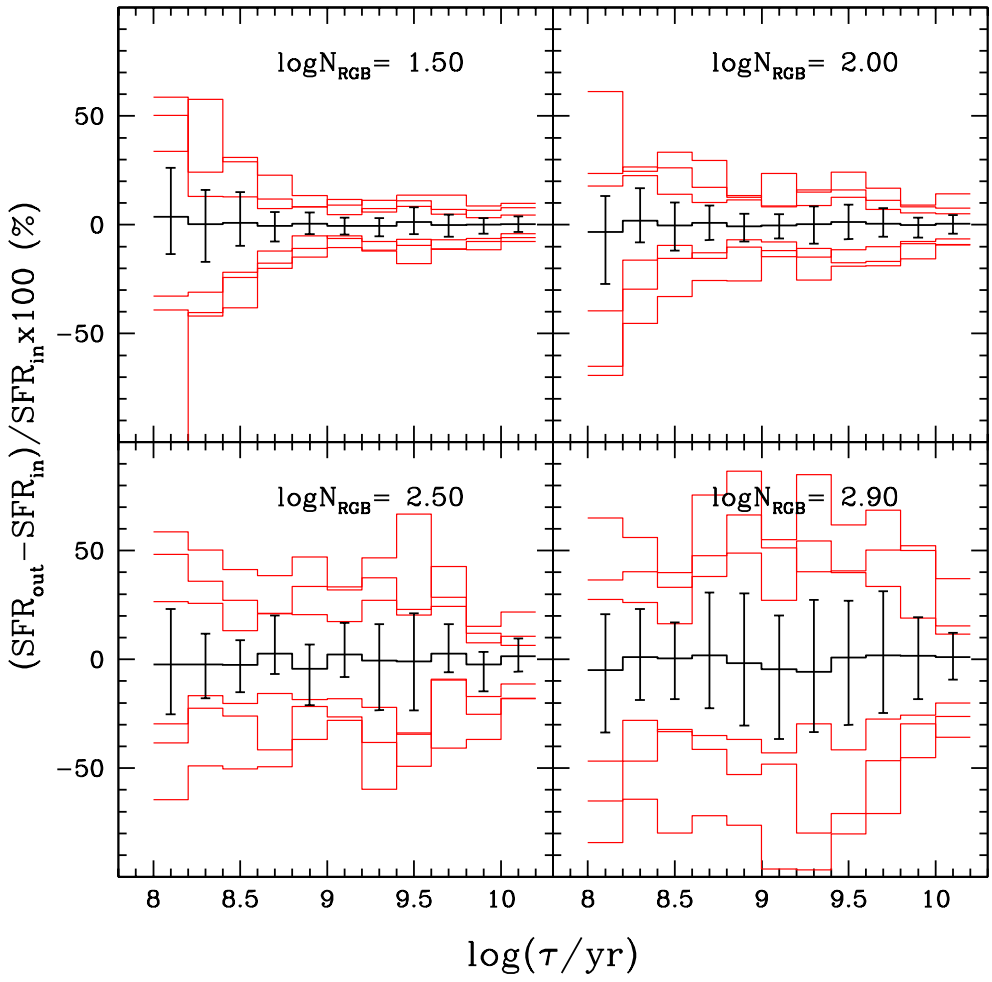

Figure 3.10: Errors in the recovered SFR(t) for four different stellar densities, from the outer LMC disk (top-left panel) to the LMC centre (bottom-right panel). The thick black solid line corresponds to the median solution found using 4×10^5 stars, whereas the error bars correspond to a confidence level of 70%. The thin red lines outline the same confidence level for a decreasing number of stars: 2×10^5, 10^5, 5×10^4 stars.

Random errors for a known AMR

In order to estimate the expected random errors in the SFR(t) for the LMC we performed controlled experiments similar to the one shown in Fig. 3.9, but covering a wide range of conditions in regard to the stellar statistics and crowding. Fig. 3.10 presents the results for four different levels of density, from the outer LMC disk (top-left panel) to the LMC centre (bottom-right panel), for a number of stars (or area) varying by a factor of 8. As can be seen, these two factors dramatically change the level of accuracy than can be achieved in the recovered SFR(t): an increase in the number of stars reduces the errors whereas an increase in crowding for a fixed number of stars acts in the opposite way.

The errors in the recovered SFR(t) as a function of the covered area, for all simulated density levels, are shown in Fig. 3.11 for partial models of four different ages, from young (top-left panel) to old ones (bottom-right panel). Here, a very interesting result can be seen: for stars older than $\log(t/\mathrm{yr}) \sim 8.60$ ($t \sim 0.4$ Gyr) the curves for different levels of density are almost superposed, revealing that for a fixed area the accuracy in the recovered SFR(t) is roughly independent of the level of crowding. It can be understood as a counterbalanced effect between the loss of stars due to a decrease in completeness, and the gain of stars due to an increase in density. Therefore, it seems that the SFR(t) for this wide range in age can be determined with random errors below 20% if an area of 0.10 deg^2 is used. Increasing the area by a factor of four means that the level of uncertainty drops to below 10%.

On the other hand, for partial models younger than $\log(t/\mathrm{yr}) \sim 8.60$ ($t \sim 0.4$ Gyr) a fixed area does not imply a constant level of accuracy in the SFR(t), being the errors significantly greater in the less dense regions. Since stars in this small age range are mainly identified in the upper main sequence at $18 \lesssim K \lesssim 20$, and in the core-helium burning phases at $14 \lesssim K \lesssim 18$ (see Fig. 3.7), this effect can be understood by the fact that for these brighter stars the increase in stellar density is not followed by a significant decrease in completeness. Indeed, Fig. 6.5 indicates the completeness is in general higher than 60% and 90%, for $18 \lesssim K \lesssim 20$ and $14 \lesssim K \lesssim 18$ stars, respectively, for the entire range of stellar densities of the LMC. In this situation, what determines the accuracy for a fixed area is simply the number of observed stars, which is proportional to the density. In particular, our simulations reveal the lack of stellar statistics in the outermost and less dense LMC regions, which require great areas to reach a statistically significant number of young stars. For instance, a level of uncertainty 20 % in the recovered young

[12] As a consequence, the total integral of the SFR is also well recovered.

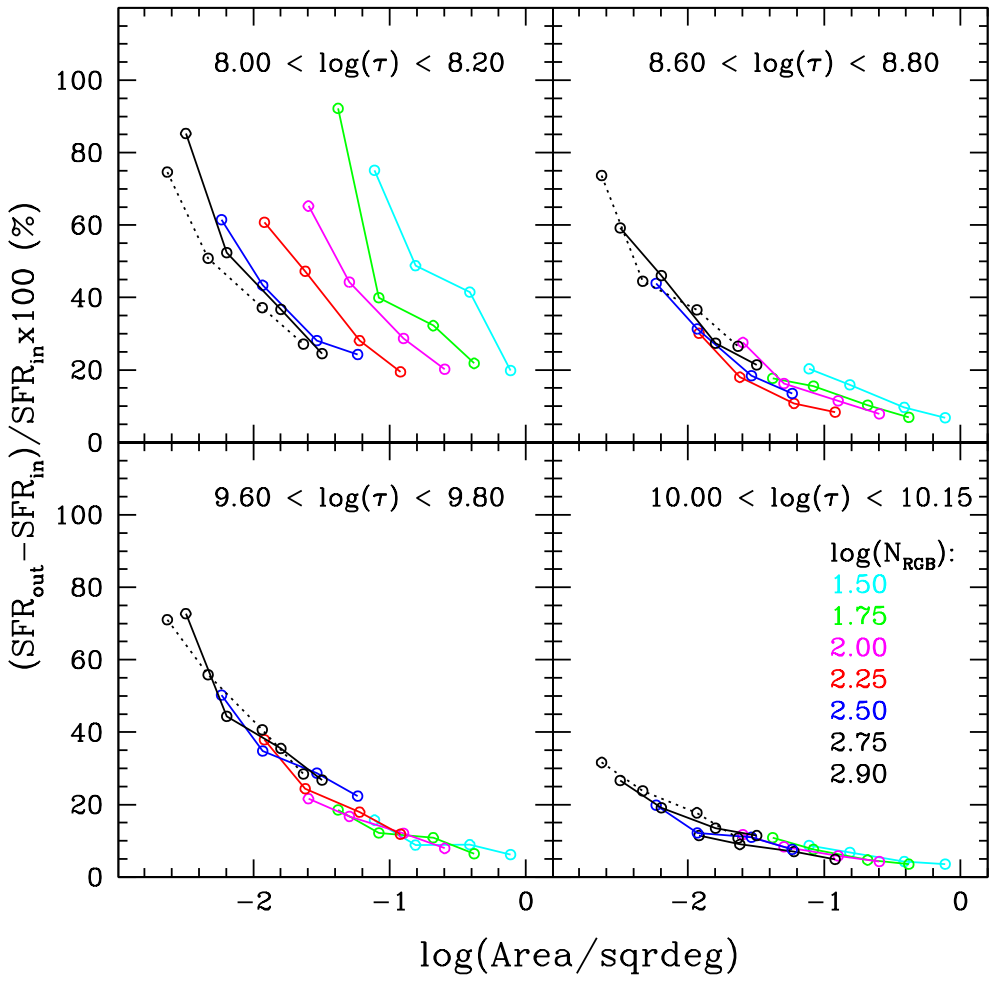

Figure 3.11: Errors in the recovered SFR(t) as a function of covered area and density of stars (different lines) for 4 partial models of different ages (different panels).

SFR(t) is obtained for an area ~ 10 times larger (~ 1 deg^2) in the periphery of the LMC than in more central regions.

The errors in the SFR(t) were also compared with those expected by the Poisson statistics in the number of observed stars for each partial model, as presented by Fig. 3.12. This figure reveals that the errors in the SFR(t) can be roughly understood as a propagation of the Poisson errors by a factor ~ 10. This explains why errors are smaller for the older ages, despite the fact that the different partial models are – due to the adoption of a logarithmic age scale – roughly uniformly separated in the CMD.

Random errors for an unknown AMR

In our previous discussion we have naively assumed that the AMR of the LMC is well known, by using a set of partial models which strictly follows the AMR used in the simulations. The real situation is much more complicated. Not only the AMR is not well established, but also it may present significant spreads (for a single age), and vary from place to place over the LMC disk. In order to face this situation, it is advisable to allow a more flexible approach for the SFH-recovery, in which for every age bin we have different partial models covering a significant range in metallicity.

We adopt the scheme illustrated in the top panel of Fig. 3.13, that is: for every age bin, we build partial models of 5 different metallicities, centered at the [M/H] value given by the reference AMR, and separated by steps of 0.2 dex. This gives a total of 56 partial models, and drastically increases the CPU time (by a factor of ~ 100) needed by StarFISH to converge towards the χ^2-like statistics minimum. Once the minimum is found, for each age bin we compute the $r_j(t)$-added SFR(t) and the $r_j(t)$-weighted average [M/H](t) over the five partial models with different levels of metallicity. After doing the same for 100 realizations of the input simulation, we derive the median and the confidence level of 70% (assumed as the error bar) for the output SFR(t) and [M/H](t). Figs. 3.13 and 3.14 illustrate the results for the case of a constant input SFR(t) and $\log N_{\rm RGB} = 2.00$.

In the top panel of Fig. 3.13, the dots with error bars show the output AMR, which falls remarkably close to the input one (continuous line). The error bars are smaller than 0.1 dex at all ages. The bottom panel plots the relative errors in the derived [M/H](t), showing that they are slightly larger for populations of age $\log(t/{\rm yr}) < 9.2$. Anyway, the main result here is that the errors in [M/H](t) are always smaller than the 0.2 dex separation between the different partial models.

Figure 3.14 instead compares, for the same simulation, the errors in the SFR(t)

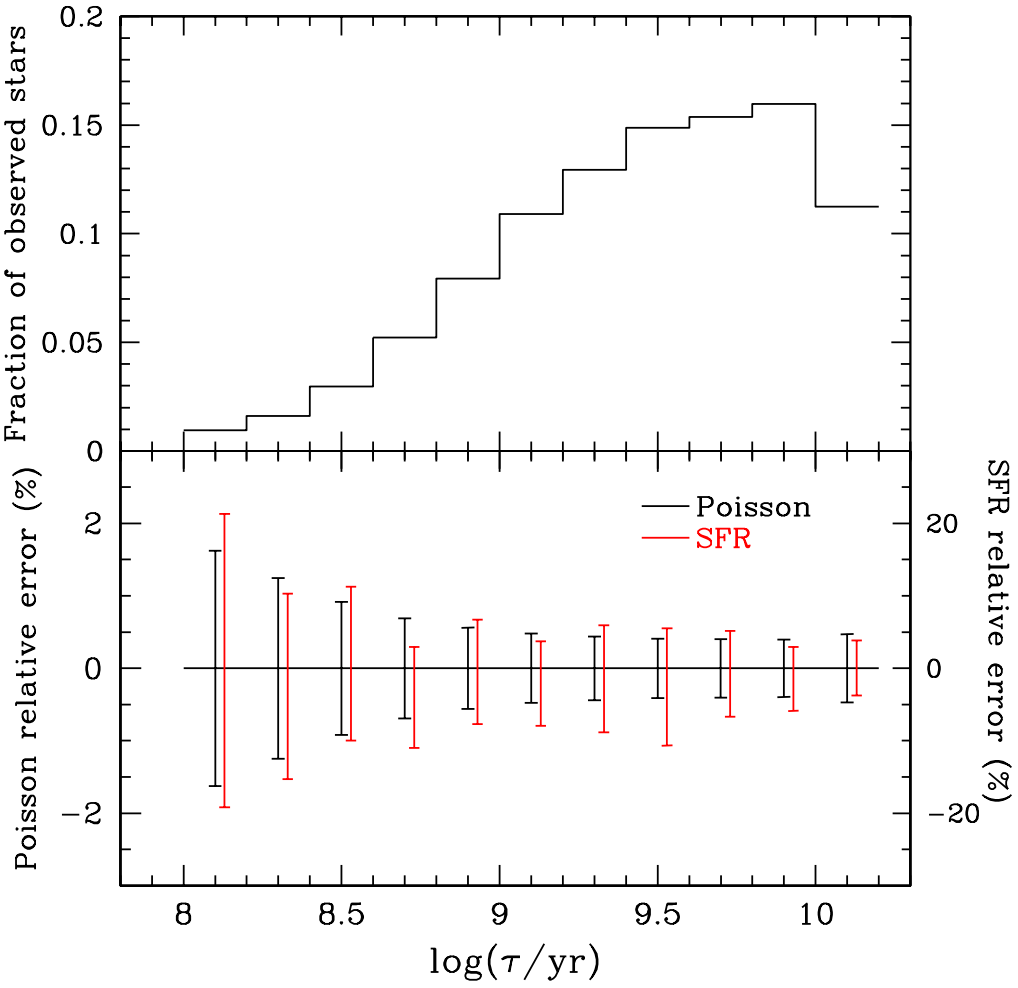

Figure 3.12: Distribution of the fraction of observed stars (top panel) and its Poisson relative errors (bottom panel, black lines) as a function age. These errors correspond to 4×10^5 simulated stars. The relative errors in the recovered SFR(t) are also shown (bottom panel, red lines) for a vertical scale 10 times larger (compare the labels of the two vertical axis in the bottom panel).

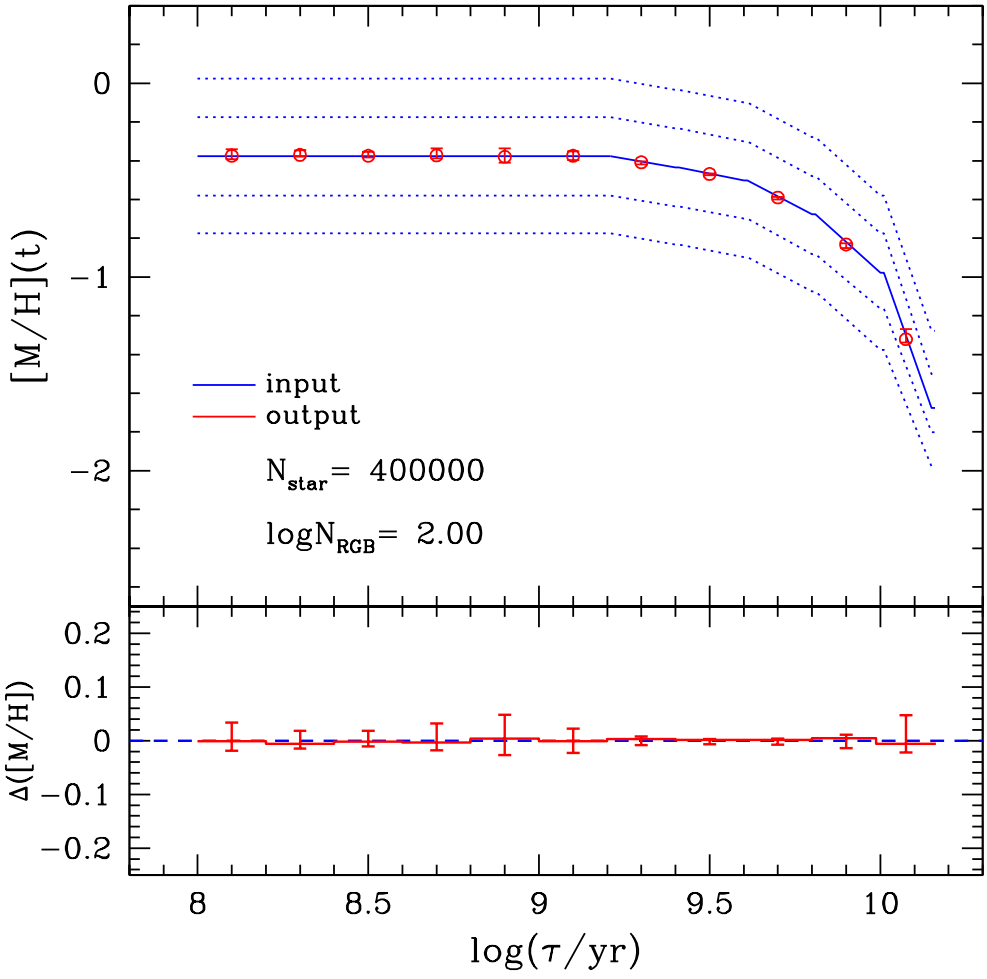

Figure 3.13: The top panel shows the distribution of metallicities of the partial models adopted in this work: The central solid line is the AMR adopted as a reference, and is used in all of our SFH-recovery experiments. At every age (or age bin), 4 additional partial models (along the dotted lines) can be defined and inserted in the SFH-recovery, then allowing us to access the AMR and its uncertainty (see text for details). The bottom panel shows the difference between the input and output AMRs for the case in which 5 partial models were adopted for each age bin.

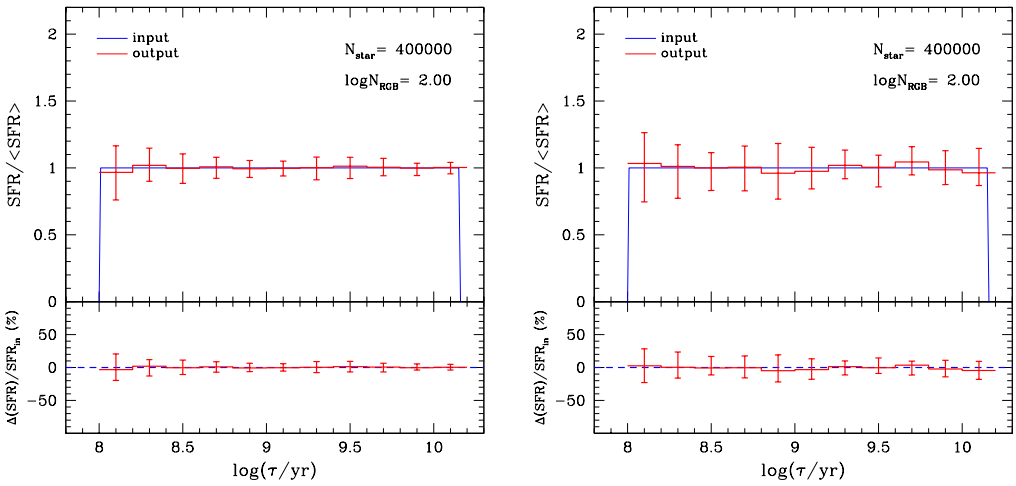

Figure 3.14: Errors in the recovered SFR(t) in terms of the mean SFR(t) (top panels) and input SFR(t) (bottom panels), for a typical LMC disk region inside the area of 8 VIRCAM detector (0.25 deg^2). The left panel correspond to a SFH-recovery that uses partial models distributed over a single AMR, whereas the right one uses 5 partial models for each age bin. The central solid line corresponds to the median solution found over 100 realizations of the same simulation, whereas the error bars correspond to a confidence level of 70%.

that result either considering (right panel) or not (left panel) the partial models with metallicity different from the reference AMR one. In other words, the left panel shows the SFR(t) that would be recovered if the AMR were exactly known in advance, whereas the right panel shows the SFR(t) for the cases in which the AMR is unknown – or, alternatively, affected by significant observational errors. It can be easily noticed that the SFR(t) is correctly recovered in both cases, although errors in the second case (right panel) are about 2 or 3 times larger than in the first case. Needless to say, the second situation is the more realistic one, and will likely be the one applied in the analysis of VMC data.

Systematic errors related to distance and reddening

Accessing all the systematic errors in the derived SFR(t) is beyond the scope of this work. However, the errors associated with the variations in the distance and reddening are of particular interest here, since both quantities are expected to vary sensibly across the LMC, hence having the potential to affect the patterns in the spacially-resolved SFH. Fortunately, these errors are very easily accessed with our method, since we know exactly the $(m-M)_0$ and A_V values of the simulations, as well as those assumed during the SFH-recovery.

The propagation of the uncertainties in the assumed distance modulus and reddening in the recovered SFR(t) was explored in a series of control experiments, in which a simulation performed with the canonical $(m-M)_0 = 18.50$ and $E_{B-V} = 0.07$ was submitted to a series of SFH-recovery analyses covering a range of $(m-M)_0$ and E_{B-V}. More specifically, $(m-M)_0$ was varied from 18.40 to 18.60, and E_{B-V} from 0.04 to 0.1. The results of these tests can be seen in Fig. 3.15, which presents the effect of wrong choices in these parameters not only in the recovered SFR(t) (bottom panel) but also in the minimum value for the χ^2-like statistics (top panels).

As expected, the absolute minimum value for the χ^2-like statistics was found for the synthetic Hess diagrams with the right distance modulus and reddening. Based on the χ^2-like statistics dispersion for 100 simulations we estimated that the errors in these parameters are about $\Delta(m-M)_0 = \pm 0.02$ mag and $\Delta E_{B-V} = \pm 0.01$ mag. These errors also imply systematic errors in the recovered SFR(t) of up to $\sim 30\%$ (Fig. 3.15, bottom panel).

The above experiments clearly suggest us that the mean distance and reddening should be considered as free parameters in the analysis, and varied by a few 0.01 mag so that we can identify the best-fitting values of $(m-M)_0$ and E_{B-V} together with the best-fitting SFH. This kind of procedure has been adopted by e.g.

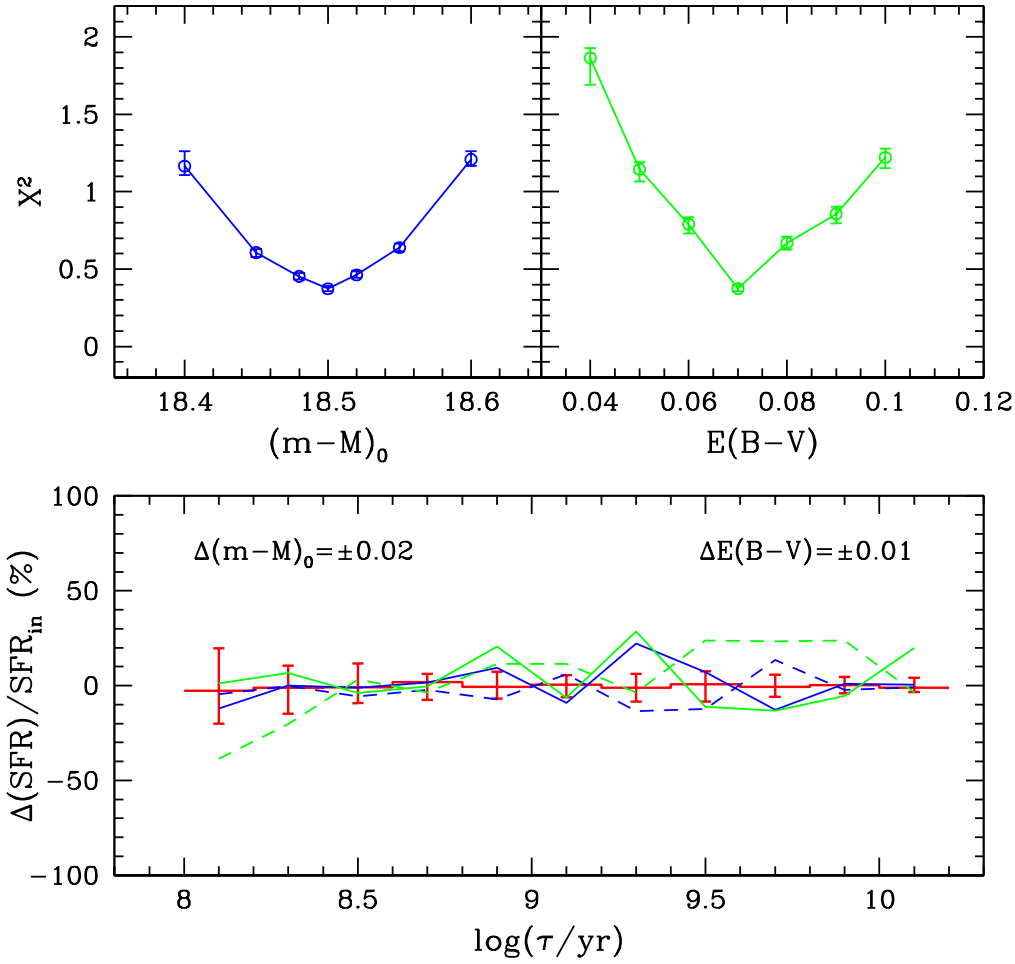

Figure 3.15: The top panels show the minimum χ^2-like statistics value as a function of distance modulus (blue) and reddening (green) adopted to build the synthetic Hess diagrams. The bottom panel illustrate the systematic variations that the errors in these two parameters cause in the recovered SFR(t) (continuous lines for an overestimation of $(m-M)_0$ and $E_{B\text{-}V}$, dashed lines for an underestimation).

Holtzman et al. (1997) and Olsen (1999) in their study of small regions over the LMC, and it is also implemented in the MATCH SFH-recovery package by Dolphin (2002). Occasionally, one could also consider small spreads in both $(m-M)_0$ and $E_{B\text{-}V}$ and test whether they further improve the χ^2-like statistics minimization. Once applied to the entire VMC area, the final result of this procedure will be independent maps of the geometry and reddening across the MC system, that can complement those obtained with other methods.

3.5 Concluding remarks

In this work we have performed detailed simulations of the LMC images expected from the VMC survey, and analysed them in terms of the expected accuracy in determining the space-resolved SFH. Our main conclusions so far are the following:

1. For a typical 0.10 deg^2 LMC field of median stellar density, the random errors in the recovered SFR(t) will be typically smaller than 20% for 0.2 dex-wide age bins.

2. For all ages larger than 0.4 Gyr, at increasing stellar densities the better statistics largely compensates the effects of increased photometric errors and decreased completeness, so that good-quality SFR(t) can be determined even for the most crowded regions in the LMC bar. The SFR(t) errors decrease roughly in proportion with the square of the total number of stars. The exception to this rule regards the youngest stars, which because of their brightness are less affected by incompleteness. In this latter case, however, the stellar statistics is intrinsically small and large areas are necessary to reach the same SFR(t) accuracy as for the intermediate-age and old LMC stars.

3. Although the AMR [M/H](t) can be recovered with accuracies better than 0.2 dex, the uncertainties in the AMR can significantly affect the quality of the derived SFR(t), increasing their errors by a factor of about 2.5.

4. The minimisation algorithms allow to identify the best-fitting reddening and distance with accuracies of the order of 0.02 mag in distance modulus, and 0.01 mag in $E_{B\text{-}V}$.

All of the above trends were derived from analysis of small LMC areas, that we have considered to be homogeneous in all of their properties (AMR, distance

and reddening). The errors were derived by varying each one of these parameters separately. The real situation will be, of course, much more complicated, with significant spatial variations of all of these quantities across the LMC. This consideration may lead us to suppose that errors here derived are underestimated. However, the above-mentioned parameters can be further constrained by simply taking into consideration additional data – for instance the available reddening maps, the limits on the relative distances provided by other independent distance indicators, the metallicity distributions of field stars, etc. – in our analysis. Moreover, our work indicates clearly how the random errors are reduced when we increase the area to be analysed. It is natural that, once the systematic errors are fully assessed, we will increase the area selected for the analysis, so that random errors become at least smaller than the systematic ones.

It is also worth mentioning that our present results were obtained using the $Y-K$ colour only. VMC will also provide CMDs involving the J passband, and their use in the SFH analysis can only reduce the final errors.

Another factor to be considered, in the final analysis, is that for old ages the SFR(t) is expected to vary very smoothly across the LMC, as indicated for instance by Cioni et al. (2000) and Nikolaev & Weinberg (2000b). This large-scale correlation in the old SFR(t) may be used as an additional constraint during the SFH-recovery, and may help to reduce the errors in the SFR(t) at all ages.

A forthcoming work will discuss in more detail the expected accuracy over the complete VMC area, including the SMC, and how this accuracy depends on other variables and constraints which were not discussed in this work (binaries, depth in distance, reddening variations, IMF, etc.). Anyway, the present work already illustrates the excellent accuracy in the measurements of the space-resolved SFH, that will be made possible by VMC data. Moreover, it demonstrates that detailed SFH-recovery using deep near-infrared photometry is also feasible, as much it has always been for the case of visual observations.

Chapter 4

The SMC star cluster NGC 419: its dual red clump and star formation history

4.1 Introduction

In the last decade, wide field imagers and the Hubble Space Telescope (HST) have provided detailed CMDs for the star fields in the Magellanic Clouds. One of the main surprises was the discovery that the red clump of core-He burners is not a compact feature, but may present extensions amounting to a few 0.1 mag departing from its top and bottom parts, as well as a blue extension that connects with the horizontal branch of the old metal-poor populations.

The ground-based observations from Bica et al. (1998) and Piatti et al. (1999) evinced a $\sim$0.4 mag extension of the red clump to fainter magnitudes, spread over wide areas of the outer LMC disk. Girardi (1999) gave a clear interpretation to this extention – thereafter named *secondary red clump* – claiming that it is made of the stars just massive enough to start burning He in non-degenerate conditions, at ages of $\sim$ 1 Gyr, whereas the main body of the red clump is made of all the intermediate-age and old stars which passed through degenerate cores and the He-core flash at the tip of the RGB. The same feature was suggested to be present in the Hipparcos CMD for the Solar Neighbourhood (Girardi et al. 1998), and provides an explanation to the vertical extension – amounting to about 0.8 mag in the $F814W$ band (see e.g. Holtzman et al. 1997) – of the red clump in the sharp CMDs obtained by the HST for several LMC fields.

Plots of the red clump magnitude versus age for star clusters – as in Girardi (1999, figs. 3 and 4), and Grocholski & Sarajedini (2002, fig. 6) – seem to confirm the theoretical framework that led to Girardi's (1999) prediction of a secondary clump: the In this work, we apply to the NGC 419 data the classical method of star formation history (SFH) recovery via CMD reconstruction, deriving for the first time this function for a star cluster with multiple turn-offs. The values for the cluster metallicity, reddening, distance and binary fraction, were varied within the limits allowed by present observations. The global best-fitting solution is an excellent fit to the data, reproducing all the CMD features with striking accuracy. The corresponding star formation rate is provided together with estimates of its random and systematic errors. Star formation is found to last for at least 700 Myr, and to have a marked peak at the middle of this interval, for an age of 1.5 Gyr. Our findings argue in favour of multiple star formation episodes (or continued star formation) being at the origin of the multiple main sequence turn-offs in Magellanic Cloud clusters with ages around 1 Gyr. It remains to be tested whether alternative hypotheses, such as a main sequence spread caused by rotation, could produce similarly good fits to the data clearly indicate a red clump decreasing in luminosity up to $\sim$ 1 Gyr, then a jump upwards by about 0.4 mag, and a much slower evolution thereafter.

A handful of faint red clump stars are also found among the radial velocity members of the open clusters NGC 752 and 7789, and possibly also in NGC 2660 and 2204 (Mermilliod et al. 1998; Girardi et al. 2000b). The latter authours associated these stars with the secondary clump feature, and tried to figure out how it could appear in an object for which the age spread was supposedly very small. Indeed, from their discussion it is clear that a single cluster age corresponds to a very narrow range of red clump masses and hence to the sampling of either the faint (secondary) or the bright (classical) red clump. The two red clumps could not appear together in a single star cluster, unless some other mechanism – e.g. a dispersion in the mass loss along the RGB, or in the efficiency of overshooting on the main sequence (MS) – were invoked.

The reasoning from Girardi et al. (2000b) would however now fail, at least for the star clusters in the Magellanic Clouds. Indeed, now *we know* that many of them do not represent single ages, but rather a range of ages that can extend up to a few 100 Myr (Mackey et al. 2008; Milone et al. 2009) – or equivalently, to a range of MS turn-off (MSTO) masses of a few 0.05 $M_{\odot}$.

By visual inspection of the CMDs for a few SMC star clusters studied by Glatt et al. (2008), we came across what was *very evidently* a composite structure of main+secondary red clump in NGC 419. The presence of a secondary clump in

this cluster was indeed noticed by Glatt et al. (2008, their sect. 3.6), who however have suggested it to be "a red clump of the old SMC field star population". They also noticed the composite structure in the MS, attributing it to an extended period of star formation, similarly to the one claimed by Mackey et al. (2008) for three LMC clusters.

In the following, we demonstrate that the composite structure of the red clump in NGC 419 is real and undubiously associated to the cluster (Sect. 4.2). We show that it corresponds to the simultaneous presence of stars which have started burning He under non-degenerate and degenerate conditions (Sect. 4.3). We then illustrate that this rare occurrence in a cluster allows us to set stringent constraints on the cluster age and amount of convective core overshoooting during the MS evolution (Sect. 4.4). We then briefly suggest that NGC 419 is not a unique case, and draw some final comments in Sect. 4.5.

4.2 NGC 419 photometry and CMD

We have retrieved from the HST archive the NGC 419 data obtained by GO-10396 (PI: J.S. Gallagher). The dataset consists of a 740 arcsec^2 area observed with the Advanced Camera for Surveys (ACS) High Resolution Channel (HRC) centered on NGC 419, plus a 4.24×10^4 arcsec^2 area observed with the ACS Wide Field Channel (WFC) 37 arcsec offset from the cluster centre. Both datasets were reduced via standard procedures (Sirianni et al. 2005). The HRC data, given its high spatial resolution, is the most useful for the study of the NGC 419 population, whereas the WFC dataset provides the comparison data for interpreting the SMC field.

We have performed aperture and PSF photometry on the calibrated HRC image, finding that both provide CMDs very similar to the Glatt et al. (2008) ones. We have then opted for the PSF catalogue and cutted it at $(\mathrm{sharp}^2_{F555W}+\mathrm{sharp}^2_{F814W})^{1/2} < 0.2$. This quality cut eliminates many outliers from the CMD, especially at the faintest magnitudes, but do not affect the morphology of features at the red clump and MSTO level.

The HRC data is plotted in Fig. 4.6, which shows both the global CMD and separate panels detailing the red clump and the MSTO regions. The extended nature of the red clump is evident in the figure[1]. It seems to be formed by a

[1]The choice of the $F814W$ band for the ordinate is not casual, since $F814W$ presents flatter bolometric corrections than $F555W$, over the $T_{\rm eff}$ range of the red clump. This improves the separation in magnitude of the clump substructures, and at the same time keeps the subgiant branch

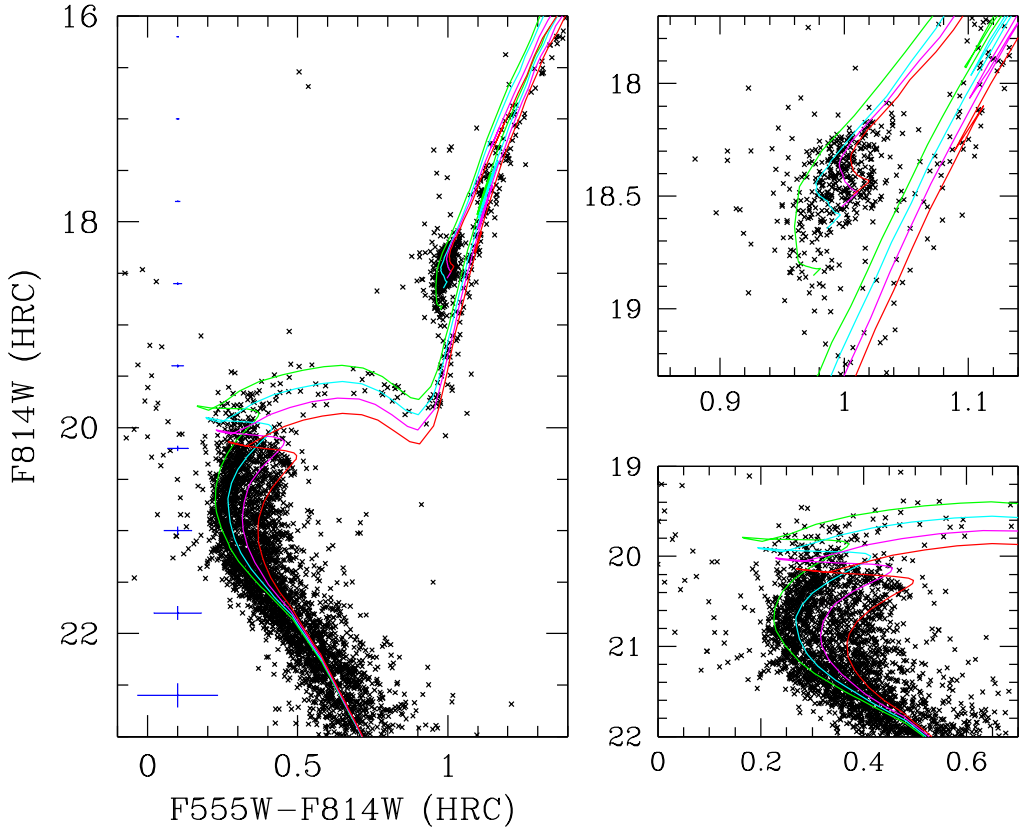

Figure 4.1: The CMD for NGC 419 as derived from the HRC data centered on the cluster (left panel). The 1σ error bars, as derived from artificial star tests, are drawn at the left. The right panels detail the red clump (top) and MSTO regions (bottom). The overlaid isochrones are from Marigo et al. (2008), for a metallicity $Z = 0.004$, ages varying from $\log(t/\mathrm{yr}) = 9.10$ to 9.25 with a constant spacing of 0.05 dex, $E_{F555W-F814W} = 0.09$, and $(m-M)_{F814W} = 18.85$. Notice that these particular isochrones describe reverse sequences in the MSTO and red clump regions of the CMD: whereas the MSTO gets dimmer for increasing ages, the red clump gets brighter.

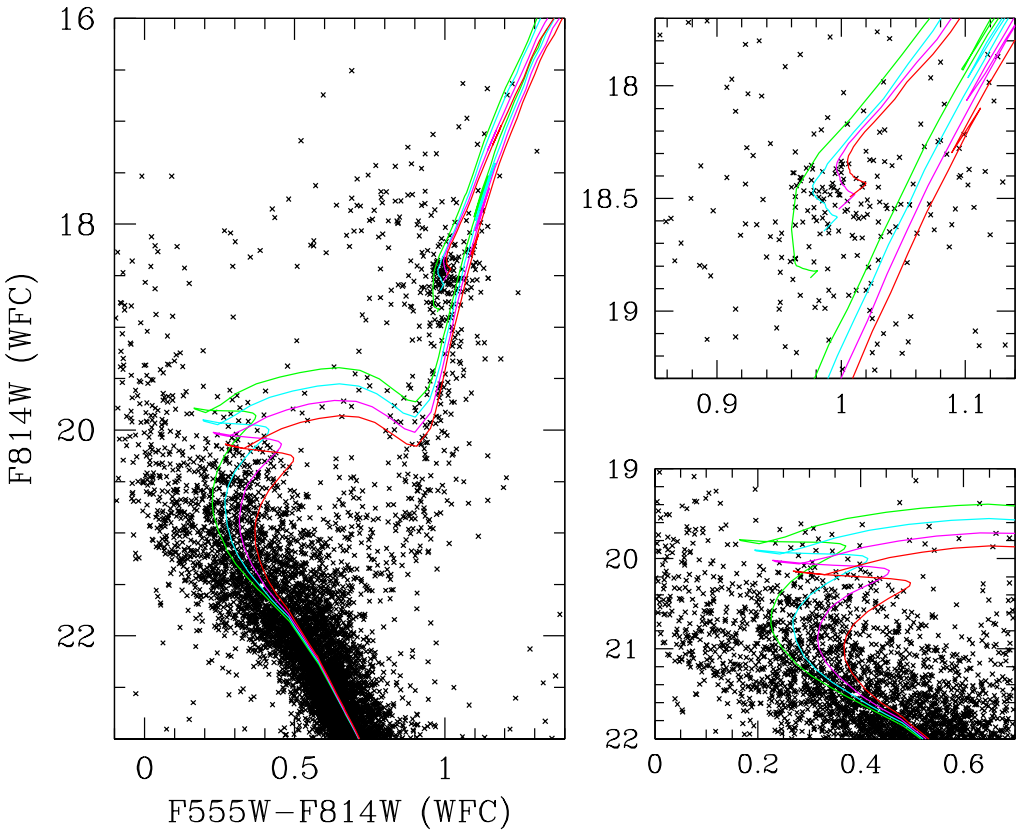

Figure 4.2: The CMDs for 2.47×10^4 arcsec^2 field around NGC 419, as derived from the WFC data after subtracting a circular area of radius 75 arcsec around the cluster. The overlaid isochrones are the same as in Fig. 4.6, and are plotted for reference only. The bulk of the red clump is below the saturation limit at $F555W \sim 17.9$.

main blob located between $F814W = 18.1$ and 18.65, followed by a well-defined faint wing between $F814W = 18.65$ and 19.0, which we tentatively identify as the secondary clump. We note that there is no similar wing extending from the top of the red clump. These sequences are about 0.08 mag bluer (in $F555W - F814W$) than the ridgeline of RGB stars. In addition, the red part of the CMD shows a well delineated subgiant branch, and the bump of early asymptotic giant branch (AGB) stars centered at $F814W = 17.7$.

There are 55 stars between $F814W = 18.65$ and 19.0, 8 out of which are red enough to belong to the RGB rather than to the secondary clump. The main red clump instead contains 341 stars. These numbers correspond to the HRC effective area of 740 arcsec^2, centered on NGC 419. We verified that both sets of stars distribute all over the HRC image, and share similar distributions of photometric errors and sharpness. So, it is unlikely that the secondary clump could be an artifact of a given subsample of the data.

Can the field SMC stars account for the 47 stars in the secondary clump, as suggested by Glatt et al. (2008)? To answer this question, we look at the WFC data of Fig. 4.2, which covers an area 33 times larger than the HRC one. It was obtained subtracting from the complete WFC catalogue – without applying any quality cut – a circular area of 75 arcsec in radius around NGC 419. The remaining area of 2.47×10^4 arcsec^2 was considered to be "SMC field", and contains 150 red clump stars in the $F814W$ range between 18.1 and 19.0. Therefore, the expected number of these stars in the 740 arcsec^2 area of HRC is of just 4.5. Moreover, their typical magnitudes are closer to those of the main red clump in NGC 419, rather than to the secondary one. We conclude that the field cannot contribute with more than ∼10% of the 47 stars observed in the secondary clump, and probably contribute much less. *The bulk of the secondary clump observed in HRC data indeed belongs to NGC 419*.

4.3 Modelling the two clumps

Our interpretation of the red clump structure in NGC 419 is already clear in Fig. 4.6 and in the discussion of Sect. 4.1: the fainter secondary red clump is explained by the core-He burning stars belonging to the younger isochrones, which have just avoided e^--degeneracy before igniting He. This feature has been throughfully discussed in Girardi (1999) and Girardi et al. (1998), in the context of galaxy

out of its magnitude range.

field populations. It appears naturally in simulations of star-forming galaxies with moderate-to-high metallicities, provided that the underlying stellar models do present a fine resolution in mass (better than 0.1 $M_{\odot}$; see Girardi 1999).

In the following, we discuss the specific case of NGC 419 by means of newly-computed evolutionary tracks of initial composition ($Z = 0.004, Y = 0.250$). The input physics is the same as in Bertelli et al. (2008). We have initially adopted a moderate amount of convective overshooting, i.e. $\Lambda_c = 0.5$, where Λ_c is the size of the overshooting region across the convective boundary, in pressure scale heigths, following the Bressan et al. (1981, 1993) definitions. For a limited interval of initial masses M_i, typically going from $M_{HeF} - 0.4\ M_{\odot}$ to $M_{HeF} + 0.4\ M_{\odot}$, we follow the evolution up to the thermally pulsing AGB, whereas for smaller masses (down to 0.6 $M_{\odot}$) we have computed only the MS evolution. Stellar tracks are spaced by $\Delta M_i = 0.05\ M_{\odot}$. These tracks are converted to stellar isochrones in the ACS/HRC and ACS/WFC Vegamag systems using the transformations from Girardi et al. (2008).

The isochrones are then fed to the TRILEGAL population synthesis code (Girardi et al. 2005) to simulate the photometry of star clusters at the SMC distance. We apply to the TRILEGAL output the photometric errors derived from artificial star tests performed on the original HRC images. The results are illustrated in Fig. 4.3, which shows the expected time evolution of the red clump for a cluster for two different cases: either for an almost-instantaneous burst of star formation (with a duration of $\Delta \log t = 0.01$), and for a burst spanning a range of $\Delta \log t = 0.15$. The latter case corresponds roughly to the situation indicated by the MSTO stars in Fig. 4.6. 20 % of the stars in the simulation are assumed to be detached binaries with a mass ratio comprised between 0.7 and 1 (Woo et al. 2003). Since this latter prescription is rather uncertain, binaries are always marked with a different colour in our plots.

It is evident from Fig. 4.3 that the red clump rapidly transits from a vertically-extended feature, to a much more compact and slightly brighter clump at a mean age t close to 1.25 Gyr. The transition takes place completely in an age interval of just ~ 0.1 Gyr for the case of an intanstaneous burst, and in about twice this time for the case of a $\Delta \log t = 0.15$-wide burst. From now on, we will refer to the mean age of this transition as t_{HeF}.

We note that vertically-extended red clumps are present for all ages younger than t_{HeF}, even in the intanstaneous-burst case; however, they are wider than observed in NGC 419, and present drop-shaped LFs – i.e. with a sharp cut at the bottom and a more extended tail at the top. This is not what observed in the red clump of NGC 419, which presents the maximum of its LF at the top, together with a

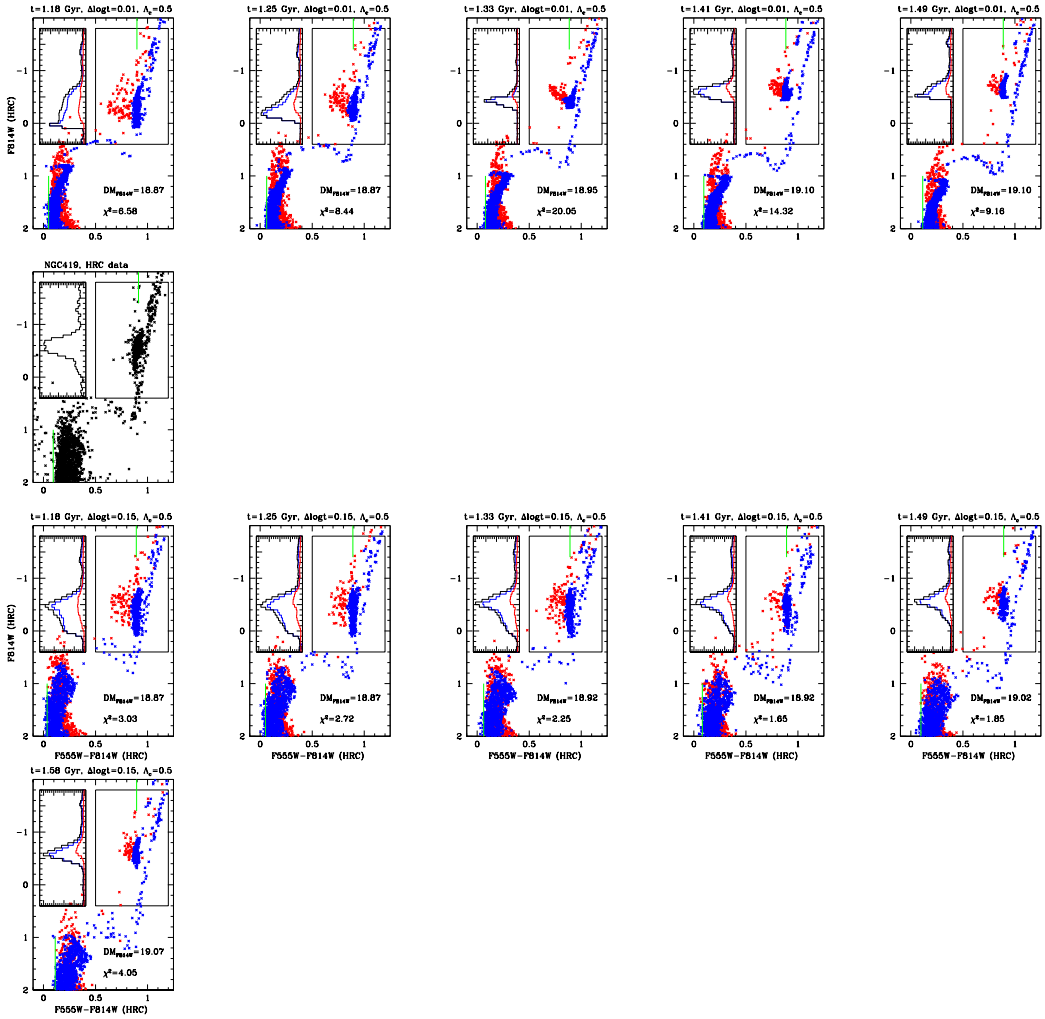

Figure 4.3: Models for the evolution of the red clump feature in the CMD as a function of mean population age t, for both a single-busrt population (top panels) and for a composite one with duration of $\Delta \log t = 0.15$ (bottom panels), in both cases with the assumption of moderate convective overshooting ($\Lambda_c = 0.5$) and $Z = 0.004$. Single stars are marked in blue, double stars in red. Each panel presents on the top right a box evincing the red clump, and on the top left the luminosity function (LF) for the stars in this box. The best-fitting distance modulus and the associated χ^2 are also displayed. For comparison, the top right panel shows the HRC data of NGC 419 on the same scale, after being arbitrarily shifted by 19.0 and 0.09 in magnitude and colour, respectively. The green vertical lines in all panels mark the median colour of the red clump, and the bluest colour of the MS (see text).

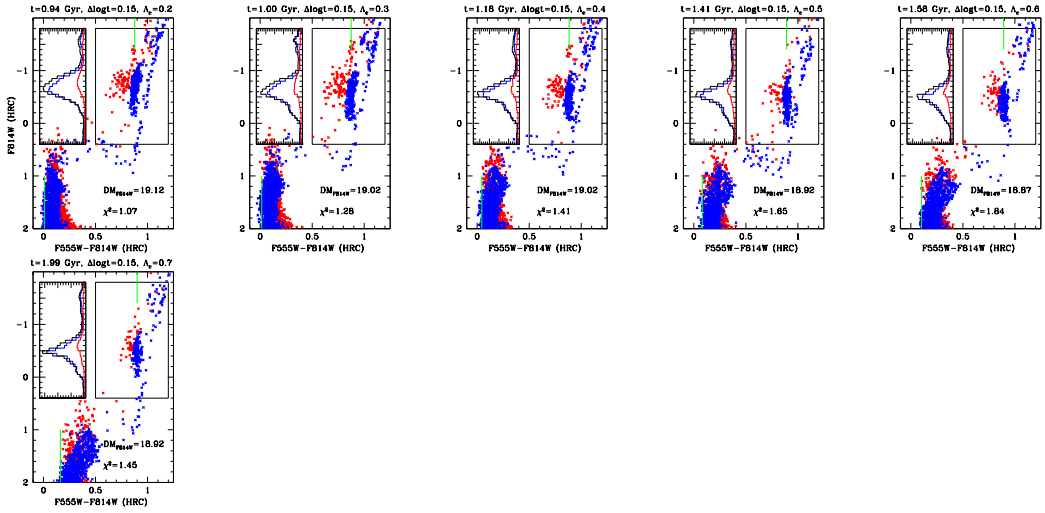

Figure 4.4: Top panels: The same as in Fig. 4.3, but now showing the models that best fit the red clump for several values of overshooting efficiency Λ_c, and for the $\Delta \log t = 0.15$ case only. Although all models reproduce the observed red clump similarly well, they differ very much in their age (from 0.94 to 1.99 Gyr, as Λ_c increases from 0.2 to 0.7), and produce different MSTO magnitudes and colours.

bump at the faintest magnitudes. A configuration similar to NGC 419 is obtained only in the extended-burst case, for ages comprised between 1.41 and 1.58 Gyr: indeed, this age range is the only one which combines the vertically-extended red clump of younger ages, with the compact and brighter red clump of older ages, in about the right proportions to explain the observations. We identify NGC 419 as belonging to this very limited – and surely very singular – age interval. In order to identify the best-fitting age, we compute the χ^2 between data and model, for the red clump region only. The distance modulus is varied until the minimum value of χ^2 is met for each age t. The results are printed in Fig. 4.3, and evince the excellent quality of the fit for the 1.41 Gyr-old model with $\Delta \log t = 0.15$.

Finally, it is worth mentioning that the MS+red clump binaries tend to draw a plume departing from the red clump towards bluer colours and brighter magnitudes, which (1) is easily identifiable in observed CMDs because of its colour separation from the red clump, and (2) do not change the drop-shaped form of the LF for the younger red clumps. Binaries cannot mimick the bimodal LF observed in the red clump of NGC 419.

A question raised by the referee is whether the two red clumps could be caused by populations with different helium content, abundances of CNO elements, or

overshooting efficiency. Although nothing can be excluded, so far there are no indications of such effects in clusters as young as NGC 419. Moreover, it is Occam's razor to refrain us from looking for more complicate alternatives: in fact, our explanation requires *only* standard physics added to a quite simple distribution of stellar ages – the same one indicated by the clusters' MSTO – while keeping all other parameters constant. We recall that the transition between faint and bright red clump is something that inevitably happens, sooner or later, for *every* single stellar population, causing *always* about the same amount of brightening in the red clump over a similar timescale (which is dictated mainly by the equation of state of partially-degenerate matter). Therefore, there is no free parameter to be fixed in order to explain the presence and position of the two red clumps, there is just the very loose requirement of "a prolonged-enough duration of the star formation".

4.4 Overshooting and the age scale

According to the interpretation given in this work, the red clump in NGC 419 corresponds to stars with a precise internal configuration after H-exhaustion: their cores have a mass very close to 0.33 $M_{\odot}$, as their central temperatures approach $T_{\rm c} = 10^8$ K. Slighty higher core masses lead to non-degenerate He-ignition. Slightly smaller core masses lead to e^--degeneracy, which halts the core contraction and is followed by the cooling of the central core by plasma neutrinos; as a consequence the He-ignition is postponed to a later stage – namely the RGB tip – at which the core masses have grown up to 0.45 $M_{\odot}$ (see Sweigart et al. 1990).

These core masses after H-exhaustion do also correspond to a narrow interval of initial masses, comprehending the transition between intermediate- and low-mass stars, $M_{\rm HeF}$. It has long been known that convective core overshooting changes the relation between the initial mass and the H-exhausted core mass, hence directly affecting the value of $M_{\rm HeF}$, and its corresponding age $t_{\rm HeF}$ (e.g. Bressan et al. 1993). Even if the efficiency $\Lambda_{\rm c}$ can be constrained by means of several methods which use either the morphology of the CMD or star count ratios (e.g. Woo et al. 2003, and references therein), this is still a main source of uncertainty in settling the age scale of intermediate-age clusters, and in the theory of stellar populations in general.

Can the NGC 419 giants help us to set constraints on $M_{\rm HeF}$ and $t_{\rm HeF}$, and hence on $\Lambda_{\rm c}$? Probably yes, considering that higher $M_{\rm HeF}$ values (lower $\Lambda_{\rm c}$) imply bluer MSTOs. Once we identify a star cluster during the particular age $t_{\rm HeF}$, fixing the position of its red clump(s) in the CMD, the relative position of the MSTO should

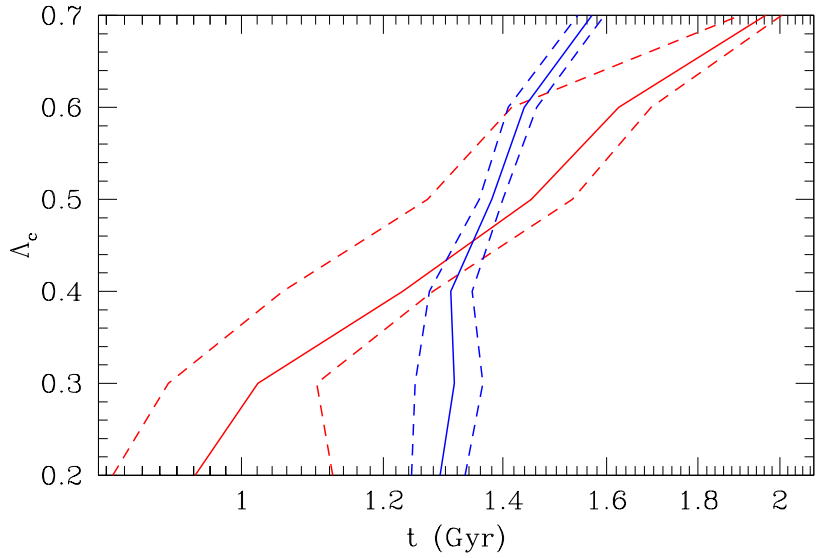

Figure 4.5: Confidence regions in the t vs. Λ_c plane. The continuous red line follow the locus of minimum χ^2 values derived from the fitting of the red clump morphology (see also Fig. 4.4). The continuous blue line describe the models which perfectly fit the colour difference between the red clump and MSTO. Dashed lines present the estimated 70% confidence limits.

depend mainly on overshooting.

With this idea in mind, we have computed several set of stellar evolutionary tracks and isochrones, with Λ_c varying from 0.2 to 0.7. For each one of these sets we identify the age at which, for a $\Delta \log t = 0.15$ star formation burst, the red clump morphology is best reproduced (just as in Fig. 4.3). Indeed, Fig. 4.4 shows that similarly good fits of the red clump morphology are obtained for all values of Λ_c, but at different ages $t_{\rm HeF}$. We recall that these different fits actually represent *very similar distributions of the core mass after H-exhaustion.*

We then measure the colour difference between the median of the red clump, and the bluest border of the MSTO region defined by the 98% percentile of the star counts above an absolute magnitude of 2.5. This quantity is little sensitive to the fraction of binaries, and our simulations indicate that it can be measured with a 1σ error of 0.006 mag. Fig. 4.5 shows this quantity in the t vs. Λ_c plane, together with the estimated 70% confidence level region of the best-fitting model to the red clump morphology. The best simultaneous fit of the two quantities is obtained for $\Lambda_c = 0.47^{+0.14}_{-0.04}$ and $t = 1.35^{+0.11}_{-0.04}$ Gyr (with random errors only).

Importantly, these t and Λ_c determinations are largely free from uncertainties in the cluster distance and reddening. However, they may be slightly affected by other factors like the assumed fraction of binaries, the mixing-length parameter, and the detailed star formation history of NGC 419. More detailed analysis (in preparation) will aim to reduce these uncertainties by using information from the complete CMD, and better exploring the parameter space. A few preliminary conclusions can be advanced here: (1) Models for $\Delta \log t$ values of 0.1 and 0.2 do also provide good fits of the red clump morphology, with their best-fitting ages differing by less than 6% from those we find for $\Delta \log t = 0.15$; these age differences are comparable to the above-mentioned random errors. However, such models have to be excluded because they clearly provide a worst description of the MSTO region of the CMD. (2) On the other hand, models with a fraction of binaries as small as 10% tend to provide slightly better fits of the red clump LF, at essentially the same ages as those found with 20% of binaries, and with just a modest impact in the morphology of the MSTO.

4.5 Final considerations about the dual clump

NGC 419 can be definitely added to the list of star clusters with a secondary red clump, together with the Milky Way open clusters NGC 752 and 7789, and possibly also NGC 2660 and 2204, which were already discussed by Girardi et al. (2000b). This time, however, we are facing a very populous cluster which presents a CMD rich of details, from its lower MS up to the AGB carbon star sequence (see Fig. 4.6, and Frogel et al. 1990). The secondary red clump itself is very well populated and its detection can hardly be controversial. This fine CMD feature provides strong constraints to the core mass reached by its MS stars. All these aspects make of NGC 419 an excellent tool for calibrating stellar evolution models, as well as the age sequence of intermediate-age populations.

Can we identify additional star clusters in the Magellanic Clouds, having the same secondary clump feature? Probably yes, since these galaxies contain dozens of populous clusters with ages around 1 Gyr, and the presence of multiple turn-offs is a common feature among them (Milone et al. 2009). Indeed, from a rapid eye inspection of published CMDs obtained with HST/ACS, we notice that dual (main+secondary) red clump structures seem to be present also in the LMC clusters NGC 1751, 1783, 1806, 1846, 1852, and 1917 – see figs. 7, 8, 9, 16 and 17 in Milone et al. (2009), and fig. 1 in Mackey et al. (2008). All these clusters have multiple turn-offs, with the youngest one being at $F814W \sim 19.5$, which is

comparable with the NGC 419 one if we consider the ~ 0.5 mag difference in the SMC–LMC distance moduli. A subsequent work will examine these clusters in close detail, in the perspective of deriving more stringent constraints to stellar evolutionary models. Cluster fundamental parameters such as the age, distance and reddening, will be re-evaluated as well.

4.6 The prolonged SFH

4.6.1 Aims

Back in the nineties, the *Hubble Space Telescope* Wide Field Planetary Camera 2 (*HST*/WFPC2) opened a new era in the study of stellar populations in the Magellanic Clouds. Starting from Gallagher et al. (1996), many authors were able to derive the detailed star formation history of LMC and SMC fields, via the analysis of deep CMDs reaching well below the oldest main sequence turn-offs (MSTO). It became possible as well the accurate measurement of the properties and structure of many populous star clusters (e.g. Mighell et al. 1996; Elson et al. 1998b; Rich et al. 2000, 2001; Gouliermis et al. 2004; Kerber et al. 2007).

The higher efficiency and larger area of the Advanced Camera for Surveys (ACS) further improved the situation. One of the latest achievements in the field was the conclusive evidence, based on ACS data, that many star clusters in the LMC with ages typically larger than 1 Gyr, present double or multiple main sequence turn-offs (MMSTO; Mackey & Broby Nielsen 2007; Mackey et al. 2008; Milone et al. 2009). This effect was, in precedence, already indicated by ground-based deep CMDs (Bertelli et al. 2003; Baume et al. 2007), which however were far from presenting the fine details of the ACS ones.

While there is firm observational basis for the presence of MMSTOs in star clusters, their interpretation is far from being settled. Once it has been demonstrated that the presence of binaries cannot mimick the detailed shape of MMSTOs (see Mackey et al. 2008; Goudfrooij et al. 2009) the most obvious interpretation is that they are the signature of stellar populations spanning several hundreds of Myr in age. This interpretation however poses a major challenge to the understanding of star formation and dynamics in star clusters, since it is not obvious how objects with relatively shallow potential wells could retain their gas and continue forming stars for so long a time. Bekki & Mackey (2009) propose a mechanism to explain the bluest MSTOs as being due to a second event of star formation driven by the collision with a giant molecular cloud; this hypothesis however does only

explain *double* MSTOs and not the continuous MMSTO structures observed by Goudfrooij et al. (2009) in NGC 1846.

Whether the MMSTO phenomenum can be explained by stellar populations of single or multiple ages, bears very much in the interpretation of CMDs of nearby galaxies in general. In deriving SFH of galaxies, one assumes that their CMDs are made by the superposition of populations of different ages, each one presenting a narrow MSTO. Were the MSTOs of single-burst populations intrinsically broad, most works of SFH-recovery in nearby galaxies would have to be revised to some extent.

Given the above situation, we decided to test if the extended-SFH hypothesis could really explain the MMSTOs in $\sim$ 1-Gyr old star clusters in the Magellanic Clouds. As a first target, we choose the rich SMC star cluster NGC 419. Two aspects make this cluster an ideal target for our goals. First, it does not only present a MMSTO (Glatt et al. 2008) but also has a dual clump of red giants (Girardi et al. 2009), which is the signature of stars close to the transition between those that form an electron-degenerate core after H-exhaustion, and those that do not. This additional fine structure of the CMD provides strong constraints to the cluster mean age and to the efficiency of convective core overshooting in stars (Girardi et al. 2009), probably helping to limit the family of stellar models that can be fit in the process of SFH-recovery. Second, the central region of NGC 419 counts with extremely accurate photometry provided by the High Resolution Channel (HRC) of ACS. As a bonus, the field contamination is almost negligible for this cluster.

4.7 Preparing NGC 419 for SFH-recovery

The dataset used in this work has been retrieved from the HST archive (GO-10396, PI: J.S. Gallagher) and consists of a 740 arcsec^2 area centered on NGC 419, observed with the ACS/HRC in the filters F555W and F814W. The same images have already been analysed by Glatt et al. (2008, 2009) and Girardi et al. (2009). Girardi et al. (2010, its figure 1) provide a false-color version of these HRC images, together with a comparison with the much wider ACS Wide Field Channel (WFC) images of the same cluster. There, one may notice that the HRC field samples just the very inner part of the cluster, and that the distribution of stars over its area is quite uniform.

The original data has been re-reduced as described in Girardi et al. (2009). Essentially, we have accessed the archival images already processed and calibrated using the standard procedures mentioned in Sirianni et al. (2005). Aperture and

Point Spread Function (PSF) photometry with the DAOPHOT package (Stetson 1987) were performed within a 2 pix radius, and aperture corrections were applied. The resulting CMDs are very similar to those described in Glatt et al. (2008). The PSF photometry was then preferred and used for all subsequent applications.

Fig. 4.6 shows the ACS/HRC data for NGC 419, in the F814W vs. F555W – F814W CMD. This plot will be used as a reference to our analysis.

In order to characterize the errors in the photometry and the completeness of the sample, we have performed a series of artificial star tests (AST) on the reduced images (see e.g. Gallart et al. 1999; Harris & Zaritsky 2001). The procedure consists of adding stars of known magnitude and colour at random places in the F555W and F814W images, and redoing the photometry exactly in the same way as before. The artificial stars are then searched in the photometric catalogues, and when recovered the changes in their magnitudes are stored for subsequent use.

In order to avoid the introduction of additional crowding in the images, artificial stars are positioned at distances much higher than their PSF width. We found that the PSF radius in on our ACS/HRC images is of $\lesssim 7$ pix, whereas our fitting radius is of 2 pix. So, our AST are distributed on a grid spaced by 20 pix, which is each time randomly displaced over the image.

A total of 3.4×10^9 ASTs were performed, covering in an almost uniform way the CMD area of the observed stars as well as the area for which we build the "partial models" to be used in the SFH analysis (see Sect. 5.4.2 below). Then, the ratio between recovered and input stars gives origin to the completeness map of Fig. 4.7. Note that the 90 % completeness limit is located at F814W $\sim$ 21.7, which is well below the position of the MMSTOs in NGC 419.

Another important aspect is that the stellar density is quite constant over the HRC images, as well as the completeness. For instance, at magnitudes 22.15, from the image center to the borders the completeness changes from 0.87 to 0.90 for the F555W filter, and from 0.78 to 0.85 for F814W. Since this difference is very small and the bottom part of the CMD will not be used in our analysis, we do not apply any position-dependent completeness to the CMDs, but simply the average values derived from all the ASTs.

Figure 4.8 presents the differences between the recovered and input magnitudes of ASTs, as a function of their input magnitudes. These differences give a good handle of the photometric errors effectively present in the data. The error distributions are slightly asymmetric because of crowding.

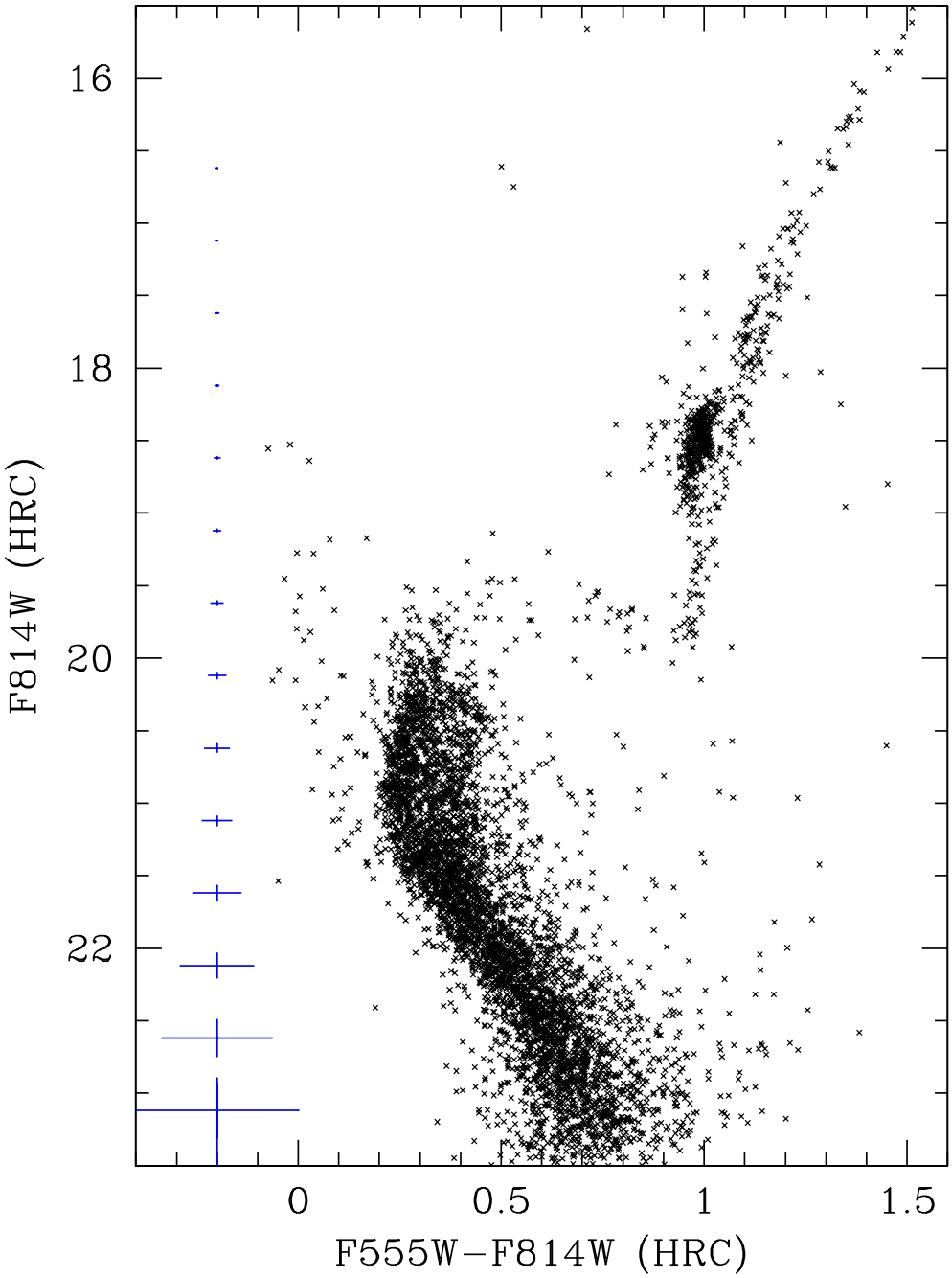

Figure 4.6: The CMD for NGC 419 as derived from the HRC data centered on the cluster, after the re-reduction described in this work and without applying any quality cut to the photometry. The 1σ error bars, as derived from artificial star tests (see Sect. 5.2.2), are drawn at the left.

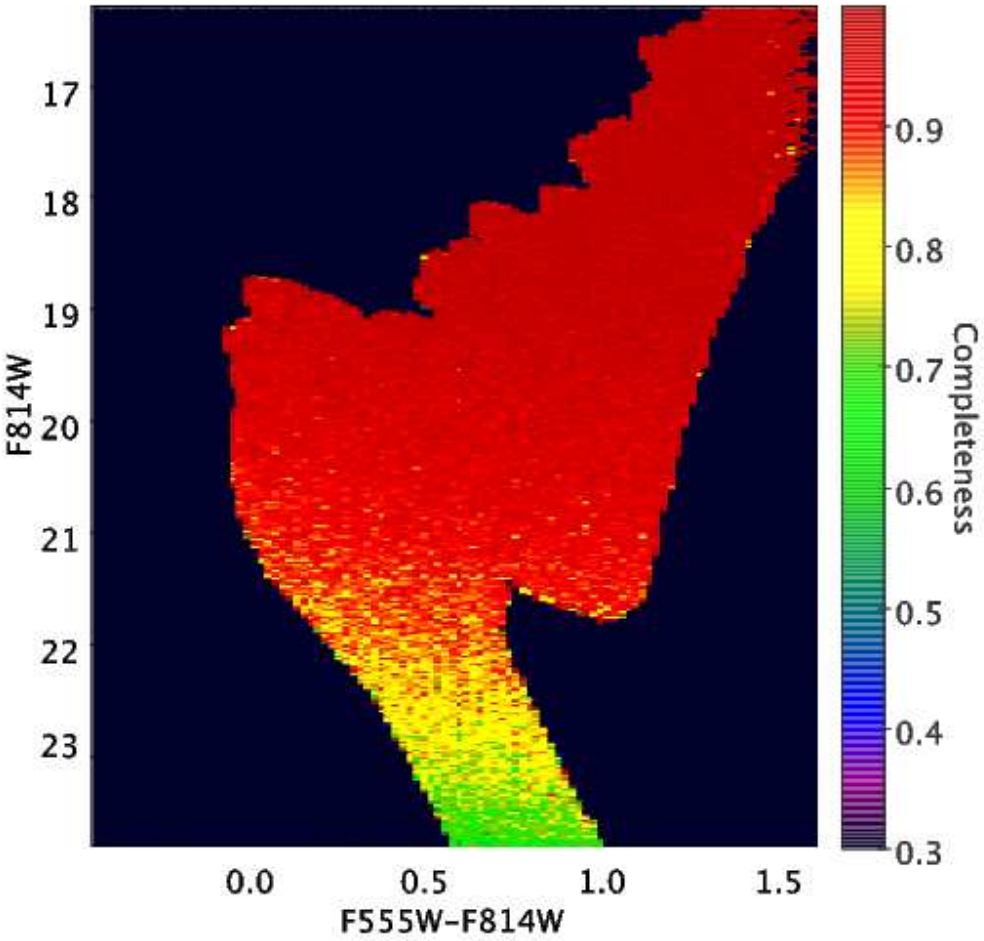

Figure 4.7: Completeness map, derived from the complete set of ASTs.

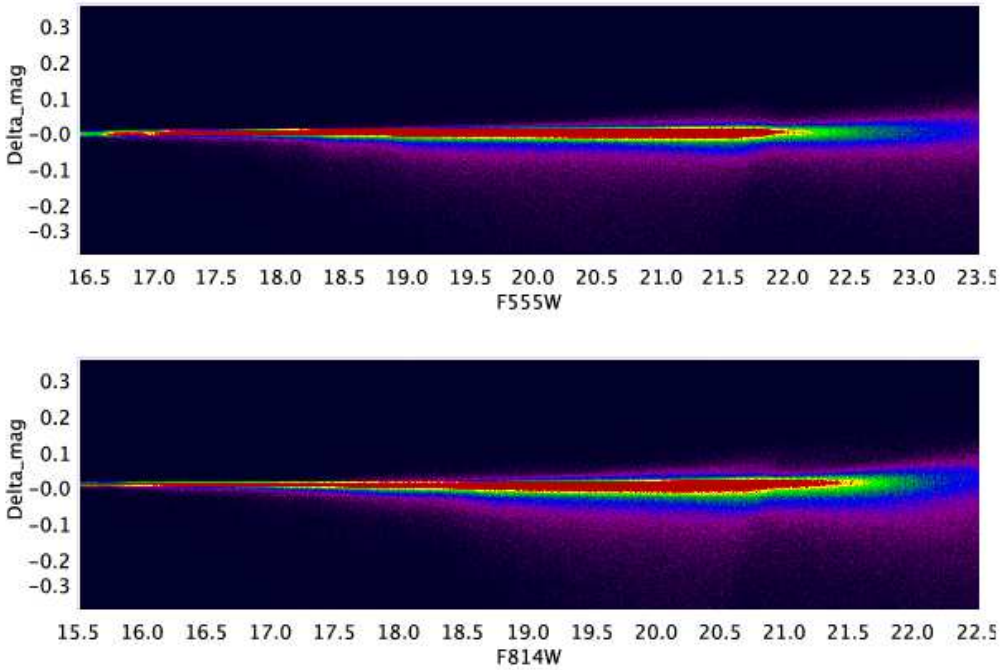

Figure 4.8: Map of photometric errors as a function of input F555W and F814W, as derived from the ASTs. The errors are defined as the difference between the recovered and input magnitudes.

4.7.1 The partial models

The basic process of SFH-recovery is the decomposition of an observed CMD as the sum of several "partial models", which represent stellar populations in very limited intervals of age and metallicity. In our case we will assume a constant age-metallicity relation (AMR) i.e., a single value for the metallicity for all ages, since so far there are no evidences for significant spreads in metallicity in star clusters like NGC 419 (e.g. Mucciarelli et al. 2008). Hence, each partial model is defined as a stellar aggregate with constant star formation over an age interval of width $\Delta \log t = 0.05$ dex. This is a fine age resolution for a work of SFH-recovery; suffice it to recall that the age bins adopted in the SFH-recovery of nearby galaxies are usually wider than 0.1 dex in $\log t$ (see e.g. Gallart et al. 1999; Harris & Zaritsky 2001; Dolphin et al. 2003, for some examples). The age interval covered by our partial models goes from $\log(t/\mathrm{yr}) = 8.9$ to 9.4, which is much wider than the interval suggested by the position of NGC 419 MMSTOs. So, for each set of parameters, we have a total of 10 partial models, completely encompassing the age interval of interest.

The other parameters defining a set of partial models are the V-band extinction A_V, the distance modulus $(m-M)_0$, the metallicity [Fe/H], and the binary fraction f_b; these will be varied in our analysis as described below. Other parameters describe the area of the CMD to be sampled, and its resolution. With basis on our Figs. 4.6 and 4.7, we decide to limit the CMD area to be analysed as: F555W − F814W between −0.4 and 1.6, and F814W between 16.32 and 22.0. Within these limits, stars are not saturated, and completeness is above 80 %. The CMD resolution is set to be 0.02 mag both in colour and in magnitude.

The partial models are simulated with the aid of the stellar population synthesis tool TRILEGAL (Girardi et al. 2005) in its version 1.3, which stands on the Marigo et al. (2008) isochrones, transformed to the ACS/HRC Vegamag photometry using Girardi et al. (2008) bolometric corrections and extinction coefficients. The IMF was assumed to be the Chabrier (2001) lognormal one. The output catalogues from TRILEGAL are first degraded applying the results from the ASTs – which results in the blurring and depopulation of the bottom part of the CMDs – and then converted into Hess diagrams. Fig. 4.9 illustrates one of such diagrams for a partial model before and after the results of ASTs have been applied.

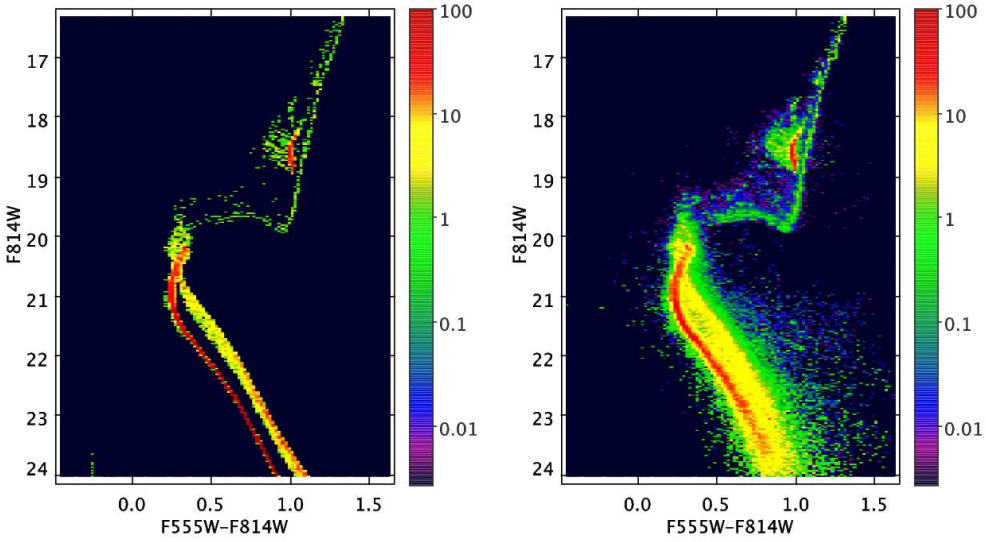

Figure 4.9: Hess diagram for a single partial model, before (left panel) and after (right panel) applying the results of ASTs. The partial model has a mean age $\log(t/\mathrm{yr}) = 9.125$, metallicity [Fe/H] $= -0.95$, and binary fraction $f_\mathrm{b} = 0.18$. The colour scale indicates the density of stars.

4.7.2 The range of cluster parameters

In our analysis, we have tried to cover the complete possible range of parameters for NGC 419, in particular:

Distance modulus $(m-M)_0$**:** Our reference value for the SMC distance modulus is $(m-M)_0 = 18.89 \pm 0.14$ (Harries et al. 2003), which is a value very similar to many other recent determinations(e.g. Crowl et al. 2001; Lah et al. 2005; North et al. 2009). In practice, however, we explored $(m-M)_0$ values between 18.75 and 18.97.

Extinction A_V**:** The Schlegel et al. (1998b) extinction maps provide $E_{B-V} = 0.10 \pm 0.01$ for an area of radius equal to 5 *arcmin* around NGC 419, which translates into $A_V = 0.32 \pm 0.03$. A similar search in the maps from Zaritsky et al. (2002), with a 12 *arcmin* radius, produces $A_V = 0.27 \pm 0.28$. In practice, we explored A_V values between 0.12 and 0.38.

Metallicity [Fe/H]**:** Works based on isochrone fitting (e.g. Durand et al. 1984) as well as Ca II triplet observations (Kayser et al. 2009) have suggested [Fe/H] values similar to -0.7 ± 0.3 for NGC 419. Interestingly, the metal abundances of other SMC clusters with similar ages are uncertain as well. Suffices it to mention the recent AMR for the SMC as derived from Parisi et al. (2009, their figure 14), which shows SMC clusters with ages smaller than 2 Gyr covering the complete [Fe/H] interval between -0.5 and -1.1. The situation is far from clear and high resolution spectroscopy of a handful of giants in 1-Gyr old SMC clusters is definitely needed. In this work, we have decided to explore the whole $-0.5 <$ [Fe/H] < -1.1 interval.

Binary fraction f_b**:** Elson et al. (1998b), using the shape of the main sequence in a deep CMD (obtained with HST) for the LMC cluster NGC 1818, determined a binary fraction from ~ 0.20 to ~ 0.35, from the center to the outer parts of the cluster. These binary fractions refer only to the binaries with high primary/secondary mass ratio, say of above 0.7, because these are the only ones which separate clearly from the single-star main sequence in CMDs. In our previous work on NGC 419 (Girardi et al. 2009), we have already noticed that the HRC CMD was indicating a binary fraction of the order of 0.2, consistent with the central region

of NGC 1818. In the following, we will adopt a reference value of $f_b \sim 0.18$; notice however that we have explored f_b values from 0.10 to 0.28. The distribution of primary/secondary mass ratios is assumed to be uniform over the interval from 0.7 to 1.0

Compared to the other parameters, the binary fraction is the less important in defining the quality of a CMD fit, as will be illustrated below. A clear advantage of exploring ranges for the other parameters – instead of taking single values from the literature – is that in this way we can partially compensate for the possible errors and offsets in the theoretical models: Errors in the zeropoints of bolometric corrections and on the helium content of stellar models could be easily compensated by a change in apparent distance modulus $(m-M)_0 + A_V$. Errors in the theoretical $T_{\rm eff}$-color relations can also be compensated by small changes in both A_V and [Fe/H]. Therefore, the final best-fitting values for these quantities are to be associated to the stellar models which we are using. Different sets of stellar models are likely to produce slightly different best-fitting values.

4.8 Recovering the Star Formation History

4.8.1 Method

To recover the SFH of NGC 419, we use an adapted version of the pipeline that is being built to analyse data from the VISTA survey of the Magellanic Clouds (VMC; see Cioni et al. 2008). The method is fully described, and tested on VMC simulated data by Kerber et al. (2009c). In brief, after building the Hess diagram for the data and partial models, the StarFISH code (Harris & Zaritsky 2001, 2004) is used to find the linear combination of partial models that minimizes a χ^2-like statistic as defined in Dolphin (2002). The solution is characterized by the minimum χ^2, $\chi^2_{\rm min}$, and by a set of partial model coefficients corresponding to the several age bins. These latter translate directly in the star formation rate as function of age, SFR(t).

The SFH-recovery is repeated for each of the $(m-M)_0$, A_V, [Fe/H], and f_b values. In order to limit the space of parameters to be covered, the procedure is essentially the following: for a given value of [Fe/H] and f_b, we cover a significant region of the $(m-M)_0$ versus A_V plane, performing SFH-recovery for each point in a grid, and then building a map of the $\chi^2_{\rm min}$ for the solutions. Examples of these maps are presented in Fig. 5.10. The maps are extended so that the minimum

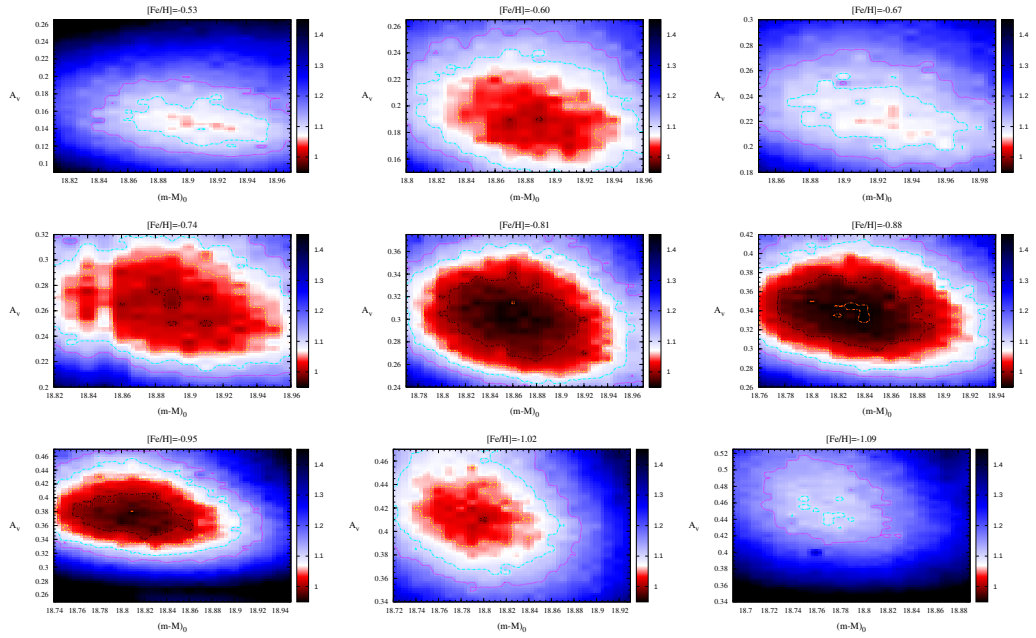

Figure 4.10: Maps of the $\chi^2_{\rm min}$ obtained during SFH-recovery, $\chi^2_{\rm min}$, as a function of $(m-M)_0$ and A_V, for several [Fe/H] values.

$\chi^2_{\rm min}$ for a given value of [Fe/H] can be clearly identified, as well as the regions in which $\chi^2_{\rm min}$ increases by a factor of about 1.5. The typical resolution of such maps is of 0.01 in $(m-M)_0$ and 0.005 in A_V.

The procedure is done for several values of [Fe/H]. $\chi^2_{\rm min}$ maps for different [Fe/H] present relative minima in slightly different positions, so that the final resulting maps do not cover exactly the same A_V and $(m-M)_0$ intervals. In any case, the relative minima are well delimitated in all cases, as illustrated in Fig. 4.13. The [Fe/H] spacing between these maps is of Δ[Fe/H] = 0.07 dex.

Among these many SFH-recovery experiments, the most interesting ones are obviously those with the relative minima and the absolute minimum $\chi^2_{\rm min}$ values. Fig. 4.11 shows the χ^2 and residuals in the Hess diagram for the best fitting solution, which is for $(m-M)_0 = 18.83$, $A_V = 0.345$ and [Fe/H] $= -0.88$ and $\chi^2_{\rm min} = 0.933$. It is already evident, in this plot, that the fitted solution is an excellent representation of the observed data, with residuals uniformly distributed over the CMD. The only point of the CMD in which there seems to be some increased residual is the bottom part of the main sequence, where according to Figs. 4.7 and 4.8, the completeness is significantly smaller than 1 (although by just 10 to 20 %),

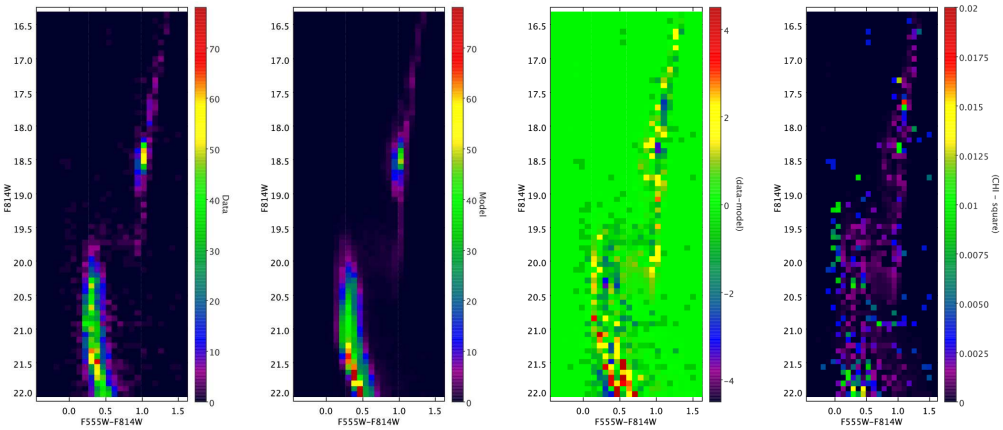

Figure 4.11: In the Hess diagram, we show the data (left), the solution found by StarFISH (middle), the data-model difference and the χ^2 map. The model is for [Fe/H] = −0.88, $(m-M)$ = 18.83, A_V = 0.345, $f_{\rm b}$ = 0.18.

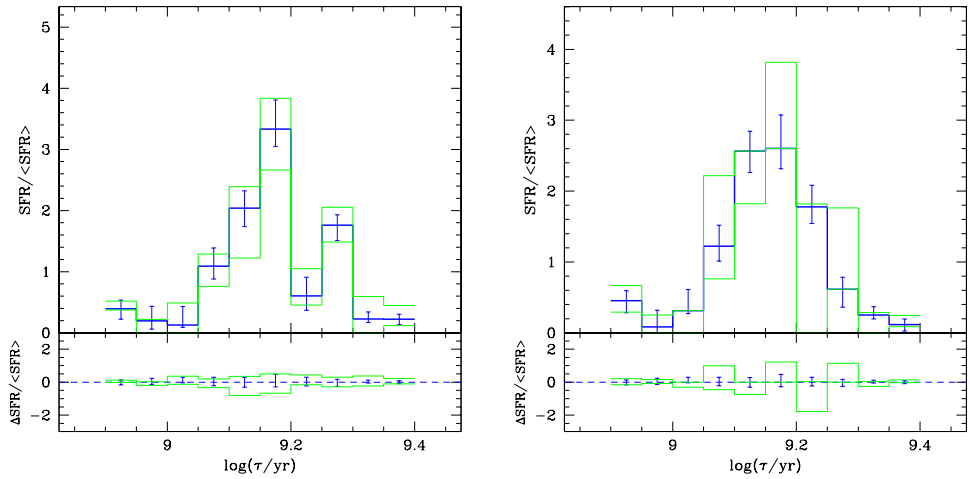

Figure 4.12: The SFR(t) corresponding to the best fitting solution (blue histogram), for metallicities [Fe/H] = −0.95 (left) and −0.81 (right). The error bars indicate the random errors, whereas the green histograms indicate the systematic errors (see Sect. 4.8.2 for more details).

and photometric errors are higher.

Figure 4.12 shows two examples of recovered SFR(t) for best-fitting solutions obtained for different values of [Fe/H]. They are qualitatively similar, with a clear presence of stars spanning ages from $\sim$ 1.2 Gyr ($\log(t/\mathrm{yr}) = 9.08$) to $\sim$ 1.9 Gyr ($\log(t/\mathrm{yr}) = 9.28$).

4.8.2 Evaluating the errors

To evaluate the errors for all involved parameters the first step was to find the correspondence between the χ^2_{min} value for each model and its significance (or confidence) level, α. This correspondence was estimated simulating 100 synthetic CMDs generated with a number of stars equal to the observed CMD, using the best-fitting SFR(t) and its parameters as the input for the simulations. So, after recovering the SFH for this sample of synthetic CMDs, it was possible to build the χ^2_{min} distribution and to establish the relation between the χ^2_{min} difference above the minimum and α.

Figure 4.13 shows the significance levels for all the solutions depicted in Fig. 5.10. As one sees, for all [Fe/H] between -0.74 and -0.95 there are ample areas of the A_V versus $(m-M)_0$ diagrams with solutions within the 95 % significance level. The best solutions, with χ^2_{min} close to 0.95 and significance levels of about 30 %, are limited to the central regions of the [Fe/H] = -0.81, -0.88, and -0.95 diagrams.

These maps can be used to estimate the mean values of the parameters that characterize the best-fitting solutions, and their errors. These are determined as the mean and standard deviation, weighted by $1-\alpha$, inside the regions in which $\alpha < 0.68$. The results are:

$$\begin{aligned} (m-M)_0 &= 18.84 \pm 0.04 \\ A_V &= 0.33 \pm 0.05 \\ [\mathrm{Fe/H}] &= -0.86 \pm 0.09 \end{aligned}$$

These numbers give an idea of the region of parameter space actually covered by the best-fitting solutions.

Fig. 4.14 presents the SFR(t) for the overall best fitting solution, obtained at [Fe/H] = -0.88, and corresponding to the Hess diagrams of Fig. 4.11. Overplotted on the SFR(t), we have the random errors due to the statistical fluctuations (associated to the number of stars); they were determined from the r.m.s. dispersion in the recovered SFR(t) for the 100 synthetic CMDs. On the other hand, the

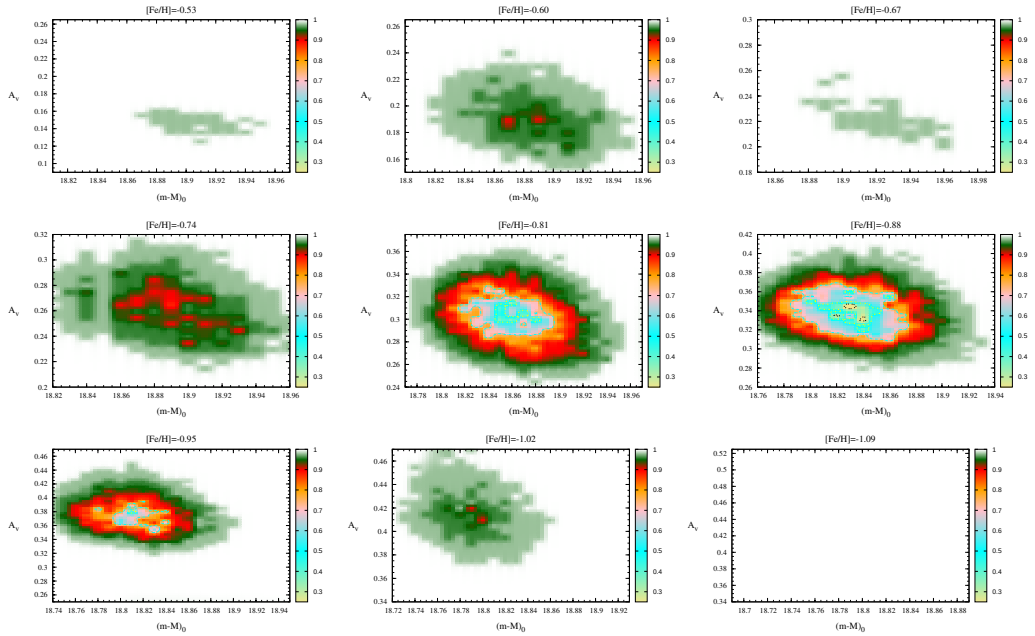

Figure 4.13: Significance level distributions for several [Fe/H] values.

systematic errors in the SFR(t) due to the uncertainties in $(m-M)_0$, A_V and [Fe/H], were determined using the minimum and maximum SFR(t) values for all models inside the 68 % significance level for all metallicities.

4.8.3 The role of the binary fraction

As anticipated previously, we have verified that the binary fraction f_b plays a relatively minor role in determining the best-fitting solution and the SFR(t). Many simulations at varying f_b were tried at several stages of our analysis, always supporting this conclusion, and always pointing to a binary fraction close to 0.2. Fig. 4.15 aims to illustrate the sort of results one gets for different f_b. To build the figure, we first define a large set of SFH-solutions for which the CMD fitting was considered to be good: namely the entire 68 % significance level area for the metallicity [Fe/H] = -0.81, in Fig. 4.13. For this region of the A_V versus $(m-M)_0$ plane, the SFH-recovery tests are repeated for all f_b values between 0.10 and 0.28, at steps of 0.02. Then, we plot the value of mean $\chi^2_{\rm min}$ and its r.m.s. dispersion as a function of f_b, as shown in Fig. 4.15. The minimum of mean $\chi^2_{\rm min}$ for $f_b = 0.18$ is evident. However, the dispersion of $\chi^2_{\rm min}$ values is also significant, and indi-

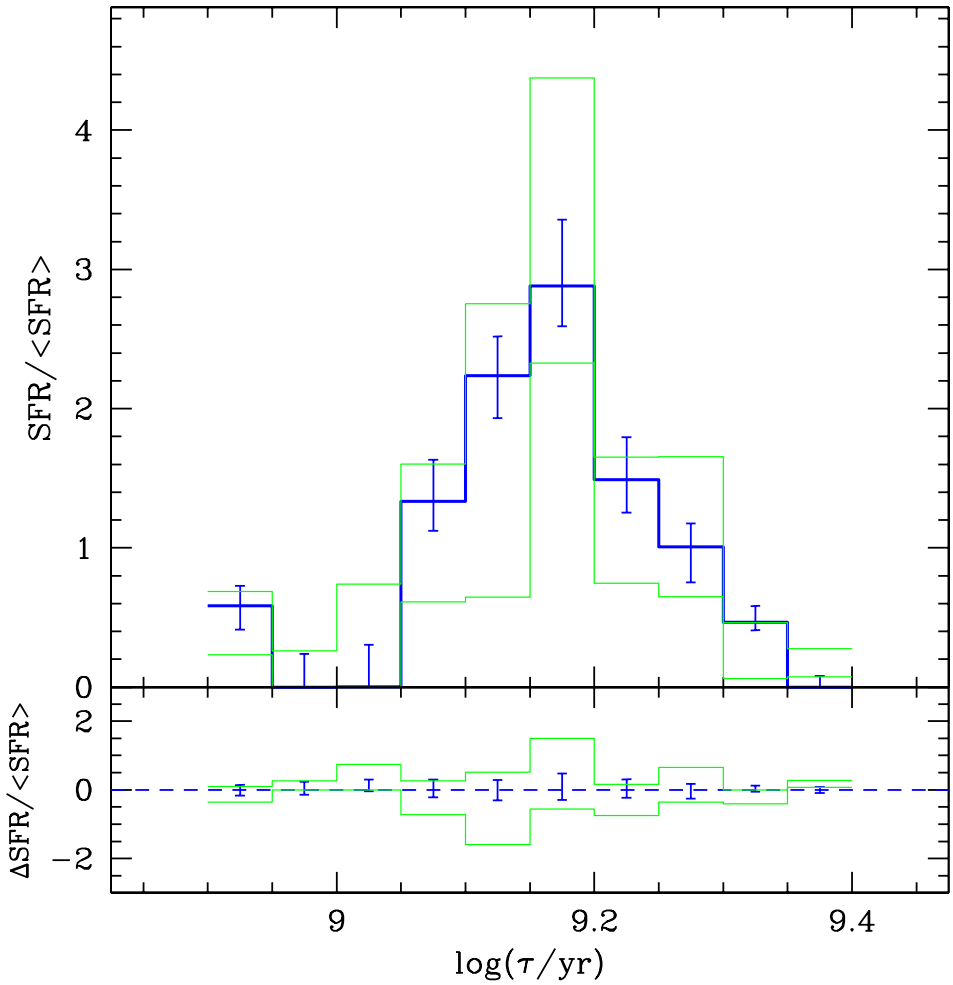

Figure 4.14: The overall best-fitting solution for the SFR(t) of NGC 419. The random (error bars) and systematic errors (solid thin lines) are also shown.

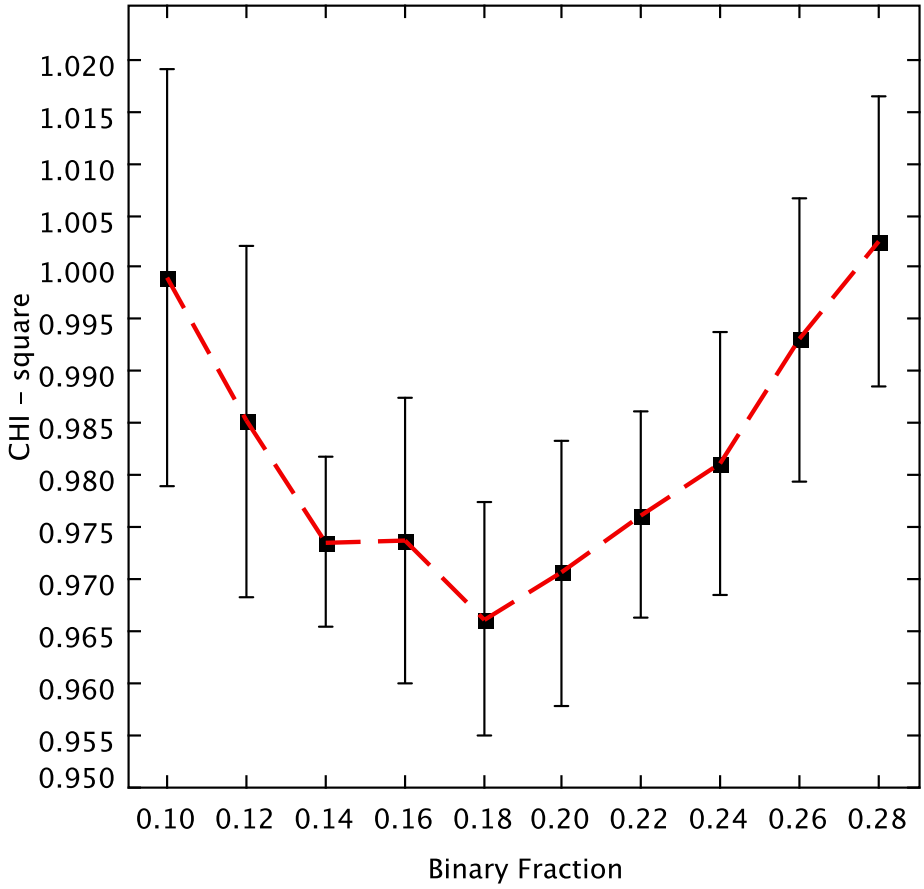

Figure 4.15: The average of the minimum $\chi^2_{\rm min}$ versus the binary fraction $f_{\rm b}$, for a series of models of metallicity [Fe/H] = −0.81.

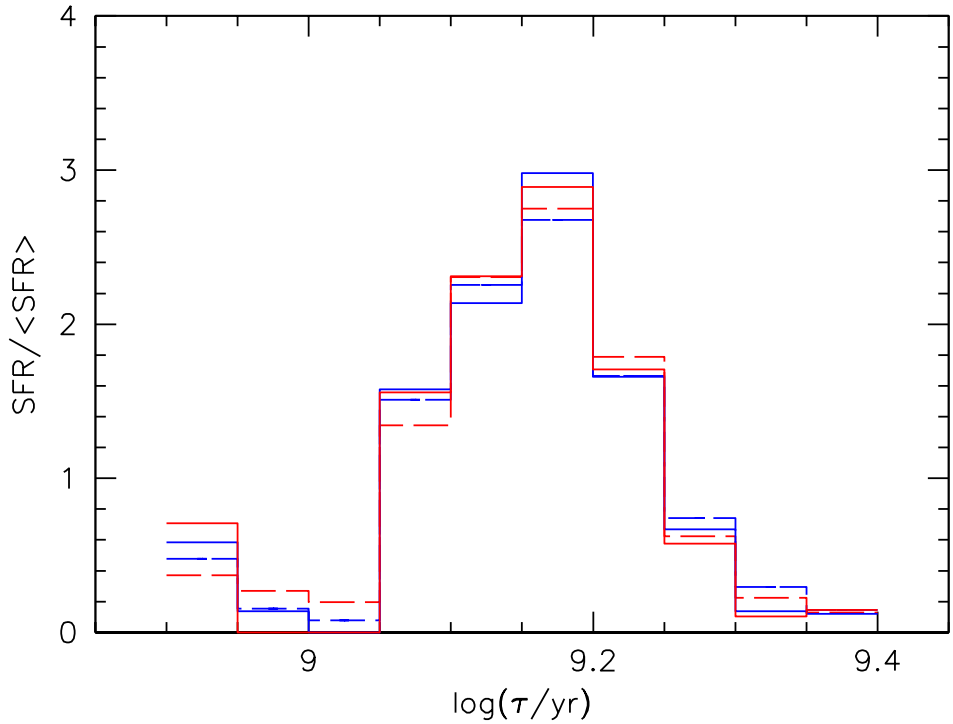

Figure 4.16: The SFR(t) for a series of SFH solutions with [Fe/H] = −0.81, $(m-M)_0$ = 18.86, A_V = 0.315, and for different binary fractions: f_b = 0.12 (blue dashed line), 0.18 (red dashed), 0.24 (blue solid), and 0.28 (red solid).

cates that a relatively wide range of f_b, from say 0.12 to 0.24, would also produce acceptable results, if compared to the f_b = 0.18 case.

It is also worth noticing that for f_b = 0.18 the 68 % significance level (α = 0.68) is about 0.038 above the minimum χ^2_{min}, as determined in the previous section. All solutions presented in Fig. 4.15 are inside this limit. So, even if there is a apparent minimum χ^2_{min} around f_b = 0.18, it is not statistically significant.

Finally, Fig. 4.16 shows the recovered SFR(t) for four different f_b values over the f_b = 0.12 to 0.28 interval. Not only the SFR(t) is seen to vary by amounts that are comparable to the random errors in Fig. 4.14, but they also do it in a non-systematic way: the mean age and shape of the SFR(t) do not show any significant trend with f_b.

4.8.4 The role of the field contamination

In this work, we have analysed the ACS/HRC photometry NGC 419 without taking into account that a fraction of the observed stars is due to the SMC field. Indeed, when first noticing the unusual structure of the red clump in these data, Glatt et al. (2008) suggested the fainter red clump could be due to the SMC field. The counter-argument by Girardi et al. (2009), however, has dramatically redimensioned the possible role of the SMC field contamination in this case: after measuring the density of red clump stars in the external parts of the ACS/WFC images of the same cluster, at radii larger than 75 *arcsec* and for a total area of 2.47×10^4 arcsec^2, they find that just 4.5 red clump stars from the SMC field are expected to be found inside the 740 arcsec^2 area of the HRC images, whereas the total observed number is of 388 (47 of them are in the secondary clump). These numbers set the probability that the secondary clump in NGC 419 is made of SMC field stars to less than 10^{-9} (Girardi et al. 2010). Moreover, they indicate that the field contamination in the red clump area of the CMD is of just ~ 1 %.

In the context of the SFH-recovery work, some additional numbers worth of consideration are the following. The number of field main sequence stars in the magnitude interval $20 < \mathrm{F814W} < 22$, for the same 2.47×10^4 arcsec^2 area in the outskirts of the WFC images, is 2640, whereas the observed number in the 740 arcsec^2 of HRC is 2395. This magnitude interval is just barely affected by incompleteness, and contains most of the observed stars. Therefore, we can estimate that just ~ 3.3 % of the stars used to study the SFH of NGC 419 are due to the SMC field. This fraction is similar to the Poisson noise in the total number of HRC stars, indicating that our SFH results cannot be affected in a significant way.

4.8.5 The age–metallicity relation

With star formation lasting for 700 Myr, one may wonder whether NGC 419 would not have enriched itself with metals ejected from its oldest stellar populations. Although we believe that the present photometric data is not enough to clarify this question, we performed an additional SFH-recovery exercise, in which the cluster [Fe/H] is not fixed, but can take four different values at each age: [Fe/H] = -0.95, -0.90, -0.85, -0.80. In practice, this is obtained by running the SFH-recovery method with a larger library of partial models, with 40 components (10 age bins times 4 metallicity bins).

This larger set of partial models provides more freedom to the StarFISH algo-

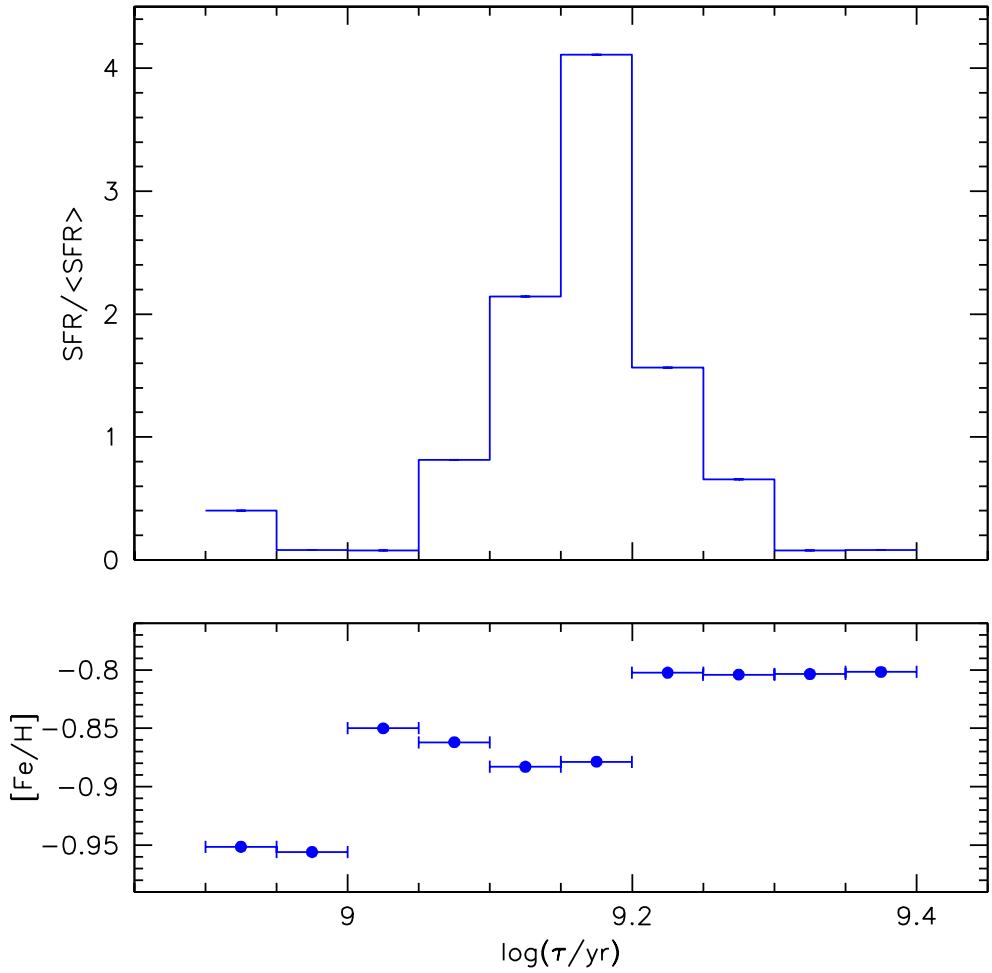

Figure 4.17: The SFR(t) and AMR obtained when the [Fe/H] is not constrained to a single value, but is let to vary between 4 different values in the $-0.95 \leq$ [Fe/H] ≤ -0.80 interval. The upper panel shows the [Fe/H]-added SFR(t), whereas the bottom panel show the SFR-averaged [Fe/H](t).

rithm, which converges to an absolute best-fitting solution with a $\chi^2_{\rm min}$ of just 0.84, for $A_V = 0.33$ and $(m-M)_0 = 18.83$. The SFH results are illustrated in Fig. 4.17: the upper panel shows the SFR(t) obtained by adding the SFR values obtained for all metallicities at each age bin, whereas the bottom panel shows the AMR as obtained by a SFR-weighted average of the four different [Fe/H] values.

This SFR(t) is actually very similar to the one obtained form the best-fitting solution with [Fe/H] $= -0.88$ (Fig. 4.14). In the age interval with significant star formation, which goes from 1.2 to 1.9 Gyr and comprises 5 age bins, the three youngest age bins are found to have a metallicity almost coincident with the [Fe/H] $= -0.88$ one, whereas the two oldest ones are found to be slightly more metal-rich, with -0.80 dex. It is not clear whether this [Fe/H] variation can be significant, since it is comparable to the estimated error of 0.09 dex in the [Fe/H] of the best-fitting solutions (Sect. 4.8.2). We conclude that our analysis does not provide evidence for self-enrichment taking place in NGC 419.

4.9 Conclusions

In this work, we have derived the SFH of the SMC star cluster NGC 419, via the classical method of CMD reconstruction. This analysis implicitly assumes that NGC 419 is formed by a sum of single-burst stellar populations (or "partial models"), each one being characterized by a well-defined and narrow MSTO. The only effects that blur these partial models in the CMDs are the sequences of binaries (which effect however is far from dramatic) and the photometric errors. With this kind of approach, the broad MMSTO observed in NGC 419 naturally translate into a continued star formation history. We find a SFR(t) lasting for 700 Myr (from 1.2 to 1.9 Gyr, see Fig. 4.14), which is quite a long period, probably at the upper limit of all values already estimated for star clusters with MMSTOs (Bertelli et al. 2003; Baume et al. 2007; Mackey & Broby Nielsen 2007; Mackey et al. 2008; Milone et al. 2009; Goudfrooij et al. 2009). Our error analysis leaves practically no room for the MMSTOs in this cluster being caused by a single episode of star formation.

It is also remarkable that the SFR(t) we derive presents a pronounced maximum at the middle of the star formation interval, at an age of 1.5 Gyr (Fig. 4.14). This is somewhat unexpected, in the context of the few suggested scenarios for the appearance of prolonged star formation in LMC star clusters (see Goudfrooij et al. 2009, for a comprehensive discussion of them). Either the merging of two star clusters (Mackey & Broby Nielsen 2007), or a second period of star forma-

tion driven by the merging with a giant molecular cloud (Bekki & Mackey 2009), would lead to strongly bimodal distributions of cluster ages, which we do not find in NGC 419. Only in the case of the best model with [Fe/H] = −0.95, there is an indication of two different peaks in the SFR(t) (see Fig. 4.12), which however are neither separated nor followed by periods of null SFR(t). Also the trapping of field stars by the forming star cluster (Pflamm-Altenburg & Kroupa 2007) would lead to different results, with the major peak of star formation being found at the youngest ages. On the other hand, our findings seem to be more in line with Goudfrooij et al. (2009)'s conclusions, based on the quite continuous distribution of stars across the MMSTO region of the LMC cluster NGC 1846. They suggest a scenario in which the star cluster continues to form stars in its center out of the ejecta of stars from previous generations. In our case, however, this process would have to proceed for a significantly more extended period of time than for NGC 1846, and peak – somewhat against the most naive expectations – at the middle of the star formation period. Also, this latter scenario might imply some amount of self-enrichment in this cluster, whereas our method instead is compatible either with a constant metallicity, or with some amount of metal dillution. Needless to say, the present observational data is not clear enough to provide unambiguous indications about the formation scenario of such clusters.

Another basic result of our analysis is that the hypothesis of continued SFH, together with current stellar evolutionary models and a modest fraction of binaries, produces *excellent fits to the CMD of NGC 419*, with $\chi^2_{\rm min}$ as small as 0.93 – or even 0.84 if the [Fe/H] is let to vary during the SFH-recovery. We have translated this result into quantitative estimates for the random and systematic errors of the derived SFR(t). It is obvious that many combinations of cluster parameters produce acceptable solutions, with significance levels smaller than 95 %. However, the really good solutions – i.e. those with significance levels better then 68 % – cover a narrow region of the parameter space, comprising less than 0.1 mag in both $(m-M)_0$ and A_V, and about 0.1 dex in [Fe/H].

Despite our success in fitting the CMD of NGC 419 as a sum of partial models, this success does not tell us about the reliability of alternative hypotheses for the origin of MMSTOs. In particular, we cannot conclude anything about Bastian & de Mink (2009)'s hypothesis based on the colour spread of coeval stars with different rotation rates, since its capability of providing a *quantitative* description of the data has not yet been tested. We urge that this test should be performed, in order to shed light into this problem.

However, we call attention to another question that has to be properly addressed: Is Bastian & de Mink (2009)'s rotation hypothesis able to produce, in

addition to the broad turn-off of Magellanic Cloud star clusters, also the dual red clump observed in NGC 419 (see Girardi et al. 2009) ? In our models with prolonged star formation, the 700 Myr spread in age translates into a $\sim$ 0.26 $M_{\odot}$ spread in turn-off masses, which in turn implies a small spread in the mass of H-exhausted cores as stars leave the main sequence. This small spread – of the order of just $\sim$ 0.01 $M_{\odot}$ – is enough to cause the appearance of a dual red clump in this cluster, as thoroughly discussed in Girardi et al. (2009, 2010). Such a feature is then *naturally present* in our best-fitting solutions, as can be appreciated in Fig. 4.11. Can rotation do the same, producing spreads of a compatible magnitude both in the main sequence and in the red clump ? Moreover, can this be achieved with a reasonable and simple enough distribution of rotation velocities ? At first sight, this seems very unlikely to us.

Chapter 5

The LMC star cluster NGC 1751: cluster and field star formation histories

5.1 Introduction

A few stars clusters in the Magellanic Clouds present in their colour–magnitude diagrams, in addition to multiple main sequence turn-offs (MMSTO; Mackey & Broby Nielsen 2007; Mackey et al. 2008; Milone et al. 2009; Goudfrooij et al. 2009; Glatt et al. 2008), also vertically extended red clumps in which the maximum stellar density occurs at its upper part (Girardi et al. 2009). The presence of such a *dual red clump* feature is the signature of the simultaneous presence in the cluster, of stars which passed, and those which did not, through electron degeneracy soon after H-exhaustion.

The MMSTO feature can be interpreted either as the presence of different generations of stars spanning several 10^8 yr in these clusters (Mackey & Broby Nielsen 2007; Mackey et al. 2008; Milone et al. 2009; Goudfrooij et al. 2009), or as the manifestation of some other effect intrinsic to coeval stars such as a dispersion in rotational velocities (Bastian & de Mink 2009). However, the simultaneous presence of a dual red clump features favours the former interpretation (Girardi et al. 2009; Rubele et al. 2010): it indicates a modest spread in the core mass of stars leaving the main sequence which is well compatible with the age spread of a few 10^8 yr deduced from the shape of the MMSTOs.

For the SMC star cluster NGC 419, which contains the most striking example

of a dual red clump to date, Rubele et al. (2010) demonstrated that the assumption of an extended star formation history (SFH), explored by means of the classical method of SFH-recovery via CMD-reconstruction, produces indeed a remarkably good quantitative description of the observed CMDs. The SFH was found to extend over a period of 700 Myr. The same analysis has produced quite stringent limits to the cluster's distance, reddening, and metallicity.

Although not explicitly discussed by Rubele et al. (2010), the dual red clump of NGC 419 has played a big role in limiting the family of stellar models that could be fit in the process of CMD-reconstruction. Moreover, as discussed by (Girardi et al. 2009), the simple presence of a dual red clump provides a direct measurement of the mean mass of H-exhausted cores of the stars leaving the main sequence, which, when coupled to the shape of the turn-off region, provides good quantitative constraints to the efficiency of convective core overshooting in stars. For NGC 419 the overshooting efficiency (as defined in Bressan et al. 1981) was estimated to be of $0.47^{+0.14}_{-0.04}$ pressure scale heights, which is well consistent with the mean value of 0.5 adopted in the stellar models (from Girardi et al. 2000a) that were used in the SFH analysis.

In this work, we examine the case of the LMC star cluster NGC 1751, which as noted by Girardi et al. (2009), does also appear to present a dual red clump. We will use the extremely accurate data available from HST/ACS, and analyses techniques similar to those applied by Girardi et al. (2009) and Rubele et al. (2010) for deriving the SFH. Sect 5.2 will briefly present the data and discuss the reality of the dual red clump. The next sections will present the SFH-recovery method and its application to the NGC 1751 surrounding LMC field (Sect. 5.3) and cluster area (Sect. 5.4). Sect. 5.5 draws the final conclusions.

5.2 The NGC 1751 data and its dual red clump

5.2.1 Data and photometry

The dataset used in this work comes from GO-10595 (PI: Goudfrooij), and consists of one short and two long exposures in F435W, F814W, and F555W with small dither pattern to avoid the ACS/WF gap between two WFC chips. A detailed description of the observations and photometry is given in Goudfrooij et al. (2009). Nevertheless, in this work we use the simultaneous ePSF fitting technique as it described in Anderson et.al. (2008), which fits the PSF simultaneously on all exposures/observations of the cluster. Differently from Goudfrooij et al. (2009),

the Charge Transfer Efficiency (CTE) correction was performed using Riess & Mack (2004) formula (ACS-ISR 2005). The derived photometry was calibrated into the Vegamag system as described in Goudfrooij et al. (2009).

Fig. 5.1 shows a spatial representation of the stars we analize in this work. We have initially located the center of NGC 1751 at the position $x_c = 2200$ pix, $y_c = 3100$ pix. Based on the appearance of the CMDs at varying radii r from this center, we have defined regions of the ACS/WFC images corresponding to

- the LMC **Field**, for $r > 1500$ pix (73.5 arcsec);
- the NGC 1751 cluster, for $r < 800$ pix (39.2 arcsec), which is further divided into:
  - the **Centre**, for $r < 350$ pix (17.2 arcsec);
  - the **Ring**, for $350 < r < 800$ pix ($17.2 < r < 39.2$ arcsec).

These regions are depicted in Fig. 5.1. The Centre, Ring and Field regions have areas of 0.385, 1.63, and 10.30 pix^2 (5.3, 22.6, 143 arcmin^2), respectively. Figure 5.2 shows how the stellar density varies as a function of radius from the NGC 1751 centre, taking into account only the stars of $F814W < 22$, for which the photometry should be close to complete. The figure clearly shows the flattening of the density for $r > 1500$ pix, which indicates that indeed that is a good choice for defining the LMC Field.

Fig. 5.3 shows the ACS data for the different regions of NGC 1751, in the F814W vs. F435W – F814 and F814W vs. F555W – F814WW CMDs. These plots will be used as a reference in our analysis.

The CMDs for the cluster Centre show very clearly the broad main sequence turn-off of this cluster, its dual red clump, and other well-known CMD features such as the sequence of binaries parallel to the main sequence, and the RGB, subgiants, and early-AGB bump. A simple comparison between the CMDs for the Centre and Field reveals that the field contamination in the cluster central regions is close to negligible. This is clear already looking at the star counts in the red clump: the 7.15 arcmin^2 of Field contain 189 red clump stars (here defined as stars with $18.05 < F814W < 19.15$, $F435W–F814W > 1.5$), therefore the 0.267 arcmin^2 of the Centre are expected to contain just ~ 7 red clump stars coming from the LMC field, which is far less than necessary to explain any of the features of its CMD. Indeed, the red clump in the Centre is made of 117 stars, which can be separated into the 89 "bright" ones ($F814W < 18.75$) – which correspond to the classical red clump made of stars which likely passed through electron degeneracy

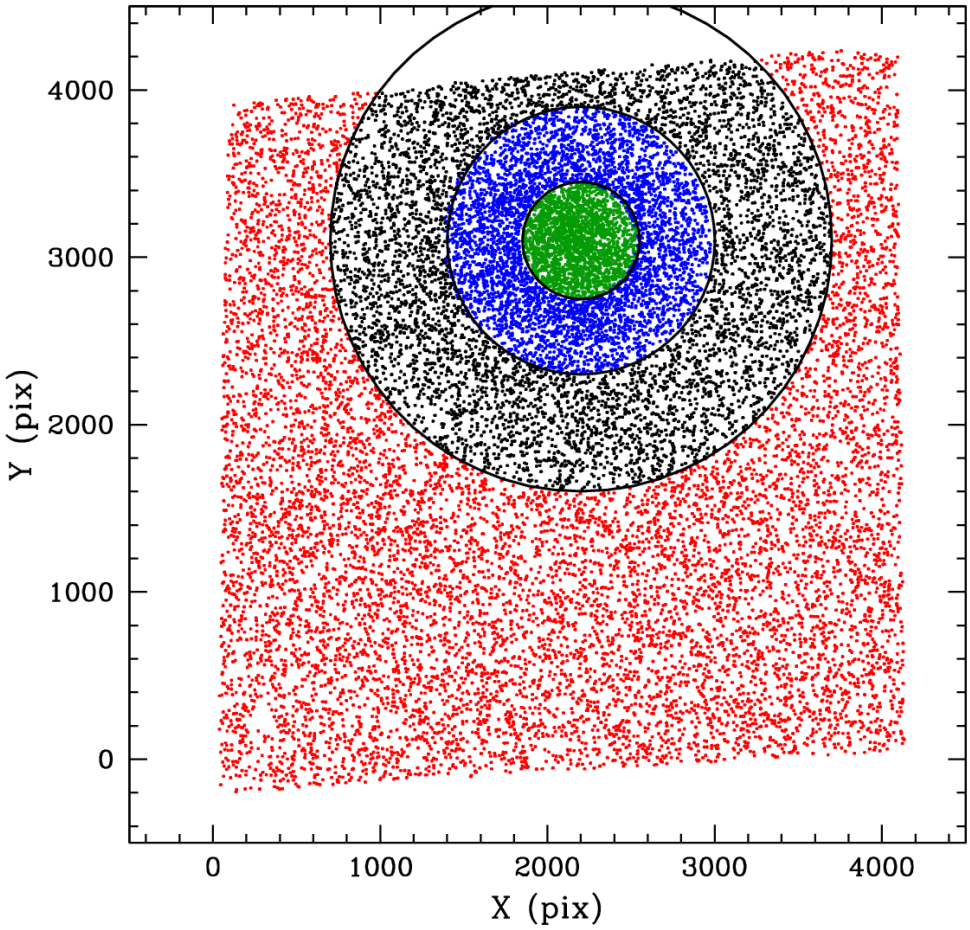

Figure 5.1: Map of the stars used in this work, in the *xy* plane of the ACS/WFC images. The scale is of about 0.05 arcsec/pix. The observed stars have been grouped in areas corresponding to the LMC field (red) and, for NGC 1751, an inner "Centre" (green) and outer "Ring" (blue).

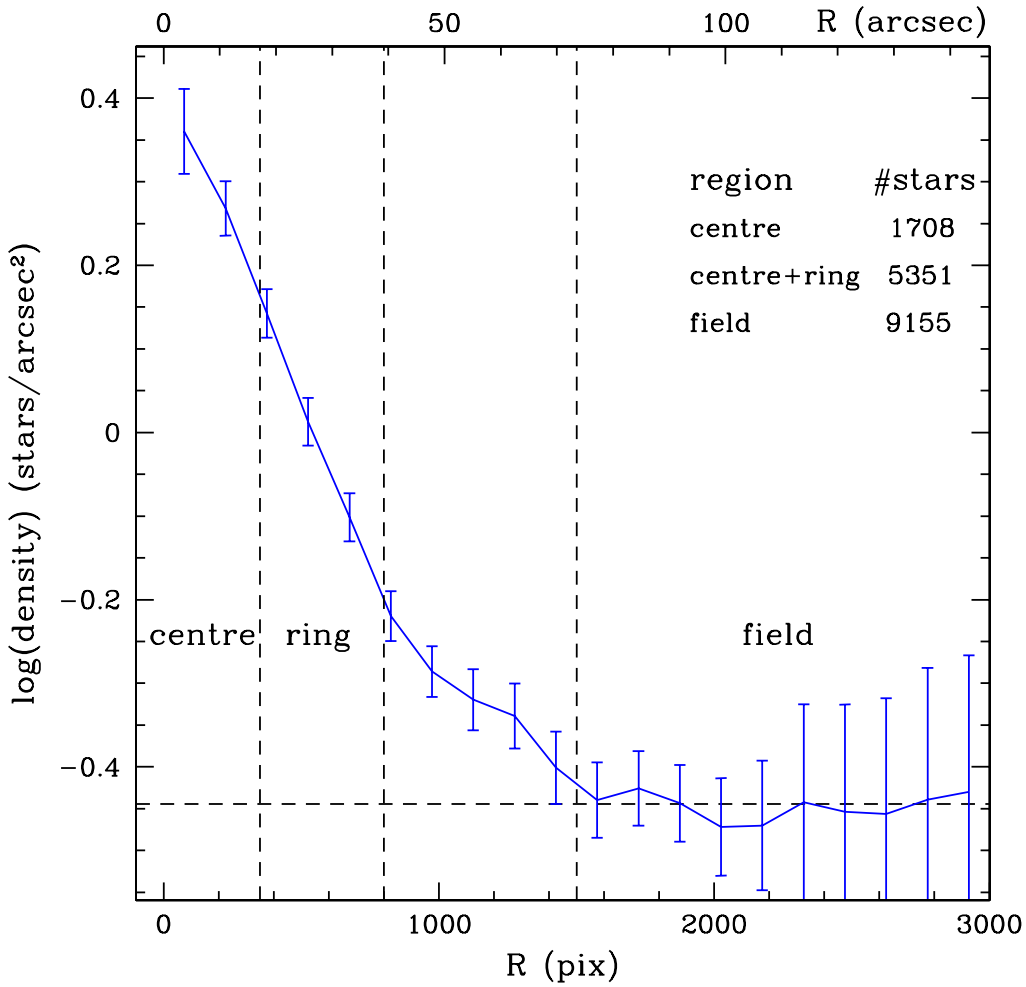

Figure 5.2: The logarithm of stellar density as a function of radius from the NGC 1751 centre. Error bars are the random errors.

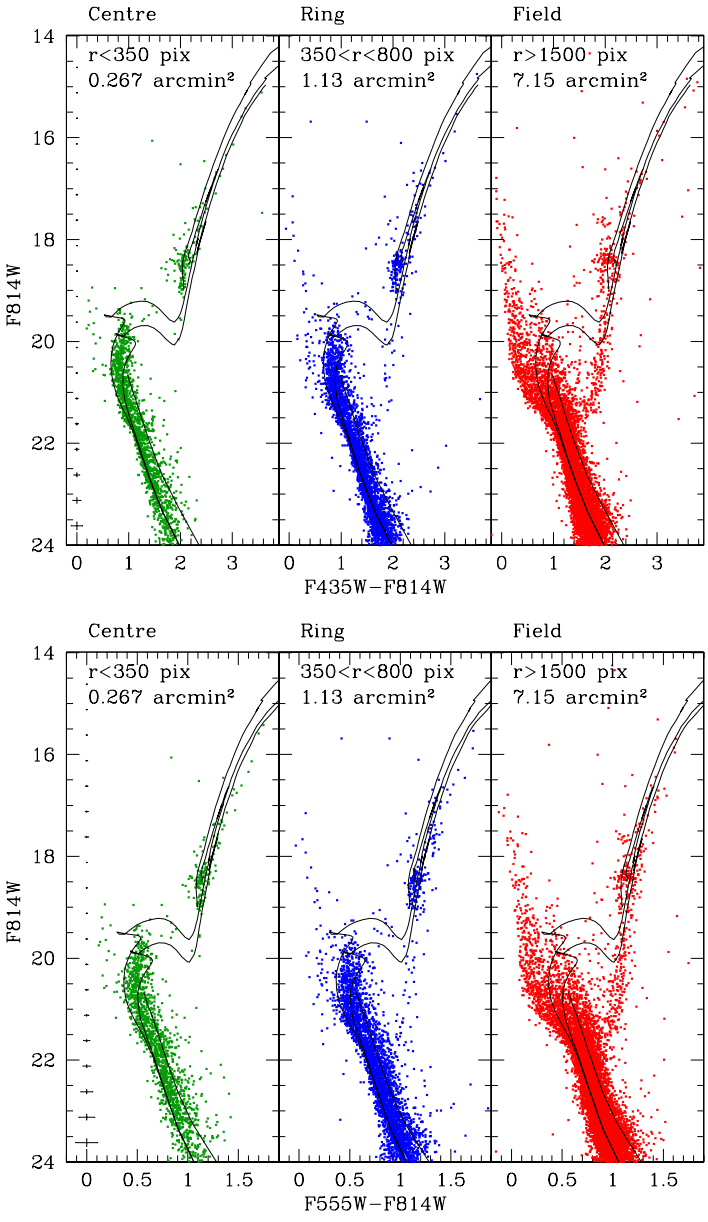

Figure 5.3: The CMDs for NGC 1751 as derived from the ACS/WFC data, using both $F435W - F814W$ (top panels) and $F435W - F814W$ (bottom panels) colors versus the $F814W$ magnitude. Panels from left to right present data for the cluster Centre and Ring, and LMC Field. As a reference to the eye, the panels also show the position of 1.12 and 1.42-Gyr isochrones of metal content $Z = 0.008$, shifted by $(m-M)_0 = 18.50$ and $A_V = 0.7$, together with the expected location of equal-mass binaries along the main sequence (continuous lines). The tiny crosses at the leftmost extreme of the left panel are 1σ error bars derived from artificial star tests in the cluster Centre (see Sect. 5.2.2). The error bars for the Ring and Field are not shown in the figure; they are of about the same size for the brightest magnitudes, becoming just $\sim$ 25 % smaller for the faintest magnitudes.

in their cores – and 28 faint or "secondary" ones ($F814W > 18.75$) – which were likely able to avoid it. We can conclude, in a way similar to the case of NGC 419 (Girardi et al. 2009, 2010), that the probability that the dual red clump observed in the centre of NGC 1751 is caused by LMC field stars is less than $P \sim 5 \times 10^{-6}$, and therefore negligible.

Note that differences are quite evident in the position of CMD features between the Centre and Field, which are obviously mixed in the CMD of the Ring. The Field presents an old main sequence turn-off and subgiant sequence extending to magnitudes as faint as $F814W < 21.5$, and a younger main sequence extending as bright as $F814W < 16.5$. Just traces of these features are present in the CMD of the Centre. Moreover, the red clump in the Field do also present a composite structure, with a ratio of faint/bright stars of 59/130. This latter feature is just expected from a field made of stars covering a wide range of ages and initial masses (see Girardi 1999), and being observed with very small photometric errors as in this case.

5.2.2 Assessing photometric errors and completeness

In order to characterize the errors in the photometry and the completeness of the sample, we have performed a series of artificial star tests (AST) on the reduced images (see e.g. Gallart et al. 1999; Harris & Zaritsky 2001).

The procedure consists of adding stars of known magnitude and colour at random places in each exposure, and redoing the photometry exactly in the same way as described in Sect. 5.2.1. The artificial stars are considered to be recovered if the input and output positions are closer than 0.5 pixels, and flux differences are less than 0.5 mag.

In order to avoid the introduction of additional crowding in the images, artificial stars are positioned at distances much higher than their PSF width. So, our AST are distributed on a grid spaced by 20 pix, which is each time randomly displaced over each set of exposures.

A total of 1.04×10^7 ASTs were performed, covering in an almost uniform way the CMD area of the observed stars as well as the area for which we build the "partial models" to be used in the SFH analysis (see Sect. 5.4.2 below). Then, the ratio between recovered and input stars gives origin to the completeness map of Fig. 5.4. Note that the 90 % completeness limit is located at F814W $\sim$ 24.5, which is well below the position of the MMSTOs in NGC 1751.

Figure 5.5 illustrates the differences between the recovered and input magnitudes of the ASTs, as a function of their input magnitudes. These differences give

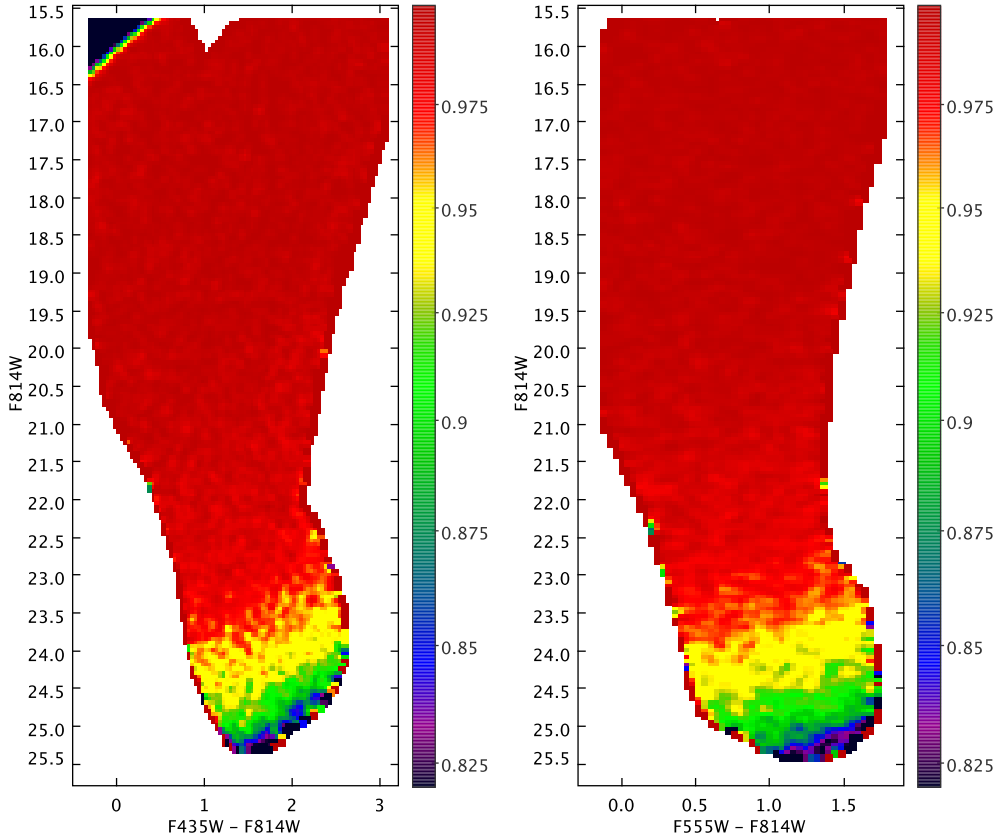

Figure 5.4: Completeness map, derived from the complete set of ASTs realised over NGC 1751 (centre plus ring areas), for both the F814W vs. F435W – F814W (left panel) and F814W vs. F555W – F814W (right panel).

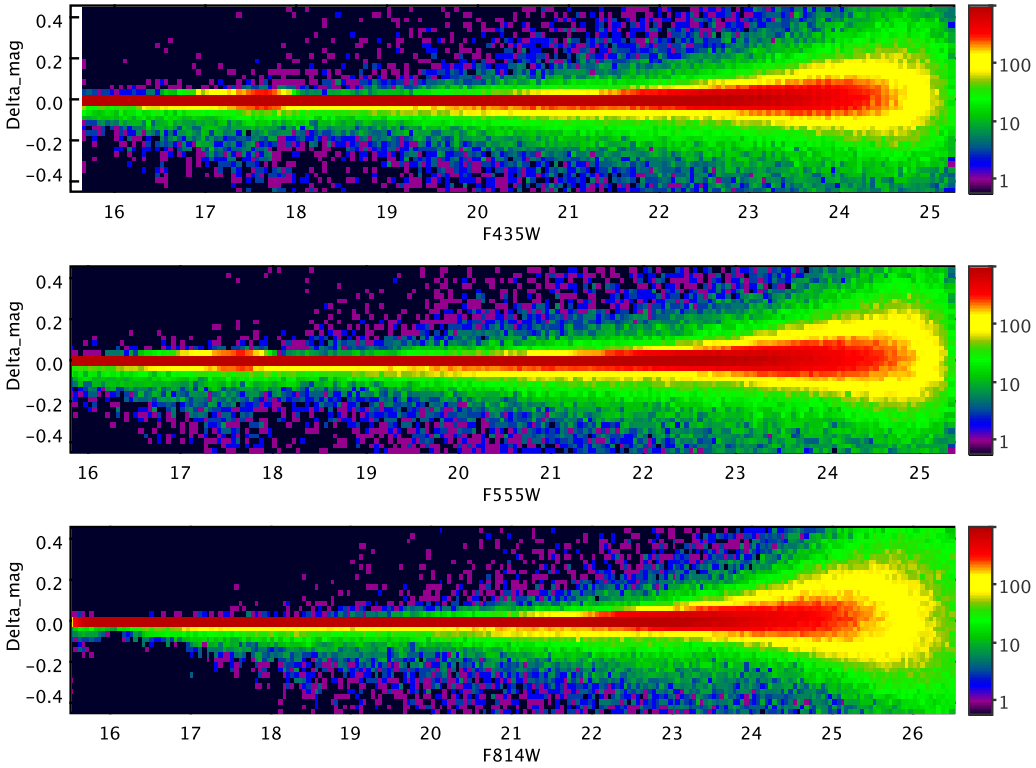

Figure 5.5: Map of photometric errors as a function of input F435W, F555W and F814W (from top to bottom), as derived from the ASTs over the entire cluster area (that is, in the Centre plus Ring). The errors are defined as the difference between the recovered and input magnitudes.

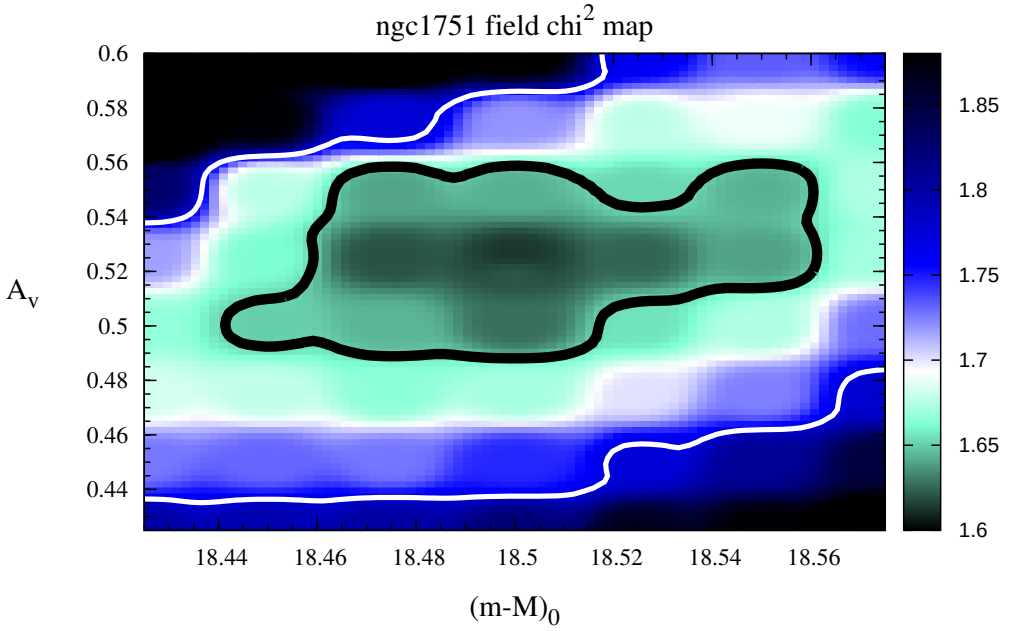

Figure 5.6: χ^2 map for the Field best-fitting solution, as a function of distance modulus and V-band extinction. The continuous lines show the 68 % (black) and 95 % (white) confidence levels for the overall best-fitting solution, which is located at $(m-M)_0 = 18.50, A_V = 0.525$.

a good handle of the photometric errors effectively present in the data. The error distributions are slightly asymmetric because of crowding.

5.3 The SFH of the LMC Field

5.3.1 Overview of the method

To recover the SFH from the ACS data, we use the pipeline built to analyse data from the VISTA survey of the Magellanic Clouds (VMC; see Cioni et al. 2008). The method has been fully described and tested by Kerber et al. (2009d) using simulated near-infrared data, and by Rubele et al. (2010) using ACS/HRC data for the SMC cluster NGC 419. The method consists in (1) building the Hess diagram for the data and a series of "partial models" which represent populations in limited intervals of age and metallicity, and (2) using the StarFISH code (Harris & Zarit-

sky 2001, 2004) to find the linear combination of partial models that minimizes a χ^2-like statistic as defined in Dolphin (2002). The solution is characterized by the minimum χ^2, $\chi^2_{\rm min}$, and by a set of partial model coefficients corresponding to the several age bins. These latter translate directly into the star formation rate as function of age, SFR(t).

The age–metallicity space occupied by the partial models depend on the object under consideration. In the present work, we have to consider two distinct cases, corresponding to the cluster and LMC field as previously defined. This section deals with the field only.

The LMC field is expected to follow a marked age-metallicity relation (AMR). This AMR has been measured by several authours using both field stars and star clusters of several ages (Mackey & Gilmore 2003; Kerber et al. 2007; Grocholski et al. 2006, 2007). In addition to the mean AMR, it is reasonable to expect a modest spread in metallicity at any given age. For this work, we adopt the scheme set by Kerber et al. (2009d), in which we build partial models at 5 different metallicities disposed around the mean AMR of the LMC. Each partial model covers a range in logarithm of age of width 0.2 dex. For stellar populations younger than 10^8 yr, the numbers of observed stars are very small and hence we assume broader age bins, of widths 0.3 dex for $7.2 \leq \log(t/{\rm yr}) \leq 8.0$, together with a single age bin of width 0.8 dex for $\log(t/{\rm yr}) < 7.2$. The [Fe/H] separation between partial models is of 0.1 dex.

For the initial mass function (IMF) we adopt the Chabrier (2001) one. The binary fraction is set to a value of 0.3 for binaries with mass ratios in the range between 0.7 and 1.0, which is consistent with the prescriptions for binaries commonly used in works devoted to recover the field SFH in the Magellanic Clouds (e.g. Holtzman et al. 1999; Harris & Zaritsky 2001; Javiel et al. 2005; Noël et al. 2009). Notice that this assumption is also in agreement with the few determinations of binary fraction for stellar clusters in the LMC (Elson et al. 1998a; Hu et al. 2008, both for NGC 1818, a stellar cluster younger than $\sim$ 100 Myr).

5.3.2 The best-fitting solution

Once the database of partial models is built, we run StarFISH to find the best-fitting solution to the observed CMDs, for a given value of distance modulus $(m-M)_0$ and extinction A_V. Both F814W $\times$ F435W – F814W and F814W $\times$ F555W – F814W Hess diagrams are used simultaneously in the process of χ^2 minimization.

$(m-M)_0$ and A_V are then varied over the possible range of values. The χ^2 map of Fig. 5.6 shows the results in the $(m-M)_0 \times A_V$ plane. The overall best-

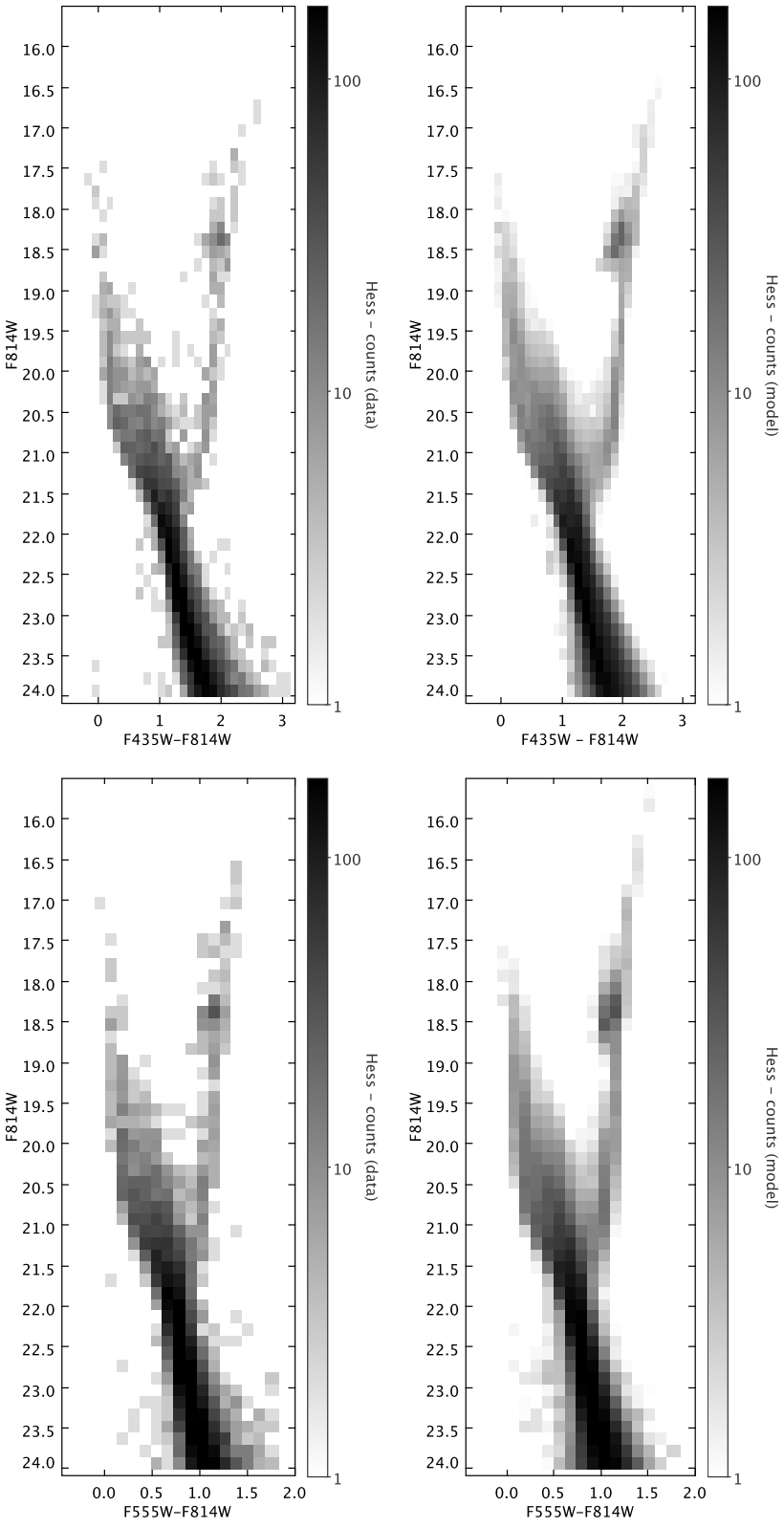

Figure 5.7: The Hess diagram for the NGC 1751 Field as derived from the ACS data (left panels), and as recovered by the best-fitting solution (right panels).

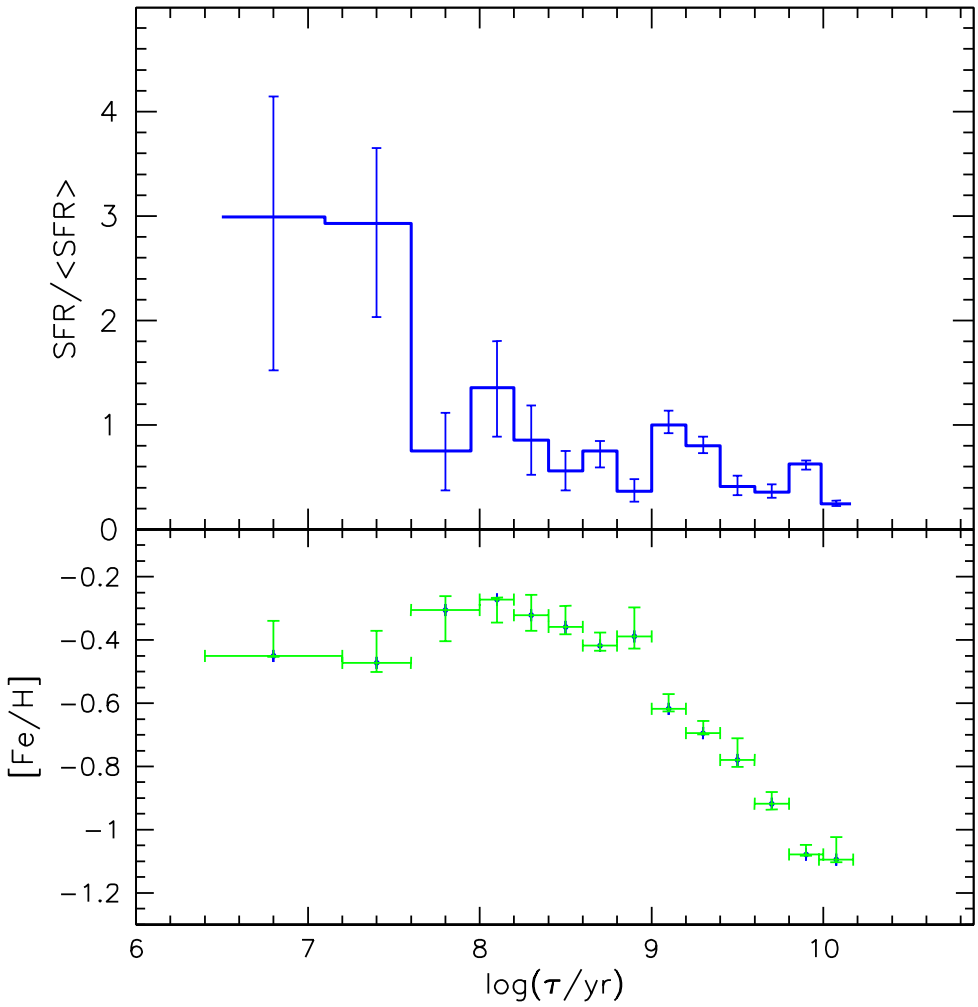

Figure 5.8: Top panel: best-fitting SFH for the field, together with the random errors (1σ). Bottom panel: the mean age–metallicity relation.

fitting solution, with a $\chi^2_{\rm min}$ of 1.6, is located at $(m-M)_0 = 18.50$ and $A_V = 0.525$. The 68 % confidence level for this solution spans a narrow range in distance and reddening, which is just $\Delta(m-M)_0 = 0.12$ mag and $\Delta A_V = 0.07$ mag wide.

Figure 5.7 compares the Hess diagrams of the field data (left panel) and its overall best-fitting model (right panel). It is evident that the solutions found by StarFISH reproduce well the observed CMD features but for the Poisson noise.

Finally, Fig. 5.8 presents the SFR(t) and age–metallicity relation (AMR) corresponding to this best-fitting solution. It is remarkable that the recovered SFR(t) presents features that are consistent with those commonly found in previous works, based on both HST data (Olsen 1999; Holtzman et al. 1999; Smecker-Hane et al. 2002; Javiel et al. 2005) and ground-based data (Harris & Zaritsky 2001, 2009). There is an initial burst of star formation followed by a quiescent period, with a marked and peaked star formation for ages younger than 4 Gyr ($\log(t/{\rm yr}) = 9.6$). In particular the peaks of star formation at approximately 1.5 Gyr ($\log(t/{\rm yr}) = 9.2$), 500 Myr ($\log(t/{\rm yr}) = 8.7$), 100 Myr ($\log(t/{\rm yr}) = 8.0$) and 10 Myr ($\log(t/{\rm yr}) = 7.0$) are in tight agreement with those found by Harris & Zaritsky (2009) for the global SFH of the LMC. Concerning the AMR, the result for the NGC 1751 field is consistent with those derived from the LMC stellar clusters (Kerber et al. 2007; Harris & Zaritsky 2009) and for the LMC field (Carrera et al. 2008).

5.4 The SFH for NGC 1751

5.4.1 Overview of NGC 1751 parameters from literature

As for the LMC field, also for the NGC 1751 cluster we need a set of physical parameters to start with the SFH-recovery work. They are based on the following works:

The cluster metallicity as determined by the Ca II method is of [Fe/H] $= -0.44 \pm 0.05$ (Grocholski et al. 2006), which is a typical value for an intermediate-age LMC cluster ([Fe/H] $= -0.48 \pm 0.09$, Grocholski et al. 2006).

Milone et al. (2009) identified a double MSTO in the HST/ACS F435W vs. F435W – F814W CMD for this cluster. Using isochrone fitting, they determined ages between 1.3 and 1.5 Gyr, a distance modulus of 18.45 mag, $E_{B\text{-}V} = 0.22$ ($A_V \simeq 0.70$), and a metallicity of $Z = 0.008$ ([Fe/H] $\simeq -0.38$).

Milone et al. (2009) also determine a binary fraction $f_{\rm b}$ of 0.13 ± 0.1 for mass ratios q larger than 0.6 in NGC 1751. Despite the small error bar quoted by them, their estimate is admitedly a preliminary one. The careful determination from

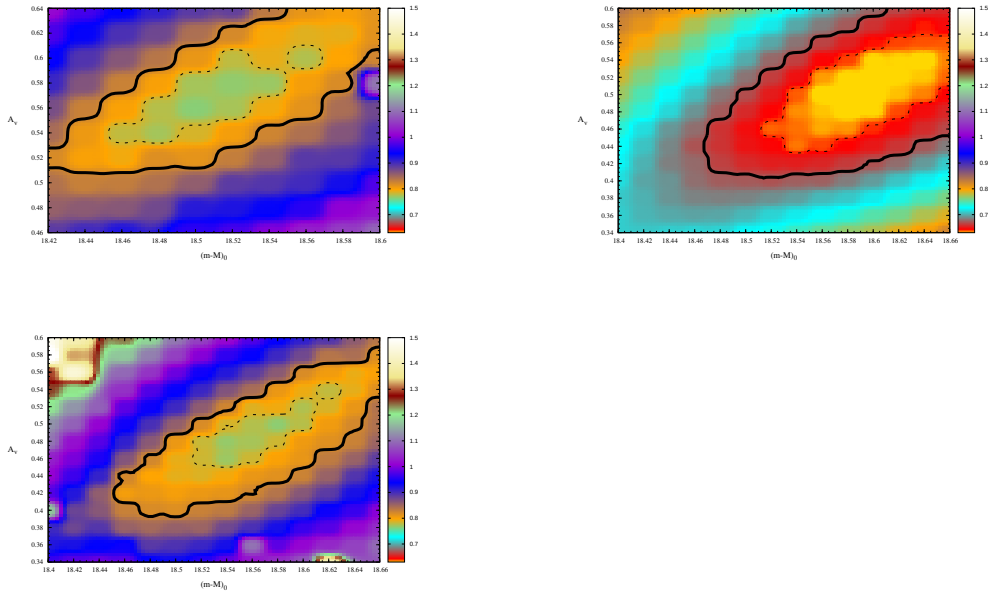

Figure 5.9: Maps of the $\chi^2_{\rm min}$ obtained during SFH-recovery in the Centre region, as a function of $(m-M)_0$ and A_V. The **left panel** shows the map for the best-fitting metallicity of [Fe/H] = −0.64, obtained in the case A (i.e. not taking into account a partial model for the LMC field). The minimum $\chi^2_{\rm min}$ is of 0.77. The **middle panel** shows the same for case B (i.e. using the LMC field partial model) and [Fe/H] = −0.44, which is the best-fitting metallicity in this case. It is evident that these solutions are characterized by a significantly smaller level of $\chi^2_{\rm min}$ overal, with a minimum at 0.62. For comparison, the **right panel** shows the best-fitting solutions for case A and [Fe/H] = −0.44. Also in this case, the $\chi^2_{\rm min}$ are significantly higher (and very close to the one in the letfmost panel).

Elson et al. (1998b) for the LMC cluster NGC 1818, finds f_b values varying from ~ 0.20 to ~ 0.35 as one goes from the cluster center to the outer parts. We adopt here the conservative value of $f_b = 0.2$ for $q > 0.7$. Our previous results for NGC 419 (Rubele et al. 2010) indicate that the results of the SFH recovery do not depend significantly on the choice of binary fraction.

As for the extinction, the reddening maps from the Magellanic Clouds Photometric Survey (MCPS; Zaritsky et al. 2004) and Pejcha & Stanek (2009) provide discrepant values for the NGC 1751 direction. Within 3 arcmin from the cluster, MCPS gives $A_V = 0.47 \pm 0.34$ for hot stars, and $A_V = 0.59 \pm 0.39$ for cool stars. From the same dataset, Pessev et al. (2008) determined $A_V = 0.65 \pm 0.06$. Pejcha & Stanek (2009) instead find $\langle E_{V-I} \rangle = 0.150 \pm 0.293$ ($\langle A_V \rangle = 0.293 \pm 0.062$), although their value is based on just 5 stars within a $2^\circ \times 2^\circ$ area.

The distance modulus to the LMC disk in the NGC 1751 direction is of about 18.55 mag, as revealed by independent methods: (van der Marel & Cioni 2001b, AGB stars); (Olsen & Salyk 2002, red clump stars); (Nikolaev et al. 2004, Cepheid stars); (Subramanian & Subramaniam 2010b, RC stars from MCPS).

The above-mentioned works provide only the initial guesses for the many cluster parameters to be determined in this work. Our final best-fitting solutions are completely independent of them.

5.4.2 The partial models for NGC 1751

For NGC 1751 we assume a constant age-metallicity relation, i.e., a single value for the metallicity for all ages, since so far there are no evidences for significant spreads in metallicity in such star clusters (e.g. Mucciarelli et al. 2008; Rubele et al. 2010). The age interval covered by our partial models goes from $\log(t/\mathrm{yr}) = 8.9$ to 9.4, which is much wider than the interval suggested by the position of NGC 1751 MMSTOs. So, for each set of parameters, we have a total of 10 partial models, completely encompassing the age interval of interest. We have explored 5 metallicity values, going from [Fe/H] from -0.75 to -0.35 at steps of 0.1 dex. For each one of these mean [Fe/H] values, a small metallicity spread of 0.02 dex is assumed.

This definition of partial models might already be good enough to our aims to find the best-fitting solution for the cluster centre. However, we know that every portion of the ACS/WFC image is contaminated from the LMC field, and that this field contamination is well evident in the observed CMDs (especially for the Ring). Therefore, it is quite tempting to add, to the above-mentioned list of partial models, an additional one corresponding to the LMC field. The hope is that this

partial model will allow StarFISH to properly fit the field contamination across the CMDs on NGC 1751, hence improving the fitting of cluster itself.

There are then two different ways at which this partial model for the field can be built. (1) The simplest one is that of taking the observed Hess diagrams for the field region (left panels in Fig. 5.7). This diagram however is marked by the Poisson fluctuations in the numbers of stars, so that it might not describe in a suitable way the field actually observed in other parts of the ACS images. (2) The second alternative is to use the Hess diagram built from the best-fitting solution of the field (right panels in Fig. 5.7) which is obviously much more continuous and smooth over the CMDs than the observed one. This model has another clear advantage: the Hess diagram can be easily re-built using the output SFH for the field *together* with the ASTs derived for the cluster Centre or Ring. In this way, we are able to simulate the field under the same conditions of crowding met in the cluster data. We indeed adopt this latter alternative in the following.

5.4.3 The SFH for the cluster Centre

Results with and without the LMC field

The SFH-recovery is performed assuming a given set of $(m-M)_0$, A_V, and [Fe/H] values and fixing the binary fraction at a value of 0.2 in the case of cluster models. In order to limit the space of parameters to be covered, the procedure is essentially the following: for a given value of [Fe/H], we perform SFH-recovery for each point in a grid covering a significant region of the $(m-M)_0$ versus A_V plane, so as to build a map of the $\chi^2_{\rm min}$ for the solutions. Examples of these maps are presented in Fig. 5.10. The maps are extended enough so that the minimum $\chi^2_{\rm min}$ for a given value of [Fe/H] can be clearly identified, as well as the regions in which $\chi^2_{\rm min}$ increases by a factor of about 1.5. The typical resolution of such maps is of 0.02 mag in $(m-M)_0$ and 0.02 mag in A_V.

Let us first start discussing the case of the cluster Centre. Fig. 5.9 shows the maps of $\chi^2_{\rm min}$ as a function of $(m-M)_0$ and A_V, for two series of SFH-recovery experiments made under very similar conditions, i.e. using the same data and ASTs. The only difference is that in some cases (hereafter **case A**), we do not use the partial model for the LMC field in StarFISH, whereas in other cases we do it (hereafter **case B**). The result of considering the LMC field is quite evident: although in both A and B cases the best-fitting solution is found for about the same value of $(m-M)_0$ and A_V, in case B the $\chi^2_{\rm min}$ values are systematically smaller, which means better overall fits of the CMDs. Moreover, it is evident that in case A

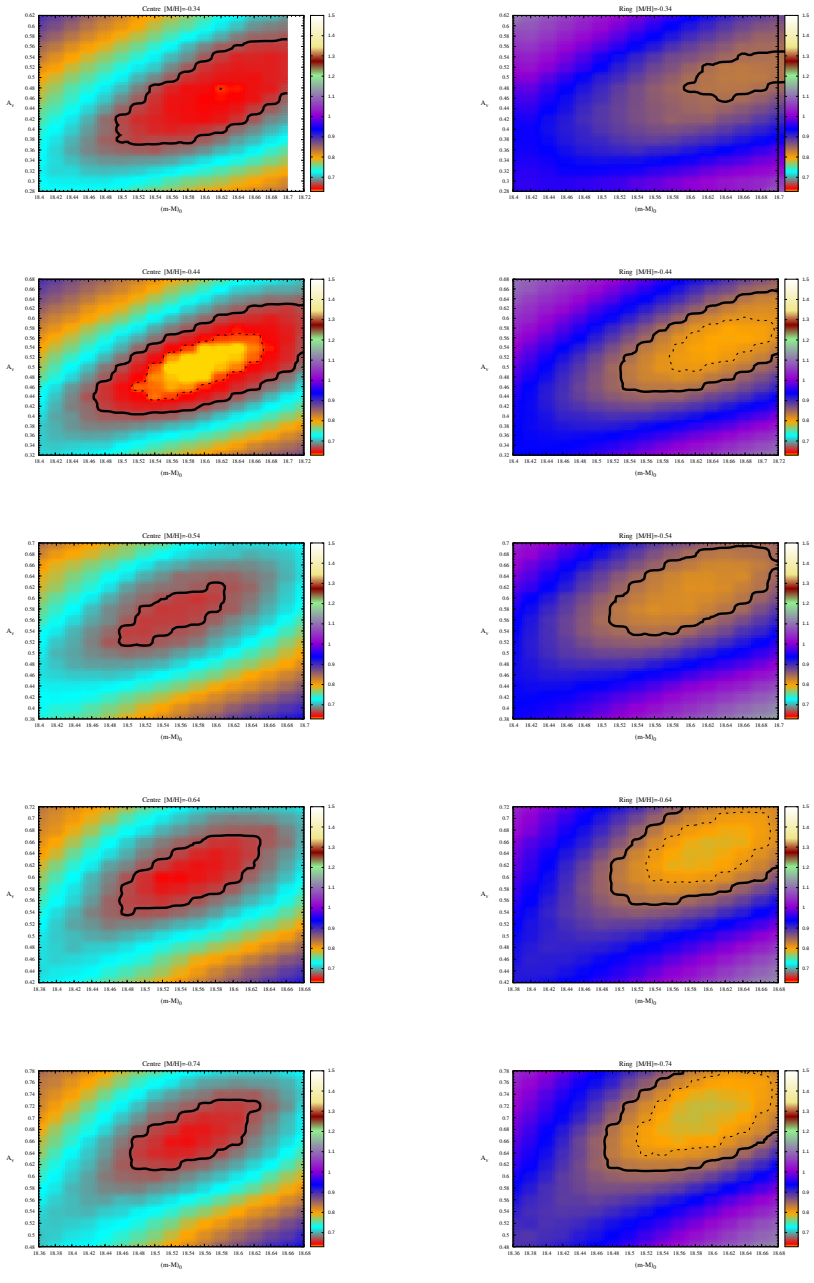

Figure 5.10: Maps of the $\chi^2_{\rm min}$ obtained from the SFH-recovery, as a function of $(m-M)_0$ and A_V, for several [Fe/H] values (from -0.34 to -0.74 at steps of -0.1 dex, from top to bottom) and for both the cluster Centre and Ring (left and righ panels, respectively). The black lines delimit the regions within a 68 % (continuous line) and 95 % confidence levels (dotted lines) of the absolute best solution, which is found at -0.34 dex for the Centre, and at -0.74 dex for the Ring. The $\chi^2_{\rm min}$ for the Centre best solution is of 0.625.

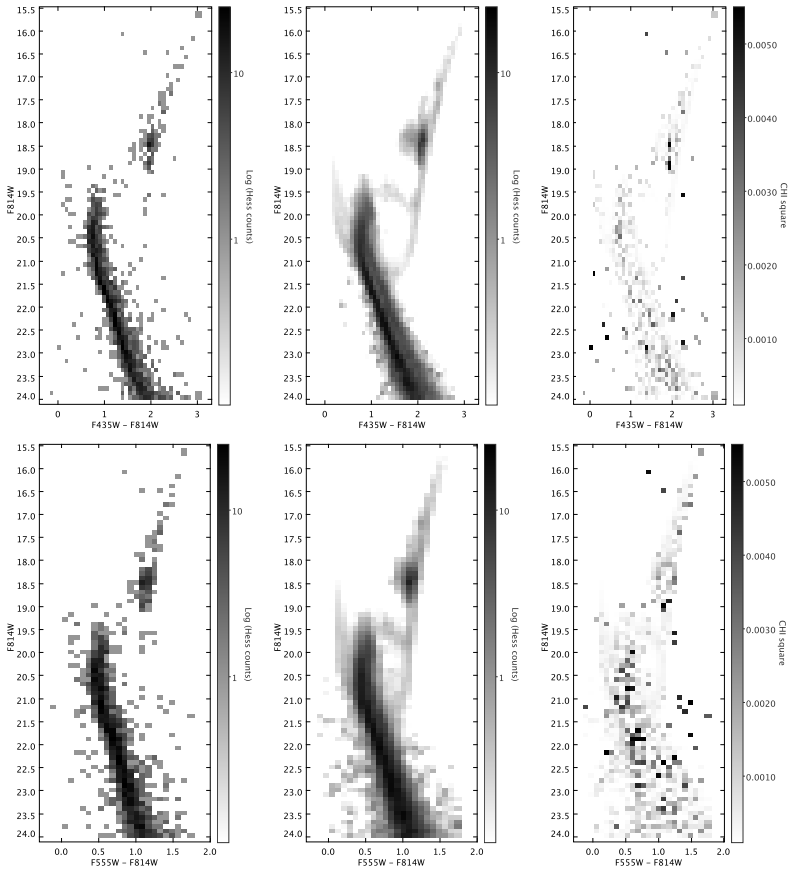

Figure 5.11: The Hess diagrams for the NGC 1751 Centre data (left panels), its best-fitting solution model (central panels), and the χ^2 map (right panels). The top panels are for the F435W – F814W vs. F814W diagrams, the bottom ones for F555W – F814W vs. F814W.

the presence of the LMC field falses the determination of the best-fitting cluster metallicity: indeed, in case A the best-fitting model of [Fe/H] = −0.64 is found to be slightly favoured over the one with [Fe/H] = −0.44. In case B, instead, the best-fitting solution at [Fe/H] = −0.44 is clearly favoured. Notice that, at the ∼ 1.5 Gyr old ages of NGC 1751, the field is found to have a metallicity of about −0.65 (see Fig. 5.8), which probably helps, in case A, to move the $\chi^2_{\rm min}$ minimum to [Fe/H] = −0.64.

These experiments demonstrate that even a small fraction of field contamination may affect significantly the results of SFH-recovery, if not properly taken into account. In the following, we adopt case B as the default, since it demonstrately takes the LMC field into account and improves the quality of the final results for the Centre of NGC 1751.

Characteristics of the best-fitting solution

Complete maps of $\chi^2_{\rm min}$ for the Centre, as a function of $(m-M)_0$, A_V and metallicity, are presented in the left panels of Fig. 5.10. It may be noticed that the best solution is indeed for [Fe/H] = −0.44, $(m-M)_0$ = 18.58, and A_V = 0.50, with a $\chi^2_{\rm min}$ = 0.62. Such a small $\chi^2_{\rm min}$ is already an indication of an excellent fit to the observational data.

This best-fitting solution and map of residuals are also presented in the Hess diagrams of Fig. 5.11. Finally, the best-fitting solution for the cluster Centre is in the left panel of Fig. 5.12.

Evaluating the errors

To evaluate the errors for all involved parameters, the first step is to find the correspondence between the $\chi^2_{\rm min}$ value for each model and its significance (or confidence) level, α. This correspondence was estimated simulating 100 synthetic CMDs generated with a number of stars equal to the observed CMD, using the best-fitting SFR(t) and its parameters as the input for the simulations. So, after recovering the SFH for this sample of synthetic CMDs, it was possible to build the $\chi^2_{\rm min}$ distribution and to establish the relation between the $\chi^2_{\rm min}$ difference above the minimum and α.

In the $\chi^2_{\rm min}$ maps of Fig. 5.10, we superimposed the 68 % and 95 % significance levels for all the solutions for the centre. Only for the [Fe/H] = −0.44 map we find ample areas of the A_V versus $(m-M)_0$ diagram with solutions within the 68 % significance level of the best solution. Based on this figure, we determine

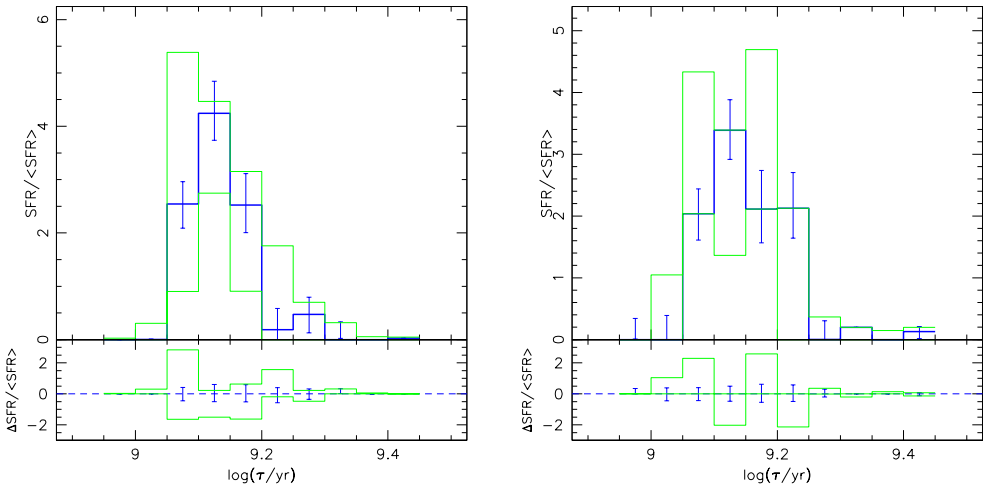

Figure 5.12: The blue lines show the SFR(t) for the cluster Centre (left panel) and for the Ring (right panel). The error bars are random errors. The green lines indicate the systematic errors, inside the area of 68 % confidence level in Fig. 5.10.

$(m-M)_0 = 18.58 \pm 0.07$ and $A_V = 0.50 \pm 0.05$ for the cluster Centre (with random errors at the 68 % significance level).

The left panel of Fig. 5.12 shows the SFR(t) for the cluster Centre together with error bars. The most basic feature in this plot is that the SFR(t) is clearly non-null for three age bins, spanning the $\log(t/\mathrm{yr})$ interval from 9.05 to 9.2 (ages from 1.12 to 1.58 Gyr). Note that this result is not only valid for the best fitting model, but also across the entire 68 % significance level area of the A_V versus $(m-M)_0$ diagram. Moreover, it is non-null even in the case we adopt more restrictive limits for the random errors, i.e. if we plot the random errors for the 95 % significance level.

Then, one may wonder how the solution for the Centre changes if we adopt a better age resolution in the SFH-recovery. This is shown in Fig. 5.13, where we compare the solution for $\Delta\log(\mathrm{age}) = 0.05$ dex with the one obtained with the same data and methods, but for an age resolution of $\Delta\log(\mathrm{age}) = 0.025$ dex. As we see, within the error bars the two solutions are essentially the same. The finer resolution in age is compensated by an increase in random errors.

Therefore, we find evidence that in the NGC 1751 Centre the SFR(t) has lasted for a timespan of 460 Myr. This is about twice longer than the $\sim$ 200 Myr estimated by Milone et al. (2009) for the same cluster, based on a simple comparison

with the MSTO locations of different isochrones.

5.4.4 The SFH for the cluster Ring

We have performed the same experiments of SFH-recovery separately for the Ring, as illustrated in the $\chi^2_{\rm min}$ maps at the central and right panels of Fig. 5.10. In these cases, the levels of $\chi^2_{\rm min}$ are significantly higher than for the cluster Centre. This result may seem surprising, considering that the Ring has a lower level of crowding and hence deeper photometry than the Centre. We consider as unlikely that these higher $\chi^2_{\rm min}$ for the Ring could be simply caused by its higher level of contamination from the LMC field, since this field is very well modeled anyway, and fully taken into account in the SFH recovery.

Instead, the main reason for the worst fits could be on the presence of a differential reddening of about $E_{B-V} \sim 0.10$ mag within the ACS field, as found by Milone et al. (2009) and Goudfrooij et al. (in preparation).

To test for the presence of differential reddening we have followed a similar procedure as described by Milone et al. (2009), following the position of fiducial lines in the F435W – F555W vs. F555W – F814W diagram. So by means of the relative shifts in the fiducial lines in this colour-colour diagram along the reddening arrow we have found an extra reddening in the Ring region in relation to the Centre, with a magnitude in $E_{\rm F555W-F814W}$ similar to the one presented by Milone et al. (2009). This extra reddening occurs prevalently in the bottom and upper extremities of the Ring in Fig. 5.1.

Notice also that the extinction values for the Ring, found during the experiments of SFH-recovery are systematically higher than the ones found for the Centre region (see Fig. 5.10), which independently confirms the presence of differential reddening detected by us and Milone et al. (2009) using fiducial lines.

Unfortunately the recovered best-fitting $(m-M)_0$ and [Fe/H] values for the Ring are obviously spurious, since they are not consistent with the ones found for the Centre – which is a such small region that one can consider it free from differential reddening. Considering the high quality of the SFH-recovery for the cluster Centre (as demonstrated by the much smaller $\chi^2_{\rm min}$), we assume that the correct distance and reddening of the Ring are the same ones as for the Centre, namely $(m-M)_0 = 18.58$ and $A_V = 0.50$. The right panel of Fig. 5.12 shows the Ring SFH for these parameters.

It is interesting to note that the Ring SFR(t), considering just the random errors, seems to be slightly more spread in age than the one for the Centre. Indeed, the SFR(t) is found to be non-null in an additional, older age bin, as compared

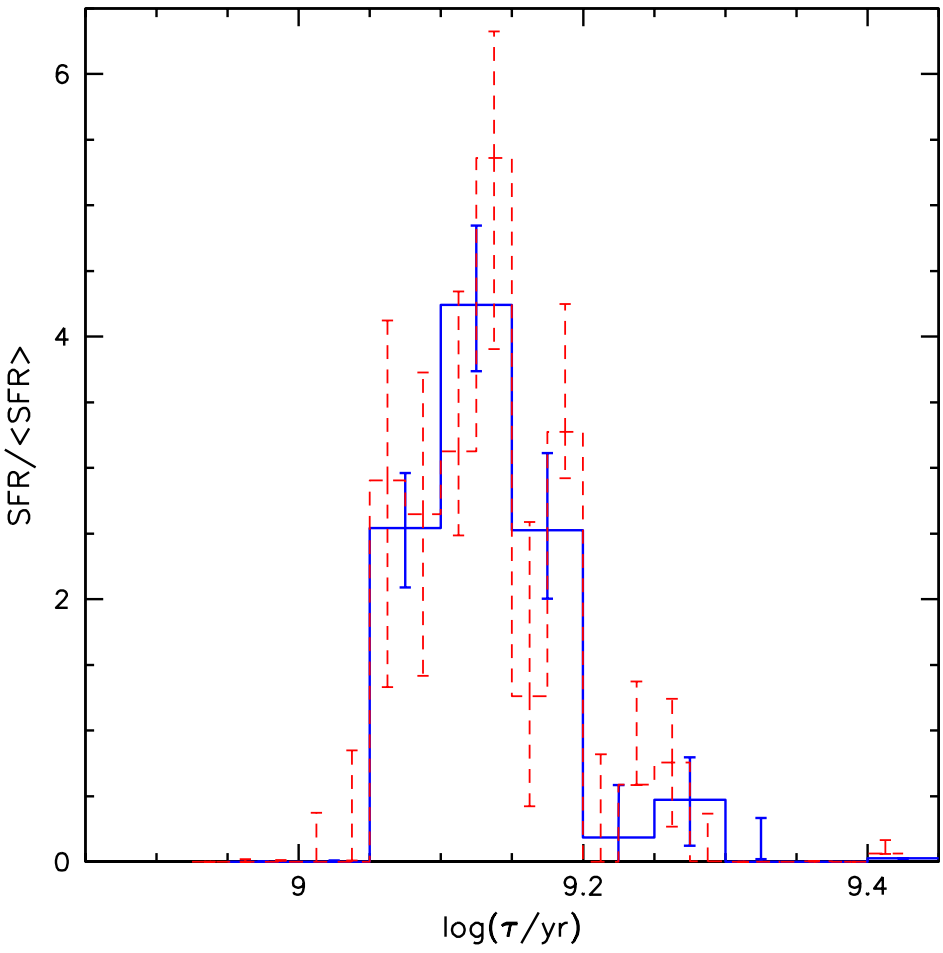

Figure 5.13: Comparison between the SFR(t) for two best-fitting solutions for the cluster Centre, obtained with different age resolutions: with $\Delta \log t = 0.050$ dex (blue continuous line) and with $\Delta \log t = 0.025$ dex (red dashed line).

to the cluster Centre. However, when one considers the systematics errors in this bin, it is clear that this result is not solid. It becomes then impossible to take any conclusion in relation to a possible dependence of the SFR(t) with the cluster radius.

5.5 Concluding remarks

In this work, we perform SFH-recovery via the classical method of CMD reconstruction with the sum of single-burst stellar populations. The basic result is that in the cluster Centre star formation is found to last for a timespan of 460 Myr. The same result is consistently found irrespective of the method used to take field contamination into account, of the age resolution adopted, and for a significant region of the A_V versus $(m-M)_0$ plane. The age resolution of the method is at least 3 times smaller than this interval. In addition, the best-fitting model is indeed a quite good representation of the observed data. On the other hand, the CMD for the cluster Centre is so obviously sharp and clean from the LMC field, that it is hard to imagine that some important effect has not been properly considered in our analysis.

For the cluster Ring, the results indicate a SFR timespan of at least 460 Myr, with a significantly lower quality of the results, as indicated by the larger $\chi^2_{\rm min}$ and by the best fitting model being found for a distance different from the cluster Centre. These failures probably depend on the presence of significant differential reddening across the Ring. So, we prefer not to take any conclusion from this region. Unfortunately, our method finishes in not providing any indication about possible variations in the spatial distribution of the stars with different ages, which would be important for the goals of understanding the mechanism of extended star formation (see Goudfrooij et al. 2009).

Together with our previous findings for the SMC cluster NGC 419 (Rubele et al. 2010), the results for the NGC 1751 Centre argue in favour of multiple star formation episodes (or continued star formation) being at the origin of the MMSTOs in Magellanic Cloud clusters with ages around 1.5 Gyr. The hypothesis of a spread caused by the presence of fast rotators among the upper main sequence stars, as advanced by Bastian & de Mink (2009), is discussed in the paper Girardi et al. (2011). They advance that this latter hypothesis does not seem to offer a valid alternative to the conclusions reached in this paper.

Chapter 6

The star formation history of the LMC from real VMC data: preliminary results

6.1 Introduction

We present the preliminary results on the recovery of the SFH for 3 VMC fields located around the LMC main body. Following the method described in Kerber et al. (2009a), Harris & Zaritsky (2004), and Gallart et al. (1999) we evaluated the SFH deriving at the same time the Age Metallicity Relation (AMR), the distance modulus $(m-M)_0$, and the extinction A_V .

When possible we have compared our results with other works as Zaritsky et al. (2004) for the A_V parameter and Nikolaev et al. (2004),van der Marel & Cioni (2001b) and van der Marel et al. (2002) for the $(m-M)_0$ parameter.

6.2 VMC data

We have recovered the SFH on VISTA data for 3 VMC fields located around the main body of the LMC and for wich the VISTA imaging is more complete.

The LMC fields used to recover the SFH are 8_8, (located at α=05:59:23.136, δ=-66:20:28.680), 8_3 (located at α=05:04:53.952, δ=-66:15:29.880) and 4_3 (located at α=04:55:19.512, δ=-72:01:53.400), with a completion of $\sim$ 100%, 75%, and 63%, respectively, in the K_s filter. Figure 6.1 shows the location of all LMC

fields of the VMC survey. The black circles evidence fields used to recover the SFH in this work.

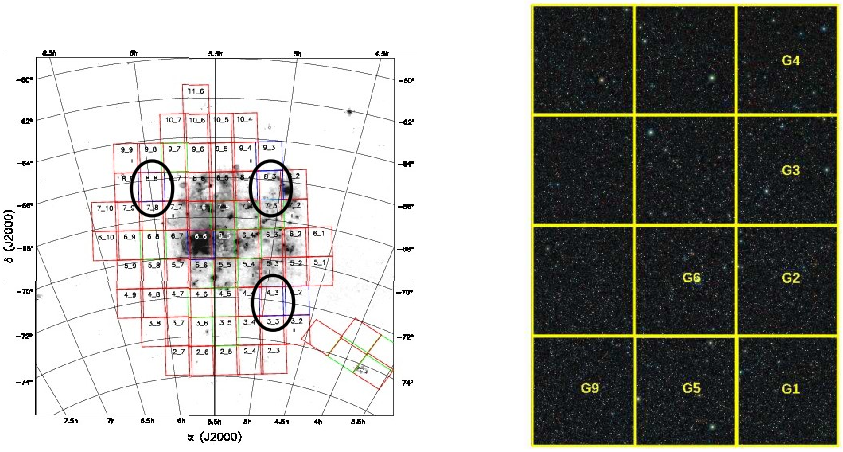

Figure 6.1: Left: LMC fields considered in this work. Right: 12 subregions in a false RGB color image of the 8_3 tile .

We have combined pre-reduced Paw-Print images (Irwin 2010) downloaded from the CASU VISTA Science Archive (VSA) [1] to produce deep tiles using the SWARP tool (Bertin et al. 2002b). Each tile covering an area of ~ 1.6 deg^2 , was subdivided in 12 sub-regions of ~ 0.12 deg^2. Figure 6.1 shows an example of sub regions overplotted on a color image of field 8_3 .

6.2.1 Photometry and ASTs

We have performed Aperture Photometry (AP) and Point Spread Function (PSF) photometry using the IRAF daophot packages (Stetson 1987), producing photometric catalogs and CMDs. Figure 6.2 shows an example of CMDs, in $Y - K_s$ vs. K_s, of the sub-region G3 of fields 8_8, 8_3 and 4_3.

[1] http://horus.roe.ac.uk/vsa/login.html

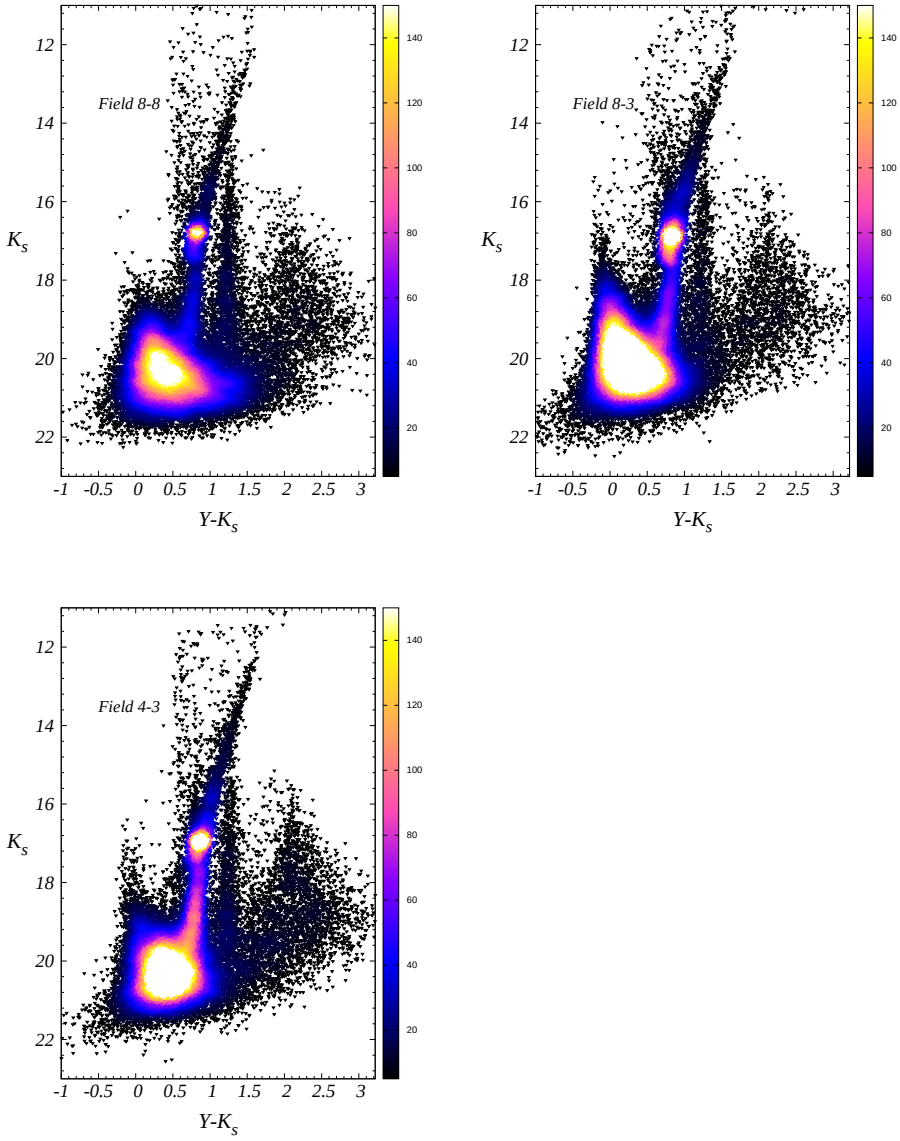

Figure 6.2: Example of CMDs ($Y - K_s$ vs K_s) in three sub regions of the fields 8_8, 8_3, and 4_3 .

To prevent galaxy contamination we have recovered the SFH using two CMDs simultaneously, namely $(Y - K_s)$ vs. (K_s) and $(J - K_s)$ vs. (K_s), in which most

of galaxies and stars have been separated using colors. Aperture photometry was made on a radius of 3 pixels ($\sim 1 arcsec$), that correspond to an encircled energy of $\sim 75\%$ at a PSF FWHM of 0.8 *arcsec*, and corrected using 2MASS data converted to the VISTA system using equations 6.1 below. In the case of PSF fitting photometry we used the IRAF psf package to produce the psf model, and the allstar package to make the photometry on a radius of 3 pixels. We have run massive Artificial Star Tests (AST) to estimate completeness and error distributions of ours data set in each part of the CMD. Figure 6.4 shows an example of the error distribution derived from AST in Y, J, K_s magnitude vs. the difference between the output and input magnitude made on a sub region of the field 8_3. On each tile's sub-region we have run ~ 1500000 AST in the same way as described in Kerber et al. (2009a) and Rubele et al.(2011), using a spatial grid with 30 pixels of width and with a distribution in magnitude proportional to the square magnitude.This latter choice allow us to better map completeness and errors in less complete regions of the CMD. Figure 6.3 shows an example of the completeness distribution for a sub-region of field 8_3; the gray scale map code the completeness level in the CMD $(J - K_s)$ vs. (K_s).

6.2.2 Bringing VISTA data to a Vega mag system

Because the Zero Points (ZP) of VISTA data are not in a Vega magnitude system (Vegamag) we have corrected them as shown in figures 6.5 using simulated population models of the MW foreground. We have estimated the differences between the calibration equations provided by the CASU:

$$\begin{aligned} Z_{VISTA} - J_{2MASS} &= 0.950(J-H)_{2MASS} \\ Y_{VISTA} - J_{2MASS} &= 0.550(J-H)_{2MASS} \\ J_{VISTA} - J_{2MASS} &= -0.070(J-H)_{2MASS} \\ H_{VISTA} - H_{2MASS} &= 0.060(J-H)_{2MASS} \\ Ks_{VISTA} - Ks_{2MASS} &= 0.020(J-K)_{2MASS} \end{aligned} \tag{6.1}$$

and those predicted by the theoretical models, which are, by construction, strictly on a Vegamag system (where Vega has a magnitude of 0 in all filters).

In short, we proceed as follows:
We have simulated a Milky Way (MW) region of ~ 1.4 deg^2, and added the 2MASS errors following Bonatto et al. (2004). They dominate the error distribution compared to VISTA data. Then, we have fitted the best linear solution in the

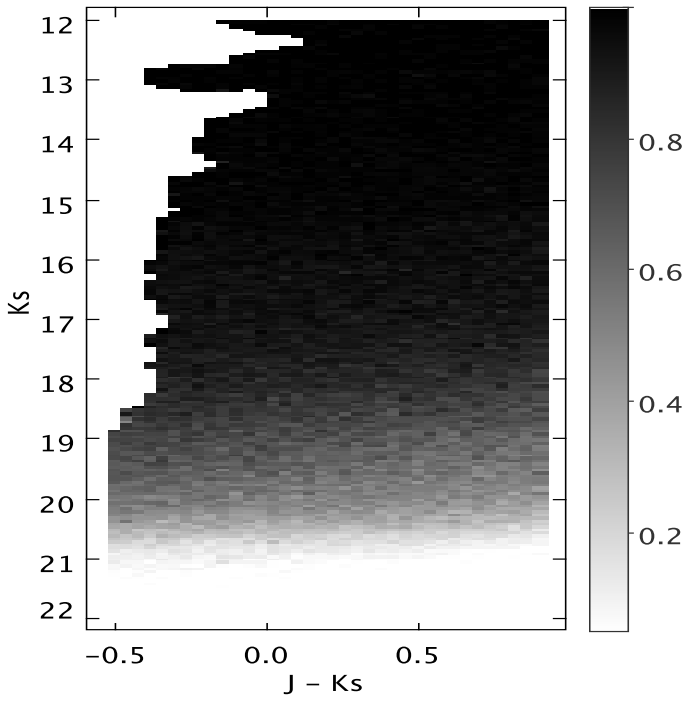

Figure 6.3: Example of completeness map distribution derived from the ASTs on a $J - K_s$ vs K_s CMD.

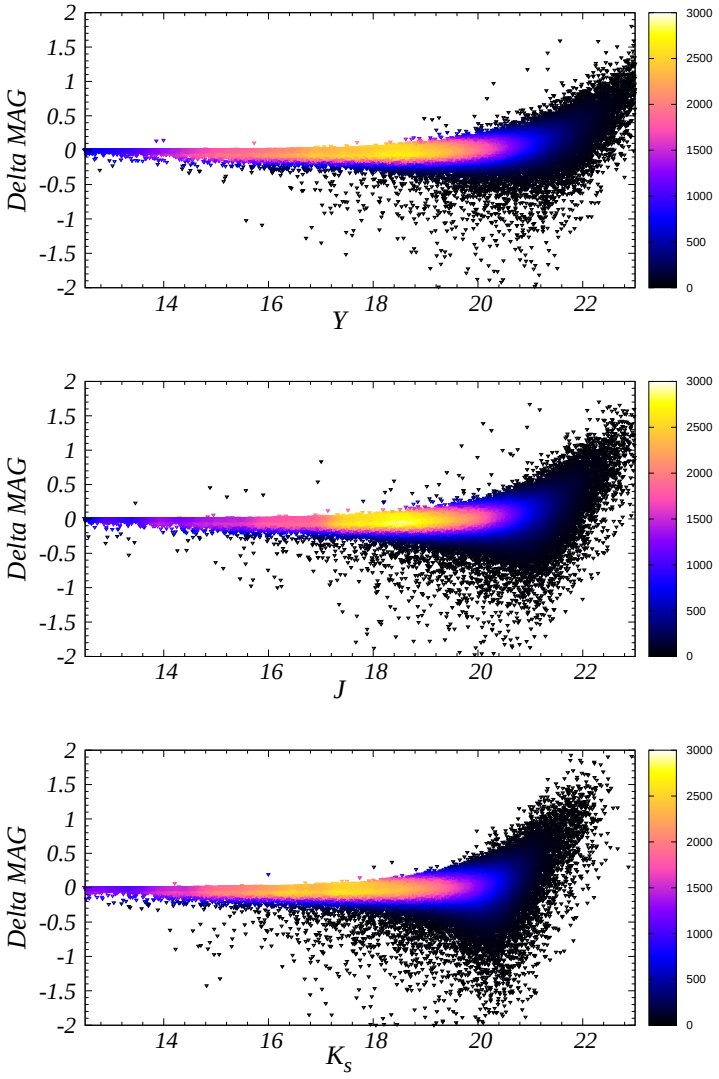

Figure 6.4: Example of error distributions derived from ASTs, in Y, J, K_s VISTA filters for a sub region in the field 8_3.

colour-colour diagrams (see figures 6.5) fixing the slope as in equations (6.1). We have used a sigma clipping of 3σ. The offsets between the CASU and the model equations give the ZP corrections to the Vegamag system.

We have found a difference in ZP of 0.0989 in Y, 0.021 in J and 0.0 in Ks bands, with respect to the CASU calibrations.Then we have corrected our Stellar Partial Models (SPM) by this difference before recovering the SFH .

6.3 The SFH recovery

To recover the SFH we used partial models distributed according to 5 Age Metallicity Relations (AMR) distributed and on 14 age intervals that cover from $log(t/yr) =$ 6.6 to 10.15 and most of the observed AMR given by stellar clusters (Olszewski et al. 1991; Mackey & Gilmore 2003; Grocholski et al. 2006; Kerber et al. 2007) and field stars (Cole et al. 2005; Carrera et al. 2008). This totals 70 SPM, plus a Milky Way foreground model simulated with TRILEGAL (Girardi et al. 2005). Table 6.1 shows the center of the age and metallicity bin per each SPM. The width of models is 0.15 dex in [Fe/H] and 0.2 dex in $\Delta log(t)$. In the case of the 3 youngest models we used $\Delta log(t)$ widths of 0.6, 0.4 and 0.4 respectively. In figures 6.9, 6.10, 6.11 SPM are shows as red points.

Using these SPMs we have recovered the SFH in different conditions of A_V and $(m-M)_0$ on a grid spaced by 0.03 mag and 0.025 mag, respectively, with limits: from 0.06 to 0.60 in A_V , in all 3 fields; and from 18.40 to 18.525 in $(m-M)_0$ infield 8_3, 18.40 to 18.65 in 4_3 and 18.275 to 18.45 in the 8_8 field. The SFH was recovered using 2 CMDs, $J-K_s$ vs. K_s with limits -0.52 to 0.88 in color and 12.10 to 20.45 in magnitude, and $Y-K_s$ vs. K_s with limits - 0.82 to 1.56 in color and 12.10 to 20.15 in magnitude. These constraints in color and magnitude allow to separate the LMC stars from most of the contamination by galaxies (see as example figure 6.2 were most of the galaxies are clearly well separated up to $K_s = 19.5$ and locate in the faintest and redder part of the CMDs).

Figures 6.6, 6.7, and 6.8, show the χ^2 solution map, as a function of A_V and $(m-M)_0$, of all subregions in each field investigated. Black dashed and continuous lines code the confidence error limit at 1σ and 3σ. Figures 6.9, 6.10, and 6.11, show for all sub regions in each field the SFR(t) (blue histograms, top panel) with stochastic errors (blue errors bars) and the systematic SFR(t) variations inside the confidence level (green histograms). Panels in the center show the best fit AMR(t) recovered (green points) with stochastic errors (green vertical bars) and the systematic AMR variations inside the confidence level (blue dashed lines).

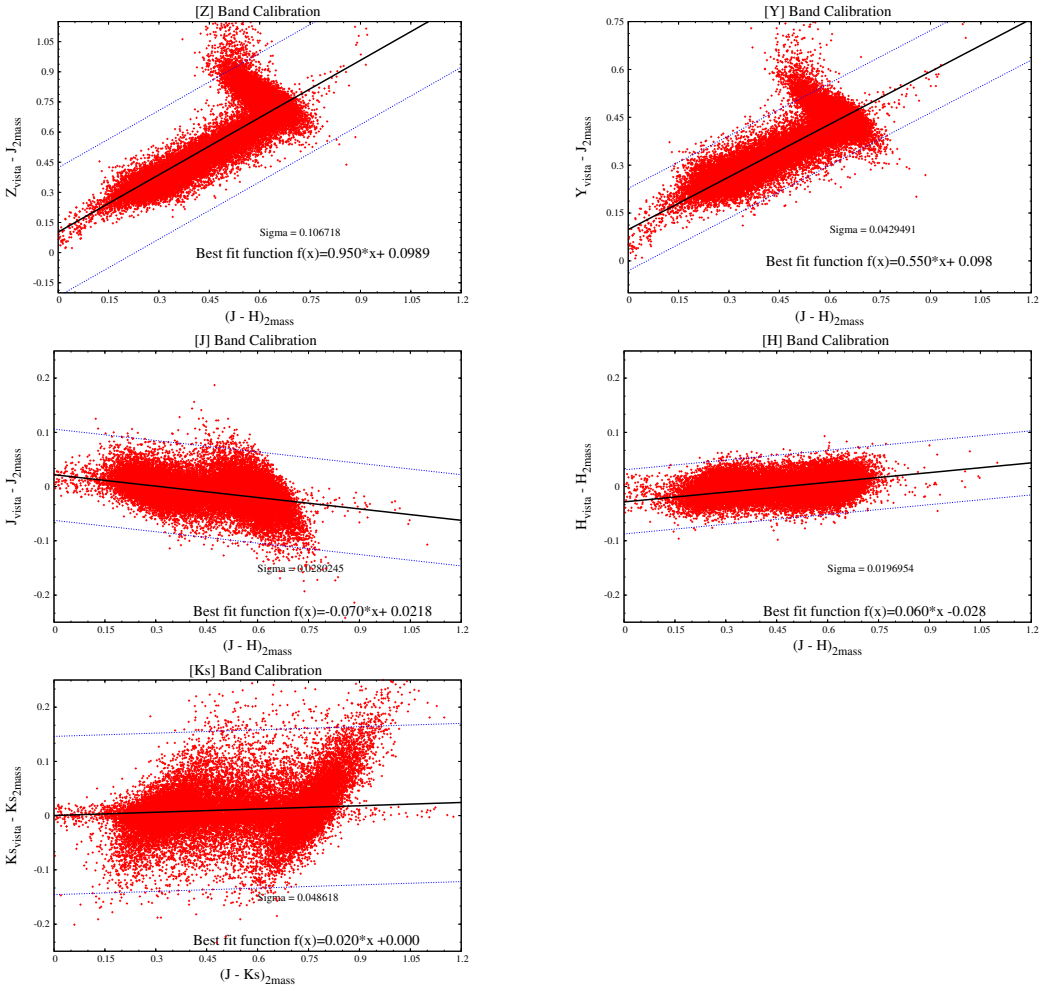

Figure 6.5: Calibration to a Vegamag system. The red points show Milky Way model stars corrected by the 2MASS errors on an area of $\sim$ 1.4 deg^2, the blue lines code the 3σ clipping and the black line show the best fit linear relation with a fixed slope as in equations 6.1.

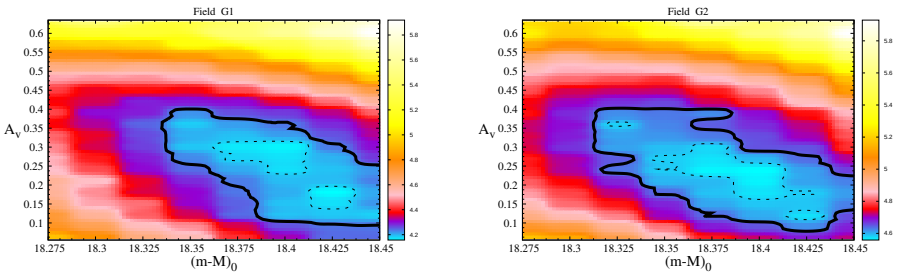

Figure 6.6: χ^2maps of sub regions in the 8_8 field. These maps show the quality of the STARFISH χ^2 fit in function of $(m-M)_0$ and A_V. The blacks contour lines illustrate the random errors to a confidence level of 1σ (dashed line) and 3σ (tick continuous line).

The red points are the center of SPM used in the recovering the SFH (6.1). The bottom panel illustrates the variation of the SFR solution considering stochastic (blue line) and systematic errors (green line).

6.4 Distance modulus $(m-M)_0$ and Extinction A_V

We have completed the recovery of the SFH on 10 subregions in field 8_3, and on 2 subregions in 8_8 and 4_3 fields. We have evaluated the average A_V and $(m-M)_0$ parameters in each sub region in all 3 fields as the average value inside the 68% confidence level and then we have compared our results with values obtained in Zaritsky et al. (2004) for the A_V parameter, and Nikolaev et al. (2004), van der Marel & Cioni (2001b) and van der Marel et al. (2002) to the $(m-M)_0$.

All results are show in table 6.2 and 6.3 in which G1, G2, etc. correspond to the subregion considered. In table 6.3 the parameters A_V^{CS} and A_V^{HS} are the A_V in Zaritsky et al. (2004) in the case of Cool Stars and Hot Stars, respectively, whereas A_V^{TW} and $(m-M)_0^{TW}$ are the A_V and $(m-M)_0$ parameters found in this work. In table 6.2 we compared results for the $(m-M)_0$ parameter obtained in this work with the LMC spatial models of: Nikolaev et al. (2004) (with i the inclination and *P.A.* the Position Angle of line of nodes) in the case of $i = 30.7°$ and *P.A.* $= 151.0°$, van der Marel & Cioni (2001b) and van der Marel et al. (2002) with parameters $i = 34.7°$, *P.A.* $= 122.5°$ and *P.A.* $= 129.9°$, respectively.

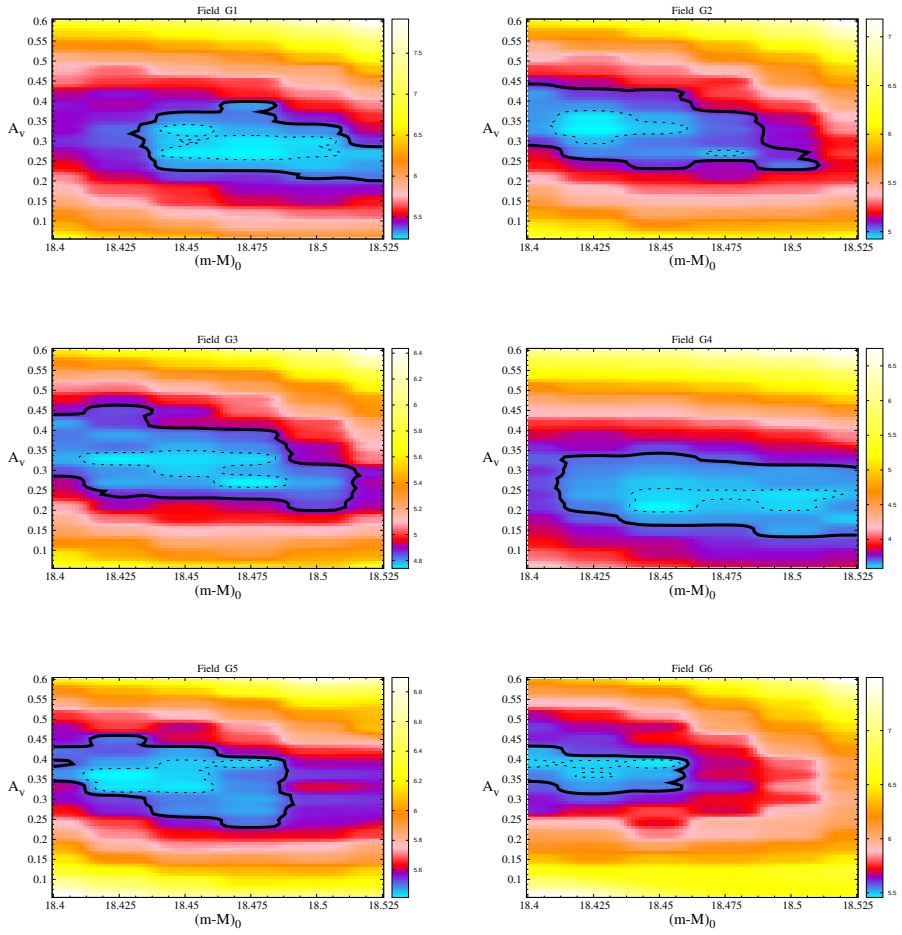
Field G1
Field G2
Field G3
Field G4
Field G5
Field G6
A_V
$(m\text{-}M)_0$
0.6
0.55
0.5
0.45
0.4
0.35
0.3
0.25
0.2
0.15
0.1
18.4
18.425
18.45
18.475
18.5
18.525

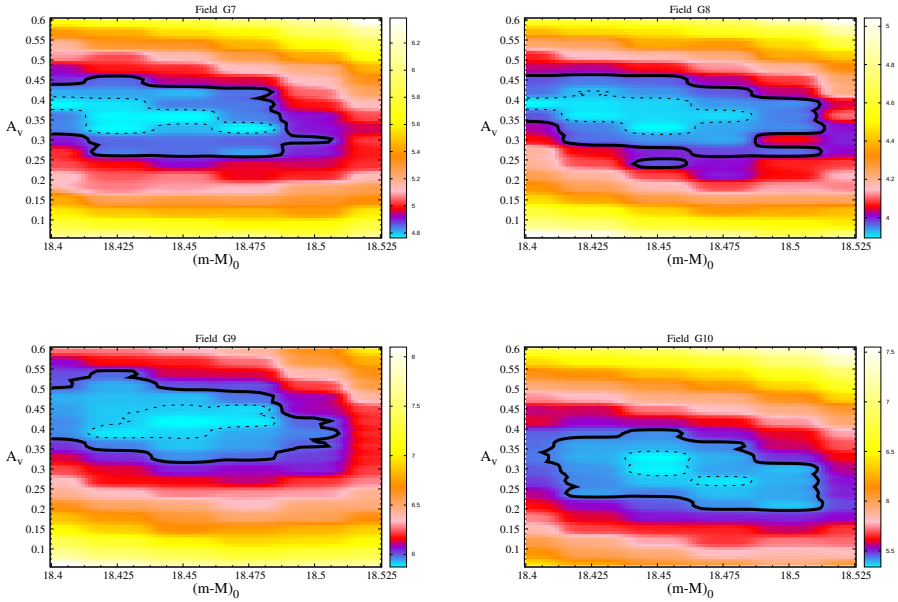

Figure 6.7: χ^2maps for a sub region in the 8_3 field, see caption in figure 6.6.

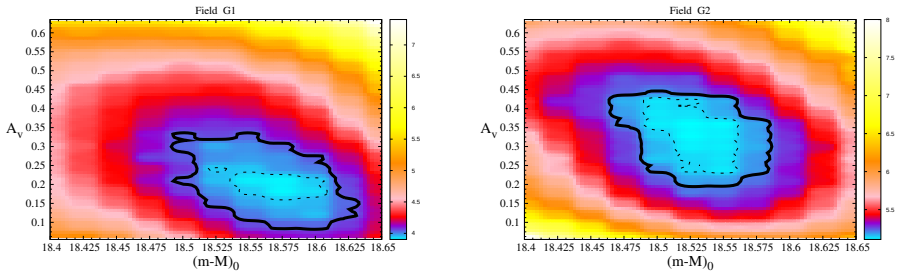

Figure 6.8: χ^2 maps of sub-region in the 4_3 field, see caption in figure 6.6.

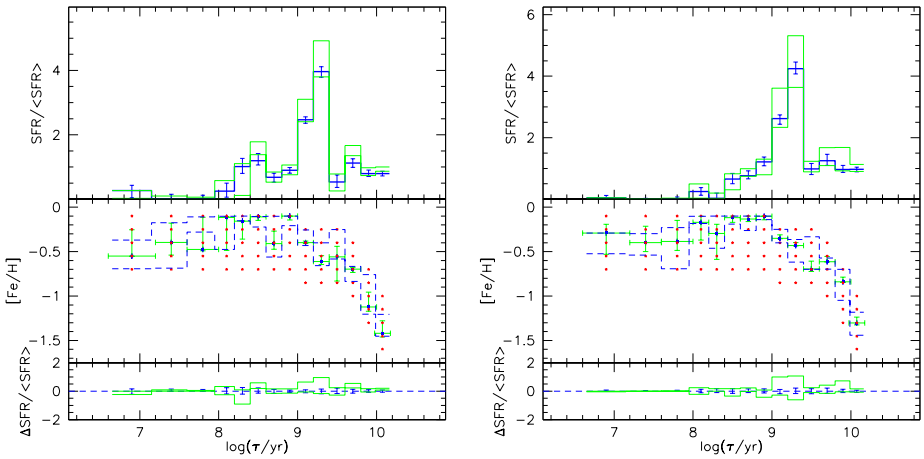

(a) SFR of sub region G1 and G2

Figure 6.9: SFR and AMR of sub-regions in field 8_8

6.5 Discussion and conclusions

We have recovered the SFH on three VMC LMC fields evaluating simultaneously the best fitting SFR, AMR, A_V and $(m-M)_0$, and the stochastic and systematic errors inside the 68% confidence level in each subregion for each field. The comparison of A_V parameter derived in our work with Zaritsky et al. (2004) shows a good agreement. The $(m-M)_0$ values are in agreement with Nikolaev et al. (2004), van der Marel & Cioni (2001b) and van der Marel et al. (2002) works. Only the field 8_8 has a completion of 100%, so results of fields 8_3 and 4_3 will be improved in the future.

6.5.1 Field 8_3

- As mentioned before in this field the A_V and $(m-M)_0$ values we find are in agreement with literature works giving average values of 0.335 and 18.45 mag, respectively.

- The trend of the AMR in each subregion do not change inside the evaluation region so we conclude that the AMR on this field is little space dependent. In subregions poor of stars younger than $log(t/yr) = 8$ (null or low SFR), errors are large and it is not possible to evaluate the metallicity with accu-

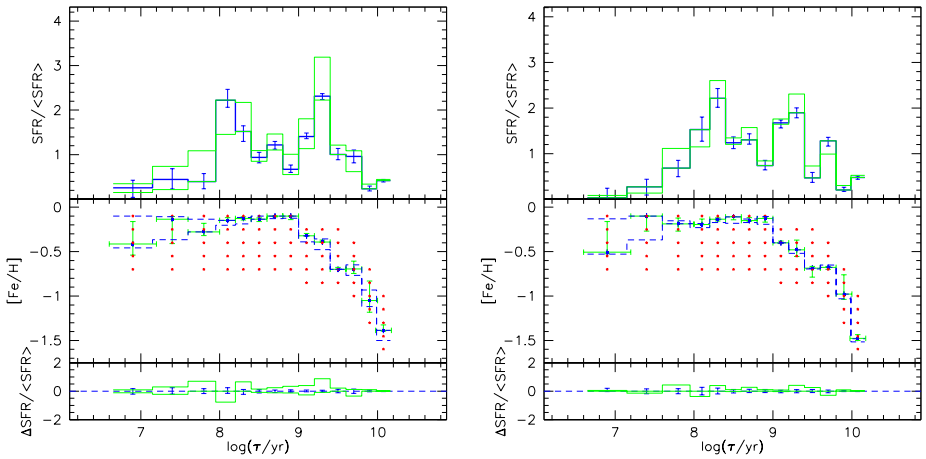

(a) SFR of sub region G1 and G2

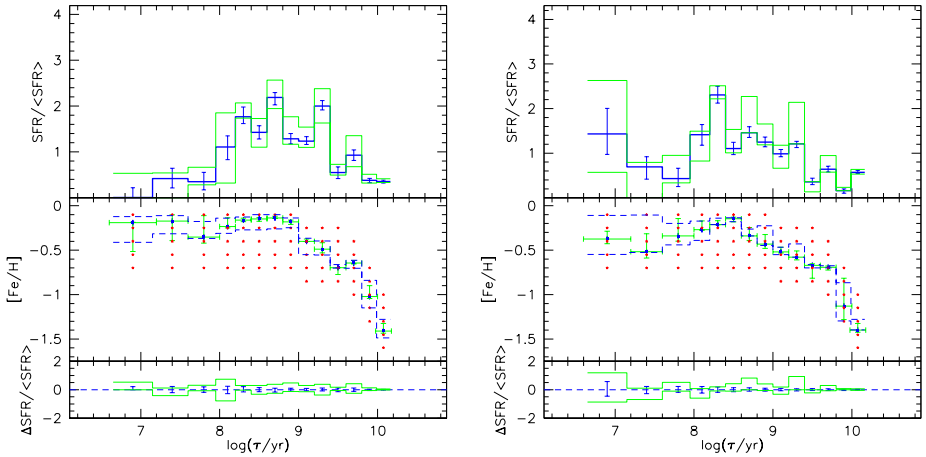

(b) SFR of sub region G3 and G4

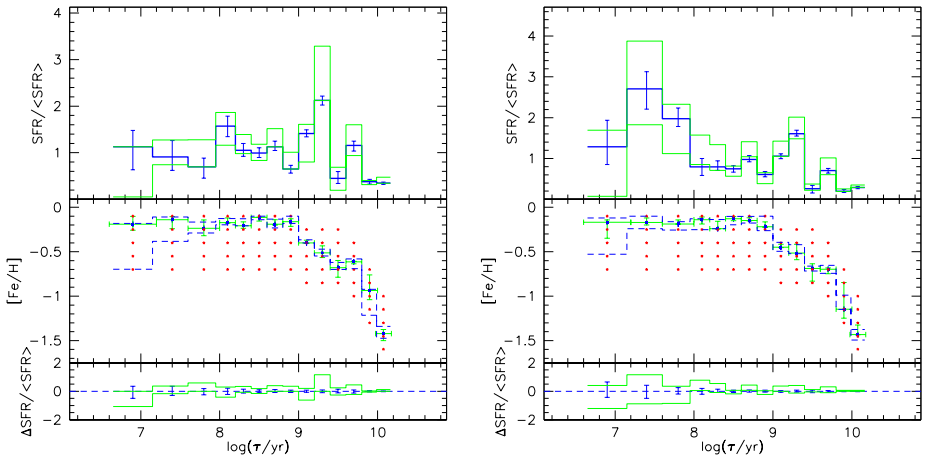

(c) SFR of sub region G5 and G6

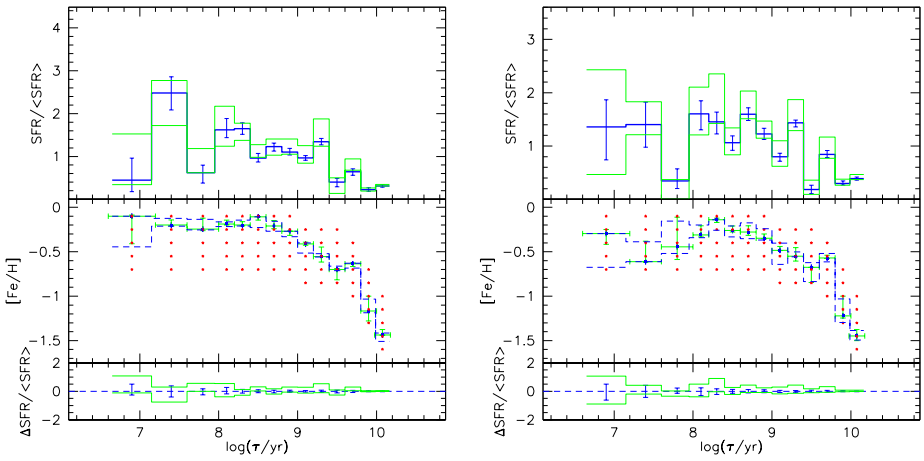

(d) SFR of sub region G7 and G8

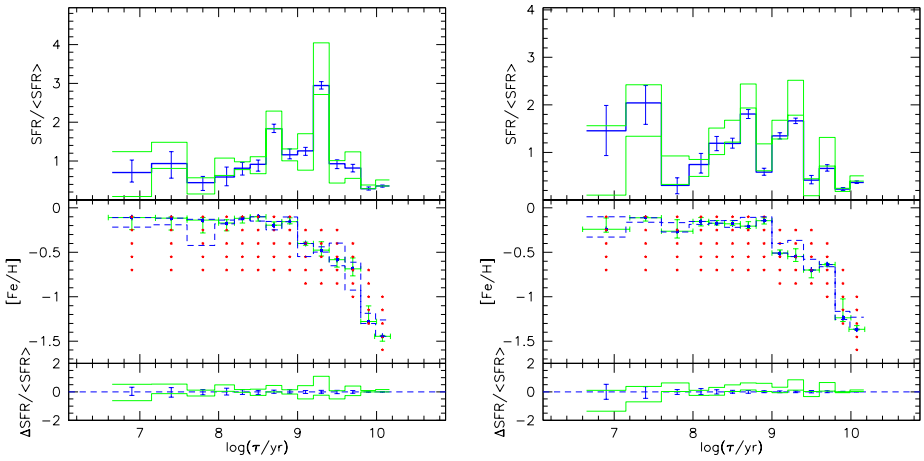

(e) SFR of sub region G9 and G10

Figure 6.10: SFR and AMR of sub-regions in field 8_3

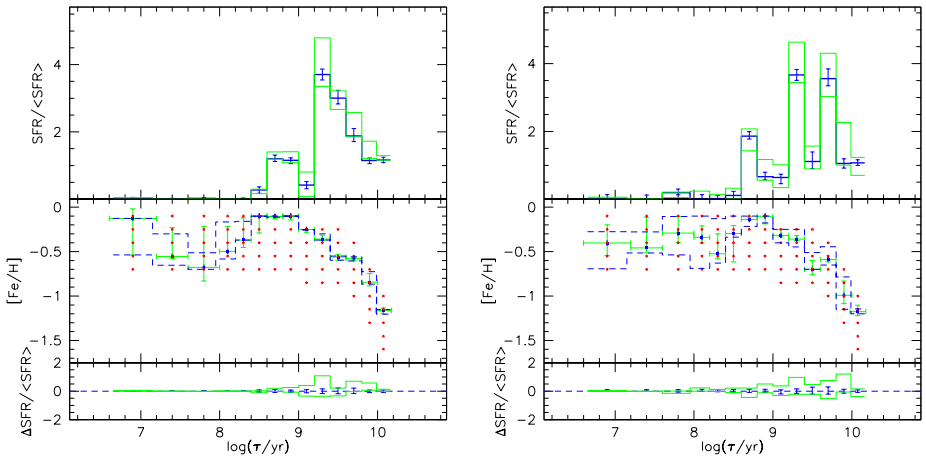

(a) SFR of sub region G1 and G2

Figure 6.11: SFR and AMR of sub-regions in field 4_3

racy. Otherwise in subregions richer of young stars the trend of the AMR is well evaluated.

- The SFH on this field changes from subregion to subregion but in all of them it is possible to evidence 3 main Star Formation (SF) episodes:

  1. The first SF main episode is located at $log(t/yr) = 9.7$ and with a [Fe/H] $\sim$ -0.70 [dex].
  2. From $log(t/yr) = 9$ to 9.4 and with an average [Fe/H] $\sim$ -0.475 [dex], which corresponds in age and metallicity to values found in LMC intermediate age clusters (Kerber et al. 2007; Olszewski et al. 1991; Mackey & Gilmore 2003; Grocholski et al. 2006) (see as example figure 3.7).
  3. A younger and in some cases prolonged SF episode from $log(t/yr) = 8$ to 8.6, 9 is present in all subregions on this field, the average [Fe/H] of this population is $\sim$ -0.175.

  SF for ages less than $log(t/yr) = 8$ are present in few sub-regions and present large errors.

AMR							
Log(Age)	6.9	7.4	7.8	8.1	8.3	8.5	8.7
[Fe/H]1	-0.10	-0.10	-0.10	-0.10	-0.10	-0.10	-0.10
[Fe/H]2	-0.25	-0.25	-0.25	-0.25	-0.25	-0.25	-0.25
[Fe/H]3	-0.40	-0.40	-0.40	-0.40	-0.40	-0.40	-0.40
[Fe/H]4	-0.55	-0.55	-0.55	-0.55	-0.55	-0.55	-0.55
[Fe/H]5	-0.70	-0.70	-0.70	-0.70	-0.70	-0.70	-0.70
Log(Age)	8.9	9.1	9.3	9.5	9.7	9.9	10.075
[Fe/H]1	-0.10	-0.25	-0.25	-0.25	-0.40	-0.70	-1.00
[Fe/H]2	-0.25	-0.40	-0.40	-0.40	-0.55	-0.85	-1.15
[Fe/H]3	-0.40	-0.55	-0.55	-0.55	-0.70	-1.00	-1.30
[Fe/H]4	-0.55	-0.70	-0.70	-0.70	-0.85	-1.15	-1.45
[Fe/H]5	-0.70	-0.85	-0.85	-0.85	-1.00	-1.30	-1.6

Table 6.1: AMR grid of stellar partial models used in the recovery the SFH.

Field 8_3	
Nikolaev et al. (2004)	$(m-M)_0 = 18.496 \pm 0.028$
van der Marel & Cioni (2001b)	$(m-M)_0 = 18.462 \pm 0.034$
van der Marel et al. (2002)	$(m-M)_0 = 18.466 \pm 0.035$
Sub-region	$(m-M)_0^{TW}$
G1	18.48±0.045
G2	18.44±0.035
G3	18.45±0.025
G4	18.47±0.03
G5	18.45±0.025
G6	18.43±0.025
G7	18.433±0.042
G8	18.439±0.036
G9	18.454±0.030
G10	18.458±0.017
Field 4_3	
Nikolaev et al. (2004)	$(m-M)_0 = 18.56 \pm 0.010$
van der Marel & Cioni (2001b)	$(m-M)_0 = 18.581 \pm 0.011$
van der Marel et al. (2002)	$(m-M)_0 = 18.576 \pm 0.012$
G1	18.562±0.027
G2	18.530±0.023
Field 8_8	
Nikolaev et al. (2004)	$(m-M)_0 = 18.392 \pm 0.016$
van der Marel & Cioni (2001b)	$(m-M)_0 = 18.387 \pm 0.016$
van der Marel et al. (2002)	$(m-M)_0 = 18.378 \pm 0.018$
G1	18.40±0.025
G2	18.385±0.04

Table 6.2: Table with $(m-M)_0$ values obtained in this work ($(m-M)_0^{TW}$) compared to values obtained in Nikolaev et al. (2004), van der Marel & Cioni (2001b) and van der Marel et al. (2002)

Sub-region	A_V^{CS}	A_V^{HS}	A_V^{TW}	$(m-M)_0^{TW}$
Field 8_3				
G1	0.45 ±0.32	0.57±0.44	0.282±0.045	18.48±0.045
G2	0.38±0.30	0.52±0.46	0.323±0.042	18.44±0.035
G3	0.35±0.26	0.49±0.41	0.33±0.045	18.45±0.025
G4	0.39±0.28	0.54±0.41	0.236±0.034	18.47±0.03
G5	0.41±0.32	0.54±0.45	0.36±0.033	18.45±0.025
G6	0.38±0.28	0.48±0.46	0.37±0.04	18.43±0.025
G7	0.33±0.26	0.45±0.41	0.36±0.030	18.433±0.042
G8	0.40±0.30	0.52±0.41	0.369±0.039	18.439±0.036
G9	0.37±0.26	0.63±0.48	0.42±0.033	18.454±0.030
G10	0.33±0.26	0.51±0.48	0.30±0.03	18.458±0.017
Field 4_3				
G1	0.42±0.32	0.73±0.43	0.21±0.03	18.562±0.027
G2	0.36±0.32	0.57±0.42	0.328±0.10	18.530±0.023
Field 8_8				
G1	0.25±0.2	0.67±0.49	0.28±0.093	18.4±0.025
G2	0.31±0.23	0.83±0.45	0.24±0.11	18.385±0.04

Table 6.3: Table with $(m-M)_0$ and A_V obtained in this work and compared to the A_V values obtained in Zaritsky et al. (2004)

Chapter 7

Conclusions

The Magellanic System has yet many challenging aspects that new surveys, with the increased quality of the coming data and new theoretical models and their ability to explain detail observations, aim to resolve in the next decade.

Prior to new facilities like GAIA, JWST and ALMA we need to exploit data from VISTA and similarly powerful telescopes at other wavelengths. Surveys like VMC will provide unique and high quality data for science and training of young astronomers.

- In chapter 3 we have performed detailed simulations of the LMC images expected from the VMC survey, and analysed them in terms of the expected accuracy in determining the space-resolved SFH. Our main conclusions from that work are the following:

    1. For a typical 0.10 deg^2 LMC field of median stellar density, the random errors in the recovered SFR(t) will be typically smaller than 20% for 0.2 dex-wide age bins.
    2. For all ages larger than 0.4 Gyr, at increasing stellar densities the better statistics largely compensates the effects of increased photometric errors and decreased completeness, so that good-quality SFR(t) can be determined even for the most crowded regions in the LMC bar. The SFR(t) errors decrease roughly in proportion with the square of the total number of stars. The exception to this rule regards the youngest stars, which because of their brightness are less affected by incompleteness. In this latter case, however, the stellar statistics is intrinsically small and large areas are necessary to reach the same SFR(t) accuracy as for the intermediate-age and old LMC stars.

3. Although the AMR [M/H](t) can be recovered with accuracies better than 0.2 dex, the uncertainties in the AMR can significantly affect the quality of the derived SFR(t), increasing their errors by a factor of about 2.5.
4. The minimisation algorithms allow to identify the best-fitting reddening and distance with accuracies of the order of 0.02 mag in distance modulus, and 0.01 mag in $E_{B\text{-}V}$.

All of the above trends were derived from analysis of small LMC areas, that we have considered to be homogeneous in all of their properties (AMR, distance and reddening). The errors were derived by varying each one of these parameters separately. The real situation will be, of course, much more complicated, with significant spatial variations of all of these quantities across the LMC. This consideration may lead us to suppose that errors here derived are underestimated. However, the above-mentioned parameters can be further constrained by simply taking into consideration additional data – for instance the available reddening maps, the limits on the relative distances provided by other independent distance indicators, the metallicity distributions of field stars, etc. – in our analysis. Moreover, our work indicates clearly how the random errors are reduced when we increase the area to be analysed. It is natural that, once the systematic errors are fully assessed, we will increase the area selected for the analysis, so that random errors become at least smaller than the systematic ones.

It is also worth mentioning that our present results were obtained using the $Y-K$ colour only. VMC does also provide CMDs involving the J passband, and their use in the SFH analysis can only reduce the final errors.

Another factor to be considered, in the final analysis, is that for old ages the SFR(t) is expected to vary very smoothly across the LMC, as indicated for instance by Cioni et al. (2000) and Nikolaev & Weinberg (2000b). This large-scale correlation in the old SFR(t) may be used as an additional constraint during the SFH-recovery, and may help to reduce the errors in the SFR(t) at all ages.

The present work already illustrates the excellent accuracy in the measurements of the space-resolved SFH, that is possible by VMC data. Moreover, it demonstrates that detailed SFH-recovery using deep near-infrared photometry is also feasible, as much it has always been for the case of visual observations.

- In chapter 4, we have derived the SFH of the SMC star cluster NGC 419, via the classical method of CMD reconstruction. This analysis implicitly assumes that NGC 419 is formed by a sum of single-burst stellar populations (or "partial models"), each one being characterized by a well-defined and narrow MSTO. The only effects that blur these partial models in the CMDs are the sequences of binaries (which effect however is far from dramatic) and the photometric errors. With this kind of approach, the broad MMSTO observed in NGC 419 naturally translate into a continued star formation history. We find a SFR(t) lasting for 700 Myr (from 1.2 to 1.9 Gyr, see Fig. 4.14), which is quite a long period, probably at the upper limit of all values already estimated for star clusters with MMSTOs (Bertelli et al. 2003; Baume et al. 2007; Mackey & Broby Nielsen 2007; Mackey et al. 2008; Milone et al. 2009; Goudfrooij et al. 2009). Our error analysis leaves practically no room for the MMSTOs in this cluster being caused by a single episode of star formation.

  It is also remarkable that the SFR(t) we derive presents a pronounced maximum at the middle of the star formation interval, at an age of 1.5 Gyr (Fig. 4.14). This is somewhat unexpected, in the context of the few suggested scenarios for the appearance of prolonged star formation in LMC star clusters (see Goudfrooij et al. 2009, for a comprehensive discussion of them). Either the merging of two star clusters (Mackey & Broby Nielsen 2007), or a second period of star formation driven by the merging with a giant molecular cloud (Bekki & Mackey 2009), would lead to strongly bimodal distributions of cluster ages, which we do not find in NGC 419. Only in the case of the best model with [Fe/H] $= -0.95$, there is an indication of two different peaks in the SFR(t) (see Fig. 4.12), which however are neither separated nor followed by periods of null SFR(t). Also the trapping of field stars by the forming star cluster (Pflamm-Altenburg & Kroupa 2007) would lead to different results, with the major peak of star formation being found at the youngest ages. On the other hand, our findings seem to be more in line with Goudfrooij et al. (2009)'s conclusions, based on the quite continuous distribution of stars across the MMSTO region of the LMC cluster NGC 1846. They suggest a scenario in which the star cluster continues to form stars in its center out of the ejecta of stars from previous generations. In our case, however, this process would have to proceed for a significantly more extended period of time than for NGC 1846, and peak – somewhat against the most naive expectations – at the middle of the star formation pe-

riod. Also, this latter scenario might imply some amount of self-enrichment in this cluster, whereas our method instead is compatible either with a constant metallicity, or with some amount of metal dillution. Needless to say, the present observational data is not clear enough to provide unambiguous indications about the formation scenario of such clusters.

Another basic result of our analysis is that the hypothesis of continued SFH, together with current stellar evolutionary models and a modest fraction of binaries, produces *excellent fits to the CMD of NGC 419*, with $\chi^2_{\rm min}$ as small as 0.93 – or even 0.84 if the [Fe/H] is let to vary during the SFH-recovery. We have translated this result into quantitative estimates for the random and systematic errors of the derived SFR(t). It is obvious that many combinations of cluster parameters produce acceptable solutions, with significance levels smaller than 95 %. However, the really good solutions – i.e. those with significance levels better then 68 % – cover a narrow region of the parameter space, comprising less than 0.1 mag in both $(m-M)_0$ and A_V, and about 0.1 dex in [Fe/H].

- In chapter 5, we perform SFH-recovery for NGC1751 via the classical method of CMD reconstruction with the sum of single-burst stellar populations. The basic result is that in the cluster Centre star formation is found to last for a timespan of 460 Myr. The same result is consistently found irrespective of the method used to take field contamination into account, of the age resolution adopted, and for a significant region of the A_V versus $(m-M)_0$ plane. The age resolution of the method is at least 3 times smaller than this interval. In addition, the best-fitting model is indeed a quite good representation of the observed data. On the other hand, the CMD for the cluster Centre is so obviously sharp and clean from the LMC field, that it is hard to imagine that some important effect has not been properly considered in our analysis.

  For the cluster Ring, the results indicate a SFR timespan of at least 460 Myr, with a significantly lower quality of the results, as indicated by the larger $\chi^2_{\rm min}$ and by the best fitting model being found for a distance different from the cluster Centre. These failures probably depend on the presence of significant differential reddening across the Ring. So, we prefer not to take any conclusion from this region. Unfortunately, our method finishes in not providing any indication about possible variations in the spatial distribution of the stars with different ages, which would be important for the goals of

understanding the mechanism of extended star formation (see Goudfrooij et al. 2009).

Together with our previous findings for the SMC cluster NGC 419 (Rubele et al. 2010), the results for the NGC 1751 Centre argue in favour of multiple star formation episodes (or continued star formation) being at the origin of the MMSTOs in Magellanic Cloud clusters with ages around 1.5 Gyr. The hypothesis of a spread caused by the presence of fast rotators among the upper main sequence stars, as advanced by Bastian & de Mink (2009), has be discussed by Girardi et al. (2011), who conclude that it does not offer a valid alternative to the presence of an age spread.

- In chapter 6 we have recovered the SFH on three VMC LMC fields evaluating simultaneously the best fitting SFR, AMR, A_V and $(m-M)_0$, and the stochastic and systematic errors inside the 68% confidence level in each subregion for each field. The comparison of A_V parameter derived in our work with Zaritsky et al. (2004) shows a good agreement. The $(m-M)_0$ values are in agreement with Nikolaev et al. (2004), van der Marel & Cioni (2001b) and van der Marel et al. (2002) works.

  Only the field 8_8 has a completion of 100%, so results of fields 8_3 and 4_3 will be improved in the future. In the case of field 8_3 we have recovered the SFH on the most part of the field (10 subregion on a total of 12), on which we conclude:

  - As mentioned before in this field the A_V and $(m-M)_0$ values we find are in agreement with literature works giving average values of 0.335 and 18.45 mag, respectively.
  - The trend of the AMR in each subregion do not change inside the evaluation region so we conclude that the AMR on this field is not space dependent. In subregions poor of stars younger than $log(t/yr)$ = 8 (null or low SFR), errors are large and it is not possible to evaluatethe metallicity with accuracy. Otherwise in subregions richer of young stars the trend of the AMR is well evaluated.
  - The SFH on this field changes from subregion to subregion but in all of them it is possible to evidence 3 main Star Formation (SF) episodes:
    1. The first SF main episode is located at $log(t/yr)$ = 9.7 and with a [Fe/H] $\sim$ -0.70 [dex].

2. From $log(t/yr) = 9$ to 9.4 and with an average [Fe/H] $\sim$ -0.475 [dex], which corresponds in age and metallicity to values found in LMC intermediate age clusters (Kerber et al. 2007; Olszewski et al. 1991; Mackey & Gilmore 2003; Grocholski et al. 2006) (see as example figure 3.7).
3. A younger and in some cases prolonged SF episode from $log(t/yr) = 8$ to 8.6, 9 is present in all subregions on this field, the average [Fe/H] of this population is $\sim$ -0.175.

SF for ages less than $log(t/yr) = 8$ are present in few sub-regions and present large errors.

Most of this work is already published, accepted or submitted :

- Recovery of the star formation history of the LMC from the VISTA survey of the Magellanic system (Kerber et al. 2009d)
- Discovery of two distinct red clumps in NGC 419: a rare snapshot of a cluster at the onset of degeneracy (Girardi et al. 2009)
- The star-formation history of the Small Magellanic Cloud star cluster NGC 419 (Rubele et al. 2010)
- The VMC Survey - I. Strategy and First Data (Cioni et al. 2010)
- The star formation history of the Large Magellanic Cloud star cluster NGC 1751 (Rubele et al. 2011)
- Star Formation History of Magellanic System I (Rubele et al. in preparation)

The last part on the SFH from VMC data is in preparation.

Bibliography

Alves, D. R. 2004, New Astronomy Review, 48, 659

Aparicio, A., Gallart, C., & Bertelli, G. 1997, AJ, 114, 680

Ardeberg, A., Gustafsson, B., Linde, P., & Nissen, P.-E. 1997, A&A, 322, L13

Arnaboldi, M., Dietrich, J., Hatziminaoglou, E., et al. 2008, The Messenger, 134, 42

Arnaboldi, M., Petr-Gotzens, M., Rejkuba, M., et al. 2010, The Messenger, 139, 6

Bastian, N. & de Mink, S. E. 2009, MNRAS, 398, L11

Battinelli, P. & Demers, S. 1992, AJ, 104, 1458

Baume, G., Carraro, G., Costa, E., Méndez, R. A., & Girardi, L. 2007, MNRAS, 375, 1077

Bekki, K. & Mackey, A. D. 2009, MNRAS, 394, 124

Bertelli, G., Bressan, A., Chiosi, C., Fagotto, F., & Nasi, E. 1994, A&AS, 106, 275

Bertelli, G., Girardi, L., Marigo, P., & Nasi, E. 2008, A&A, 484, 815

Bertelli, G., Mateo, M., Chiosi, C., & Bressan, A. 1992, ApJ, 388, 400

Bertelli, G., Nasi, E., Girardi, L., et al. 2003, AJ, 125, 770

Bertin, E. & Arnouts, S. 1996, A&AS, 117, 393

Bertin, E., Mellier, Y., Radovich, M., et al. 2002a, in Astronomical Society of the Pacific Conference Series, Vol. 281, Astronomical Data Analysis Software and Systems XI, ed. D. A. Bohlender, D. Durand, & T. H. Handley, 228–+

Bertin, E., Mellier, Y., Radovich, M., et al. 2002b, in Astronomical Society of the Pacific Conference Series, Vol. 281, Astronomical Data Analysis Software and Systems XI, ed. D. A. Bohlender, D. Durand, & T. H. Handley, 228–+

Besla, G., Kallivayalil, N., Hernquist, L., et al. 2007, ApJ, 668, 949

Bica, E., Bonatto, C., Dutra, C. M., & Santos, J. F. C. 2008, MNRAS, 389, 678

Bica, E., Geisler, D., Dottori, H., et al. 1998, AJ, 116, 723

Bonatto, C., Bica, E., & Girardi, L. 2004, A&A, 415, 571

Bonnarel, F., Fernique, P., Bienaymé, O., et al. 2000, A&AS, 143, 33

Bothun, G. D. & Thompson, I. B. 1988, AJ, 96, 877

Bressan, A., Fagotto, F., Bertelli, G., & Chiosi, C. 1993, A&AS, 100, 647

Bressan, A. G., Chiosi, C., & Bertelli, G. 1981, A&A, 102, 25

Calabretta, M. R. & Greisen, E. W. 2002, A&A, 395, 1077

Capaccioli, M., Mancini, D., & Sedmak, G. 2005, The Messenger, 120, 10

Cardelli, J. A., Clayton, G. C., & Mathis, J. S. 1989, ApJ, 345, 245

Carrera, R., Gallart, C., Hardy, E., Aparicio, A., & Zinn, R. 2008, AJ, 135, 836

Chabrier, G. 2001, ApJ, 554, 1274

Chiosi, E. & Vallenari, A. 2007, A&A, 466, 165

Cioni, M., Bekki, K., Clementini, G., de Blok, W. J. G., & Emerson, e. a. 2008, Publications of the Astronomical Society of Australia, 25, 121

Cioni, M., Clementini, G., Girardi, L., et al. 2010, ArXiv e-prints

Cioni, M. . L., Bekki, K., Clementini, G., et al. 2007, ArXiv e-prints, 710

Cioni, M.-R. L., Girardi, L., Marigo, P., & Habing, H. J. 2006a, A&A, 448, 77

Cioni, M.-R. L., Girardi, L., Marigo, P., & Habing, H. J. 2006b, A&A, 452, 195

Cioni, M.-R. L., Habing, H. J., & Israel, F. P. 2000, A&A, 358, L9

Clementini, G., Gratton, R., Bragaglia, A., et al. 2003, AJ, 125, 1309

Cole, A. A., Skillman, E. D., Tolstoy, E., et al. 2007, ApJ, 659, L17

Cole, A. A., Tolstoy, E., Gallagher, III, J. S., & Smecker-Hane, T. A. 2005, AJ, 129, 1465

Cross, N. J. G., Collins, R. S., Hambly, N. C., et al. 2009, MNRAS, 399, 1730

Crowl, H. H., Sarajedini, A., Piatti, A. E., et al. 2001, AJ, 122, 220

da Silva, L., Girardi, L., Pasquini, L., et al. 2006, A&A, 458, 609

Dalton, G. B., Caldwell, M., Ward, A. K., et al. 2006, in Presented at the Society of Photo-Optical Instrumentation Engineers (SPIE) Conference, Vol. 6269, Society of Photo-Optical Instrumentation Engineers (SPIE) Conference Series

Dolphin, A. 1997, New Astronomy, 2, 397

Dolphin, A. E. 2002, MNRAS, 332, 91

Dolphin, A. E., Saha, A., Skillman, E. D., et al. 2003, AJ, 126, 187

Dolphin, A. E., Walker, A. R., Hodge, P. W., et al. 2001, ApJ, 562, 303

Durand, D., Hardy, E., & Melnick, J. 1984, ApJ, 283, 552

Elson, R. A. W., Gilmore, G. F., & Santiago, B. X. 1997, MNRAS, 289, 157

Elson, R. A. W., Sigurdsson, S., Davies, M., Hurley, J., & Gilmore, G. 1998a, MNRAS, 300, 857

Elson, R. A. W., Sigurdsson, S., Davies, M., Hurley, J., & Gilmore, G. 1998b, MNRAS, 300, 857

Emerson, J., McPherson, A., & Sutherland, W. 2006, The Messenger, 126, 41

Emerson, J. & Sutherland, W. 2010, The Messenger, 139, 2

Ferraro, F. R., Fusi Pecci, F., Tosi, M., & Buonanno, R. 1989, MNRAS, 241, 433

Foucaud, S., Almaini, O., Smail, I., et al. 2007, MNRAS, 376, L20

Freedman, W. L., Madore, B. F., Gibson, B. K., et al. 2001, ApJ, 553, 47

Frogel, J. A., Mould, J., & Blanco, V. M. 1990, ApJ, 352, 96

Gallagher, J. S., Mould, J. R., de Feijter, E., Holtzman, J., & Stappers, e. a. 1996, ApJ, 466, 732

Gallart, C., Aparicio, A., Bertelli, G., & Chiosi, C. 1996a, AJ, 112, 2596

Gallart, C., Aparicio, A., & Vilchez, J. M. 1996b, AJ, 112, 1928

Gallart, C., Freedman, W. L., Aparicio, A., Bertelli, G., & Chiosi, C. 1999, AJ, 118, 2245

Gallart, C., Stetson, P. B., Hardy, E., Pont, F., & Zinn, R. 2004, ApJ, 614, L109

Gallart, C., Zoccali, M., & Aparicio, A. 2005, ARA&A, 43, 387

Gardiner, L. T. & Hatzidimitriou, D. 1992, MNRAS, 257, 195

Gaustad, J. E., McCullough, P. R., Rosing, W., & Van Buren, D. 2001, PASP, 113, 1326

Girardi, L. 1999, MNRAS, 308, 818

Girardi, L., Bertelli, G., Bressan, A., et al. 2002, A&A, 391, 195

Girardi, L., Bressan, A., Bertelli, G., & Chiosi, C. 2000a, A&AS, 141, 371

Girardi, L., Dalcanton, J., Williams, B., et al. 2008, PASP, 120, 583

Girardi, L., Eggenberger, P., & Miglio, A. 2011, ArXiv e-prints

Girardi, L., Groenewegen, M. A. T., Hatziminaoglou, E., & da Costa, L. 2005, A&A, 436, 895

Girardi, L., Groenewegen, M. A. T., Weiss, A., & Salaris, M. 1998, MNRAS, 301, 149

Girardi, L., Mermilliod, J.-C., & Carraro, G. 2000b, A&A, 354, 892

Girardi, L., Rubele, S., & Kerber, L. 2009, MNRAS, 394, L74

Girardi, L., Rubele, S., & Kerber, L. 2010, in IAU Symposium, Vol. 266, IAU Symposium, ed. R. de Grijs & J. R. D. Lépine, 320–325

Glatt, K., Grebel, E. K., Gallagher, J. S., et al. 2009, AJ, 138, 1403

Glatt, K., Grebel, E. K., Sabbi, E., et al. 2008, AJ, 136, 1703

Goudfrooij, P., Puzia, T. H., Kozhurina-Platais, V., & Chandar, R. 2009, AJ, 137, 4988

Gouliermis, D., Keller, S. C., Kontizas, M., Kontizas, E., & Bellas-Velidis, I. 2004, A&A, 416, 137

Grocholski, A. J., Cole, A. A., Sarajedini, A., Geisler, D., & Smith, V. V. 2006, AJ, 132, 1630

Grocholski, A. J. & Sarajedini, A. 2002, AJ, 123, 1603

Grocholski, A. J., Sarajedini, A., Olsen, K. A. G., Tiede, G. P., & Mancone, C. L. 2007, AJ, 134, 680

Gullieuszik, M., Held, E. V., Rizzi, L., et al. 2008, ArXiv e-prints, 805

Hambly, N. C., Collins, R. S., Cross, N. J. G., et al. 2008, MNRAS, 384, 637

Harries, T. J., Hilditch, R. W., & Howarth, I. D. 2003, MNRAS, 339, 157

Harris, J. 2007a, ApJ, 658, 345

Harris, J. 2007b, ApJ, 658, 345

Harris, J. 2007c, ApJ, 658, 345

Harris, J. & Zaritsky, D. 2001, ApJS, 136, 25

Harris, J. & Zaritsky, D. 2004, AJ, 127, 1531

Harris, J. & Zaritsky, D. 2007, ArXiv e-prints, 712

Harris, J. & Zaritsky, D. 2009, AJ, 138, 1243

Hatzidimitriou, D., Stanimirovic, S., Maragoudaki, F., et al. 2005, MNRAS, 360, 1171

Hernandez, X., Gilmore, G., & Valls-Gabaud, D. 2000, MNRAS, 317, 831

Hernandez, X. & Valls-Gabaud, D. 2008, MNRAS, 383, 1603

Hernandez, X., Valls-Gabaud, D., & Gilmore, G. 1999, MNRAS, 304, 705

Hewett, P. C., Warren, S. J., Leggett, S. K., & Hodgkin, S. T. 2006, MNRAS, 367, 454

Hodgkin, S. T., Irwin, M. J., Hewett, P. C., & Warren, S. J. 2009, MNRAS, 394, 675

Holtzman, J. A., Gallagher, III, J. S., Cole, A. A., et al. 1999, AJ, 118, 2262

Holtzman, J. A., Mould, J. R., Gallagher, III, J. S., et al. 1997, AJ, 113, 656

Hu, Y., Deng, L., deGrijs, R., Goodwin, S. P., & Liu, Q. 2008, ArXiv e-prints, 801

Imara, N. & Blitz, L. 2007, ApJ, 662, 969

Irwin, M. 2009, 25

Irwin, M. 2010, 26

Irwin, M. J. 1991, in IAU Symposium, Vol. 148, The Magellanic Clouds, ed. R. Haynes & D. Milne, 453–+

Irwin, M. J., Lewis, J., Hodgkin, S., et al. 2004, in Society of Photo-Optical Instrumentation Engineers (SPIE) Conference Series, Vol. 5493, Society of Photo-Optical Instrumentation Engineers (SPIE) Conference Series, ed. P. J. Quinn & A. Bridger, 411–422

Javiel, S. C., Santiago, B. X., & Kerber, L. O. 2005, A&A, 431, 73

Jørgensen, B. R. & Lindegren, L. 2005, A&A, 436, 127

Kallivayalil, N., van der Marel, R. P., & Alcock, C. 2006a, ApJ, 652, 1213

Kallivayalil, N., van der Marel, R. P., Alcock, C., et al. 2006b, ApJ, 638, 772

Kato, D., Nagashima, C., Nagayama, T., et al. 2007, PASJ, 59, 615

Kayser, A., Grebel, E. K., Harbeck, D. R., et al. 2009, The Age-Metallicity Relation of the SMC, ed. S. Richtler, T. Larsen, 157–+

Kerber, L. O., Girardi, L., Rubele, S., & Cioni, M. 2009a, A&A, 499, 697

Kerber, L. O., Girardi, L., Rubele, S., & Cioni, M. 2009b, A&A, 499, 697

Kerber, L. O., Girardi, L., Rubele, S., & Cioni, M.-R. 2009c, A&A, 499, 697

Kerber, L. O., Girardi, L., Rubele, S., & Cioni, M.-R. 2009d, A&A, 499, 697

Kerber, L. O., Santiago, B. X., & Brocato, E. 2007, A&A, 462, 139

Kroupa, P. 2001, MNRAS, 322, 231

Kroupa, P. 2002, Science, 295, 82

Lah, P., Kiss, L. L., & Bedding, T. R. 2005, MNRAS, 359, L42

Lasker, B. M., Lattanzi, M. G., McLean, B. J., et al. 2008, AJ, 136, 735

Lawrence, A., Warren, S. J., Almaini, O., et al. 2007, MNRAS, 379, 1599

Mackey, A. D. & Broby Nielsen, P. 2007, MNRAS, 379, 151

Mackey, A. D., Broby Nielsen, P., Ferguson, A. M. N., & Richardson, J. C. 2008, ApJ, 681, L17

Mackey, A. D. & Gilmore, G. F. 2003, MNRAS, 338, 85

Marigo, P. & Girardi, L. 2007, A&A, 469, 239

Marigo, P., Girardi, L., Bressan, A., et al. 2008, A&A, 482, 883

Marigo, P., Girardi, L., & Chiosi, C. 2003a, A&A, 403, 225

Marigo, P., Girardi, L., & Chiosi, C. 2003b, A&A, 403, 225

Mastropietro, C. 2009, in IAU Symposium, Vol. 256, IAU Symposium, ed. J. T. van Loon & J. M. Oliveira, 117–121

McClure-Griffiths, N. M., Pisano, D. J., Calabretta, M. R., et al. 2009, ApJS, 181, 398

Mermilliod, J.-C., Mathieu, R. D., Latham, D. W., & Mayor, M. 1998, A&A, 339, 423

Mighell, K. J., Rich, R. M., Shara, M., & Fall, S. M. 1996, AJ, 111, 2314

Milone, A. P., Bedin, L. R., Piotto, G., & Anderson, J. 2009, A&A, 497, 755

Mucciarelli, A., Carretta, E., Origlia, L., & Ferraro, F. R. 2008, AJ, 136, 375

Muller, E., Staveley-Smith, L., Zealey, W., & Stanimirović, S. 2003, MNRAS, 339, 105

Naylor, T. & Jeffries, R. D. 2006, MNRAS, 373, 1251

Nikolaev, S., Drake, A. J., Keller, S. C., et al. 2004, ApJ, 601, 260

Nikolaev, S. & Weinberg, M. D. 2000a, ApJ, 542, 804

Nikolaev, S. & Weinberg, M. D. 2000b, ApJ, 542, 804

Noël, N. E. D., Aparicio, A., Gallart, C., et al. 2009, ApJ, 705, 1260

Noël, N. E. D., Gallart, C., Costa, E., & Méndez, R. A. 2007, AJ, 133, 2037

Nordström, B., Mayor, M., Andersen, J., et al. 2004, A&A, 418, 989

North, P. L., Gauderon, R., & Royer, F. 2009, in IAU Symposium, Vol. 256, IAU Symposium, ed. J. T. van Loon & J. M. Oliveira, 57–62

Olsen, K. A. G. 1999, AJ, 117, 2244

Olsen, K. A. G. & Salyk, C. 2002, AJ, 124, 2045

Olszewski, E. W., Schommer, R. A., Suntzeff, N. B., & Harris, H. C. 1991, AJ, 101, 515

Parisi, M. C., Grocholski, A. J., Geisler, D., Sarajedini, A., & Clariá, J. J. 2009, AJ, 138, 517

Pejcha, O. & Stanek, K. Z. 2009, ApJ, 704, 1730

Pessev, P. M., Goudfrooij, P., Puzia, T. H., & Chandar, R. 2008, MNRAS, 385, 1535

Pflamm-Altenburg, J. & Kroupa, P. 2007, MNRAS, 375, 855

Piatek, S., Pryor, C., & Olszewski, E. W. 2008, AJ, 135, 1024

Piatti, A. E., Geisler, D., Bica, E., et al. 1999, AJ, 118, 2865

Rich, R. M., Shara, M., Fall, S. M., & Zurek, D. 2000, AJ, 119, 197

Rich, R. M., Shara, M. M., & Zurek, D. 2001, AJ, 122, 842

Riess, A. & Mack, J. 2004, Time Dependence of ACS WFC CTE Corrections for Photometry and Future Predictions, Tech. rep.

Rubele, S., Kerber, L., & Girardi, L. 2010, MNRAS, 403, 1156

Schaefer, B. E. 2008, AJ, 135, 112

Schlegel, D. J., Finkbeiner, D. P., & Davis, M. 1998a, ApJ, 500, 525

Schlegel, D. J., Finkbeiner, D. P., & Davis, M. 1998b, ApJ, 500, 525

Sirianni, M., Jee, M. J., Benítez, N., et al. 2005, PASP, 117, 1049

Skillman, E. D., Tolstoy, E., Cole, A. A., et al. 2003, ApJ, 596, 253

Smecker-Hane, T. A., Cole, A. A., Gallagher, III, J. S., & Stetson, P. B. 2002, ApJ, 566, 239

Stappers, B. W., Mould, J. R., Sebo, K. M., et al. 1997, PASP, 109, 292

Staveley-Smith, L., Kim, S., Calabretta, M. R., Haynes, R. F., & Kesteven, M. J. 2003, MNRAS, 339, 87

Stetson, P. B. 1987, PASP, 99, 191

Subramaniam, A. 2005, A&A, 430, 421

Subramanian, S. & Subramaniam, A. 2010a, A&A, 520, A24+

Subramanian, S. & Subramaniam, A. 2010b, A&A, 520, A24+

Sweigart, A. V., Greggio, L., & Renzini, A. 1990, ApJ, 364, 527

Tolstoy, E. & Saha, A. 1996, ApJ, 462, 672

Tosi, M., Greggio, L., & Focardi, P. 1989, Ap&SS, 156, 295

Tosi, M., Greggio, L., Marconi, G., & Focardi, P. 1991, AJ, 102, 951

van der Marel, R. P., Alves, D. R., Hardy, E., & Suntzeff, N. B. 2002, AJ, 124, 2639

van der Marel, R. P. & Cioni, M. 2001a, AJ, 122, 1807

van der Marel, R. P. & Cioni, M.-R. L. 2001b, AJ, 122, 1807

Vanhollebeke, E., Groenewegen, M. A. T., & Girardi, L. 2008, A&A, submitted

Vergely, J.-L., Köppen, J., Egret, D., & Bienaymé, O. 2002, A&A, 390, 917

Warren, S. J., Hambly, N. C., Dye, S., et al. 2007, MNRAS, 375, 213

Westerlund, B. E. 1997, The Magellanic Clouds (Book,)

Woo, J.-H., Gallart, C., Demarque, P., Yi, S., & Zoccali, M. 2003, AJ, 125, 754

Yuk, I.-S. & Lee, M. G. 2007, ApJ, 668, 876

Zaritsky, D., Harris, J., & Thompson, I. 1997, AJ, 114, 1002

Zaritsky, D., Harris, J., Thompson, I. B., & Grebel, E. K. 2004, AJ, 128, 1606

Zaritsky, D., Harris, J., Thompson, I. B., Grebel, E. K., & Massey, P. 2002, AJ, 123, 855

Appendix A

VMC survey

A.1 VMC tile centres

Tables A.1 and A.2 show the centres of VMC tiles covering the LMC, while Table A.3 shows the centres of tiles covering the SMC and Table A.4 shows the centres of tiles covering the Bridge. The tile identification is formed of two numbers. The first number indicates the row and the second number the column that correspond to the location of a given tile. Row numbers increase from bottom to top while column numbers increase from right to left. Refer to Figures A.1, A.2 and A.3 for the location of tiles across the LMC, SMC and Bridge components of the Magellanic system, respectively. For the Stream the central coordinates of two distinct tiles are indicated in Table A.5. Note that since tiles were generated from almost rectangular grids, some outer tiles were removed leading to the tile numbers shown here.

Table A.1: LMC tile centres

Tile	α	δ	Comments
2_3	04 : 48 : 04.752	−74 : 54 : 11.880	
2_4	05 : 04 : 42.696	−75 : 04 : 45.120	
2_5	05 : 21 : 38.664	−75 : 10 : 50.160	
2_6	05 : 38 : 43.056	−75 : 12 : 21.240	
2_7	05 : 55 : 45.720	−75 : 09 : 17.280	
3_2	04 : 37 : 05.256	−73 : 14 : 30.120	
3_3	04 : 51 : 59.640	−73 : 28 : 09.120	
3_4	05 : 07 : 14.472	−73 : 37 : 49.800	
3_5	05 : 22 : 43.056	−73 : 43 : 25.320	started
3_6	05 : 38 : 18.096	−73 : 44 : 51.000	
3_7	05 : 53 : 51.912	−73 : 42 : 05.760	
3_8	06 : 09 : 16.920	−73 : 35 : 12.120	
4_2	04 : 41 : 30.768	−71 : 49 : 16.320	started
4_3	04 : 55 : 19.512	−72 : 01 : 53.400	started
4_4	05 : 09 : 24.288	−72 : 10 : 49.800	
4_5	05 : 23 : 39.816	−72 : 15 : 59.760	
4_6	05 : 38 : 00.408	−72 : 17 : 20.040	started
4_7	05 : 52 : 20.064	−72 : 14 : 49.920	
4_8	06 : 06 : 32.952	−72 : 08 : 31.200	
4_9	06 : 20 : 33.408	−71 : 58 : 27.120	
5_1	04 : 32 : 43.848	−70 : 08 : 40.200	
5_2	04 : 45 : 19.440	−70 : 23 : 43.800	
5_3	04 : 58 : 11.664	−70 : 35 : 27.960	
5_4	05 : 11 : 16.704	−70 : 43 : 46.200	
5_5	05 : 24 : 30.336	−70 : 48 : 34.200	started
5_6	05 : 37 : 47.952	−70 : 49 : 49.440	
5_7	05 : 51 : 04.872	−70 : 47 : 31.200	
5_8	06 : 04 : 16.416	−70 : 41 : 40.560	
5_9	06 : 17 : 18.096	−70 : 32 : 20.760	
6_1	04 : 36 : 49.488	−68 : 43 : 50.880	
6_2	04 : 48 : 39.072	−68 : 57 : 56.520	
6_3	05 : 00 : 42.216	−69 : 08 : 54.240	
6_4	05 : 12 : 55.800	−69 : 16 : 39.360	started
6_5	05 : 25 : 16.271	−69 : 21 : 08.280	
6_6	05 : 37 : 40.008	−69 : 22 : 18.120	30 Dor – completed
6_7	05 : 50 : 03.168	−69 : 20 : 09.240	
6_8	06 : 02 : 21.984	−69 : 14 : 42.360	in queue
6_9	06 : 14 : 32.832	−69 : 05 : 59.640	
6_10	06 : 26 : 32.280	−68 : 54 : 05.760	

Table A.2: LMC tile centres (continue)

Tile	α	δ	Comments
7_2	04 : 51 : 34.992	−67 : 31 : 57.000	
7_3	05 : 02 : 55.200	−67 : 42 : 14.760	in queue
7_4	05 : 14 : 23.976	−67 : 49 : 30.720	
7_5	05 : 25 : 58.440	−67 : 53 : 42.000	in queue
7_6	05 : 37 : 35.544	−67 : 54 : 47.160	
7_7	05 : 49 : 12.192	−67 : 52 : 45.480	
7_8	06 : 00 : 45.240	−67 : 47 : 38.040	
7_9	06 : 12 : 11.736	−67 : 39 : 26.640	
7_10	06 : 23 : 28.800	−67 : 28 : 14.880	
8_2	04 : 54 : 11.568	−66 : 05 : 47.760	
8_3	05 : 04 : 53.952	−66 : 15 : 29.880	started
8_4	05 : 15 : 43.464	−66 : 22 : 19.920	
8_5	05 : 26 : 37.704	−66 : 26 : 15.720	
8_6	05 : 37 : 34.104	−66 : 27 : 15.840	
8_7	05 : 48 : 30.120	−66 : 25 : 19.920	
8_8	05 : 59 : 23.136	−66 : 20 : 28.680	Gaia − completed
8_9	06 : 10 : 10.632	−66 : 12 : 43.560	
9_3	05 : 06 : 40.632	−64 : 48 : 40.320	started
9_4	05 : 16 : 55.464	−64 : 55 : 07.680	
9_5	05 : 27 : 14.256	−64 : 58 : 49.440	
9_6	05 : 37 : 34.872	−64 : 59 : 44.520	
9_7	05 : 47 : 55.128	−64 : 57 : 52.920	in queue
9_8	05 : 58 : 12.816	−64 : 53 : 15.000	
9_9	06 : 08 : 25.848	−64 : 45 : 52.560	
10_4	05 : 18 : 01.536	−63 : 27 : 54.000	
10_5	05 : 27 : 48.912	−63 : 31 : 22.800	
10_6	05 : 37 : 37.800	−63 : 32 : 13.200	
10_7	05 : 47 : 26.352	−63 : 30 : 24.840	
11_6	05 : 37 : 42.432	−62 : 04 : 41.520	

Table A.3: SMC tile centres

Tile	α	δ	Comments
2_2	00 : 21 : 43.920	−75 : 12 : 04.320	
2_3	00 : 44 : 35.904	−75 : 18 : 13.320	
2_4	01 : 07 : 33.864	−75 : 15 : 59.760	
2_5	01 : 30 : 12.624	−75 : 05 : 27.600	
3_1	00 : 02 : 39.912	−73 : 53 : 31.920	
3_2	00 : 23 : 35.544	−74 : 06 : 57.240	
3_3	00 : 44 : 55.896	−74 : 12 : 42.120	started
3_4	01 : 06 : 21.120	−74 : 10 : 38.640	
3_5	01 : 27 : 30.816	−74 : 00 : 49.320	started
3_6	01 : 48 : 06.120	−73 : 43 : 28.200	
4_1	00 : 05 : 33.864	−72 : 49 : 12.000	
4_2	00 : 25 : 14.088	−73 : 01 : 47.640	
4_3	00 : 45 : 14.688	−73 : 07 : 11.280	
4_4	01 : 05 : 19.272	−73 : 05 : 15.360	NGC 419
4_5	01 : 25 : 11.088	−72 : 56 : 02.760	
4_6	01 : 44 : 34.512	−72 : 39 : 44.640	
5_2	00 : 26 : 41.688	−71 : 56 : 35.880	started
5_3	00 : 45 : 32.232	−72 : 01 : 40.080	
5_4	01 : 04 : 26.112	−71 : 59 : 51.000	NGC 411 − started
5_5	01 : 23 : 09.336	−71 : 51 : 09.720	
5_6	01 : 41 : 28.800	−71 : 35 : 47.040	in queue
6_2	00 : 28 : 00.192	−70 : 51 : 21.960	
6_3	00 : 45 : 48.792	−70 : 56 : 09.240	
6_4	01 : 03 : 40.152	−70 : 54 : 25.200	
6_5	01 : 21 : 22.560	−70 : 46 : 11.640	
7_3	00 : 46 : 04.728	−69 : 50 : 38.040	
7_4	01 : 03 : 00.480	−69 : 48 : 58.320	

Table A.4: Bridge tile centres

Tile	α	δ	Comments
1_2	01 : 49 : 51.960	−74 : 43 : 31.800	
1_3	02 : 11 : 35.232	−75 : 05 : 04.560	
2_3	02 : 14 : 46.584	−74 : 00 : 47.520	started
2_4	02 : 35 : 28.440	−74 : 13 : 18.840	
2_7	03 : 39 : 43.800	−74 : 04 : 51.960	
2_8	04 : 00 : 21.072	−73 : 46 : 37.560	started
2_9	04 : 20 : 05.640	−73 : 21 : 14.040	
3_3	02 : 17 : 35.496	−72 : 56 : 22.200	
3_4	02 : 37 : 24.888	−73 : 08 : 16.440	
3_5	02 : 57 : 33.288	−73 : 12 : 52.200	started
3_6	03 : 17 : 43.776	−73 : 10 : 03.720	
3_7	03 : 37 : 39.240	−72 : 59 : 54.600	in queue
3_8	03 : 57 : 03.888	−72 : 42 : 37.800	

Table A.5: Stream tile centres

Tile	α	δ	Comments
1_1	03 : 30 : 03.87	−64 : 25 : 24.8	started
2_1	00 : 11 : 59.30	−64 : 39 : 31.8	started

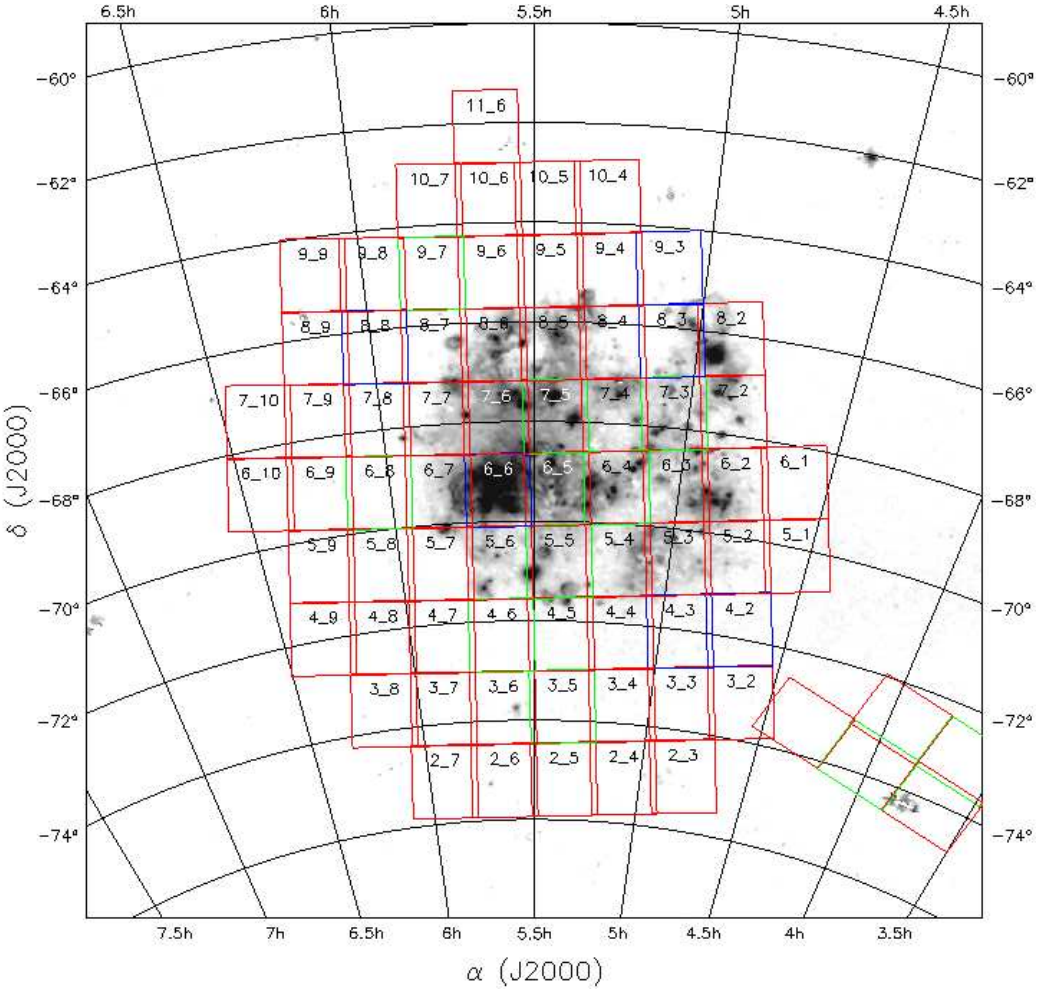

Figure A.1: LMC area tiled for VMC observations. The underlying image shows the Hα distribution (Gaustad et al. Gaustad et al. (2001)). VISTA tiles are colour-coded as in Fig. 2.4.

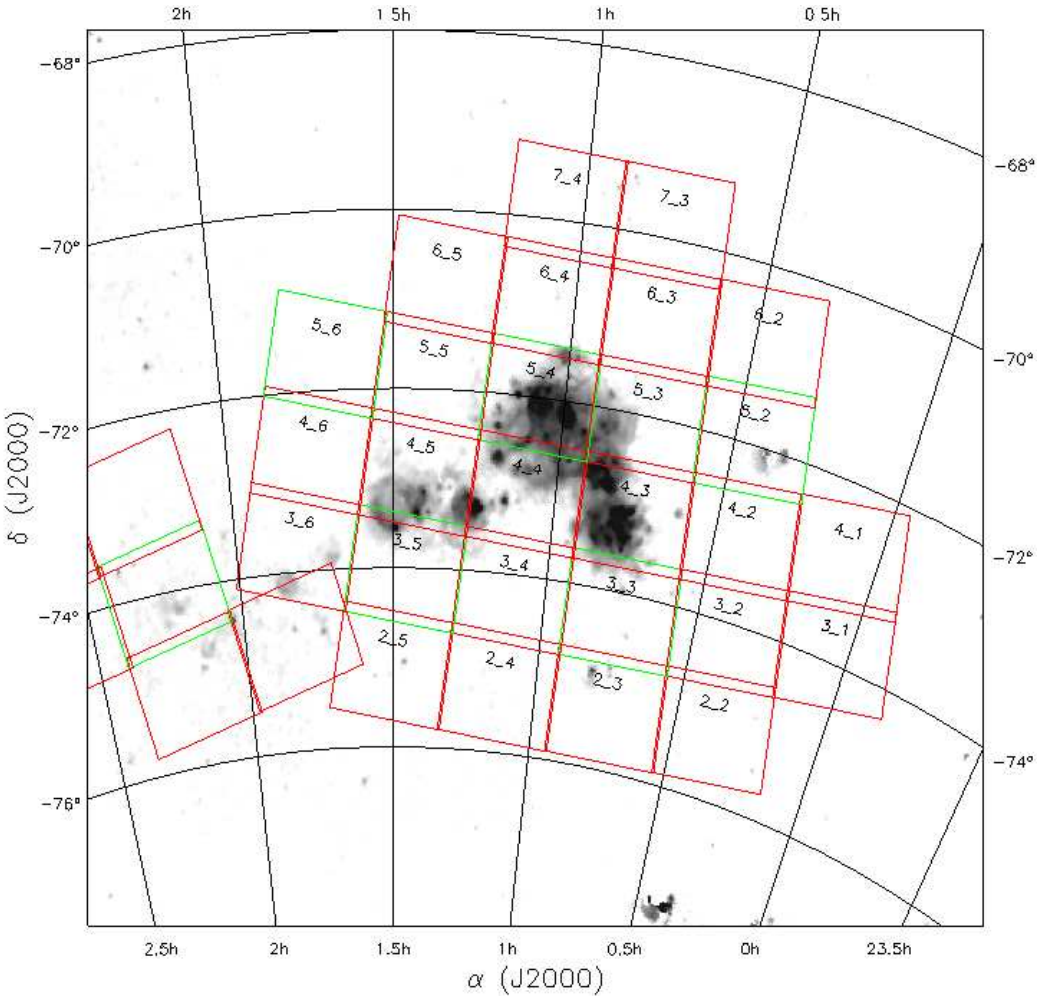

Figure A.2: SMC area tiled for VMC observations. The underlying image shows the Hα distribution (Gaustad et al. Gaustad et al. (2001)). VISTA tiles are colour-coded as in Fig. 2.4.

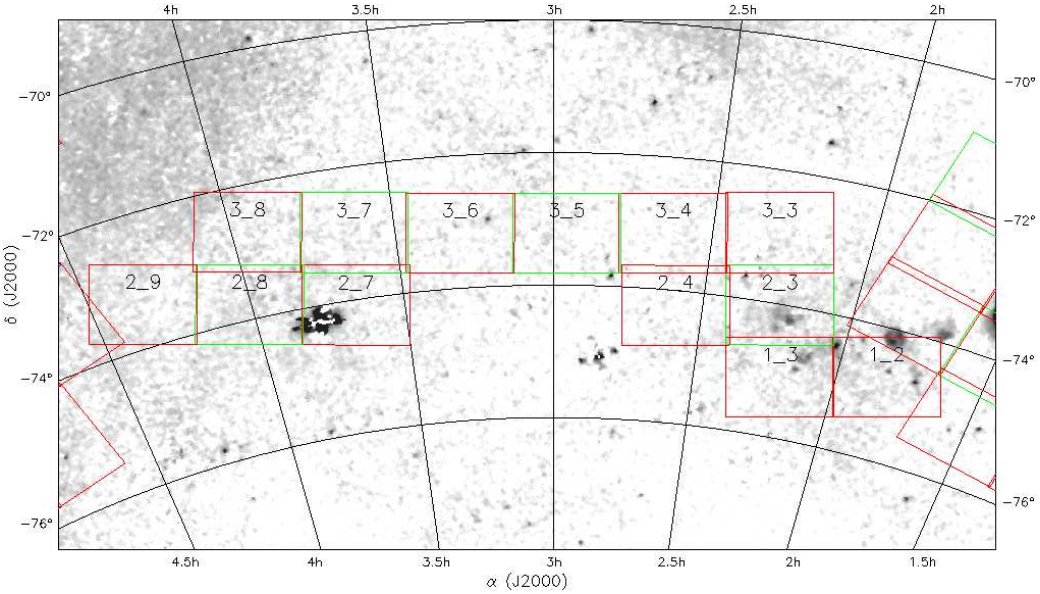

Figure A.3: Bridge area tiled for VMC observations. The underlying image shows the Hα distribution (McClure-Griffiths et al. McClure-Griffiths et al. (2009)). VISTA tiles are colour-coded as in Fig. 2.4.